Measurement of the photon polarization using B0 s $\rightarrow$ $\phi\gamma$ at LHCb

Mostafa Hoballah

Numéro d'Ordre : DU 2555 PCCF T 1502
EDSF : 817

UNIVERSITÉ BLAISE PASCAL DE
CLERMONT-FERRAND
(U.F.R. Sciences et Technologies)

ÉCOLE DOCTORALE DES SCIENCES FONDAMENTALES

THÈSE

présentée pour obtenir le grade de

DOCTEUR D'UNIVERSITÉ
Spécialité : PHYSIQUE des PARTICULES

par

Mostafa HOBALLAH

Measurement of the photon polarization using $B_s^0 \to \phi\gamma$ at LHCb.

Thèse soutenue publiquement le 03 Mars 2015, devant la commission d'examen:

M. A. FALVARD	*Président du jury*
M. A. A. GALLAS TORREIRA	*Rapporteur*
Mme. E. TOURNFIER	*Rapporteur*
M. K. TRABELSI	*Examinateur*
M. O. DESCHAMPS	*Directeur de thèse*
M. P. PERRET	*Directeur de thèse*

Résumé

Cette thèse est dédiée à l'étude des désintégrations $B_s^0 \to \phi\gamma$ au LHCb afin de mesurer la polarisation du photon . Au niveau des quarks, ces désintégrations procèdent via une transition pingouin $b \to s\gamma$ et sont sensibles aux eventuelles contributions virtuelles de Nouvelle Physique. La mesure de la polarisation du photon permet de tester la structure $V - A$ du couplage du Modèle Standard dans les processus des diagrammes de boucles de pingouin. Cette mesure peut être réalisée en étudiant le taux de désintégration dépendant du temps des mésons B. Une analyse délicate a été faite pour comprendre la distribution du temps propre et l'acceptance de sélection qui affecte cette distribution. Afin de contrôler l'acceptance de temps propre, des méthodes basées sur les données ont été développées. Plusieurs stratégies utilisées dans la mesure de la polarisation des photons sont introduites et des résultats préliminaires sont présentés. De plus, une étude de certains effets systématiques est discutée. Dans le cadre de l'étude des désintégrations radiatives, une nouvelle procedure d'identification de photons a été développée et nous avons fourni un outil pour calibrer la performance de la variable de séparation photon/pion neutre sur la simulation. Ces outils sont d'intérêt général pour la collaboration LHCb et sont largement utilisés.

Mots clés: LHCb detector - Heavy Flavor Physics - Radiative Decays - Effective Field Theories - $B_s^0 \to \phi\gamma$ - Photon Polarization - Proper Time - Photon Identification - Photon/π^0 separation.

Abstract

This thesis is dedicated to the study of the photon polarization in $B_s^0 \to \phi\gamma$ decays at LHCb. At the quark level, such decays proceed via a $b \to s\gamma$ penguin transition and are sensitive to possible virtual contributions from New Physics. The measurement of the photon polarization stands also as a test of the $V - A$ structure of the Standard Model coupling in the processes mediated by loop penguin diagrams. The measurement of the photon polarization can be done through a study of the time-dependent decay rate of the B meson. A delicate treatment has been done to understand the proper time distribution and the selection acceptance affecting it. To control the proper time acceptance, data driven control methods have been developed. Several possible strategies to measure the photon polarization are introduced and preliminary blinded results are presented. A study of some of the systematic effects is discussed. In the context of studying radiative decays, the author has developed a new photon identification procedure and has provided a tool to calibrate the performance of the photon/neutral pion separation variable on simulation. Those tools are of general interest for the LHCb collaboration and are widely used.

Keywords:

LHCb detector - Heavy Flavor Physics - Radiative Decays - Effective Field Theories - $B_s^0 \to \phi\gamma$ - Photon Polarization - Proper Time - Photon Identification - Photon/π^0 separation.

Remerciements

My acknowledgements go to everyone who has contributed in some way to the development of this work. I begin by thanking the director of the LPC, Alain Falvard, for granting me the chance to prepare my thesis in good conditions.

I want to thank the région d'Auvergne for having financially supported this work during three years and also for having granted me extra financial support to participate to conferences and present my work.

I am so happy to have been part of the LHCb team in the LPC. I would like to thank all the members of the team especially Olivier Deschamps and Régis Lefevre who have worked hard with me so as to elaborate this work and make it in a good condition. In the past three years I have experienced the most difficult but also the most beautiful moments, memories that will stay engraved in my mind till the day I die.

I would like also to thank all the members of the radiative analysis working group in the LHCb collaboration your help is very well appreciated.

My fellow students and friends in the LPC, Ibrahim, Marouen, Mohamad, Jan.. I would like to thank you for all your help and all your time that you have spent with me. Marouen, I will never forget all the times that we spent on the balcony smoking -me being as a passive smoker- those moments were the best moments of a working day.

Also, I am very grateful to Alain Falvard, Karim Trabelsi, Edwige Tournefier and Abraham Gallas for having accepted to be a part of my thesis jury.

I am to mention my daughter Ilyana since her presence has made me realize more and more the importance of my parents in my life. Since the day I knew she was coming I started to live a new kind of emotions, emotions that I knew my father has felt when he knew that I was coming, I can not just pass by such situation without realizing how much my parents cared about me and how much they sacrificed. Thanking them would not express the enormous amount of gratitude that I have towards them. I can now feel how much they are happy to see that their son has achieved something in this life.

On several unthought occasions your shadow would come to my mind flashing back a series of beautiful memories that I have lived by your side. Your smile has given me a lot of energy when I was feeling stressed. I would like to thank you for having knew you... Mariam.

فكأنَّ الدُنْيا لمْ تكُنْ وكأنَّ الآخِرَةَ لمْ تَزَلْ[1]

الحُسَيْنُ ابْنُ عَلِيِّ ابْنِ ابِي طَالِب

à ma famille,

à Mariam,

à Ilyana...

1. «Comme si la vie n'a jamais existé, et que la vie de l'au-delà est toujours là» , Hussain ibn Ali Ibn Abi Taleb. Quand Hussain ibn Ali Ibn Abi Taleb s'est rapproché de sa mort, il s'apercevait plus que jamais que le temps qu'il a passé en vie n'était qu'un voyage vers un autre monde plus joli, et surtout, un monde éternel.

Contents

Introduction

The Standard Model (SM) of particle physics provides a successful interpretation of most of the observed phenomena. There are several theoretical or experimental open questions as the origin of the mass hierarchy, the leptons family number, the electric charge quantification, the existence of dark matter and the asymmetries in the universe. These open questions may suggest that more fundamental symmetries are at play and justify the search for new phenomena beyond the standard model. This New Physics search can be done either by searching for new heavy particles or with precision validation of the SM predictions.

The validity of the SM can be checked in many ways one of which is the study of b hadron decays. One of the main experiments that study b flavor is the LHCb at CERN. The b quark transitions proceeding via Flavor-Changing Neutral Current (FCNC) loop processes provide an efficient indirect probe for the search of new particles possibly propagating inside the virtual loops. Precision measurements in the flavor sector can help to observe such NP effects.

One of the most promising probes of NP is the measurement of the photon polarization in $b \to s\gamma$ penguin transitions. The photon in $b \to s\gamma$ is predominantly left handed in the SM due to the left handed nature of the electroweak interactions. The right handed component is suppressed by the ratio of m_s/m_b. The exact level of suppression depends on QCD effects where, for certain modes, diagrams with gluon emission can contribute to the matrix element through their mixing. The measurement of the photon polarization would then aim at evaluating the fraction of right handed photons in hopes of finding deviation from the SM.

The determination of the photon polarization in $b \to s\gamma$ transitions is one of the important measurement of the LHCb physics program. Measuring the photon polarization can be done through the measurement of the time dependent decay rate of $B_s^0 \to \phi\gamma$.

This thesis introduces the analysis of the data collected by the LHCb detector during the 2011-2012 run I period in view of the first extraction of the photon polarization in the time-dependent decay rate of the $B_s^0 \to \phi\gamma$ decays. This analysis results from a collaborative work that involves several institutes, the LPC Clermont, the EPFL Lausanne, the IFIC Valencia and Barcelona groups working in the Radiative sub-group of the Rare Decays working group of the LHCb collaboration. This document presents my personal contribution to the teamwork. The analysis not being yet finalized, some preliminary results on the ratio of left to right photon polarization amplitudes are discussed.

This document is organized as follows. The first chapter serves as an introduction to the Standard Model of particle physics. The phenomenology of $b \to s\gamma$ transition based on the framework of effective field theories and Operator Product Expansion is introduced. An experimental overview with the recent results on radiative B decays are presented.

The second chapter introduces the LHCb detector at the LHC. The different subdetectors are presented. Since the work presented in this thesis is focused on radiative decays, care has been taken in explaining the calorimeter part of the detector for its major role in reconstructing photons.

The photon being extremely important to reconstruct the final state of the decay, chapter three has been dedicated to the reconstruction and identification of the photon. The author is directly implicated in the development of the photon identification tools at LHCb.

Chapter four presents the analysis performed to extract the photon polarization from $B_s^0 \to \phi\gamma$.

Finally, chapter five presents the preliminary results.

Technical details are collected in the appendices.

Chapter 1

The Electroweak interaction

Contents

The present understanding of the fundamental interactions is summarized into the so-called Standard Model of particle physics (SM). The later describes all known phenomenology of elementary particles from very low energy scales up to the highest experimental ones. Certain aspects of the SM have been tested with high precision and no significant deviation has been found. However, there are some phenomena which are not explained within the SM such as neutrino masses and the hierarchy problem.
In this chapter, the theoretical and the phenomenological framework is recalled. The SM of particle physics is briefly introduced followed by a description of the flavor changing neutral processes. Finally the radiative decay of interest is presented and the experimental status is shown.

1.1 The Standard Model

The Standard Model of particle physics is a renormalizable quantum field theory based on the gauge group $SU(3)_{\mathrm{c}} \times SU(2)_{\mathrm{L}} \times U(1)_{\mathrm{Y}}$ where the $SU(3)_{\mathrm{c}}$ is the gauge group of the Quantum Chromodynamics (QCD) part and $SU(2)_L \times U(1)_{\mathrm{Y}}$ induces the electroweak interaction. The gauge group has 12 generators corresponding to eight gluons for the strong interaction, three weak bosons $W^{\pm}$ and Z^0 and the photon mediating the electromagnetic interaction.
The matter fields, being the quarks and the leptons, are grouped into multiplets of the gauge group, i.e. they have to be assigned electroweak and strong quantum numbers.
Parity violation in weak interactions is implemented by assigning different weak quantum numbers to left- and right-handed components of the matter fields. In other words, the left- and right-handed components of the quarks and leptons are associated with different multiplets of the electroweak $SU(2)_{\mathrm{L}} \otimes U(1)_{\mathrm{Y}}$ group. The left-handed leptons are grouped into doublets of $SU(2)_{\mathrm{L}}$ in the following way:

$$L_{j,L} = \begin{pmatrix} \nu_j \\ l_j \end{pmatrix}_L \quad \text{where} \quad l_j \in \{e, \mu, \tau\}$$

where the subscript L means the left-handed projection of the spinor fields

$$\psi_L = \frac{1}{2}(1 - \gamma_5)\,\psi$$

Similarly, for the quarks the assignment is

$$Q_{j,L} = \begin{pmatrix} U_j \\ D_j \end{pmatrix}_L$$

where, assuming that there are six quarks and no more, $U_j \in \{u, c, t\}$ are the up-type quarks with a charge $Q = 2/3$ and $D_j \in \{d, s, b\}$ are the down-type quarks having a charge of $-1/3$.
The right-handed quarks and leptons are singlets in the SM. Thus

$$L_{j,R} = \Big(l_j\Big)_R \quad , \quad Q^U_{j,R} = \Big(U_j\Big)_R \quad \text{and} \quad Q^D_{j,R} = \Big(D_j\Big)_R$$

for the right handed leptons, up-type quarks and down-type quarks respectively. It is important to mention that the right-handed components are not sensitive to weak interactions. Only the left-handed group $SU(2)_{\mathrm{L}}$ is gauged and yields the usual couplings of the gauge bosons to the quarks and leptons.

The hypercharge assignment is determined in terms of the electric charge Q and the third component of the weak isospin I_3 quantum numbers,

$$Y = 2(Q - I_3)$$

Table 1.1 shows the different behavior of the left- and right- handed particles under $SU(2)_{\mathrm{L}}$ transformations where the left-handed particles are written as doublets and the right-handed ones as singlets. It also shows the quantum numbers assigned for the fermion, gauge and scalar fields in the SM.

1.1.1 The Lagrangian of the Standard Model

The SM gauge symmetry $SU(3)_{\mathrm{c}} \times SU(2)_{\mathrm{L}} \times U(1)_{\mathrm{Y}}$ is spontaneously broken as $SU(2)_{\mathrm{L}} \times U(1)_{\mathrm{Y}} \rightarrow U(1)_{\mathrm{Q}}$. The electroweak theory, proposed by Glashow, Salam and Weinberg [1, 2] is a non-abelian theory based on $SU(2)_{\mathrm{L}} \times U(1)_{\mathrm{Y}}$ describing the electromagnetic and weak interaction between quarks and leptons. In addition to the SU(2) generators, $I_{\pm}$ and I_3, the hypercharge $Y = 2(Q - I_3)$, where Q is the electric charge, is introduced in order to accommodate the difference between the electric charges for the left-handed doublets.

	Fields	$SU(3)_{\text{color}} \otimes SU(2)_{\text{L}} \otimes U(1)_{\text{Y}}$	Q	I_3
Leptons	$L_{j,L} \equiv \begin{pmatrix} \nu_j \\ l_j \end{pmatrix}_L$	(1,2,-1)	$\begin{pmatrix} 0 \\ -1 \end{pmatrix}$	$\begin{pmatrix} 1/2 \\ -1/2 \end{pmatrix}$
	$l_{j,R}$	(1,1,-2)	-1	0
Quarks	$Q_{j,L} \equiv \begin{pmatrix} U_j \\ D_j \end{pmatrix}_L$	(3,2,1/3)	$\begin{pmatrix} 2/3 \\ -1/3 \end{pmatrix}$	$\begin{pmatrix} 1/2 \\ -1/2 \end{pmatrix}$
	$U_{j,R}$	(3,1,4/3)	2/3	0
	$D_{j,R}$	(3,1,-2/3)	-1/3	0
Gauge fileds	B_μ	(1,1,0)		
	$W^a_\mu\,(a=1,2,3)$	$(1,3,0)$		
	$G^a_\mu\,(a=1,\cdots,8)$	$(8,1,0)$		
Scalar field	$\Phi \equiv \begin{pmatrix} \phi^+ \\ \phi^0 \end{pmatrix}_L$	(1,2,1)	$\begin{pmatrix} 1 \\ 0 \end{pmatrix}$	$\begin{pmatrix} 1/2 \\ -1/2 \end{pmatrix}$

Table 1.1: Quantum numbers assigned for the fermion, gauge and scalar fields in the SM.

The EW Lagrangian can be built as follows. The free Lagrangian with fermion matter fields reads

$$\mathscr{L}_0 = \bar{\psi}_L\, i\gamma^\mu D_\mu \psi_L + \bar{\psi}_R\, i\gamma^\mu D_\mu\, \psi_R \tag{1.1}$$

The requirement for local gauge invariance entails the redefinition of the partial derivatives $D_\mu \psi_{L,R}$

$$\begin{cases} D_\mu \psi_L = \left[\partial_\mu + i g_1 \sum_{a=1}^{3} \tau^a W^a_\mu + i g_2 \frac{1}{2} Y(\psi_L) B_\mu\right] \psi_L \\ D_\mu \psi_R = \left[\partial_\mu + i g_2 \frac{1}{2} Y(\psi_R) B_\mu\right] \psi_R \end{cases} \tag{1.2}$$

The two real numbers g_1 and g_2 are the couplings associated with $SU(2)$ and $U(1)$ respectively, and Y is the $U(1)$ hypercharge.
Thus, four gauge fields are present: W^a, corresponding to the three $SU(2)$ generators, and B corresponding to $U(1)$. Introducing the field strengths

$$B_{\mu\nu} = \partial_\mu B_\nu - \partial_\nu B_\mu \tag{1.3}$$
$$\mathscr{W}^A_{\mu\nu} = \partial_\mu W^A_\nu - \partial_\nu W^A_\mu - g_1 \varepsilon_{ABC} W^B_\mu W^C_\nu \tag{1.4}$$

where ε_{ABC} is the totally antisymmetric Levi-Civita tensor, one can then construct the kinetic Lagrangian of the gauge fields

$$\mathscr{L}_{\text{kin}} = -\frac{1}{4} B_{\mu\nu} B^{\mu\nu} - \frac{1}{4} \sum_{a=1}^{3} \mathscr{W}^a_{\mu\nu} \mathscr{W}^{a\mu\nu} \tag{1.5}$$

Gauge symmetry forbids mass terms for the gauge bosons and the fermions. Thus, the $SU(2)_L \otimes U(1)_Y$ Lagrangian contains only massless fields.

The interactions of the fermions with the gauge bosons are given by

$$\mathscr{L}_{\text{int}} = -g_1 \bar{\psi}_L \gamma^\mu \widetilde{W}_\mu \psi_L - g_2 \, B_\mu \sum_{\substack{\psi_j \in \ell_j, \nu_{\ell_j}, \\ Q^u_j, Q^d_j}} y(\psi_j) \bar{\psi}_j \gamma^\mu \psi_j \tag{1.6}$$

where $\widetilde{W}_\mu(x) \equiv \tau^a W^a_\mu(x)/2$ and $y(\psi_j) \equiv Y_W(\psi_j)/2$.

However, the $SU(2)_L \otimes U(1)_Y$ Lagrangian cannot describe the observed dynamics because the gauge bosons and the fermions are still massless.
The QCD Lagrangian can be built as follows. The free Lagrangian with massless quark fields reads

$$\mathscr{L}^0_q + \mathscr{L}^I_{Aq} = \bar{\psi}_i \left(i\gamma^\mu (D_\mu)_{ij} \right) \psi_j \tag{1.7}$$

where $\mathscr{L}^0_q$ and $\mathscr{L}^I_{Aq}$ stand for the free quark Lagrangian and quark-gluon interaction Lagrangian respectively.
To take into account the effect of a local color gauge transformation on the dynamics of

the quark field, the covariant derivative is defined as

$$D_\mu \psi_i \ = \left[\partial_\mu \ + i g_s \frac{1}{2} \lambda_a A^a_\mu \right] \psi_i \tag{1.8}$$

where g_s is the coupling constant of the strong interaction, λ_a are the Gell-Mann generators of the SU(3) group and A_μ represents the gluon field.

The gauge invariant gluon field strength tensor is defined as

$$G^a_{\mu\nu} \ = \partial_\mu A^a_\nu \ - \partial_\nu A^a_\mu - g_s f^{abc} A^b_\mu \, A^c_\nu \tag{1.9}$$

where f^{abc} are the structure constants of SU(3) group. The dynamical term for gluons can be expressed by the gauge and Lorentz invariant Lagrangian density defined as

$$\mathscr{L}^0_A + \mathscr{L}^I_A \ = -\frac{1}{2} Tr(G_{\mu\nu} G^{\mu\nu}) \tag{1.10}$$

where $G^{\mu\nu} = \frac{1}{2} \lambda^a G^{a,\mu\nu}$ and Tr stands for Trace. $\mathscr{L}^0_A$ and $\mathscr{L}^I_A$ are the free gluon and gluon-gluon interaction Lagrangians.

With some mathematical manipulation, this dynamical term can be reduced to the form

$$\mathscr{L}^0_A + \mathscr{L}^I_A \ = -\frac{1}{4} G^a_{\mu\nu} G^{a,\mu\nu} \tag{1.11}$$

developing this using 1.9 one will arrive to the form

$$\begin{aligned} \mathscr{L}^0_A + \mathscr{L}^I_A \ = -\frac{1}{4} \left(\partial_\mu A^a_\nu \ - \partial_\nu A^a_\mu\right)^2 - g_s f_{abc} \partial^\mu A^\nu_a A^b_\mu A^c_\nu \\ - \frac{g_s^2}{4} f_{abc} f_{ab'c'} A^b_\mu A^c_\nu A^{b'\mu} A^{c'\nu} \end{aligned} \tag{1.12}$$

it can be noticed that besides the kinetic term for the free gluons, the Lagrangian contains three- and four- gluon coupling terms.

to summarize, the QCD Lagrangian can be written as

$$\mathscr{L}_{\mathrm{QCD}} \ = \ \mathscr{L}^0_{\mathrm{q}} \ + \ \mathscr{L}^0_{\mathrm{A}} \ + \ \mathscr{L}^I_{\mathrm{Aq}} \ + \ \mathscr{L}^I_{\mathrm{A}} \tag{1.13}$$

For completeness, it is important to mention that the QCD Lagrangian has two extra terms incorporating "ghost" fields and their interactions. Ghost fields were introduced by Faddeev and Popov into gauge quantum field theories to maintain the consistency of the

path integral formulation. The gluon propagator was singular, could not be defined, and fixing a gauge, by introducing the Faddeev-Popov determinant, lead to the emergence of those purely mathematical, and non-physical, objects, hence the naming "ghosts".

To this extent the SM Lagrangian can be defined as the combination of 1.13 , 1.1, 1.5 and 1.6.

1.1.2 Higgs sector

The origin of mass in the SM is a consequence of the spontaneous symmetry breaking (SSB) of the $SU(2)_L \otimes U(1)_Y$ triggered by the Higgs mechanism (developed by Higgs, Brout, Englert, Guralnik, Hagen and Kibble) [3–6]. Consider an $SU(2)_L$ doublet of complex scalar fields

$$\phi \equiv \begin{pmatrix} \phi^{(+)} \\ \phi^{(0)} \end{pmatrix} \tag{1.14}$$

The scalar Lagrangian is

$$\mathscr{L}_S = (D_\mu \phi)^\dagger D^\mu \phi - \mu^2 \phi^\dagger \phi - h\left(\phi^\dagger \phi\right)^2 \qquad (h > 0, \mu^2 < 0) \tag{1.15}$$

with the covariant derivative

$$D^\mu \phi = \left[\partial^\mu + i g_1 \widetilde{W}_\mu + i g_2 y(\phi) B^\mu\right] \phi \qquad \text{with} \quad y(\phi) = \frac{1}{2} \tag{1.16}$$

The Lagrangian $\mathscr{L}_S$ is invariant under local $SU(2)_L \otimes U(1)_Y$ transformations.
There is an infinite set ($\mathscr{S}$) of degenerate states with minimum energy, satisfying

$$\langle 0 \,|\, \phi^{(0)} \,|\, 0 \rangle = \sqrt{\frac{-\mu^2}{2h}} \equiv \frac{v}{\sqrt{2}} \tag{1.17}$$

where v is the vacuum expectation value (VEV) of the neutral scalar. Since the electric charge is conserved, the VEV of ϕ^+ must vanish. Once the system has chosen a particular state belonging to ($\mathscr{S}$), the $SU(2)_L \otimes U(1)_Y$ symmetry is spontaneously broken to the electromagnetic group $U(1)_{\text{em}}$ which remains a true symmetry of the vacuum, i.e.

$$SU(2)_L \otimes U(1)_Y \to U(1)_{\text{em}} \tag{1.18}$$

The scalar doublet is parameterized as

$$\phi(x) \;=\; \exp\left\{ i\frac{\sigma_i \theta^i}{2} \right\} \; \frac{1}{\sqrt{2}} \; \begin{pmatrix} 0 \\ v + H(x) \end{pmatrix} \tag{1.19}$$

with four real fields $\theta^1(x)$, $\theta^2(x)$, $\theta^3(x)$ and $H(x)$.
Local $SU(2)_L$ invariance allows to rotate away any dependence on $\theta^i(x)$. These three fields are precisely the would-be massless Goldstone bosons associated with the SSB mechanism. The condition $\theta^i(x) = 0$ is called the physical or unitary gauge.
The scalar field $H(x)$ is the so-called Brout-Englert-Higgs (BEH) boson. Recently at LHC, a spin-0 boson has been discovered [7, 8] which is consistent with the BEH boson.

Gauge field masses

The covariant derivative couples the scalar doublet to the gauge bosons. The kinetic piece of the scalar Lagrangian is

$$\begin{aligned} (D_\mu \phi)^\dagger \, D^\mu \phi \xrightarrow{\theta^i = 0} \; & \frac{1}{2} \partial_\mu H \partial^\mu H \; + \; \frac{g_1^2 \, v^2}{8} \; \left[\left(W_\mu^1 \right)^2 \; + \left(W_\mu^2 \right)^2 \right] \\ & + \frac{v^2}{8} \; \left[g_1 W_\mu^3 \; - g_2 B_\mu \right]^2 \; + \text{cubic} \; + \text{quartic terms} \end{aligned} \tag{1.20}$$

If one redefines the fields as follows

$$W_\mu^\pm \;=\; \frac{W_\mu^1 \mp i W_\mu^2}{2} \tag{1.21}$$

and rotates the B_μ and W_μ^3 fields as

$$\begin{pmatrix} W_\mu^3 \\ B_\mu \end{pmatrix} \;\equiv\; \begin{pmatrix} \cos\theta_W & \sin\theta_W \\ -\sin\theta_W & \cos\theta_W \end{pmatrix} \; \begin{pmatrix} Z_\mu \\ A_\mu \end{pmatrix} \tag{1.22}$$

where θ_W is the weak-mixing angle defined as

$$\tan\theta_W \;=\; \frac{g_2}{g_1} \tag{1.23}$$

one verifies that the kinetic part of the scalar Lagrangian written in terms of Z_μ, A_μ and $W_\mu^\pm$ now contains quadratic terms for the $W_\mu^\pm$ and the Z. In other words, the $W^\pm$ and

Z gauge bosons acquire masses

$$M_Z \cos\theta_W \;=\; M_{W^\pm} \;=\; \frac{1}{2}\, v\, g_1 \tag{1.24}$$

while A_μ is identified with the electromagnetic vector potential and remains massless. The electromagnetic current is thus conserved: the coupling of the electromagnetic interaction is identified with the electron charge e

$$g_1 \sin\theta_W \;=\; g_2 \cos\theta_w \;=\; e \tag{1.25}$$

and the conserved quantum number is

$$Q'^f \;=\; I_3^f \;+\; \frac{Y_W^f}{2} \tag{1.26}$$

where Q'^f is the electric charge generator (in units of e), I_f^3 is the third component of the weak isospin and Y_W^f is the hypercharge of the fermionic field f.
Equation 1.25 is intuitive to understand the electro-weak unification in the sense that it shows how the weak and the electromagnetic coupling constants g_1 and g_2 are unified within one relation and how they are exchangeable.

Fermion masses

A fermionic mass term $\mathscr{L}_m \;= -m\overline{\psi}\psi \;= -m(\overline{\psi}_L\psi_R \;+\overline{\psi}_R\psi_L)$ is not allowed, because it explicitly breaks the gauge symmetry: left- and right-handed fields transform differently under $SU(2)_L \otimes U(1)_Y$. However, the bilinear Yukawa interactions of left- and right-handed fermions with the scalar field are invariant under $SU(2)_L \times U(1)_Y$

$$\mathscr{L}_{\text{Yukawa}} \;=\; Y_{ij}^u\, \bar{Q}_{iL}\, \phi^c\, Q_{jR}^u \;+\; Y_{ij}^d\, \bar{Q}_{iL}\, \phi\, Q_{jR}^d \;+\; Y_{ij}^\ell\, \bar{L}_{iL}\, \phi\, \ell_{jR} \;+\; \text{h.c.} \tag{1.27}$$

where the first term involves the charge-conjugate scalar field $\phi^c \equiv i\tau^2\phi^*$. The matrices $Y_{ij}^{u(d)}$ and Y_{ij}^ℓ are the Yukawa couplings for the up (down) quarks and the charged leptons, respectively. After EW symmetry breaking, quarks and leptons become massive and their masses are described by the Lagrangian[1]

$$\mathscr{L}_{\text{mass}} \;=\; \bar{Q}_{iL}^u\, M_{ij}^u\, Q_{jR}^u \;+\; \bar{Q}_{iL}^d\, M_{ij}^d\, Q_{jR}^d \;+\; \bar{\ell}_{iL}\, M_{ij}^\ell\, \ell_{jR} \;+\; \text{h.c.} \tag{1.28}$$

[1]Since the original formulation of the SM did not include right-handed neutrinos (nor Higgs triplets), neutrinos remain strictly massless to all orders in perturbation theory.

with the mass matrices defined by

$$M^u_{ij} \;=\; vY^u_{ij}\;,\; M^d_{ij} \;=\; vY^d_{ij}\;,\; M^\ell_{ij} \;=\; vY^\ell_{ij} \tag{1.29}$$

In general, the Yukawa couplings and hence the mass matrices are not diagonal. The above mass matrices can be diagonalized through the bi-unitary transformations

$$\begin{aligned} V^{u\dagger}_L\; M_u\; U^u_R &= \mathrm{diag}(m_u,\; m_c,\; m_t) \;\equiv\; d_u \\ V^{d\dagger}_L\; M_d\; U^d_R &= \mathrm{diag}(m_d,\; m_s,\; m_b) \;\equiv\; d_d \\ V^{\ell\dagger}_L\; M_\ell\; U^\ell_R &= \mathrm{diag}(m_\ell,\; m_\mu,\; m_\tau) \;\equiv\; d_\ell \end{aligned} \tag{1.30}$$

where the U and V are the 3×3 unitary matrices which relate flavor (unprimed) and mass eigenstates (primed). Applying the transformations

$$Q^u_L \;\to\; V^u_L\; Q'^u_L\;, \quad Q^d_L \;\to\; V^d_L\; Q'^d_L\;, \quad \ell_L \;\to\; V^\ell_L\; \ell'_L \tag{1.31}$$

$$Q^u_R \;\to\; U^u_R\; Q'^u_R\;, \quad Q^d_R \;\to\; U^d_R\; Q'^d_R\;, \quad \ell_R \;\to\; U^\ell_R\; \ell'_R \tag{1.32}$$

to the Lagrangian given in Eq. (1.28), one obtains

$$\mathscr{L}_{\mathrm{mass}} \;=\; \sum_{Q^u_i, Q^d_i, \ell_i} \Big(m_{Q^u_i}\; \bar{Q}'^u_{iL}\; Q'^u_{iR} \;+\; m_{Q^D_i}\; \bar{Q}'^d_{iL}\; Q'^d_{iR} \;+\; m_{\ell_i}\; \bar{\ell}'_{iL}\; \ell'_{iR} \;+\; \mathrm{h.c.} \Big) \tag{1.33}$$

Henceforth, the fermions have mass terms.

Charged Currents

The charged current (CC) Lagrangian will now read

$$\mathscr{L}^{(q)}_{CC} \;=\; -\frac{g_1}{\sqrt{2}} \Big[W^+_\mu\; \overline{Q}'^u_{iL}\; \gamma^\mu\; (V_{\mathrm{CKM}})_{ij}\; Q'^d_{jL} \;+\; W^-_\mu\; \bar{\ell}'_{iL}\; \gamma^\mu\; (\delta)_{ij}\; \nu'_{\ell_j\, L} \;+\; \mathrm{h.c.} \Big] \tag{1.34}$$

where the unitary matrix $V_{\mathrm{CKM}} \;=\; V^{u\prime}_L\, V^d_L$ is the so-called Cabibbo-Kobayashi-Maskawa matrix [9,10] which encodes flavor violation in CC. In the case of three quark generations, it is a 3×3 unitary mixing matrix [10]

$$V_{\mathrm{CKM}} \;=\; \begin{pmatrix} V_{ud} & V_{us} & V_{ub} \\ V_{cd} & V_{cs} & V_{cb} \\ V_{td} & V_{ts} & V_{tb} \end{pmatrix} \tag{1.35}$$

It can be shown that it depends on four parameters: three angles and a phase. In the absence of a fundamental theory of flavor, there is no theoretical prediction for the values of these parameters which should be determined experimentally.

Figure 1.1: Charged current vertices describing the coupling of fermion pairs (quarks or leptons) to vector boson $W^\pm$.

Weak charged currents are the only tree-level interactions in the SM that change flavor. Fig. 1.1 depicts the CC vertices in the SM. These vertices are the building blocks of the $b \to s\gamma$ transition matrix element. As said before, only the left-handed group $SU(2)_{\rm L}$ is gauged and yields the usual couplings of the gauge bosons to the quarks and leptons. This means that the W boson will only couple to left handed quarks and the photon emitted in the $b \to s\gamma$ transition is predominantly left handed with small correction of the order of m_b with the exact level of suppression being mode dependent due to QCD effects [11, 12]. More details are given on this matter in section 1.2.

Neutral Currents

In terms of the mass eigenstate fields Z_μ and A_μ, the neutral part of the weak interaction Lagrangian is

$$\begin{aligned}\mathscr{L}_{\rm NC} \;=\; -\sum_{\psi_j} \bar{\psi}_j \gamma^\mu \Big\{ A_\mu \left[g_1 \frac{\tau_3}{2} \sin\theta_W \;+\; g_2\, y(\psi_j) \cos\theta_W \right] \\ + Z_\mu \left[g_1 \frac{\tau_3}{2} \cos\theta_W \;-\; g_2\, y(\psi_j)\; \cos\theta_W \right] \Big\} \psi_j\end{aligned} \tag{1.36}$$

This neutral current (NC) Lagrangian can be decomposed as

$$\mathscr{L}_{\rm NC} \;=\; \mathscr{L}_{\rm QED} + \;\mathscr{L}^Z_{\rm NC} \tag{1.37}$$

where $\mathscr{L}_{\rm QED}$ is the usual QED Lagrangian, and

$$\mathscr{L}^{Z}_{\rm NC} \;=\; -\frac{e}{2\sin\theta_W\cos\theta_W}\, J^{\mu}_{Z}\, Z_{\mu} \tag{1.38}$$

which contains the interaction of the boson with the neutral fermionic current J^{μ}_{Z}. Equivalently, $\mathscr{L}^{Z}_{\rm NC}$ has the form (see Fig. 1.2)

$$\mathscr{L}^{Z}_{\rm NC} \;=\; -\frac{e}{2\sin\theta_W\cos\theta_W}\, Z_{\mu} \sum_{f} \bar{\psi}_f \gamma^{u}(v_f - a_f\gamma_5)\psi_f \tag{1.39}$$

where the coefficients $a_f = T^f_3$ and $v_f = T^f_3\left(1 - 2Q'^{f}\sin^2\theta_W\right)$ represent the axial (A) and vector (V) couplings of the Z^0 boson to fermions.

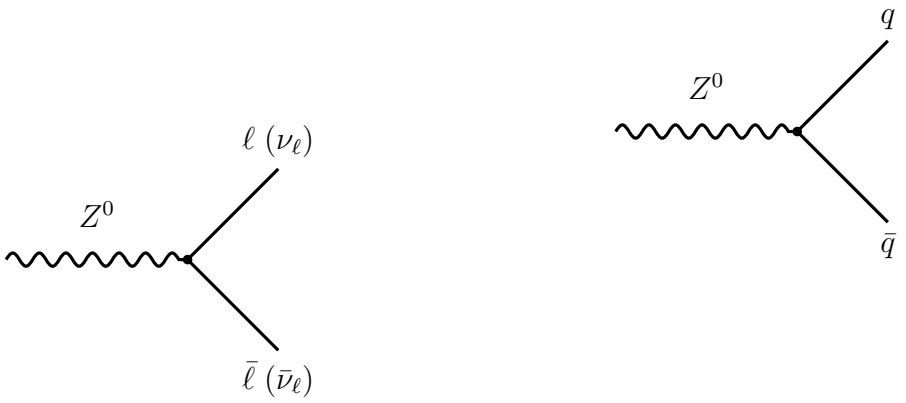

Figure 1.2: Neutral current vertices describing the coupling of fermion pairs (quarks or leptons) to Z^0 boson.

It can be deduced that NC at tree level in the SM do not change flavor. Hence, Flavor Changing Neutral Currents (FCNC) can only occur at higher order, $\geq$ loop, processes. The $b \to s\gamma$ transition is a FCNC and hence, at first order, a one loop process. More details are given on this matter in section 1.2.

1.2 Radiative B hadron decays

Radiative decays of B hadrons caused by $b \to q\gamma$ transition, with $q = d, s$, are an interesting example of flavor-changing neutral current processes. From the theoretical point of view such processes are forbidden at tree-level and the lowest contribution to

the amplitude comes from the one-loop process, see Figure 1.3. Hence, as with any loop process in quantum field theory, the decay pattern may be sensitive to the structure of heavy degrees of freedom of the theory. Moreover, the weak, electromagnetic and perturbative strong parts of the physics behind radiative decays are well under theoretical control. It is also advantageous that one can formulate theoretical predictions for a variety of different observables, such as decay rates, CP and isospin asymmetries, angular distributions, and cross-check in this way the robustness of the SM framework [13].

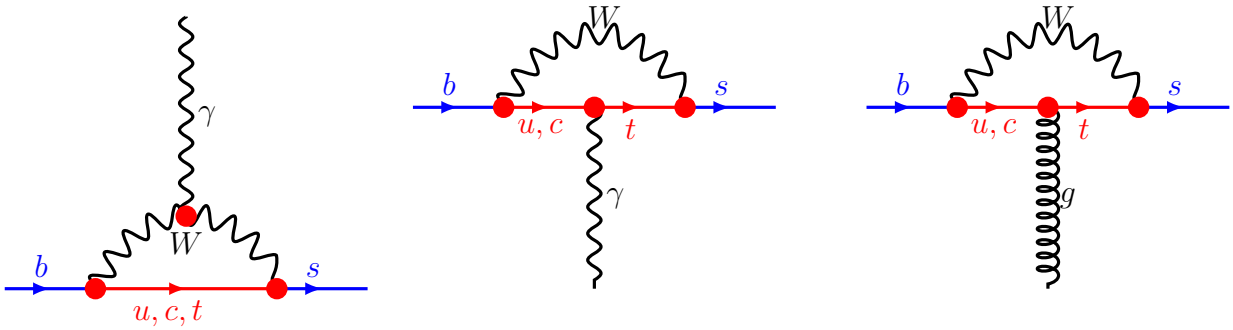

Figure 1.3: Flavor Changing Neutral Current loops for $b \to s\gamma$. Self-energy like diagrams are omitted. The third diagram contributes through its mixing.

1.2.1 Effective field theories

Since there are several energy scales involved in the weak decay of mesons, there are subtleties in studying FCNC processes. The energy scales pertinent to B decays are: the QCD scale ($\Lambda_{\rm QCD}$), the mass of the b quark, m_b, the electroweak scale which is of the order of the masses of the W and Z bosons and the top quark, and higher scales of possible new physics. An important theoretical tool which allows for the description of separate scales as well as the convenient inclusion of NP effects, is operator product expansion (OPE).

Within the OPE framework, the weak scales are separated, leading to an effective weak Hamiltonian. This Hamiltonian is described in terms of effective operators and their associated effective couplings, referred to as Wilson coefficients. While all the short distance effects are contained in the Wilson coefficients, there are long distance contributions from the hadronic matrix elements of the effective operators. The long distance

effects usually include non-perturbative QCD effects which are the major source of theoretical uncertainties.

1.2.1.1 Effective Hamiltonian of $b \to s\gamma$

The effective $\Delta F = 1$ Hamiltonian is given as

$$\mathcal{H}_{\text{eff}} = \frac{G_F}{\sqrt{2}} \sum_{p=u,c} \lambda_p^{(q)} \left[C_1 Q_1^p + C_2 Q_2^p + \sum_{i=3}^{8} C_i Q_i \right], \tag{1.40}$$

where CKM factors are given by $\lambda_p^{(q)} = V_{pq}^* V_{pb}$, and the unitarity relationship has been used. The Wilson coefficients C_i encode physics at large mass scales and hence carry information about heavy particles - SM as well as NP ones, while matrix elements of hadronic operators Q_i are describing long-distance physics dominated by non-perturbative strong interactions. Poor knowledge of these latter factors is the main source of uncertainty of theoretical predictions. At leading order the dominant contribution comes from the electromagnetic penguin operator

$$Q_7 = -\frac{e\,\overline{m}_b(\mu)}{8\pi^2}\,\bar{q}\,\sigma^{\mu\nu}\,[1+\gamma_5]\,bF_{\mu\nu} \tag{1.41}$$

Here $q = d$ or s.The factor $\overline{m}_b(\mu)$ is the $\bar{M}S$ mass of the b quark. The Wilson coefficients C_i have been known within the next-to-leading logarithmic approximation (NLL) for over a decade (for a review, see [14]), and have been recently calculated at next-to-next-to-leading logarithmic order (NNLL) in a series of papers [15–18].
The standard theoretical procedure used for evaluation of hadronic matrix elements is based on the QCD factorization idea, augmented by soft-collinear effective theory. The latter separates the matrix element of interest into non-perturbative but universal soft functions (form-factors, decay constants, light-cone distribution amplitudes) and hard scattering kernels calculated as perturbative series in α_s. These calculations have been done in next-to-leading and partly in next-to- next-to-leading order [15]. However the whole factorization approach makes sense only in the leading order with respect to the small parameter Λ_{QCD}/m_b and the question of a systematic construction of the $1/m_b$ expansion remains open. Needless to say, having reliable SM theoretical predictions is a necessary prerequisite for addressing any NP scenario.

1.2.1.2 Photon polarization

We can express the Hamiltonian for $b \to s\gamma$ in the following form:

$$\Delta\mathcal{H} = -\sqrt{8}G_F \frac{e\,\overline{m}_b(\mu)}{16\pi^2} F_{\mu\nu} \left[\mathcal{A}_L \bar{s}\sigma^{\mu\nu}\frac{1+\gamma_5}{2}b + \mathcal{A}_R \bar{s}\sigma^{\mu\nu}\frac{1-\gamma_5}{2}b \right]. \tag{1.42}$$

Here $\mathcal{A}_L(\mathcal{A}_R)$ corresponds to the amplitude for the emission of left (right) handed photons in the $b \to s_L\gamma_L(b \to s_R\gamma_R)$ decays. This can be easily seen by writing the electromagnetic field tensor for left (right) polarized photons as $F^{L,R}_{\mu\nu} = \frac{1}{2}(F_{\mu\nu} \pm \tilde{F}_{\mu\nu})$ where $\tilde{F}_{\mu\nu} = \frac{1}{2}\epsilon_{\mu\nu\sigma\rho}F^{\sigma\rho}$. Using the identity $\sigma_{\mu\nu}\gamma_5 = \frac{i}{2}\epsilon_{\mu\nu\alpha\beta}\sigma^{\alpha\beta}$, one can see that only the $F^L_{\mu\nu}$ part survives in the first term of the right-hand side of 1.42 and only $F^R_{\mu\nu}$ in the second one. In the SM the amplitude ratio, representing the fraction of "wrong" helicity photons, $\mathcal{A}_R/\mathcal{A}_L$ is proportional to the mass ratio m_s/m_b, since in the SM only the left-handed components of the external fermions couple to the W boson. Thus the leading contribution is given by the operator in equation 1.41 . This naive m_s/m_b scaling can however be destroyed by corrections, which take into account gluon emission. This effect may affect significantly the purity of the photon polarization. In papers [12, 19] these contributions were estimated to be sufficiently large, about 10 %, however these results were based mainly on dimensional estimations.

Thus, it can be concluded that the polarization of emitted photons in radiative decays is a good example of a nontrivial experimental observable sensitive to the Lorentz structure of effective Hamiltonian operator containing the photon emission vertex.
The admixture of photons with the "wrong" polarization may be rather large in some SM extensions like e.g. the Left Right Symmetric Model (LRSM). Here the enhancement of the right-handed photon fraction is due to $W_L - W_R$ mixing, and chirality flip along the internal t-quark line in the loop leads to a large factor m_t/m_b in the amplitude for producing right-handed photons. It was shown that within the unconstrained minimal supersymmetric model (uMSSM) a strong enhancement of order $m_{\tilde{g}}/m_b$ is possible due to chirality flip along the gluino line and left-right squark mixing. In this case the degree of photon polarization, λ_γ, defined as

$$\lambda_\gamma = \frac{|\mathcal{A}_R| - |\mathcal{A}_L|}{|\mathcal{A}_R| + |\mathcal{A}_L|} \tag{1.43}$$

can take any value between -1 and 1 [20].

1.2.2 Experimental status

In this section, the state of the art of the measurement of the photon polarization in radiative penguin transitions in b hadron decays is presented.

Experimental overview

The aim of the experimental study is to measure the ratio of right-to-left photon polarization amplitude

$$\frac{|\mathcal{A}(B \to \Phi\gamma_R)|}{|\mathcal{A}(B \to \Phi\gamma_L)|}$$

where Φ represents some final hadronic state. There is no clear experimental way to measure photon polarization directly, but there are several indirect strategies. The first one is the study of angular distributions of the Φ decay products [21,22]. In this way one is able to measure only the square of the amplitude ratio. In such a case, the amplitudes corresponding to left-handed and right-handed photons do not interfere since the polarization of the photon in the final state can be measured independently. By studying the angular distribution one can extract the photon polarization, in other words the method makes use of angular correlations among the decay products in $B \to [\Phi \to P_1P_2P_3]\gamma$, where P_i is either a pion or a kaon. Notice that there must be at least three particles in the final state so as to define a reference plane with which the orientation of the photon is studied. This technique was used for the decay $B \to K\pi\pi\gamma$ [21–23] with the sum over intermediate hadronic resonances. The first direct observation of the photon polarization in the $b \to s\gamma$ transition using $B \to K\pi\pi\gamma$ is done by LHCb with a significance of 5.2σ [23]. The radiative decay mode $B \to [\phi \to K^+K^-]K\gamma$ is considered in [24]. This mode is rather distinctive with many desirable features from the experimental point of view: the final state is a photon plus only charged mesons for charged B mesons, the fact that ϕ is narrow reduces the effects of intermediate resonances interference, etc. However the actual situation is rather involved. The possibility of measuring the photon polarization in this way depends on a delicate partial-wave interference pattern. The latter may be unfavorable and the asymmetry may escape detection [24].

It would be advantageous to measure the absolute value of the amplitude ratio as it is. There are two possible ways to do that. The first one makes use of the fact that some photons convert in the detector material into electron-positron pairs. Thus it is possible to have the interference between the amplitudes corresponding to left- and right-

handed photon emission. It can be shown that for these processes the distribution in the angle θ between the e^+e^- plane and the plane defined by the final state hadrons (e.g. $K\pi$ resulting from K^* decay) should be isotropic for purely circular polarization, while the deviations from this isotropy includes the same parameter A_R/A_L, indicating the presence of right-handed photons [25–28]. However multiple scattering does not allow to identify the decay plane for the low invariant mass e^+e^-pair. This is not the case for pair creation from virtual photons where one can select pair masses above 30 MeV/c^2 without losing too much rate. However in this case other diagrams contribute with longitudinal virtual photons. This measurement is discussed in [29]. The branching ratio of the decay $B^0 \to K^*(892)^0e^+e^-$ has been measured in the dilepton mass range of (30-1000) MeV/c^2 [30] and found to be

$$\mathcal{B}(B^0 \to K^*(892)^0e^+e^-)^{30-1000\ \mathrm{MeV/c^2}} = (3.1\,^{+0.9}_{-0.8}\,^{+0.2}_{-0.3} \pm 0.2) \times 10^{-7}.$$

An angular analysis of the $B \to K^{*0}e^+e^-$ decay is also performed at LHCb [31]. Using proton-proton collision data, corresponding to an integrated luminosity of 3.0 fb^{-1}, collected in 2011 and 2012. Angular observables are measured for the first time in an effective q^2 range from 0.0020 ± 0.0008 to 1.120 ± 0.060 GeV^2/c^4. The results are

$$\begin{aligned} F_{\mathrm{L}} &= 0.16 \pm 0.06 \pm 0.03 \\ A_{\mathrm{T}}^{(2)} &= -0.23 \pm 0.23 \pm 0.05 \\ A_{\mathrm{T}}^{\mathrm{Im}} &= +0.14 \pm 0.22 \pm 0.05 \\ A_{\mathrm{T}}^{\mathrm{Re}} &= +0.10 \pm 0.18 \pm 0.05, \end{aligned}$$

where the first contribution to the uncertainty is statistical and the second systematic. Where F_{L} is the fraction of longitudinal polarisation of the vector meson and the amplitude A_{T}^j - with j being either (2), Im or Re - are related to the different polarization states of the K^{*0} meson. In the limit when $q^2 \to 0$, the electromagnetic penguin diagram where the leptons are produced by a virtual photon is dominant and the observables $A_{\mathrm{T}}^{(2)}$ and $A_{\mathrm{T}}^{\mathrm{Im}}$ can be expressed as simple functions of the $\mathcal{C}_7$ and $\mathcal{C}_7'$ Wilson coefficients [32]

$$A_{\mathrm{T}}^{(2)}(q^2 \to 0) = \frac{2\mathcal{R}e(\mathcal{C}_7\mathcal{C}_7'^*)}{|\mathcal{C}_7|^2 + |\mathcal{C}_7'|^2} \quad \text{and} \quad A_{\mathrm{T}}^{\mathrm{Im}}(q^2 \to 0) = \frac{2\mathcal{I}m(\mathcal{C}_7\mathcal{C}_7'^*)}{|\mathcal{C}_7|^2 + |\mathcal{C}_7'|^2}. \tag{1.44}$$

The measurements of $A_{\mathrm{T}}^{(2)}$ and $A_{\mathrm{T}}^{\mathrm{Im}}$ therefore provide information on photon polarisation amplitudes.

Another way is to study the time evolution of $B^0_{(s)} \to \Phi^{CP}\gamma$ decays, where Φ^{CP} is a CP-eigenstate. In this case the amplitudes of the right- and left handed photon polarization interfere in the final state. The time-dependent decay rate is given as

$$\Gamma_{B(\bar{B})^0_{(s)}\to\Phi^{CP}\gamma}(t) = |A|^2 e^{-\Gamma_{(s)}t}\left(\cosh(\Delta\Gamma_{(s)}t/2) + \mathcal{A}_\Delta \sinh(\Delta\Gamma_{(s)}t/2) \right. \\ \left. \pm\mathcal{C}_{\mathcal{CP}}\cos(\Delta m_{(s)}t) \mp \mathcal{S}_{\mathcal{CP}} sin(\Delta m_{(s)}t)\right) \quad (1.45)$$

Within the SM one has [33]

$$\mathcal{C}_{\mathcal{CP}} \sim 0 \quad (1.46)$$
$$\mathcal{S}_{\mathcal{CP}} \sim sin2\Psi sin\phi_{(s)} \quad (1.47)$$
$$\mathcal{A}_\Delta \sim sin2\Psi \cos\phi_{(s)}, \quad (1.48)$$

where Ψ is defined as

$$tan\Psi = \left|\frac{\mathcal{A}_R}{\mathcal{A}_L}\right| \quad (1.49)$$

and related to the fraction of "wrongly"-polarized photons. $\phi_{(s)}$ is the sum of $B^0_{(s)}$ mixing phase and CP-odd weak phases for right A_R and left A_L amplitudes.
From equations 1.48 and 1.49 one can see that the measurement of $\mathcal{A}_\Delta$ and $\mathcal{S}_{\mathcal{CP}}$ directly determines the "wrongly"-polarized photon fraction [33].

For the B^0 system the parameter $\Delta\Gamma$ is negligible, $\Delta\Gamma_d/\Gamma_d = 0.001 \pm 0.010$ [34], and as a result the term proportional to A_Δ vanishes and the photon polarization can only be accessed through the measurement of $\mathcal{S}_{\mathcal{CP}}$. The decay rate reduces to

$$\Gamma_{B^0\to\Phi^{CP}\gamma}(t) = |A|^2 e^{-\Gamma t}\left(1 - \mathcal{S}_{\mathcal{CP}} sin(\Delta m t)\right) \quad (1.50)$$
$$\Gamma_{\bar{B}^0\to\Phi^{CP}\gamma}(t) = |A|^2 e^{-\Gamma t}\left(1 + \mathcal{S}_{\mathcal{CP}} sin(\Delta m t)\right) \quad (1.51)$$

where one expects from the SM to have $sin\phi = sin(2\beta - \phi_p) \sim sin2\beta$ (ϕ_p is the CP-odd

weak penguin phase) and hence, $\mathcal{S}_{\mathcal{CP}}$ is given as

$$\mathcal{S}_{\mathcal{CP}} = sin2\Psi sin2\beta. \tag{1.52}$$

This approach can be accessed from the decay channel $B^0 \to [K^{*0} \to K_s\pi^0]\gamma$, it has been done at BABAR and Belle [35, 36] (figure 1.4) but very challenging at LHCb due to the presence of only neutrals in the final state.
An inclusive $B^0 \to K_S\pi^0\gamma$ analysis has been performed by Belle using the invariant mass range up to 1.8 GeV/c^2. Belle also gives results for the $K^*(892)$ region: 0.8 GeV/c^2 to 1.0 GeV/c^2. BaBar has measured the CP-violating asymmetries separately within and outside the $K^*(892)$ mass range: 0.8 GeV/c^2 to 1.0 GeV/c^2 is again used for $B^0 \to K^{*0}(892)\gamma$ candidates, while events with invariant masses in the range 1.1 GeV/c^2 to 1.8 GeV/c^2 are used in the $B^0 \to K_S\pi^0\gamma$ analysis [35]. Figure 1.4 summarizes the results of BaBar and Belle concerning the measurement of $\mathcal{S}_{\mathcal{CP}}$.
For the B_s^0 system the parameter $\Delta\Gamma_s$ is not negligible, providing a non- zero sensitivity to A_Δ. In the SM ϕ_s is expected to be small, $sin\phi_s = sin(2\beta_s - \phi_p) \approx 0$, thus the term with S vanishes:

$$\Gamma_{B^0_{(s)}\to\Phi^{CP}\gamma}(t) = \Gamma_{\bar{B}^0_{(s)}\to\Phi^{CP}\gamma}(t) = |A|^2 e^{-\Gamma_{(s)}t}\left(\cosh(\Delta\Gamma_{(s)}t/2) + \mathcal{A}_\Delta \sinh(\Delta\Gamma_{(s)}t/2)\right) \tag{1.53}$$

and finally one has

$$A_\Delta^{B_s^0} \sim sin2\Psi, \tag{1.54}$$

thus opening the possibility for the direct measurement of the photon polarization parameter $sin2\psi$ [37]. It is worth to stress here that contributions from $\mathcal{S}_{\mathcal{CP}}$ and $\mathcal{C}_{\mathcal{CP}}$ vanish when considering the inclusive $\Gamma_{B_s} + \Gamma_{\bar{B}_s}$ assuming the $B_s/\bar{B}_s$ production asymmetry vanish. The analysis of $B_s^0 \to \phi\gamma$ addressed in this thesis is based on this approach.
Alternatively, one can study baryon decays $\Lambda_b \to \Lambda^0\gamma \to p\pi\gamma$ (or $\Lambda_b \to \Lambda^*\gamma \to pK\gamma$) and measure the photon polarization via the forward-backward asymmetry of the proton with respect to the Λ_b in the Λ^0 rest frame for polarized Λ_b, (see [38–41] for details and references therein). The main problem of these two methods is the absence of interference between the amplitudes corresponding to left- and right- handed photon emission since they correspond to different and distinguishable final states. Correspondingly they are

sensitive only to the square of the amplitude ratio in the form of photon polarization λ_γ (equation 1.43). Moreover, the measurement of the photon polarization with radiative baryon decays have proved experimentally difficult due to the small polarisation of Λ_b^0 baryons produced at the LHC [42]. The polarization of Λ_b^0 is required to be non-zero for the measurement of the photon polarization.

Radiative b hadron decays provide the potential for significant future improvement in the knowledge of right-handed contributions to the $b \to s\gamma$ amplitude. To achieve this it is necessary to use all of the methods most sensitive to the photon polarisation, since they provide complementary information [43]. These methods include time-dependent asymmetries in $B^0 \to K_s\pi^0\gamma$ and $B_s^0 \to \phi\gamma$ decays, up-down asymmetries in $B^+ \to K^+\pi^+\pi^-\gamma$ decays, and angular asymmetries in $B^0 \to K^{*0}e^+e^-$ decays, baryon radiative decays $\Lambda_b \to \Lambda^*\gamma$ and many other decays. Improved searches for CP violation in both inclusive and exclusive processes are important. There are excellent prospects for progress in most of these areas at both LHCb, including its upgrade [44], and Belle II.

1.2.3 Radiative B decays at LHCb

LHCb capability of performing analysis of radiative decays has been demonstrated through several measurements [23, 30, 31, 45]. The presence of the photon, which is reconstructed in the calorimeter, in the final state makes the reconstruction of the decay experimentally challenging. The resolution of the different decay variables is driven by the resolution of the calorimeter. Moreover, the presence of a neutral particle in the decay's final state engenders a high level of background for the reconstructed radiative decay.

In addition to the analysis already cited in the previous section, LHCb has published several results on radiative B decays. First, the measurement of the ratio of branching ratios $\mathcal{B}(B_s^0 \to \phi\gamma)/\mathcal{B}(B^0 \to K^*(892)^0\gamma)$ [45] has been performed with the data collected by LHCb in 2011

$$\mathcal{B}(B_s^0 \to \phi\gamma)/\mathcal{B}(B^0 \to K^*(892)^0\gamma) = 1.23 \pm 0.06(\text{stat.}) \pm 0.04(\text{syst.}) \pm 0.10\ \text{f}_\text{s}/\text{f}_\text{d}$$

from which the branching ratio of $B_s^0 \to \phi\gamma$ can be extracted using, back when the paper was published, the 2010 HFAG [34] value for the branching ratio of $B^0 \to K^*(892)^0\gamma$

$$\mathcal{B}(B_s^0 \to \phi\gamma) = (3.5 \pm 0.4) \times 10^{-5}.$$

With the same data set, the direct CP asymmetry of $B^0 \to K^*(892)^0\gamma$ is measured [45]

$$A_{CP}(B^0 \to K^*(892)^0\gamma) = (0.8 \pm 1.7(\text{stat.}) \pm 0.9(\text{syst.}))\%.$$

LHCb has collected during the 2011-2012 run period the largest sample of $B_s^0 \to \phi\gamma$ events. The analysis performed in this thesis is based on this sample that is selected following what has been done in [45].

In Run II, the LHC will operate at a center of mass energy of $\sqrt{s} = 14$ TeV during the first year. With this increase of energy, the integrated luminosity collected by LHCb will be twice what LHCb collected during the Run I.

The huge amount of statistics will give way to new measurements in the $b \to d\gamma$ sector as well as baryon radiative decays, $\Lambda_b \to \Lambda^*\gamma$ and many other decays [41].

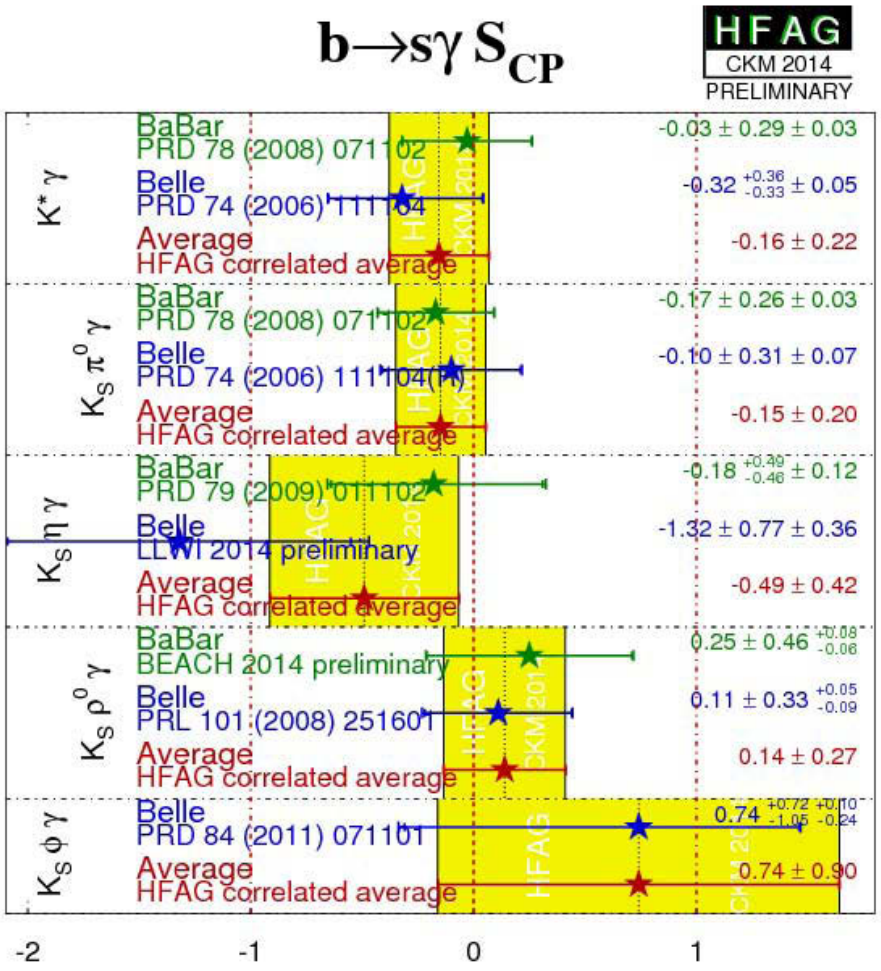

Figure 1.4: The measurement of $\mathcal{S}_{CP}$ from Belle and BaBar.

Chapter 2

The LHCb

Contents

The LHCb experiment is one of four main experiments collecting data at the Large Hadron Collider accelerator at CERN. LHCb has a wide physics program covering many important aspects of Heavy Flavor, Electroweak and QCD physics. It is mainly specialized in flavor physics and is collecting data that is used to perform measurements of the parameters of CP violation in the interactions of b-hadrons. Such studies can help to explain the Matter-Antimatter asymmetry of the Universe. The detector is also able to collect data to perform measurements of production cross sections and electroweak physics in the forward region. Its key measurements, one of which is the measurement of the photon polarization, are described in a roadmap document [46]. Many of these key measurement have already been performed. In this chapter, the LHCb experiment will be described detailing how the decay's vertex is reconstructed, how the momentum/energy of the decay's products and their tracks are measured and how these products are identified; the LHCb sub-detectors will be explained as well as the hardware and software triggers. Finally, the LHCb performance during the 2011-2012 run period will be discussed.

2.1 The LHC

The biggest particle accelerator ever built is the Large Hadron Collider (LHC). It consists of a circular tunnel of 27 km, located underground at the french-swiss border [47]. This machine has been designed for proton-proton (pp) collisions. Two beams of protons travel inside the tunnel in opposite directions inside two different pipes. Each beam consists in sets of grouped protons called bunches, each one containing 1.15×10^{11} protons on average. There are more than 2808 bunches in each beam at full intensity. The collisions occur in determined places around the rings, called interaction points, where the two bunches cross each other. This is where the detectors are located. There are four principal experiments at the LHC. The ATLAS and CMS detectors [60, 61] are general purpose experiments, mainly designed to search for the Higgs boson and for direct evidence of physics beyond the Standard Model. The ALICE experiment [62] is dedicated to the reconstruction of heavy ions collisions in order to study the formation of the quark-gluon plasma. Finally the LHCb experiment, in which this work took place, is designed for precision measurements on beauty and charm physics, specially the study of CP violation in this sector [63]. To reach those challenging physics goals, it is necessary to accumulate a big amount of data at collision energies never achieved

before. In 2010-2011 LHC ran at a center of mass energy of 7 TeV. The center of mass energy was increased to 8 TeV in 2012. The protons are injected from the Super Proton Synchrotron (SPS) at the energy of 450 GeV. Inside the LHC, protons are accelerated to reach their final energy. A general view of the LHC complex can be found in figure 2.1.

During the run I period (2011-2012), ATLAS and CMS collected about 25 fb^{-1} of integrated luminosity whereas LHCb collected almost 3 fb^{-1} for the same period. In contrast to the general purpose detectors ATLAS and CMS, LHCb is not designed to run at the maximum LHC luminosity of 10^{34} cm^{-2} s^{-1}. Instead the beams undergo a process called luminosity leveling (explained in next section) whereby they are mis-aligned slightly in the axis vertical to the LHC ring (y-axis), to obtain the design luminosity of 2 - 5 $\times$ 10^{32} cm^{-2} s^{-1} remaining constant over the entire LHC fill. This is demonstrated in figure 2.2 where the instantaneous luminosity is compared between LHCb, Atlas and CMS. This has been chosen to limit the number of pp interactions occurring per bunch crossing, a term known as "pile-up", making it easier to trace primary and secondary vertices as well as limiting the radiation damage and detector occupancy. The LHC machine was briefly shutdown for upgrades in November 2011 and restarted in March 2012.

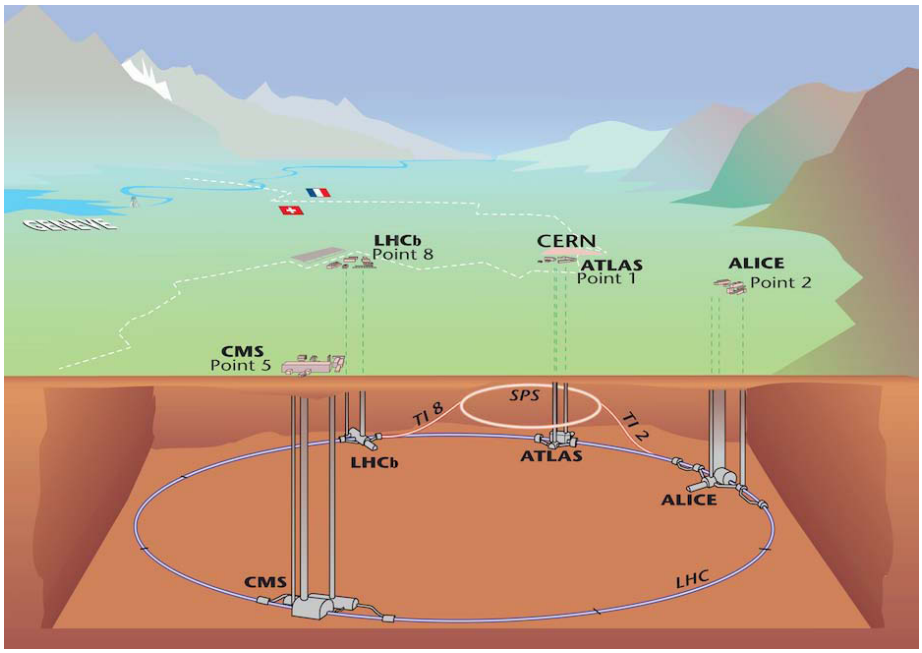

Figure 2.1: General view of the LHC.

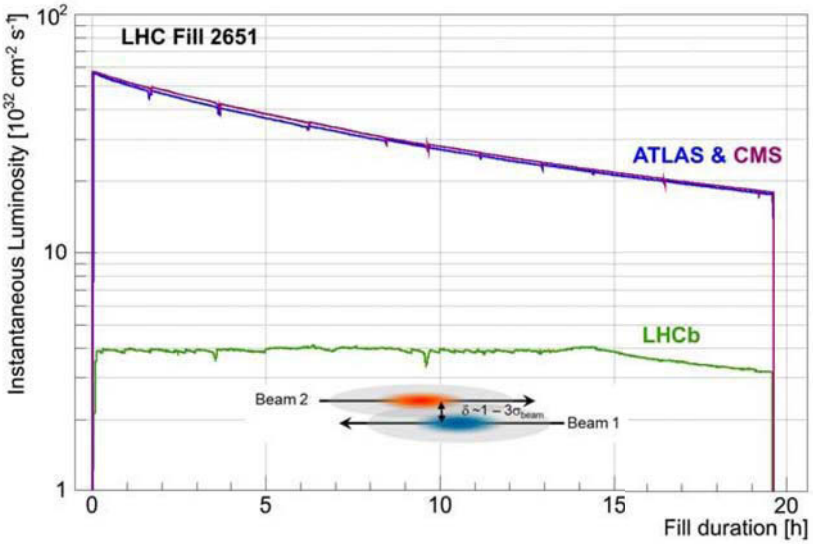

Figure 2.2: Development of the instantaneous luminosity for ATLAS, CMS and LHCb during LHC fill 2651. After ramping to the desired value of $4 \times 10^{32}\text{cm}^2\text{s}^{-1}$ for LHCb, the luminosity is kept stable in a range of 5% for about 15 hours by adjusting the transversal beam overlap.The difference in luminosity towards the end of the fill between ATLAS, CMS and LHCb is due to the difference in the final focusing at the collision points.

2.2 Data taking periods and operating conditions

At the end of 2009, LHCb recorded its first pp collisions at the injection energy of the LHC, $\sqrt{s} = 0.9$TeV. These data have been used to finalise the commissioning of the sub-detector systems and the reconstruction software, and to perform a first alignment and calibration of the tracking, calorimeter and particle identification (PID) systems. In this period, the VErtex LOcator (VELO, presented in section 2.3.1) was left in the open position, due to the larger aperture required at lower beam energies. During 2010 the operating conditions changed rapidly due to the ramp-up of the LHC luminosity. A critical parameter for LHCb performance is the pile-up, defined as the average number of visible interactions per beam-beam crossing [48]. While the highest luminosity in 2010 was already 75% of the LHCb design luminosity, the pile-up was much larger than the design value due to the low number of bunches in the machine. It was demonstrated that the trigger and reconstruction work efficiently under such harsh conditions with increased

detector occupancy due to pile-up, and that the physics output was not compromised. The LHC beam energy was 3.5 TeV during 2010 and 2011. In 2012 the LHC beam energy was increased to 4 TeV. LHCb took data at a luminosity of 4×10^{32} cm^{-2}s^{-1}, twice the LHCb design luminosity. The LHC delivered stable beams for about 30% of the operational year (figure 2.3). The integrated luminosity recorded by LHCb was 38 pb^{-1} in 2010, 1.11 fb^{-1} in 2011 and 2.08 fb^{-1} in 2012. The analysis presented in this thesis uses the data collected in 2011 and 2012.

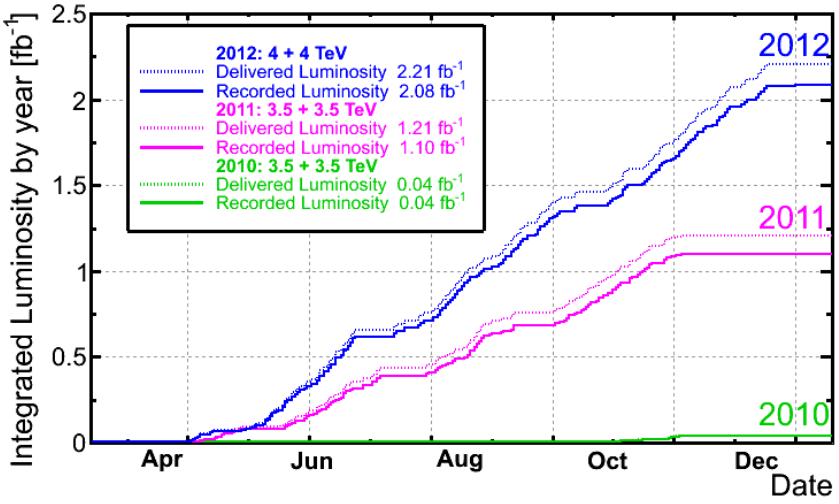

Figure 2.3: The LHCb integrated luminosity recorded over the run I period.

2.3 The LHCb detector

The fact that at LHC protons collide at high energies enhances the production of $b\bar{b}$ pairs mainly through three types of processes: gluon fusion, gluon splitting and flavor excitation (figure 2.5). The energies and luminosities reached at the LHC allows to have a large production of those particles that will hadronize to form b-hadrons. The $b\bar{b}$ cross section, 75.3±5.4±13.0 μb at 7 TeV [49], is dominated by configurations in which one of the partons has more energy than the other. The b and $\bar{b}$ quarks are then boosted along the direction of the most energetic parton: their directions are close to the direction of one of the beams. Hence, about 40% of the b and $\bar{b}$-hadrons are produced in the forward region (figure 2.4).

Therefore, the LHCb has been constructed as a single-arm forward spectrometer (figure

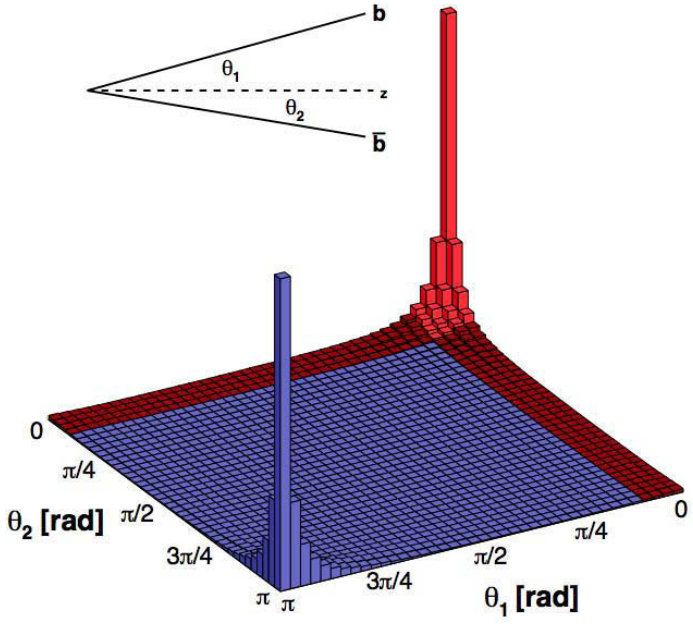

Figure 2.4: Polar angles of the b and $\bar{b}$-hadrons produced at the LHC, as obtained from a PYTHIA simulation.

2.7) with a angular acceptance ranging from 10 to 300 mrad in the magnet bending plane (plane horizontal with the LHC ring) and to 250 mrad in the plane vertical to the LHC ring (figure 2.6).

The nominal interaction point defines the center of the coordinate system. The x, y and z axes form a right handed orthogonal system: the (x, z) plane contains the accelerator with the x axis being orthogonal to the beam direction and the z axis being parallel to the beam direction. They y axis is orthogonal to the (x, z) plane.

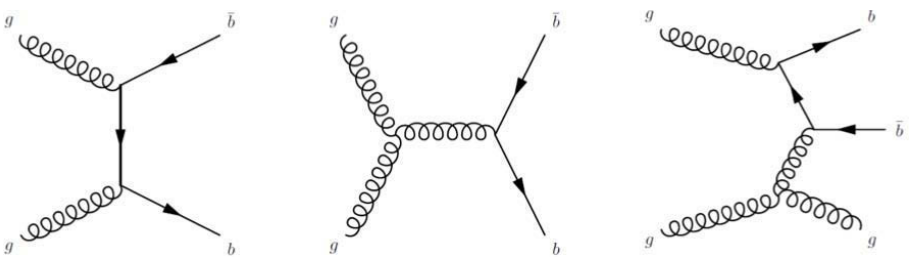

Figure 2.5: Feynman diagrams of processes related to $b\bar{b}$ production at the LHC, gluon fusion (left), gluon splitting (middle) and flavor excitation (right).

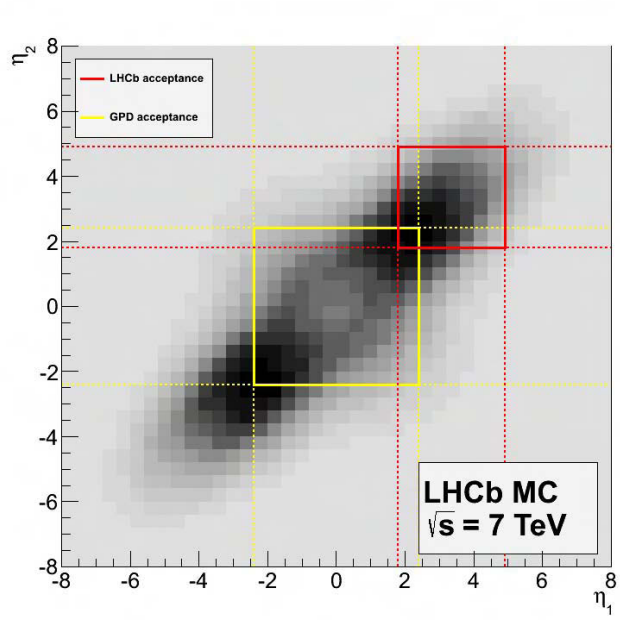

Figure 2.6: The LHCb detector acceptance compared to General Purpose Detectors (GPD) as Atlas and CMS.

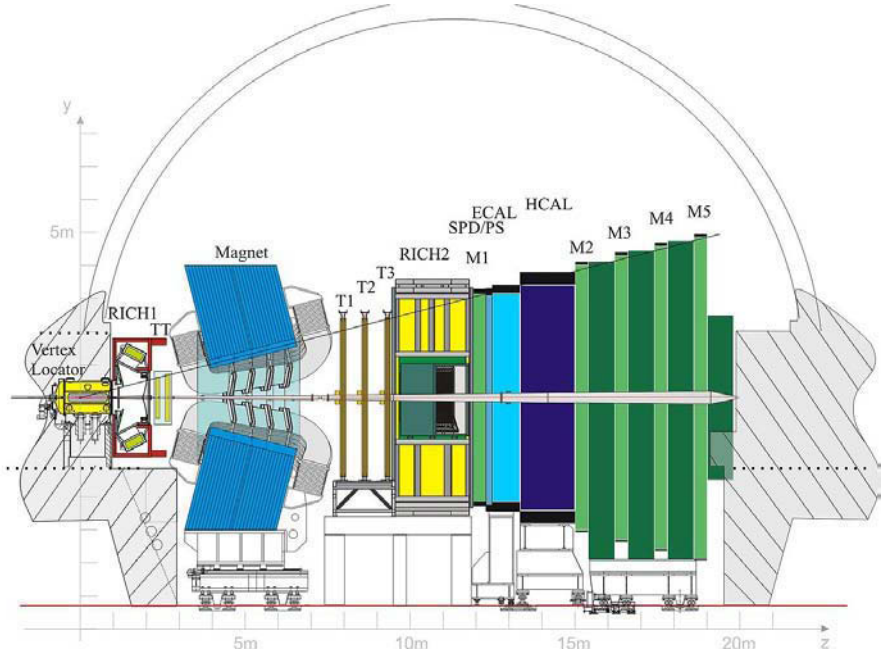

Figure 2.7: General schematic view of the LHCb detector.

The accelerator increases its delivered luminosity so as to accumulate a large statistics. This increases the average number of proton-proton collisions per bunch crossing. Increasing the number of proton-proton collisions has a cost, it increases the multiplicity of particles in the event and makes the event reconstruction more difficult. This is more critical in the forward region where the occupancy is higher. Another important point is that for an event with multiple proton-proton interactions there could be an ambiguity in associating a b-hadron to the right production vertex as the b-hadrons reconstructed in the experiment are mainly produced in the forward direction. At LHCb, the beam is less focused and the method of luminosity leveling by beam separation is used insuring a stable instantaneous luminosity. Figure 2.2 shows the concept of luminosity leveling which consists in moving the proton beams relative to each other modifying the effective crossing area. The fact that the instantaneous luminosity is stable at LHCb means that there is a stable average number of visible interactions per bunch crossing over a fill duration.

There are three stages in which b-hadrons decays are identified at LHCb. First, vertex reconstruction is essential since the b-hadron has a relatively long lifetime, about 1.5 ps (except for the B_c which lifetime is about 0.5 ps and the B^* which is strongly decaying), which means that the proton-proton interaction vertex, denoted primary vertex (PV), is different than the b-hadron decay vertex, denoted secondary vertex (SV). The separation between those two vertices is important so as to separate between tracks coming from the PV and others coming from the SV as well as to check that the latter points to the same decay point; this is assured by the vertex locator, denoted as VELO. Then comes the energy/momentum measurements which is the key point to reconstruct the mass of the b-hadron and the mass of any intermediate resonance, the better the mass resolution we can get the better is the background rejection that we can achieve. Charged particle momentum is measured by the tracking system whereas the calorimeter is responsible for the measurement of photon and neutral pion energy. The final criteria to have a well reconstructed b-hadron decay is to have a good particle identification. Pions, kaons and protons are identified by two ring imaging Cherenkov; electrons, photons and neutral pions are identified in the calorimeter and the muon chambers identify muons.

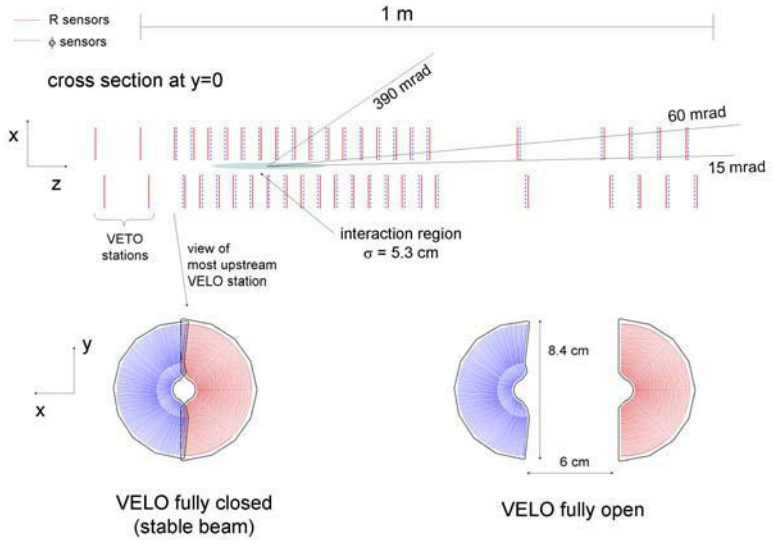

Figure 2.8: Cross section in the (x,z) plane of the VELO silicon sensors at y = 0, with the detector in the fully closed position. The front face of the first modules is also illustrated in both closed and open positions.

2.3.1 Vertex reconstruction: The VELO

The VErtex LOcator (VELO) is the sub detector closest to the interaction point. It is located within a vacuum maintained by a dedicated vessel. It consists of a series of 21 stations made of silicon modules arranged along the beam direction spreading from z = -18 cm to z = 88 cm. The stations are almost circular in shape and of 300 μm thick each. Each station of the VELO is divided in two halves completely independent.
The VELO provides a precise measurement of the track coordinates, r and ϕ (each station has its own z coordinate), which are used to reconstruct the displaced secondary vertices generated by the lifetimes of b- and c-hadron decays. The use of cylindrical geometry (z,r,ϕ coordinates), rather than a simpler cartesian scheme, is required by the LHCb trigger performance, for which 2D (rz) tracking has been demonstrated to yield a faster reconstruction with enough impact parameter resolution (IP, distance of closest approach of a track to a vertex). The VELO is designed to reconstruct primary and secondary vertices providing measurements of flight distance and of IP. It is able to detect particles within a pseudo rapidity range $1.6 < \eta < 4.9$, pseudo rapidity being defined as $\eta = -ln(tan(\theta/2))$ with θ being the angle between the momentum of the particle and

the beam axis, and emerging from interactions in the range |z| < 10.6 cm, it has a single hit precision of $\sim 4\ \mu m$ requiring high precision on its alignment.

Each half station is composed of two types of sensors: the r-sensors and the ϕ-sensors. The r-sensors consist in semi-circles centred on the beam axis. This allows the determination of the r coordinate which is the distance to the beam axis. The ϕ-sensors are divided radially to determine the ϕ-coordinate defined as the angle with respect to the x axis in the (x, y) plane. The z coordinate is obtained from the position of the station. The sensitive part of VELO sensors starts at a radius of about 8 mm, which is the smallest possible for safety reasons. During injection, however, the aperture required by the LHC machine increases, so the VELO is retracted up to a distance of 3 cm as can be seen in figure 2.8. The VELO may be closed only after stabilization of the beams. It can be fully operated in both positions, opened or closed. Two additional stations, called pile-up stations, constituted by r-sensor modules, are placed upstream of the interaction point to allow a fast determination of the number of primary vertices that can be used in the first trigger level (L0). At LHCb, to define a track, hits are required in at least three modules. The spatial resolution on the primary vertex depends on the number of tracks, but on average it is found to be about 42 μm on the z-axis direction and about 10 μm in the (r, ϕ) plane.

2.3.2 Momentum measurement: The dipole magnet

The trajectory of a charged particle is bent in the presence of a magnetic field, and thus the ratio between its electric charge and its momentum (q/p) can be measured. Hence, one of the LHCb dipole magnet tasks is to measure the momentum of charged particles. It covers a forward acceptance of $\pm$250 mrad vertically and $\pm$300 mrad vertically. The magnetic field is provided by a dipole of 1600 tons consisting of two identical coils, which weigh 54 tons each, are of conical saddle and are placed mirror-symmetrically to each other. Figure 2.9 shows a side view of the LHCb magnet system. The average value of the integrated magnetic field is 3.6 Tm in the vertical direction. The polarity of the dipole is regularity changed to reduce systematic uncertainties on CP asymmetries measurements related to potential detection asymmetries of the detector.
The design of a magnet with such configurations had to accommodate two contrasting needs: on one hand, the need of a field level inside the Ring Imaging Cherenkov (RICH,

described in section 2.3.4) envelope of less than 2 mT, and on the other hand a field as high as possible in the regions between the VELO and the Tracker Turicencis (TT, section 2.3.3). Furthermore, in order to achieve the required momentum resolution for charged tracks, the magnetic field integral $\int B.dl$ is measured with a precision of a few T/mm.

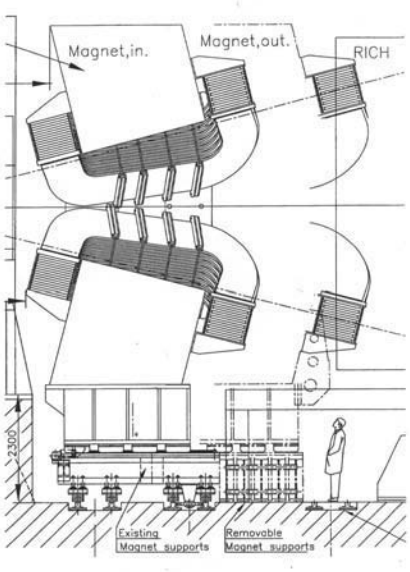

Figure 2.9: A side view of the LHCb dipole magnet.

2.3.3 Track reconstruction: Silicon Trackers and Outer Trackers

The VELO is completed by the Silicon Trackers (ST) and the Outer Trackers (OT). The ST aims at reconstructing tracks close to the beam pipe, where the occupancy is the largest, and consists of two detectors comprising four tracking stations: the Tracker Turicencis (TT) located upstream of the dipole magnet and covering the full LHCb acceptance and the Inner Tracker (IT) which is a cross-shaped region located at the center of the three tracking stations T1, T2 and T3, downstream the magnet. Both TT and IT use silicon microstrip sensors with a strip pitch of about 200 μm, which ensures a single-hit resolution of 50 μm. Each of the four ST stations has four detection layers in an (x-u-v-x) arrangement with vertical strips in the first and the last layer and strips rotated by a stereo angle of -5° in the u-direction and $+5^\circ$ in the v-direction in the second and the third layer, respectively. The OT is a drift-time detector for the tracking

of charged particles and the measurement of their momentum over a large acceptance area in the outer region of the LHCb detector. A general view of the tracking stations can be seen in figure 2.10.

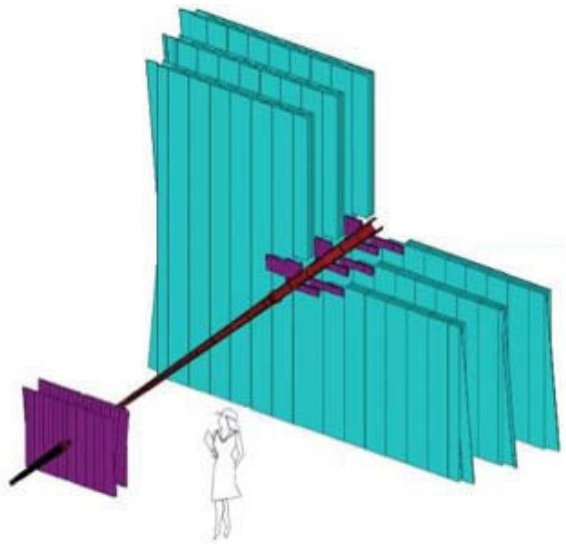

Figure 2.10: General view of the tracking stations with TT and IT in purple and OT in blue.

2.3.3.1 Track reconstruction and Tracking performance

The LHCb track reconstruction consists in combining the hits in the VELO, the TT, the OT and the IT detectors to form particle trajectories from the interaction region to the calorimeters, regardless of their origin. Depending on their trajectories through the tracking system, tracks are classified as (figure 2.11):
Long tracks cross the full tracking system from the VELO to the T stations. These have the most precise momentum determination.
Upstream tracks traverse only the VELO and the TT stations. These are low momentum tracks that are bent out of acceptance by the magnetic field, and usually have poor momentum resolution.
Downstream tracks travel only through the TT and T stations. They are relevant in the cases of long-lived particles which decay outside the VELO.
VELO tracks are measured in the VELO and are usually large angle or backward tracks, useful for primary vertex reconstruction.
T-tracks are only measured in the T stations, and are typically produced in secondary

interactions.
On data, the tracking efficiency is measured to be about 98%. The momentum resolution $\delta p/p$ is about 0.5% for particles below P of 20 GeV/c rising up to 0.8% at 100 GeV/c (figure 2.12).

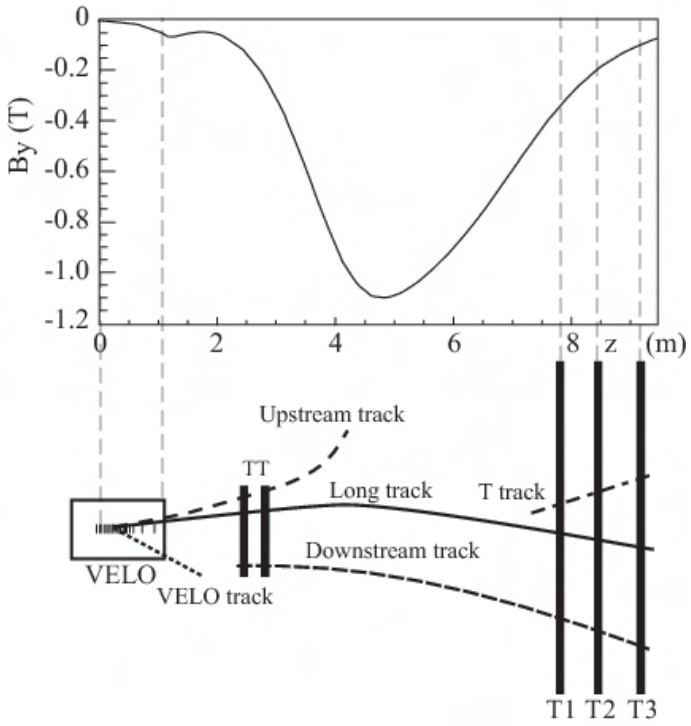

Figure 2.11: A schematic illustration of the various track types [50]: long, upstream, downstream, VELO and T tracks. For reference the main magnetic field component (B_y) is plotted above as a function of the z coordinate.

2.3.4 Ring imaging Cherenkov detectors

The RICH detectors use the Cherenkov effect to identify charged particles. The Cherenkov effect is the fact that photons are emitted by a charged particle moving in a dielectric medium with a speed greater than the speed of light in that medium.
The photons are emitted in a cone around the direction of the charged particle. The cone opening angle depends on the speed of the particle. Knowing the momentum (measured by the tracking system) and the speed of a particle, one has access to its mass and can then identify it. The Cherenkov photons are guided by a series of spherical mirrors to a photon detector plane, located outside the detector acceptance. The Cherenkov

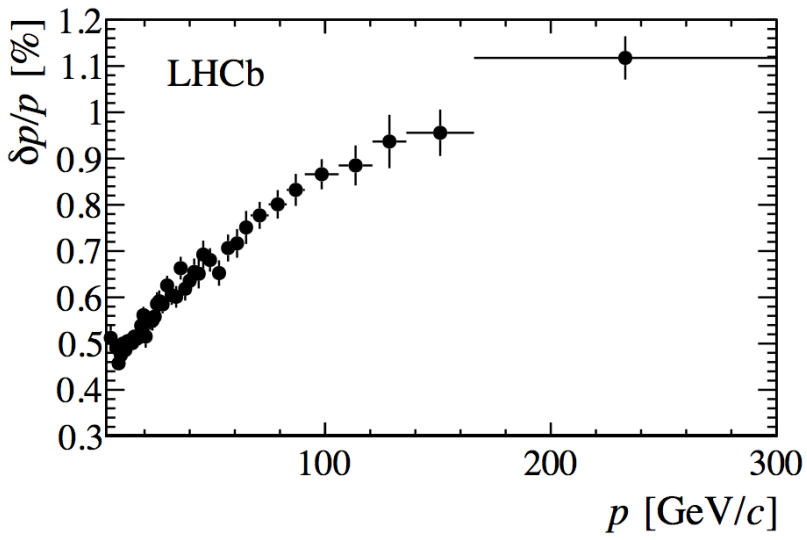

Figure 2.12: Relative momentum resolution versus momentum for long tracks in data obtained using J/ψ decays.

photons form a ring on the detector plane and the radius of the ring is directly related to the angle of the Cherenkov cone. Since the momentum spectrum at large polar angles is softer than at small polar angles, the particle identification system uses two RICH detectors with different radiators to cover the full momentum range, this is illustrated in figure 2.13.

The configuration of the two RICH detectors is shown in figure 2.14. The RICH1 detector is located upstream of the magnet, at the end of the VELO, covering the full LHCb acceptance. It covers the low momentum range, from a P_T of 1GeV/c to 60 GeV/c with the use of a silica aereogel (C_4F_{10}, 1.0014<n<1.01) gas radiator. The RICH2 detector, is located downstream of the magnet, between the T stations and the Silicon Pad Detector/PreShower (SPD/PS, explained in 2.3.5.1), and has a limited angular acceptance of ±15 mrad to ±200 mrad in the magnet bending plane and ±100 mrad in the magnet non-bending plane. It uses CF_4 (1.01<n<1.10) as dielectric medium and its momentum coverage goes from a P_T of 15 GeV/c to 100 GeV/c.

2.3.5 The Calorimeters

Located at 12.5 m from the interaction region, the calorimeter system consists in 4 consecutive elements: The Silicon Pad detector (SPD), the PreShower (PS), the Elec-

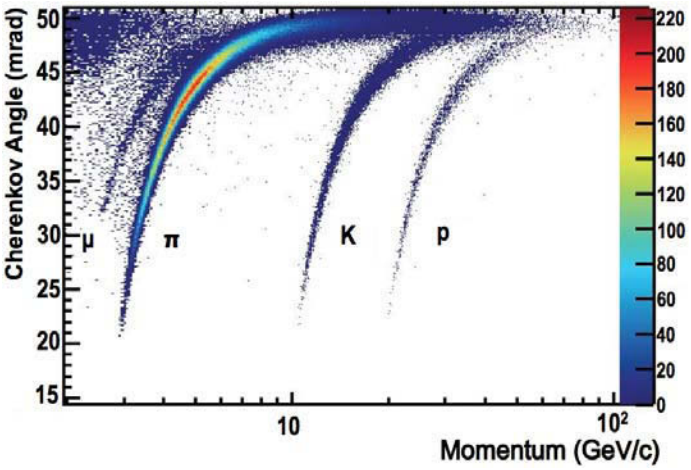

Figure 2.13: Reconstructed Cherenkov angle for isolated tracks, as a function of track momentum in the C_4F_{10} radiator [51]. The Cherenkov bands for muons, pions, kaons and protons are clearly visible.

tromagnetic CALorimeter (ECAL) and the Hadronic CALorimeter (HCAL). The SPD and PS identify the charged and electromagnetic nature of the crossing particles, respectively. ECAL and HCAL measure the energy of the electromagnetic and hadronic showering particles. The system is used at the first level trigger (L0) to rapidly separate electrons, photons and hadrons. The interaction of the various types of particles in the calorimeter is schematized in figure 2.15.

The calorimeter system play a major role in the reconstruction and selection of radiative decays from trigger to offline analysis. At L0, photon candidates are reconstructed and selected with a transverse energy threshold of 2.5 GeV in 2011, 2.72 GeV in beginning 2012 and 2.96 GeV in mid-2012.
Almost 30 % of the photons coming from the interaction region convert in electron pair before reaching the calorimeter. Three categories of photons are reconstructed offline in LHCb depending whether they convert or not in the material upstream the calorimeter system.

Unconverted photons and "late" conversions occurring after the magnet are reconstructed as a single energy deposit (cluster) in the ECAL as discussed in 3. Late conversion likely form a single ECAL cluster identified with SPD hits in front.
The electron pair from photon conversion occurring before the magnet are reconstructed

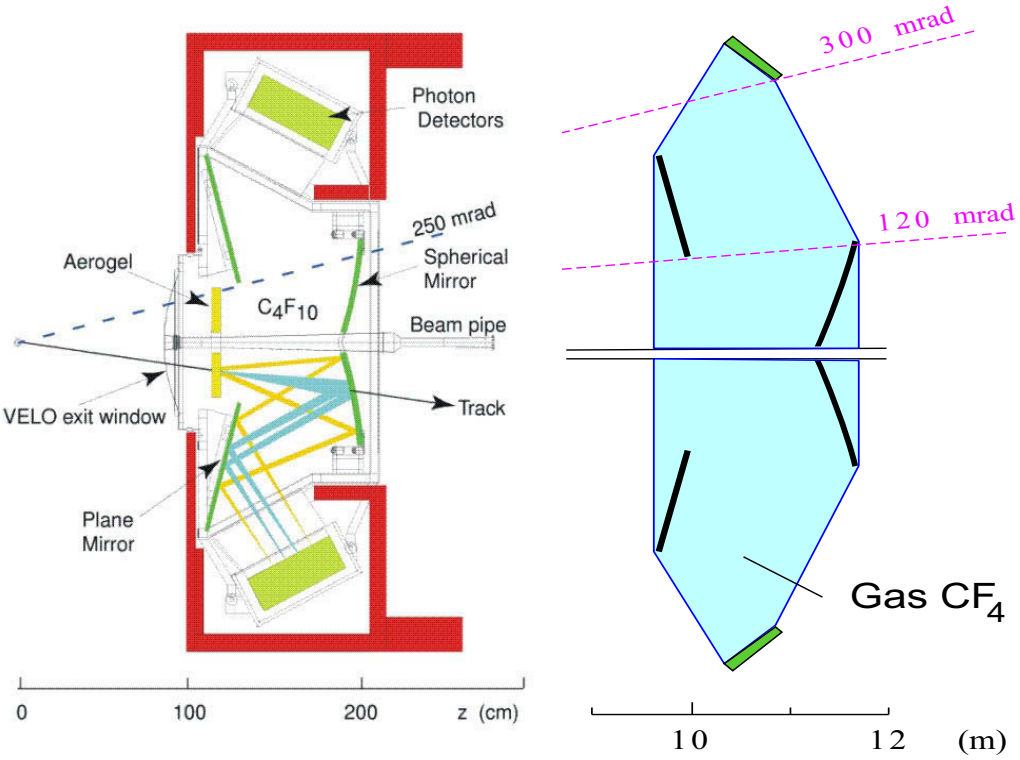

Figure 2.14: Schema of the RICH detectors, RICH1 (left) and RICH2 (right).

by the tracking system.
The invariant mass resolution of a B meson decaying to a final state with a photon -the photon reconstructed as a calorimeter object- is completely dominated by the photon energy resolution driven by the calorimeter. The invariant mass resolution of $B \to hh\gamma$ is of the order of 90 MeV/c^2 compared to that of $B \to hh$ which is of the order of 25 MeV/c^2. A good calibration of the calorimeter is an important prerequisite when doing radiative decays analysis.

The calorimeter system sub detectors are detailed in the following.

2.3.5.1 The Pad and the Preshower detectors

The SPD and PS are two planes of scintillator pads, with 6016 detection channels each, separated by a 15 mm, 2.5 X_0, thick lead sheet. A groove in each pad holds the helicoidal wavelength shifting (WLS) optical fiber which collects the scintillating light. The transmission of this light is done by long clear fibers to multi-anode photomultipliers

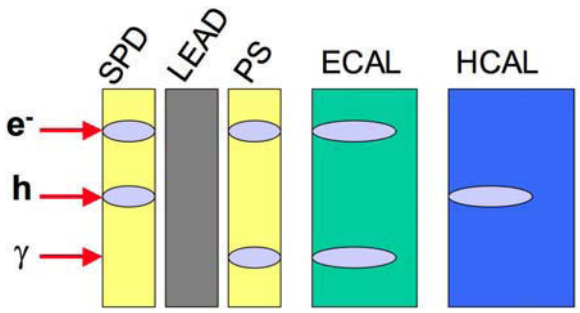

Figure 2.15: Energy deposited on the different parts of the calorimeter by an electron, a hadron, and a photon.

tubes (MAPMT) that are located, along with the Very Front End (VFE) electronics in boxes above and below the detector in order to optimize the light yield at the MAPMTs. PS and SPD VFE shapes and integrates the signal. The SPD VFE includes a discriminator that provides the binary SPD response. The PS signal is digitized in the Front End (FE) electronics placed in crates on top of the calorimeter detectors after 20-30 m of cable. The FE boards hold the data of each channel, sampled at 40 MHz, in digital pipelines waiting for the first level trigger decision. Next to the FE, the SPD Control Boards (CB) includes the functionality necessary to configure the SPD VFEs. In order to achieve a one-to-one projective correspondence with the ECAL segmentation (figure 2.16), each of the sub detectors is divided into inner, middle and outer sections with approximately 4×4, 6×6 and 12×12 cm^2 cell dimensions.

The SPD is used to identify the charged nature of the crossing particles. The distinction between charged pions and electrons is done by making use of the electromagnetic shower dispersion measured in the PS. Due to the lead sheet of 2.5 X_0 present before the PS, almost 14% of unconverted photons start depositing energy in the PS.

The energy deposit of a single minimum ionizing particle (MIP) in SPD and PS is 2.74 MeV. The 10 bit PS dynamics measure deposits in the range from 0 to 100 MIP.

2.3.5.2 The electromagnetic calorimeter

ECAL uses a Shashlik calorimeter technology, i.e. a sampling scintillator/lead structure of 6016 detection channels connected to plastic wavelength shifting (WLS) fibers readout by photomultipliers. The ECAL thickness, 25 X_0, contains the full electromag-

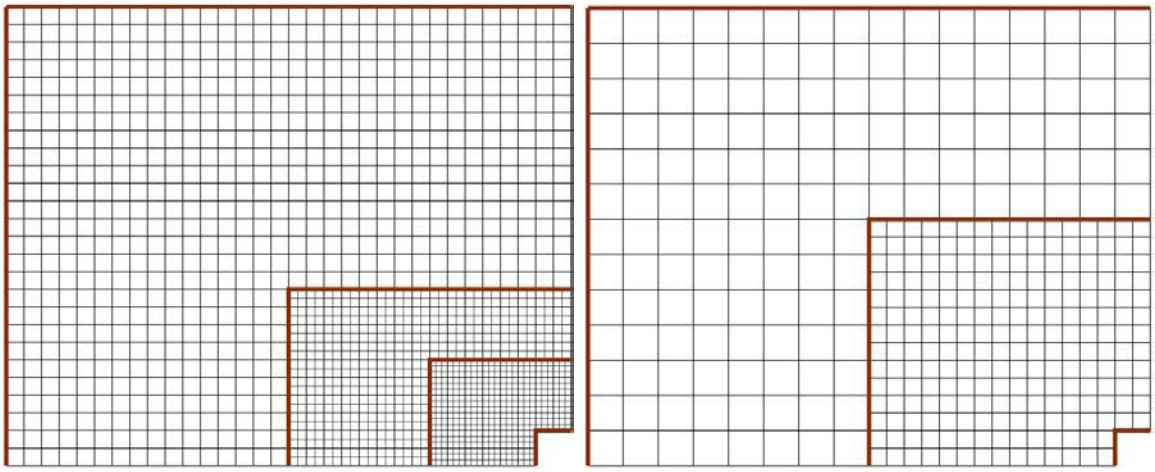

Figure 2.16: Transverse segmentation of a quadrant of the LHCb calorimeters. Left: ECAL with 4×4, 6×6 and 12×12 cm^2 cell dimensions for the inner, middle and outer regions respectively. Right: HCAL with 13×13 and 26×26 cm^2 cell dimensions for the inner and outer regions respectively.

netic shower of high energy incoming photons so as to ensure optimal energy resolution. The calorimeter system has a variable lateral segmentation which takes into account the variation in hit density of two orders of magnitude over the calorimeter surface. A segmentation into three different areas has been chosen for the ECAL with a corresponding projective geometry for the SPD and PS detectors, meaning that all of their transverse dimensions scale with the distance from the interaction point (see figure 2.16). The outer dimensions match projectively those of the tracking system, while the square hole around the beam-pipe approximately limits the inner acceptance to projective polar angles $\theta_{x,y} > 25$ mrad. The choice of using shashlik calorimeter technology was made taking into account optimal energy resolution, fast response time, acceptable radiation resistance and the reliability of this technology, used in other experiments such as HERA-B or PHENIX. The energy resolution of the ECAL modules has been measured with electron beams [52, 53]. It is given by,

$$\frac{\sigma_E}{E} = \frac{a}{\sqrt{E}} \oplus b \oplus \frac{c}{E}$$

where E is in GeV and a, b and c stand for the stochastic, constant and electronics noise terms respectively. Depending on the type of module and test beam conditions the stochastic and constant terms were measured in test beam studies [52,53] to be 8.5% $<$ a $<$ 9.5%, b $\sim$ 0.8% and c$\sim$ 0.003×θ. The term c depends upon the azimutal angle

(θ) of the cell position with respect to the beam axis.

The ECAL is placed at 12.5m from the interaction point. Its dimensions match projectively those of the tracking system, $\theta_X < 300$ mrad and $\theta_Y < 250$ mrad, but its inner acceptance is limited to $\theta_{X,Y} > 25$ mrad due to the substantial radiation dose level in that region.

The ECAL has a 12 bits dynamic range. The Analog-to-Digital Convertor (ADC) counts ranging from 0 to 4095 and the point of zero energy being at 255 ADC counts. The maximum energy per cell is limited by the possible gain applied to the PMTs and is $7{+}10/sin(\theta)$ GeV.

Calibration The performance of each of the cells of the ECAL can be slightly different, and they may suffer aging effects, i.e. detector material wearing out through out the passage of time, at different rates. Therefore, it is necessary to regularly perform a calibration procedure to obtain a set of calibration coefficients, one per cell, in order to provide the best possible operation from the whole calorimeter. In a first calibration stage, the energy flow technique allows to even out the differences between neighboring cells by making use of the smoothness of the sum of transverse energy depositions in the calorimeter. While this method allows to achieve a 5% calibration level, it cannot provide a global energy scale for the calorimeter energy. Starting from the energy flow calibration constants, the decay of resolved neutral pions into two photons is used to iteratively reach an inter calibration level of 2%. Since the calorimeter response is linear, the calibration with low energy π^0 is valid to a good approximation at high energies. The e/p ratio, where e is the calorimeter energy and p is the particle momentum measured by the tracking system, is used to correct for aging effects over small periods corresponding to an integrated luminosity of 40 pb^{-1} in calorimeter areas [54, 55].

2.3.5.3 The hadronic calorimeter

The HCAL is a sampling device made from iron and scintillating tiles, as absorber and active material respectively. The scintillating tiles run parallel to the beam axis which facilitate the readout. The iron tiles are 16 mm thick while the scintillating ones are 4 mm thick. The HCAL has a sampling fraction of 2.7% and corresponds to 5.6 interaction lengths which is not enough for containing the full hadronic shower. Therefore, it gives

only an estimation of the hadron energy with a design resolution of

$$\frac{\sigma_E}{E} = \frac{70\%}{\sqrt{E}} \oplus 10\%$$

with E being in GeV. The HCAL saturates at $E = 15/sin\theta$ GeV. The HCAL is segmented transversely into square cells of 13 cm (inner) and 26 cm (outer), as illustrated in figure 2.16.
The energy resolution and uniformity of the HCAL were measured at the calorimeter test beam. From a lateral scan of a particle beam across the prototype front surface the uniformity in response was measured to be within ±3%. The resolution extracted from a fit to the data at several energies is also in agreement with the design values [56].

Calibration The calibration of the HCAL uses two ^{137}Cs sources of almost 10mCi, one per detector side. This procedure takes about an hour during which they are transported through all of the scintillator cells by a hydraulic system. The response of the PMTs is measured by a dedicated system of current integrators. The relationship between the integrated anode current and the particle energy was measured in test-beam and is used to set the values for the HCAL parameters, obtaining a cell-to-cell inter-calibration at the level of 5%. The use of the in-situ source limits the calibration procedure of the HCAL to technical stops, which occur bi-monthly.

The performance of the ECAL and the HCAL is monitored during the data-taking periods using the built-in LED system. In addition, the distribution of e/p, for electrons in the case of the ECAL, and h/p, for hadrons in the case of the HCAL, can be compared to simulations and is used for monitoring purposes.

2.3.6 The Muon detector

Muon triggering and offline muon identification are fundamental requirements of the LHCb experiment. Muons are present in the final states of many CP-sensitive B decays, such as $B^0 \to J/\psi(\mu^+\mu^-)K^0_S$ or $B^0_s \to J/\psi(\mu^+\mu^-)\phi$, and also play a major role in CP asymmetry and oscillation measurements in semileptonic decays, in which the muon can be used to provide the tag of the initial flavor of the accompanying B meson. Furthermore, muons are involved in rare B decays such as the flavor-changing neutral current

$B_s^0 \to \mu^+\mu^-$, which could provide a hint to new physics beyond the Standard Model [46]. The muon detector provides fast information for the high-p_T muon trigger at the Level 0 (L0, section 2.4), and muon identification for the High Level Trigger (HLT, section 2.4) and offline analysis. Muons have a long lifetime $\tau_\mu = 2.1969811 \pm 0.0000022 \times 10^{-6}$s [34] and a low interaction probability, and thus they pass through the whole detector. The muon detector, shown on figure 2.17, is composed of five stations, M1–M5, of rectangular shape, with a total of 1380 chambers covering a total area of 435 m^2. The inner and outer angular acceptances of the muon detector are 20 (16) mrad and 306 (258) mrad in the bending (non-bending) plane, respectively, resulting in an acceptance of about 20% for muons from inclusive b semileptonic decays. The geometry of the stations is projective, so all their transverse dimensions scale with the distance to the interaction point.

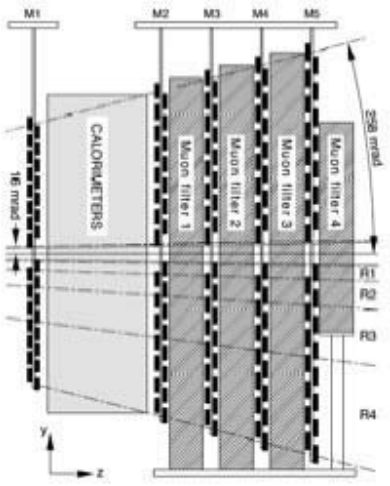

Figure 2.17: Side view of the muon chambers location, with the calorimeter between the M1 and M2–M3.

The muon stations consist of Multi-Wire Proportional Chambers (MWPC) with their planes perpendicular to the beam axis, except in the highest rate region of M1, where triple Gas Electron Multiplier (GEM) detectors are used. Station M1 is located in front of the calorimeters and is used to improve the p_T measurement in the trigger. Stations M2-M5 are placed downstream the calorimeters and are interleaved with iron absorbers 80 cm thick to select penetrating muons. The minimum transverse momentum of a muon to cross M1-M5 is 6 GeV/c since the total absorber thickness of M1-M5 and the calorimeter is $\sim$ 20 interaction lengths.

The detectors provide space point measurements of the tracks, and binary information is passed on by partitioning the detector into rectangular logical pads whose dimensions define the x, y resolution as can be seen in figure 2.18. The muon trigger is based on standalone muon track reconstruction and p_T measurement and requires aligned hits in all five stations. Stations M1-M3 are used to rapidly define the track direction with a design efficiency of 95%, and to calculate the p_T of the muon candidate with a resolution of 20%. Stations M4 and M5 have limited spatial resolution, and their main purpose is the identification of very penetrating particles.

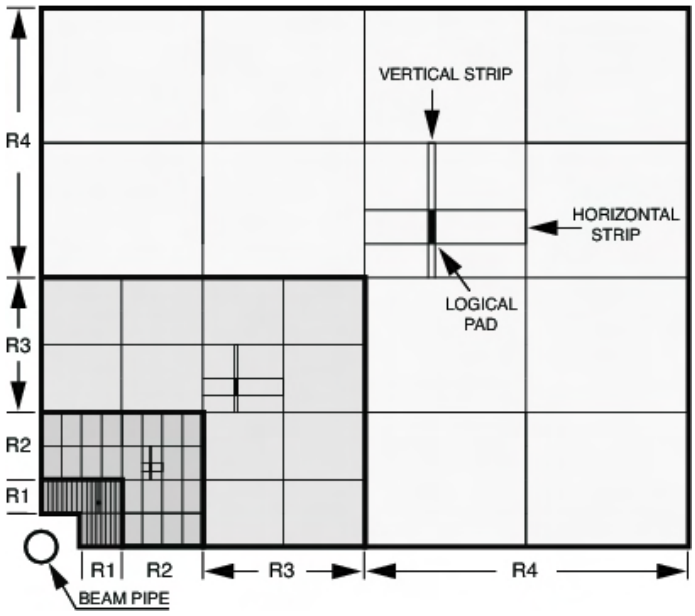

Figure 2.18: Front view of a quadrant of a muon station, with logical pads marked as dark rectangles.

2.3.7 Particle Identification

Particle identification (PID) is achieved by combining the information from several sub detectors. The two RICH detectors, the calorimeters and the muon detector are used for the identification of charged particle (e, μ, π, K, p), while the γ and π^0 are identified using the ECAL.

At LHCb startup a first particle identification procedure has been designed based on a log-likelihood difference (ΔLL). For each type of charged particle, the different particle identification contributions are combined into a ΔLL between a given PID hypothesis

and the pion hypothesis. The DLL for a particle of type a is then given by

$$\Delta LL_a = \Delta \ln \mathcal{L}_{a\pi} = \ln \mathcal{L}_a - \ln \mathcal{L}_\pi = \ln \left[\frac{\mathcal{L}_a}{\mathcal{L}_\pi} \right]$$

where $\mathcal{L}_a$ is the combination of the information of the various sub detectors used for the identification. Therefore, the DLL between two particle hypotheses a and b is given by

$$\Delta LL_{ab} = \Delta \ln \mathcal{L}_{ab} = \Delta \ln \mathcal{L}_{a\pi} - \Delta \ln \mathcal{L}_{b\pi} = \ln \left[\frac{\mathcal{L}_a}{\mathcal{L}_b} \right]$$

In 2012, an improved PID based on a neural network (NN) approach has been employed, using information from all LHCb detector subsystems to provide the probability that a track corresponds to a particular particle species. This NN based PID is used for the analysis presented in this thesis.

Hadron identification The RICH system provides excellent hadron separation over the entire momentum range. The π/K separation is important for the analysis presented in this thesis. The ϕ in $B_s^0 \to \phi\gamma$ and the K^* in $B^0 \to K^*(892)^0\gamma$ decay into $\phi \to KK$ and $K^* \to K\pi$, respectively. The average efficiency for kaon identification for momenta in the 2 - 100 GeV/c range is 95%, with an average pion misidentification rate of 5%. The RICH performance has been studied both on MC and data, and the results can be compared in figure 2.19 [57].

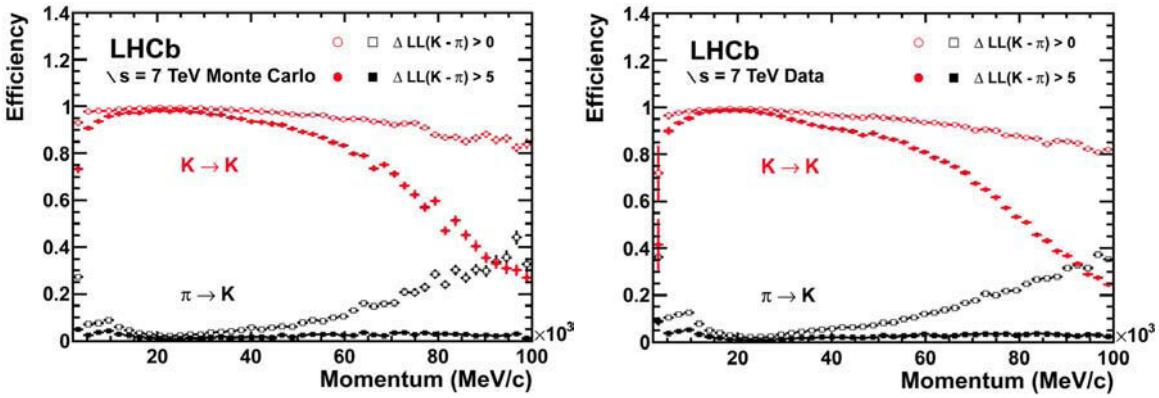

Figure 2.19: Efficiencies for kaons and pions as a function of the track momentum. Left: simulation and right: data.

Muon identification Muon identification is performed by extrapolating well reconstructed tracks with p > 3 GeV/c into the muon stations. On simulation the muon identification efficiency was measured to be $\epsilon(\mu \to \mu)$ 94%, with a corresponding misidentification $\epsilon(\pi \to \mu)$ 3%. The efficiency is a flat function of the momentum above 10 GeV/c.

Electron identification Electron identification is performed based on the information of different sub detectors: the ECAL, HCAL and the PS. Efficiency is measured to be $\epsilon(e \to e)$ 95%, with a corresponding misidentification $\epsilon(\pi \to e)$ 0.7%.

Neutral particle identification Neutral particle identification is performed using information from the calorimeter system. Since the neutral PID is an important prerequisite for radiative analysis, chapter 3 is dedicated to neutral particles reconstruction and identification where the author is directly implicated in the development of an improved neutral particle identification procedure.

2.4 The LHCb trigger system

The rate of visible pp interactions, defined as those collisions that produce at least two charged particles with enough hits in the VELO and T1-T3 to allow them to be reconstructible, is too high to store all of them. The trigger system has to select online interesting events reducing the rate from the rate of visible collisions produced at the interaction point to the rate that can be sustained by the storage system. While the rate of visible interactions that contain bb pairs is about 1/200 of the total visible interaction rate, only 15-20% of them contain at least one B meson with all its decay products inside the detector acceptance. The rate of visible collisions is given by

$$\frac{\mathcal{L}\sigma_{visible}}{\mu}\left(1 - e^{-\mu}\right)$$

where $\mathcal{L}$ is the instantaneous luminosity; $\sigma_{visible} \sim 60$ mb is the visible interaction cross section, where interactions are considered to be visible if they give at least two tracks reconstructed in the VELO pointing to the interaction region; μ is the average number of visible interactions per bunch crossing. The factor $e^{-\mu}$ accounts for the fraction of bunch crossing with no visible interaction. Given the running conditions in 2011 and 2012, the rate of visible collisions was about 12 MHz. This has to be compared to the 3

kHz of events that are written in the storage system.
The trigger system is divided in two levels [58]: the Level-0 Trigger (L0) and the High Level Trigger (HLT). The L0 uses custom electronics operating synchronously with the 40 MHz bunch crossing frequency, while the HLT is executed asynchronously on a processor farm, the Event Filter Farm, made up with commercially available equipment. Figure 2.20 shows a sketch of trigger configuration.

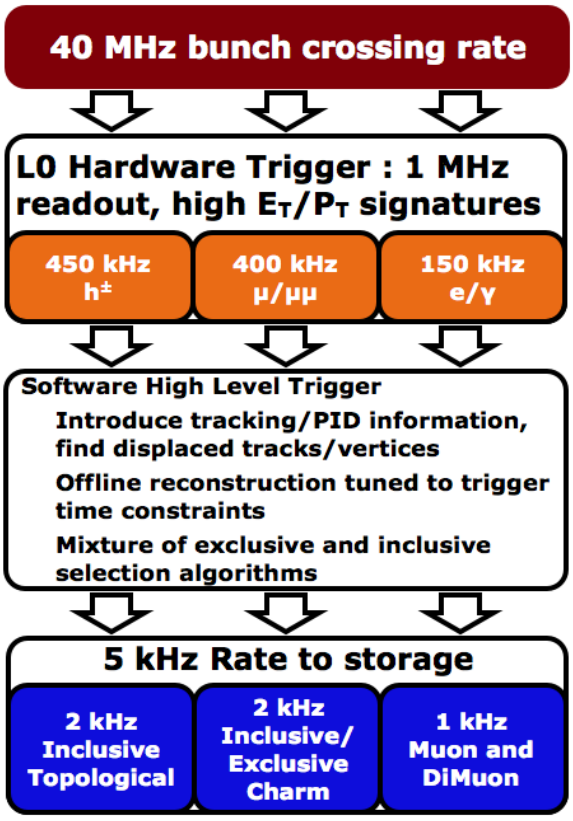

Figure 2.20: Schema of the event flow in the LHCb trigger system.

2.4.1 The Level-0 trigger

The first level of trigger (Level 0, L0) is designed to reduce the visible event rate to the 1 MHz at which the whole detector can be read out. It is implemented using custom made hardware, running synchronously with the LHC clock. The L0 information is coming from the Pile-Up (PU) sensors of the VELO, the calorimeters and the muon system. It is sent to the L0 Decision Unit (L0DU) where the L0 selection algorithms are run.

The PU system has been implemented to reject events with several primary vertices. It uses the information of the PU sensors of the VELO. Given that the experiment is running at higher μ than foreseen in the design, events with pile-up are not rejected. It is used to trigger on beam-gas events providing the number of hits in the PU stations, which are the only detector elements upstream of the interaction point.
The L0 calorimeter trigger system uses information from the four components of the calorimeter, SPD, PS, ECAL and HCAL. It computes the transverse energy deposited in 2×2 calorimeter cells clusters. From these clusters, the following three types of candidates are built. L0Hadron is the highest E_T HCAL cluster added with the energy of the associated ECAL cluster. L0Photon is the highest E_T ECAL cluster with an energy threshold of 5 MIP in the PS and no hit in the SPD cells corresponding to the PS cells. L0Electron has the same requirements as L0Photon, with the additional condition of at least one SPD cell hit in front of the PS cells. The E_T of each candidate is compared to a fixed threshold and events containing at least one candidate above threshold fire the L0 trigger. The total number of hits in the SPD is also determined, and is used to veto events that would take a disproportionately large fraction of the available processing time in the HLT.
The muon chambers perform a stand-alone muon reconstruction with a p_T resolution of $\sim 25\%$. Tracks are searched combining the pad data from the five muon stations to form towers pointing towards the interaction region. The muon stations are divided in quadrants and there is no exchange of information between the quadrants. In each quadrant, the two muon candidates with highest p_T are selected.

To select radiative decays, the event selection is triggered with L0Photon. Since around 30% of the photons are converted into electrons before the SPD detector, the L0Electron channel has to be incorporated as well to have a better efficiency.
In L0, L0Electron and L0Photon select events with an electromagnetic deposit in the ECAL with a transverse energy with respect to the beam direction, E_T, greater than a given threshold, placed at 2.5 GeV in 2011, 2.72 GeV beginning of 2012 and 2.96 GeV mid-2012. Additionally, a subset of the events that pass these two lines also pass the L0ElectronHi and L0PhotonHi lines, which require a higher E_T value of 4.2 GeV.

2.4.2 The High Level Trigger

The High Level Trigger (HLT) filters events using a software application. It uses the Online Event Filter Farm (EFF), which contains up to 20,000 CPU cores, to process and reduce the rate at which events are kept down to 3 kHz. The high rate of incoming events from the L0 trigger and the computing power limitation of the EFF do not allow the up-front use of the full event data information in the decision-making process. Thus, the HLT is divided in two stages: the first stage (HLT1) uses only a partial reconstruction to reduce the rate by a factor of 20 so that the second stage (HLT2) is able to perform full event reconstruction to further discriminate signal events. The HLT processing time per event is close to 30 ms.

2.4.2.1 HLT1

The HLT1 is designed to minimize the impact of varying running conditions on its performance. It is based around a single track trigger, which searches for a single track with high momentum, a large impact parameter (IP, shortest distance between a track and the primary vertex) with respect to all primary vertices (PV) in the event, and a good track quality [59]. the track should have an IP larger than 125 μm with respect to any PV, $p_T > 1.8$ GeV/c and p > 12.5 GeV/c. For events triggered by the Level 0 photon and electron lines, the p_T requirement is relaxed to 0.8 GeV/c.
HLT1 takes 15 ms to process an L0 accepted minimum bias event, and accepts 5% of such events with an efficiency of more than 80% on signal events for most of LHCb's benchmark B decay modes [59, 60]. The 50kHz selected by HLT1 are passed to HLT2.

In the HLT1, Hlt1TrackAllL0 and Hlt1TrackPhoton single track lines are the relevant lines for radiative B decays. They select events based on the transverse momentum of the tracks with respect to the beam direction and their impact parameter (IP, shortest distance between the track and the decay vertex). On one side, Hlt1TrackAllL0 selects low-E_T photons with a harder cut in the required track; on the other side, Hlt1TrackPhotonL0 allows to lower the transverse momentum requirement for the track at the cost of a harder E_T cut on the photon.

2.4.2.2 HLT2

The HLT2 input rate is sufficiently low to perform an almost-full-offline reconstruction, the main difference being that in the HLT2 only tracks with $p_T > 500$ MeV/c and p > 5000 MeV/c are reconstructed. Having fully reconstructed events allows the HLT2 trigger lines to use event selection criteria more in line with those used in offline analyses. Moreover, Global Event Cuts (GEC), such as the reconstructed track multiplicity, are used to reject complex events which require a big amount of processing time.
The HLT2 runs exclusive and inclusive selections. The inclusive ones search for generic B decay features such as displaced vertices or dilepton pairs and the exclusive lines select specific decays using similar selections to those used offline. Special inclusive lines have been developed to trigger on partially reconstructed b-hadron decays. These so-called topological lines are based on displaced vertices with 2, 3 or 4 associated tracks. The topological lines were first implemented as cut based selections. Moreover, to improve the performances, additional lines using a multivariate approach were then added [61,62].

In HLT2, two strategies, exclusive and inclusive, have been included to trigger on radiative B decays both with a relatively high efficiency.
The mean efficiency for the L0 muon triggers is evaluated to be about 90 %. The mean efficiency of the HLT to select decays with muons is about 80 %. The total trigger efficiency is then 70 % [63]. As for hadrons, the mean efficiency of the L0Hadron trigger is evaluated to be about 50 %, the HLT trigger efficiency to be 80 % and the total efficiency to be about 40 % [63]. Whereas for the radiative decays trigger, the mean efficiency of the L0 trigger is about 60 %. At HLT, the efficiency is evaluated to be almost 50 % resulting in a total trigger efficiency of 35 % [64].

2.5 The LHCb luminosity measurements

The number of selected events of a given process per unit of time, denoted as $\frac{dn}{dt}$, is given by

$$\frac{dn}{dt} = \sigma \mathcal{L} \epsilon$$

where σ is the process cross section, $\mathcal{L}$ is the instantaneous luminosity and ϵ is the total efficiency accounting for the detector acceptance as well as the reconstruction and selec-

tion efficiencies.
Hence, the determination of the luminosity is an essential cornerstone for the measurement of any cross section. The average instantaneous luminosity of two colliding bunches can be expressed as

$$\mathcal{L} = \frac{f N_1 N_2}{4\pi\sigma_x\sigma_y}$$

where f is the revolution frequency (11245 Hz at the LHC), N_1 and N_2 are the number of protons in the two bunches, σ_x and σ_y are the transverse sizes of the bunch at the interaction point along the x and y axis respectively.
AT LHCb two methods to determine the absolute luminosity have been implemented [65]: the Van der Meer scan in which the beams are moved in transverse directions in order to investigate the beam transverse profiles counting the interaction rate as a function of the beam offsets and the beam-imaging gas method where the high acceptance of the VELO around the interaction point is used to reconstruct beam-gas vertices produced by the collision of protons in the beam with molecules in the remaining gas of the beam pipe. The positions of the beam-gas interactions are used to determine beam angles and profiles [66]. Combining the two methods, the absolute luminosity can be determined with a relative precision of 3.5%, this allows to calculate a reference cross section of visible interactions. Then, dedicated luminosity counters are defined in order to follow the evolution of the instantaneous luminosity during the data taking. Figure 2.3 shows the LHCb integrated luminosity accumulated over the 2011-2012 run period.

2.6 The LHCb software

The LHCb software is based on the Gaudi [67,68] architecture, which provides an Object Oriented framework for all the applications used within the experiment [69]. It has the flexibility needed for running the LHCb chain from the Monte Carlo generation to the real data analysis using the same tools. Data persistency is based on the Root software [70, 71], a set of object-oriented frameworks designed to handle and analyze large amounts of data.
The simulation project is called GAUSS [72,73]. PYTHIA 6.4 [74] with a configuration specific to LHCb is used to generate pp collisions. The hadronic particle decays are described by the EvtGen [75] package in which PHOTOS [76] is used to generate final state radiations. GAUSS then connects the PYTHIA output as input of GEANT 4 [77]

which implements the interaction of the particles with the detector and the response of the active materials. The simulation of the digitization of the signals produced in the active materials is performed by the BOOLE application [78]. It includes simulation of the readout electronics as well as of the L0 hardware trigger. The simulation output is digitized data that mimics the real data coming from the detector.
The event reconstruction is performed by the BRUNEL application [79]. The MOORE application [80] can be used to run the HLT selection on reconstructed events. This is especially useful to emulate the HLT response on the simulated data. Finally, DAVINCI [81], the analysis application, computes for each event the variables used in the analysis and stores them in standard files.

2.7 Data flow in LHCb

The raw data of the events selected by the trigger system coming from the experiment are transferred to the CERN Tier-0 for further processing and archiving. These unprocessed data are then used to reconstruct the physical particles, made up from tracks and particle identification information, by making use of the raw information such as the hits or the calorimeter cluster energies. This reconstruction process is performed in the Tier-1's. Reconstructed events are saved in a Stripping Data Summary Tape (SDST) file, which contains the necessary information for further event filtering without including the raw data.
The SDST files are analyzed in order to further filter events for physical analyses by making use of the full reconstructed information and with looser timing constraints than in the HLT. This sequence is known as Stripping, and finally produces a Data Summary Tape (DST) file, to which the raw data event information is attached. DSTs are the files accessible to scientists for physics analyses. The data are reprocessed several times a year with the improvement of the reconstruction, alignment and stripping software and algorithms.

Chapter 3

Photon reconstruction and identification

Contents

The detection of photons and neutral pions decaying into photons pair is performed by the LHCb Electromagnetic CALorimeter (ECAL). Moreover, and in order to have a precise determination of photon parameters, information from the PreShower (PS) and the Silicon Pad Detector (SPD) detectors are used. In this chapter, the reconstruction technique of photons will be described in details, then, the procedure for photon identification will be discussed. Also, photon and neutral pion separation will be explained and discussed.

3.1 Photon reconstruction

3.1.1 Clusterization

The reconstruction of electromagnetic showers process begins with the identification of the ECAL cell that has an excess in energy deposition, referred to as local maximum or seed cell, compared to all its direct neighbors. The number of neighbor cells is 8 per 'regular' cells which are far from boundaries of ECAL areas, and it varies from 3 to 9 for cells near the boundaries. These cells are selected only if the transverse energy is larger than 50 MeV [82]. The identified cell will originate the cluster according to the clusterisation procedure adopted by the Cellular Automaton algorithm [83]. As direct consequence of these formal definitions, the seed cells of two reconstructed clusters are always separated at least by one cell. If a calorimeter cell is shared between two clusters the energy of the cell is shared between the clusters depending on the total cluster energy and the distance between the clusters' barycenter.
The transversal barycenter and energy of the electromagnetic shower deposit in the ECAL of the corresponding particle are calculated as

$$\epsilon = \sum_i \epsilon_i \qquad x_b = \frac{1}{\epsilon}\sum_i x_i\epsilon_i \qquad y_b = \frac{1}{\epsilon}\sum_i y_i\epsilon_i$$

where ϵ_i represents the energy measured in each cell i of the cluster, x_i and y_i give the position of the center of the cell. A 3×3 mask is applied around the seed cell for the evaluation ϵ and the transversal barycenter to limit the accumulation of electronic noise.

3.1.2 Neutral clusters selection

The selection of neutral clusters are performed using an anti-matching techniques with reconstructed tracks. Reconstructed tracks in the event are extrapolated to the calorimeter and then all-to-all matching with the reconstructed clusters are performed. A two-dimensional χ^2_{2D} is then constructed as

$$\chi^2_{2D}(\vec{P}) = \left(\vec{P}_{tr} - \vec{P}\right)^T \mathcal{C}_{tr}^{-1} \left(\vec{P}_{tr} - \vec{P}\right) + \left(\vec{P}_{cl} - \vec{P}\right)^T \mathcal{S}^{-1} \left(\vec{P}_{cl} - \vec{P}\right)$$

where $\vec{P}_{tr}$ is the extrapolated track 2D-point to the calorimeter plane, $\mathcal{C}_{tr}$ is the covariance matrix of $\vec{P}_{tr}$ parameters, $\vec{P}_{cl}$ is cluster barycenter position and S is the corresponding 2×2 covariance matrix. The χ^2_{2D} is minimized with respect to $\vec{P}$. The clusters with minimal value of χ^2_{2D} estimator in excess of 4 are selected as neutral clusters. This criteria rejects the clusters due to electrons and significantly suppress the clusters due to other charged particles keeping the high efficiency for clusters due to photons.

3.1.3 Photon reconstruction

There are two types of photons considered at LHCb, converted and unconverted. Due to the material found between the interaction point and the calorimeter, 30% of the photons coming from the interaction region convert into a e^+e^- pair before the calorimeter front face. There are two kinds of converted photons. If the photon conversion occurs before the tracking system, the tracks of the two electrons can be reconstructed. Then the photon information is coming from the reconstruction of the two separated electrons tracks. If the conversion happens after the magnet, the electrons mostly end up in a single ECAL cluster and the charged nature of the conversion can be identified using the signal left in the SPD. A cluster with no matching tracks but with a deposit in the SPD is the signature of a converted photon after the magnet. Dedicated corrections explained later are determined for converted photons.

3.1.3.1 Photon energy

The geometry of the calorimeter system has been chosen in such a way that the ECAL cells correspond to the PS and SPD cells. The photon energy is evaluated by summing the ECAL cluster energy with the energy deposit in the PS cells in front. The main energy loss comes from the fact that the cluster is reconstructed as a 3×3 matrix of ECAL

cells and the transversal energy deposited outside this matrix of cells is not accounted for. Moreover, the dead material between the modules of the calorimeter cells introduces intrinsic losses that need to be compensated. These leakages are corrected following

$$E(\gamma) = \alpha E_{ECAL} + \beta E_{PS}$$

where E_{PS} is the measured energy in the PS cells. The factor α is obtained from the photons subsample with small energy deposits in the PS and it accounts for lateral and longitudinal leakages in the ECAL and the relative position of the energy-weighted barycenter inside the cluster and inside the ECAL module frame. The passive-to-active energy -being the energy measured in the scintillator to that radiated in the lead- factor β for PS is obtained from the complementary subsample once α is determined.

3.1.3.2 Photon momentum

The transversal barycenter of the shower, x_c, y_c, is evaluated from the energy-weighted barycenter of the cluster (section 3.1.1) corrected from the non linear transversal profile of the shower shape (hereafter referred to as S-correction). Assuming the transversal shower shape fit with a single exponential, $E(r) \sim E_0 e^{-r/b}$, the S-corrected barycenter, x_c, y_c, is then given by the single parameter S-function [84]

$$(x_c, y_c) = \mathcal{S}_0[(x_b, y_b), b] = b\ asinh\left[\frac{(x_b, y_b)}{\Delta} cosh\frac{\Delta}{b}\right]$$

where (x_b, y_b) are the x,y positions of the energy-weighted barycenter, Δ the half cell size and b the decay constant of the exponential profile. The b parameter is tuned on data using electron tracks matched clusters. It is found to be about 10%, 13% and 15% of the cell size for the outer, middle and inner ECAL regions, respectively.
Moreover, the transversal barycenter position has to be corrected from left/right asymmetries in the X-direction (bottom/up in the Y-direction) that is due to the incidence angle of the photon that induces a non spherical profile of the shower spot, also, and since the single exponential is a rough approximation, an additional corrections to $\mathcal{S}_0$ is needed; the $\mathcal{S}$-correction is

$$(x_c, y_c) = \mathcal{S}_0[(x_b, y_b), b] + \mathcal{S}_1[(x_b, y_b)] + \mathcal{S}_2[(x_b, y_b)]$$

having $\mathcal{S}_1$ and $\mathcal{S}_2$ as correcting from residual S-shape and geometrical asymmetries, re-

spectively and improving the resolution on the impact position of the photon [85].

The first evaluation of the photon momentum is done assuming its origin is (0,0,0). When this photon is associated to a decay, its parameters are reevaluated according to the decay vertex. The photon direction is pointing to the 3D barycenter of the shower x_c, y_c and z_c. z_c is obtained as the ECAL position corrected from the penetration depth of the photon. The correction is scaled as the logarithm of the energy and, in order to take into account the information provided by the PS about the position of the shower beginning, a smooth dependance of the parameter β_c with E_{PS} is included

$$z_c = z_{ECAL} + \alpha_c ln(E_c) + \beta_c(E_{PS})$$

3.2 π^0 reconstruction

π^0 branching fraction into two photons is (98.823±0.034)% [86]. The π^0 signature in the ECAL depends on its kinematics, the higher is the momentum of the π^0 the closer the two photons are at the entry of the calorimeter. These two photons can then produce two separated clusters or share a single cluster in which their individual signals are not clearly distinguishable. The π^0 are classified as resolved π^0 in the former case and as merged π^0 in the latter one. The transverse momentum spectrum of merged π^0 starts around 2 GeV/c.

3.2.1 Resolved π^0

To reconstruct resolved π^0, photons are paired and their invariant mass, $m_{\gamma\gamma}$, is compared with the π^0 mass. Only photons with transverse momentum greater than 200 MeV/c and with a track matching χ^2_{2D} greater than 4 are taken into account [85]. $m_{\gamma\gamma}$ is required to be in the range 105 to 165 MeV/c^2. The measured resolution of $m_{\gamma\gamma}$ is about 7 MeV/c^2 in the 2011-2012 sample. Using those criteria and according to the simulation, the global reconstruction and identification efficiency of resolved π^0, with respect to events where both photons are in the ECAL acceptance, both with transverse momentum greater than 200 MeV/c, is about 50% [85]. The inefficiency is mostly due to photon showering in the material upstream the calorimeter. Part of this inefficiency can be measured by considering photon conversion reconstructed as a pair of electrons.

3.2.2 Merged π^0

Each electromagnetic cluster is split in two subclusters defined from the two most energetic cells in the cluster. An algorithm calculates the barycenter of each sub cluster using the expected transverse shower shape of individual photons. The positions of the two barycenters depend on the energy sharing between the two subclusters, which itself depends on the positions of the two barycenters. According to that, the calculation is done using an iterative procedure [85].

After the preparation of the two photon subclusters, the following criteria are applied to identify the cluster as coming from a π^0.

- The cluster is identified as coming from a neutral particle requiring a track matching $\chi^2_{2D} > 1$.
- The cluster energy has to be compatible with the merged π^0 hypothesis. To assure that, a cut is applied on the minimal distance allowed by the kinematics between the impacts of the two photons on the ECAL front face

$$d_{\gamma\gamma} = 2 \times z_{ECAL} \times m_{\pi^0}/E_{\pi^0} < 1.8\Delta,$$

  where Δ is the transverse size of the calorimeter cell, m_{π^0} is fixed to 135 MeV , E_{π^0} is the π^0 energy and z_{ECAL} is the position of the ECAL front face with respect to the interaction point.
- The reconstructed merged π^0 mass is required to be in the range 75 to 195 MeV/c^2. The wider mass range compared to resolved π^0 is due to the higher $m_{\gamma\gamma}$ resolution of 12-15 MeV/C^2.

The performance of neutral pion reconstruction is illustrated in figure 3.1, which shows the invariant mass distribution for $D^0 \to K^-\pi^+\pi^0$ candidates for resolved and merged π^0 candidates [87]. In this example, the estimated resolution of the invariant mass of the reconstructed D^0 is 30 MeV/c for the merged π^0 candidates and 20 MeV/c for the resolved ones.

3.3 Multivariate approaches

Particle identification algorithms at LHCb are based on multivariate approaches. Multivariate classifiers combine correlated input variables into a discriminant output. They

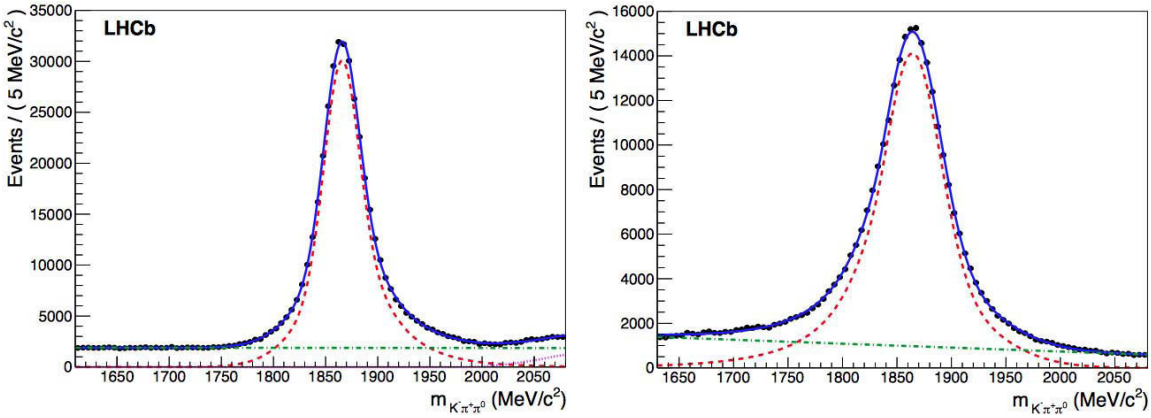

Figure 3.1: Mass distributions of reconstructed $D^0 \to K^-\pi^+\pi^0$ candidates with resolved π^0 (left) and merged π^0 (right). Both are obtained from the 2011 data sample. The overall mass fit [87] is represented by the blue curve, with the signal (red dashed line) and background (green dash-dotted line and purple dotted lines) contributions also shown.

have to be trained over signal and background samples. The training allows to determine the internal parameters of the classifier that maximize the separation between the two samples. Several multivariate approaches exist, among those are the artificial Neural Network (NN), the Boosted Decision Trees (BDT) and the ΔLL discriminant. These approaches are used in the upcoming sections and are briefly described here.

An artificial neural network consists in a set of interconnected nodes or neurons by analogy with biological neural networks. Each neuron produces a non-linear response depending on a given set of input signals. The nodes are generally organized in layers, each layer being fully connected to the next one. This type of neural networks is called a multilayer perceptron (MLP). A MLP is a NN that consists of three or more layers, an input and an output layer with one or more hidden layers. The layers contain a certain number of nodes (neurons) at which a linear combination of the value of the variables used as input. Each node i in one layer connects with a weight w_{ij} to every node j in the following layer. Hence, it receives as a signal input the value of the linear combination, denoted I_j^k, with k being the index representing the layer and j being that representing the neuron, given as

$$I_j^k = \sum_i w_{ij} O_i^{k-1}$$

with,

$$O_j^k = g(I_j^k)$$

being the value assigned to each neuron j in the layer k with $O_j^1 = \lambda_j$ where λ is the value of the input variable. g is the activation function of a node which defines its output given an input or set of inputs. The used activation function is of the type sigmoid. The role of the weights that are applied to the neural net between the input layer and the first hidden layer is to construct linear combinations of the input variables in such a way as to separate two types of classes, giving one of them high positive values of the linear combination and giving the other low negative values. Hence, the global information that is present at the input layer is propagated via the hidden layers to the output layer (forward propagation). The value of the output neuron presents the best separation between the two classes of object's.

The learning phase (training phase) of the NN consists in adjusting the weights in order to achieve the optimal separation. When the number of training cycles is large that, in the limit of a finite training sample, the pattern recognition is fine tuned for events in the training sample and give worse performance on a different sample, the classifier is said to be overtrained. Learning is based on an algorithm that necessitate the activation function to be continuous and differentiable. When the neural net is used to separate two overlapping classes of objects in the variable space, the continuity of the transfer function permits to consider the neural net as an approximation of an ideal classifier based on the probability that the events belongs to certain class. In the NN, the probability density of a certain class is deduced throughout the learning phase and need not be known in advance [88].

Hence, each object is presented to the NN and the weights are adjusted accordingly. The procedure is repeated iteratively for many times where each iteration defines a learning cycle.

The weight correction applied to the weights associated to the layers n-1 and n take into account the corrections applied to the weights associated to the layers n and n+1, hence backpropagating the error from the output layer through the hidden layers to the input layer.

When the weight optimization is done, the trained NN can be applied to a separate sample to discriminate two classes similar to the ones used for the training (learning).

Boosted Decision Trees provide another powerful event classifier. A decision tree is a sequence of binary splits of the data. Each split is done according to the input variable that, at this stage, gives the best separation between signal and background when being cut on. The process is repeated until a given number of final nodes is reached. It can also end if all nodes are pure signal or background, or if a node has too few events. Decision trees are known to be powerful but unstable as small changes in the training samples can produce large changes in the tree. They are stabilized thanks to a boosting algorithm. The training events which were misclassified have their weight increased (boosted) to form a new tree. Many trees are built up this way. They are finally combined into a single classifier given by the average of the individual decision trees.

The method of Log Likelihood ΔLL is among the most straightforward multivariate analyser approaches. The likelihood ratio, R, is defined for an event by the ratio of the signal to the signal plus background Likelihoods. The individual Likelihoods are products of the corresponding probability densities (PDF) of the discriminating input variables used. In general, polynomial splines fitted to histograms, or unbinned Gaussian kernel density estimators, are used to estimate the probability density functions (PDF) obtained from the distributions of the training variables.

3.4 Photon identification

The track matching χ^2_{2D} is complemented with information from the SPD and PS detectors to define the photon identification estimator. A study is performed on simulation to achieve a high identification power in order to select photons amongst other sources of ECAL deposits. In this section two methods are presented. A method based on the ΔLL estimator is discussed. An improved procedure developed during my thesis is detailed.

3.4.1 The ΔLL based Photon identification

The first implemented photon identification procedure at LHCb was based on a log-likelihood estimation [89].

3.4.1.1 Samples definition

Performance evaluation and separation optimization is performed on simulated data (MC). For that purpose, signal and background samples are defined in the following way:

Signal: a reconstructed photon that is associated to a simulated (MC) photon originating from the interaction region defined by ($\Delta r \leq 10mm, \Delta z \leq 150mm$) and whose energy is correctly measured in the interval

$$\Delta E \; = \; \frac{\|E^{\gamma}_{Rec} - E^{\gamma}_{MC}\|}{E^{\gamma}_{Rec}} \leq 25\%.$$

Background: all reconstructed photon candidates that do not match signal definition.

It is worth noting that the background sample contains real photons not originating from the interaction region.

3.4.1.2 Discriminating variables

The main variable used for this photon identification tool is the χ^2_{2D} of the cluster. In addition, the energy deposits in the PS of the calorimeter system is also used. The PS energy deposit is high for particles interacting electromagnetically and allows an efficient separation of the signal with charged pion background [89].
The χ^2_{2D} of the cluster (section 3.1.1) permits to apply an accurate track veto and to remove a large fraction of the electron background which is not identified by the SPD criteria. The background is very high for small χ^2_{2D} value, although the signal is not particularly peaked.
The photons distributions are built separately for converted, i.e. having an SPD signal in the cell facing the calorimeter cluster center, or not and histograms where built for each photon energy interval. The Probability Density Functions (PDF) where built for each photon energy bin. This was necessary to improve the selection efficiency as the distributions of the variables of interest depend on the cluster reconstructed energy. The energy bin width depends on the statistics in the energy region considered in order to populate the distributions and on the rapidity of the variations of the variables with respect to the energy. The non-constant bin size is to have a similar statistics in each bin.

The variables are combined as follows

$$\mathcal{L}(\vec{x}) = \frac{\prod_i s_i(x_i)}{\prod_i s_i(x_i) + \prod_i b_i(x_i)}$$

to construct the estimator. s_i and b_i are respectively the signal and background PDFs for the variable i, whose value is measured to be x_i for a specific photon candidate. The signal and background are separated in the distribution of the output discriminant. The background contains irreducible contribution from real photons not originating from the interaction region that are considered as background. This contribution will cause a serious degradation of the estimator performances. The performance of the method will be directly compared with the improved photon ID discussed in 3.4.2.

3.4.2 Improved Photon identification

The photon identification procedure discussed before has had many points from which it can be improved. First of all, the signal takes into account photons coming from the interaction region only, leading to the fact that other photons are considered as background in the optimization procedure. Moreover, new discriminating variables - from which a good separation power could be drawn- are used in the improvement. Finally, Neural Net (NN) is used as an estimator for the optimization procedure instead of ΔLL estimator.

3.4.2.1 Samples definition

As the performance evaluation is performed on simulated data, the signal and background samples are defined as
Signal: reconstructed photon candidates matching the generated photons , i.e, taking into account all the photons in the sample whether or not these photons are coming from the interaction region. All photons in simulated $B \to K^\star\gamma$ MC sample are taken into account for the training of the classifier.
Background: several background sources are considered separately.

- Reconstructed photon candidates matching a MC generated electron are taken as background so as to have a dedicated training to separate photons and electrons. Electrons are taken from simulated $B \to K^\star ee$ events and used for training the classifier.

- Reconstructed photon candidates matching a non-electromagnetic MC particle are considered as background in order to have photon/non-electromagnetic particles separation.

- Finally, a merged π^0 background where a dedicated photon/π^0 separation tool has been developed for this purpose [87, 90]. This will be explained in section 3.5.

The samples used for the improved multivariate approach cover a wide range in the photon transverse momentum (P_T), up to the saturation level of the calorimeter, this can be seen in figure 3.2 where the P_T distribution is shown for the different samples taken into account.

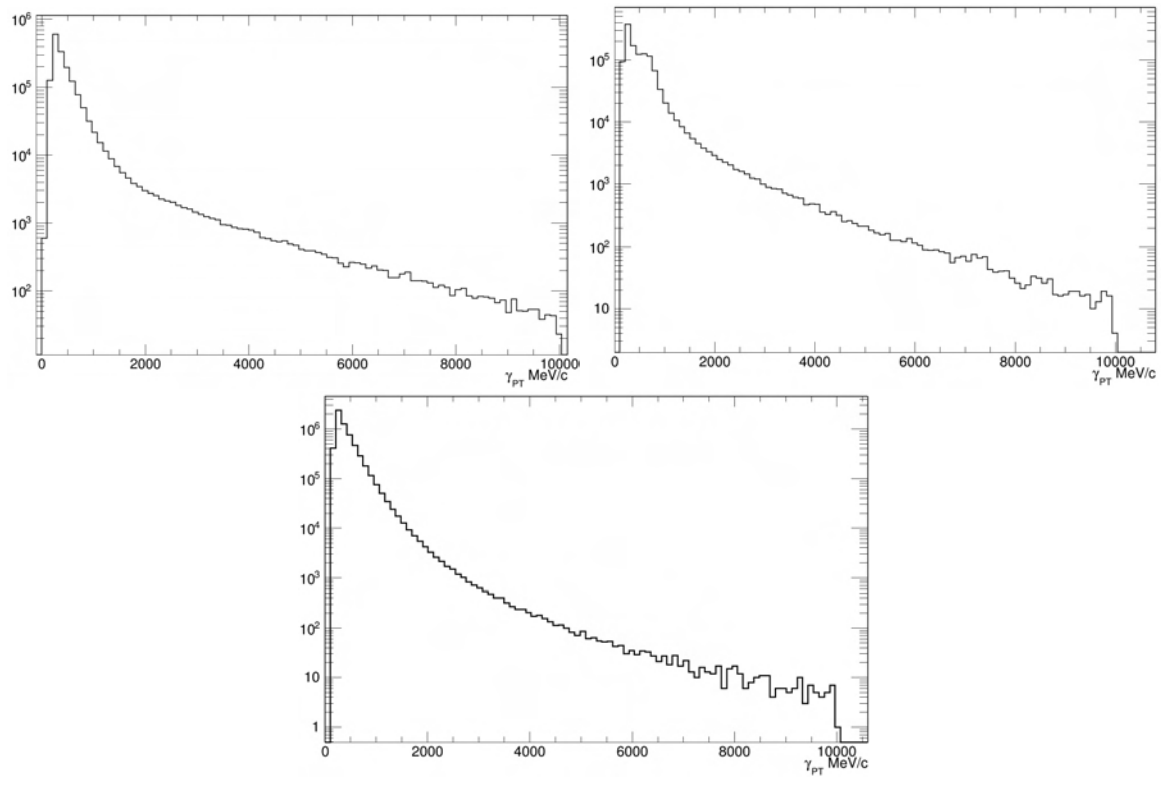

Figure 3.2: The distribution of the transverse momentum of the reconstructed photons in the samples used for the improved multivariate approach. Top left: signal photons, top right: electrons reconstructed as photons and bottom: non electromagnetic deposit.

3.4.2.2 Discriminating variables

The improved multivariate separation uses the same set of variables described in section 3.4.1.2 together with new discriminating variables described below

- The ratio of the energy of the seed cell to that of the total cluster in the ECAL: $(E_{seed}/E_{3\times3})_{ECAL}$.

- The ratio of the energy in the PS cell in front of the seed cell to that of the total PS energy: $(E_1/E_{3\times3})_{PS}$.

- The ratio of the energy in the HCAL, in the projective area matching the cluster, to the energy in the ECAL: E_{HCAL}/E_{ECAL}.

- The 2×2 matrix of PS cells with the highest energy deposit in front of the 3×3 reconstructed cluster: PSE4Max.

- The second order energy-weighted momentum of the cluster defined from

$$\begin{aligned} S_{XX} &= \frac{\sum_{i=1}^{N} e_i (x_i - x_c)^2}{\sum_{i=1}^{N} e_i}, \\ S_{YY} &= \frac{\sum_{i=1}^{N} e_i (y_i - y_c)^2}{\sum_{i=1}^{N} e_i}, \\ S_{XY} &= S_{YX} = \frac{\sum_{i=1}^{N} e_i (x_i - x_c)(y_i - y_c)}{\sum_{i=1}^{N} e_i} \end{aligned}$$

  where $(x_c,\ y_c)$ is the position of the photon defined in section 3.1. The cluster spread is defined as $S_{XX} + S_{YY}$

- The number of PS cells in front of the cluster with non-zero energy deposit: PSMulti.

- The multiplicity of hits in the 3×3 SPD cells matrix in front of the reconstructed cluster: SPDMulti.

Figures 3.3,3.4 and 3.5 show the distribution of these variables for signal and for each type of background considered in the training of the multivariate approach.

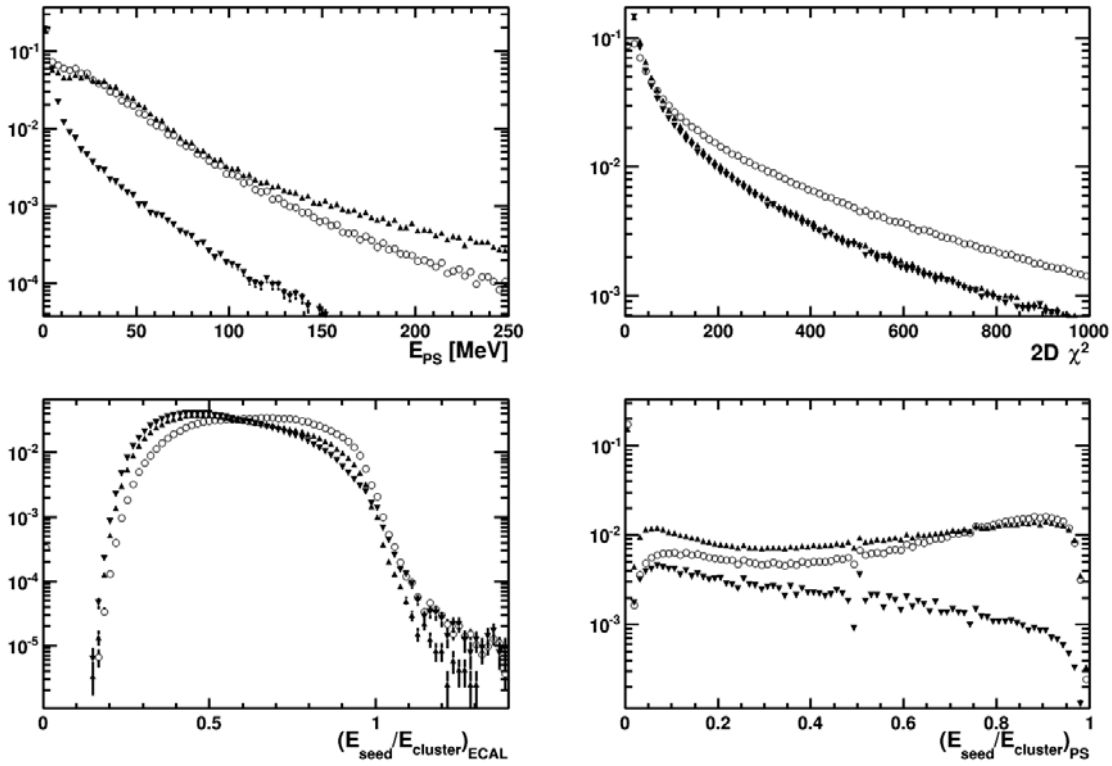

Figure 3.3: The distribution of the variables used as input for the improved photon ID multivariate tool. Photons as circles, electrons as up triangles and non electromagnetic deposits as down triangles. Top left: PS energy, top right: χ^2_{2D} of the cluster, bottom left: $(E_{seed}/E_{3\times3})_{ECAL}$ and bottom right: $(E_1/E_{3\times3})_{PS}$. See text for precise definition of variables.

The variables are combined using a multi-layer perceptron (MLP) (3.3).

3.4.2.3 Performance and results

The possible backgrounds, introduced in 3.4.2.1, are considered separately when training the NN to identify photons. A neural net is trained to separate between photon and non electromagnetic clusters in the calorimeter, the output of this NN is referred to as NN_h. Another neural net is trained to separate between photons and electrons, its output is referred to as NN_e. The package TMVA [91] is used as a framework for training the classifiers.

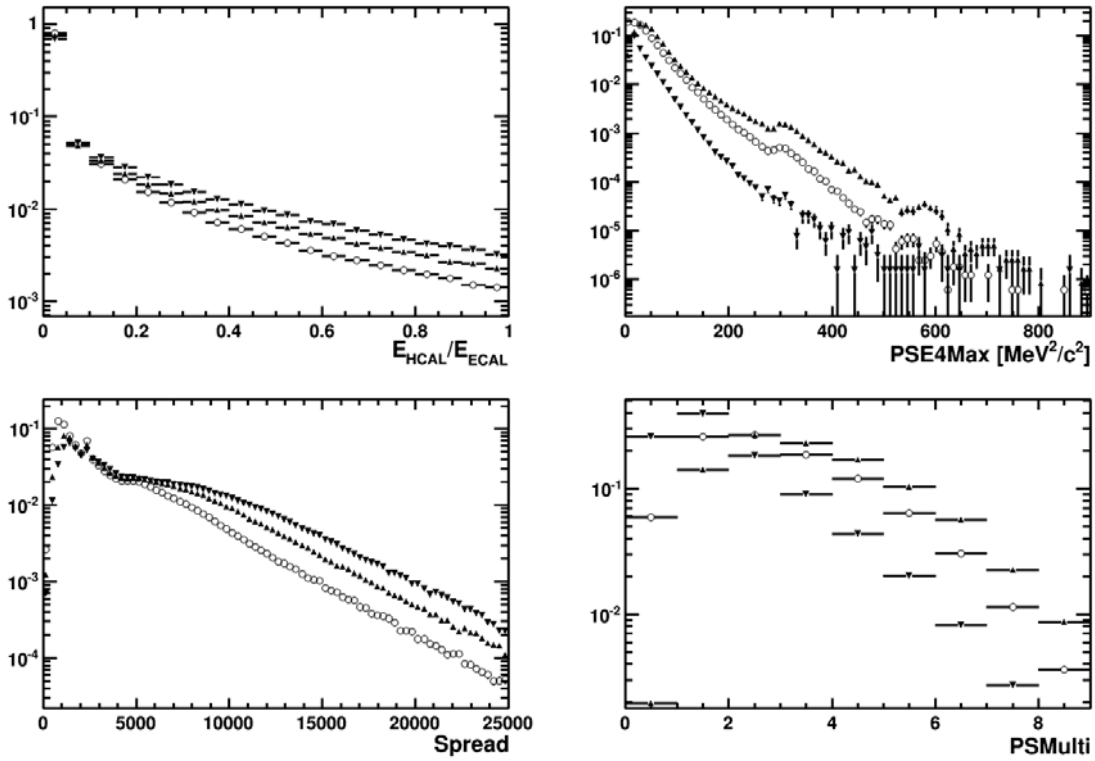

Figure 3.4: The distribution of the variables used as input for the improved photon ID multivariate tool. Photons as circles, electrons as up triangles and non electromagnetic deposits as down triangles. Top left: E_{HCAL}/E_{ECAL}, top right: PSE4Max, bottom left: cluster spread and bottom right: PSMulti. See text for precise definition of variables.

Photon/non electromagnetics separation The signal and background MC samples are split on a random basis, where half of the statistics is used for training (training sample) and the other half is used for testing (testing sample) the classifier.

Figure 3.6 shows the overtraining check of the MLP and the Boosted Decision Tree (BDT) respectively. The output of the classifier on the training and testing samples are compared and the Kolmogorov-Smirnov [92] compatibility check is applied to compare the train and test samples. The BDT, briefly discussed in 3.3, has been trained for the comparison of performance. For details about the BDT, the reader is referred elsewhere [93]. The figures show that there was no overtraining during the learning process meaning that the output performance is reliable, this can be seen in the consistency between the outputs of the classifier on the train and test samples. Figure 3.7 shows the signal efficiency versus the background rejection both for MLP and BDT classifiers.

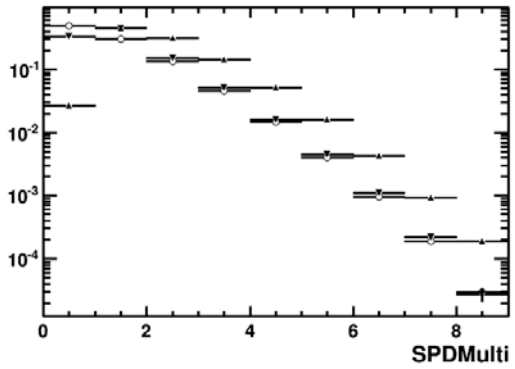

Figure 3.5: The distribution of SPDMulti used as input for the improved photon ID multivariate tool. Photons as circles, electrons as up triangles and non electromagnetic deposits as down triangles. See text for precise definition of the variable.

The MLP has a slightly better performance than the BDT.

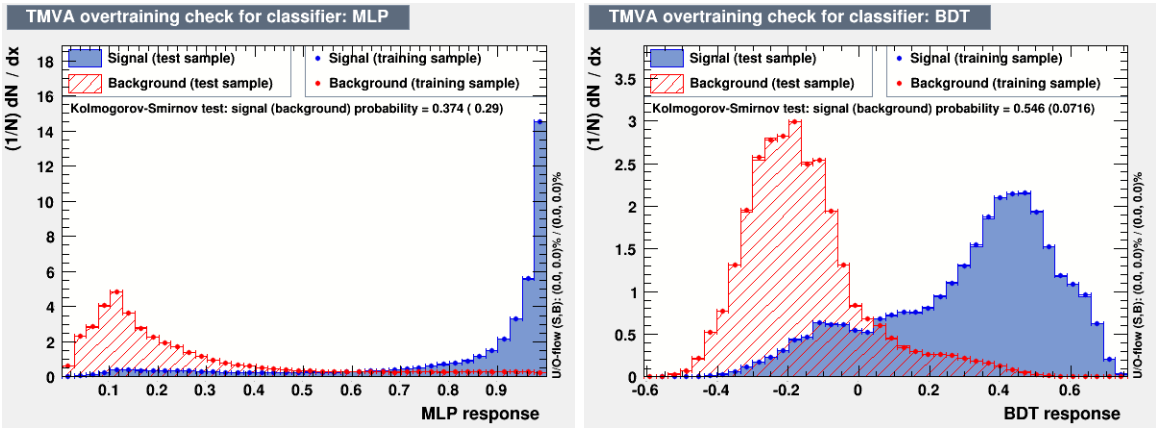

Figure 3.6: The overtraining check performed for the trained classifiers: MLP (left) and BDT (right). Signal test sample is represented by a solid histogram and background test sample is represented by a dashed histogram. The data points represent the signal and background training samples.

After training and testing, the performance of the NN MLP is validated on an independent sample and compared to the ΔLL classifier performance. Figure 3.8 shows the signal efficiency versus background rejection for the NN output variable (black curve) compared to the performance of the ΔLL based method (red curve). At 90 % signal efficiency, there is a 20 % improvement in the performance of rejecting non electromag-

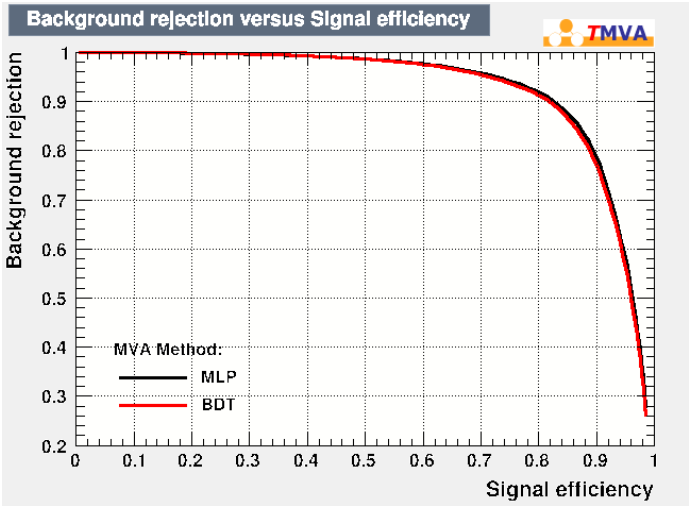

Figure 3.7: Non electromagnetic background rejection versus photon signal efficiency for both MLP (black) and BDT (red).

netic background.

The efficiency in bins of the transverse momentum is also checked. Figure 3.9 shows the signal and background efficiency in bins of the P_T where a cut at 0.2 in the NN_h output is applied. The P_T bins are of variable size starting from 200 MeV/c and up to 1 GeV/c so as to accumulate similar statistics in each bin. It is quite clear from the plot that the efficiency of signal is almost constant over the P_T range whereas background efficiency increases at high P_T. Performing the same check in the different ECAL regions one can sort out the same conclusion.

Photon/electron separation Another NN is trained to separate between photons and electrons. Hence, signal is considered to be photons matched to the true generated MC photons and background is taken to be reconstructed photon candidates matched to the true MC generated electrons. TMVA is used and the samples are split on a random basis, where half of the statistics is used for training and the other half is used for testing. Figure 3.10 shows the overtraining check. The output of the classifier on the training and testing samples are compared and the Kolmogorov-Smirnov [92] compatibility check is applied to compare the train and test samples. The figures show that there was no overtraining and the output performance is reliable, this can be seen in the consistency between the outputs of the classifier on the train and test samples. It is clear from the

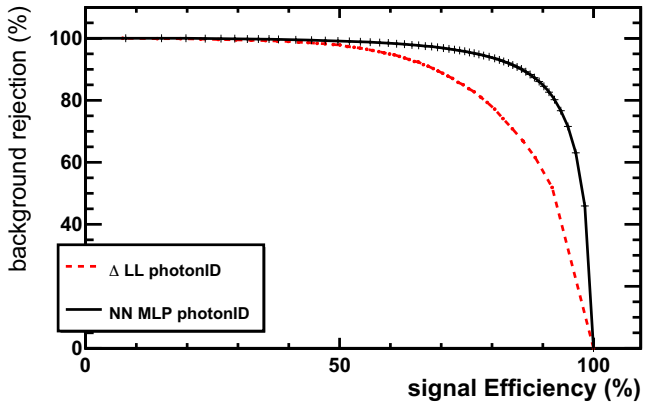

Figure 3.8: Non electromagnetic background rejection versus photon signal efficiency of the MLP classifier as obtained from a separate validation sample. The ΔLL method output (red dashed line) and the NN method output (black solid line) are compared.

variable distribution that the electron is more signal-like than the non electromagnetic deposits compared to figure 3.6 this is, of course, due to the electromagnetic nature of the electron. The performance of two different classifiers is compared, the NN MLP and the BDT. Figure 3.11 shows the signal efficiency versus the background rejection both for MLP and BDT classifiers. The MLP has a slightly better performance than the BDT.

After training and testing, the performance of the NN MLP is validated on an independent sample and compared to the ΔLL performance. Figure 3.12 shows the signal efficiency versus background rejection for the NN_e variable (black) compared to the performance of the ΔLL based tool (red). At 90 % signal efficiency, there is a 20 % improvement in the performance of rejecting electron background.

The efficiency in bins of the transverse momentum is also checked. Figure 3.13 shows the signal and background efficiency in bins of the P_T where a cut at 0.4 in the NN output is applied. The P_T bins are of variable size starting from 200 MeV and up to 1 GeV so as to accumulate enough statistics in each bin. It is quite clear from the plot that the efficiency of signal is almost constant over the P_T range whereas background efficiency increases at high P_T. Performing the same check in the different ECAL regions one can sort out the same conclusion.

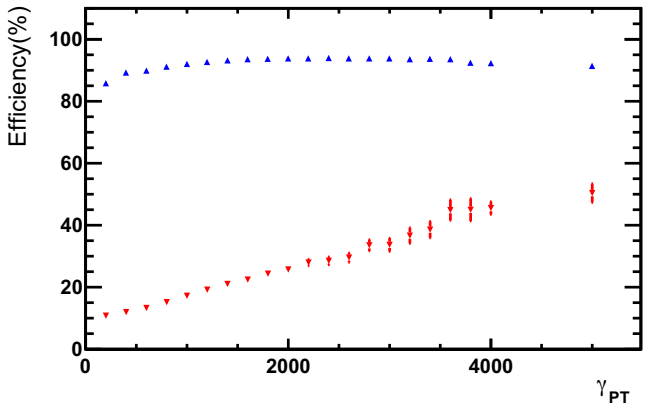

Figure 3.9: The efficiency of the cut on the NN output $\mathrm{NN}_h > 0.2$ in bins of the photon transverse momentum for both signal (blue up triangles) and background (red down triangles). The abscissa position of data points indicates the lower side of each bin.

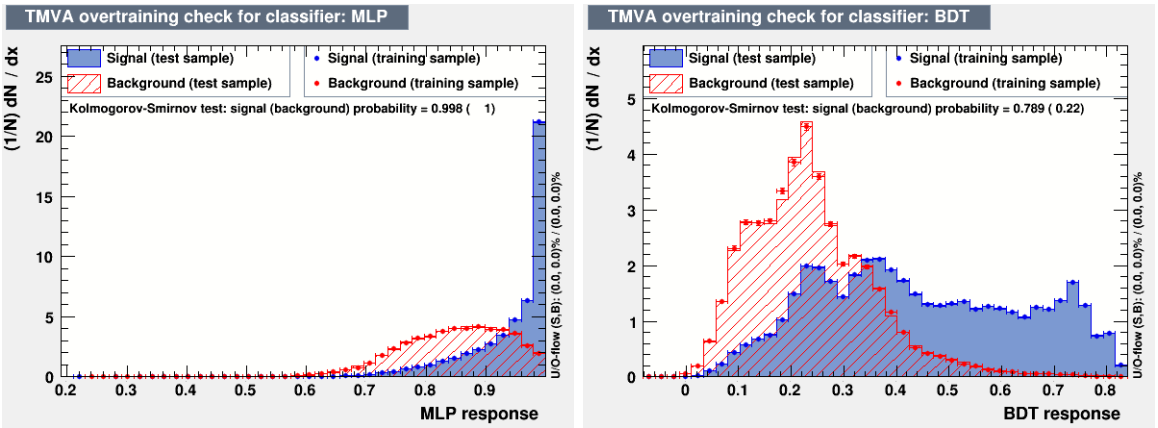

Figure 3.10: The overtraining check performed for the trained classifiers: MLP (left) and BDT (right). Signal test sample is represented by a solid histogram and background test sample is represented by a dashed histogram. The data points represent the signal and background training samples.

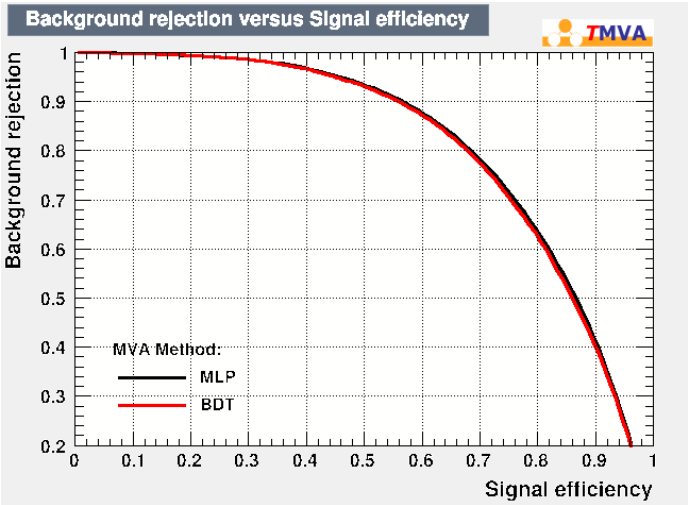

Figure 3.11: Electron background rejection versus photon signal efficiency for both MLP (black) and BDT (red).

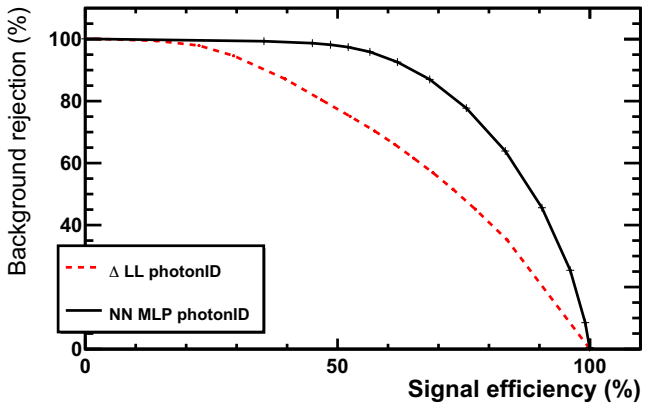

Figure 3.12: Electron background rejection versus photon signal efficiency of the MLP classifier as obtained from a separate validation sample. The ΔLL output (red dashed line) and the NN output (black solid line) are compared.

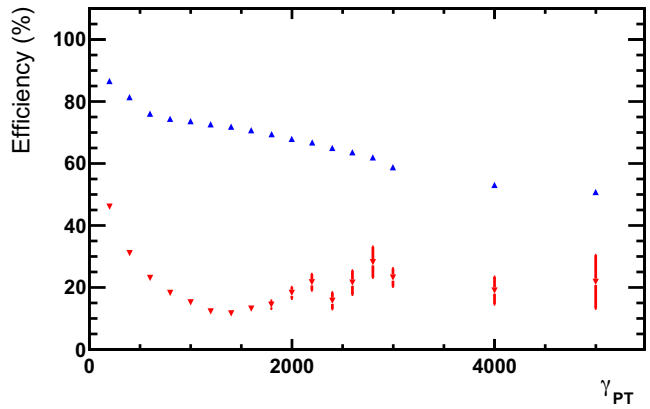

Figure 3.13: The efficiency of the cut on the NN output $\mathrm{NN}_e > 0.4$ in bins of the photon transverse momentum for both signal (blue up triangles) and background (red down triangles). The abscissa position of data points indicates the lower side of each bin.

3.4.2.4 Data/simulation comparison

The actual performance measured on data does not perfectly reproduce the performance obtained on simulation. In order to correct the MC efficiency in physics analysis, the amplitude of MC/data difference can be tabulated, as a function of the transverse momentum of the photon candidate. Such calibration tool is to be prepared based on the study presented here.
The output variables of the methods, NN_h and NN_e, are evaluated on $B \to K^*\gamma$ events collected by LHCb during the 2011-2012 run period and selected following the procedure discussed in [45]. The efficiency versus the applied cut are compared between background subtracted data and MC. Figure 3.14 shows the output variable efficiency versus the cut value both for $B \to K^*\gamma$ MC and data for both dedicated separators NN_e and NN_h. Figures 3.15, 3.16, 3.17 and 3.18 shows the same plots in bins of variable size varying from 1 GeV/c and going up to 2.5 GeV/c of the transverse momentum. The discrepancy between data and MC is clear and its dependence on the transverse momentum hints that this discrepancy can be calibrated in bins of the P_T.

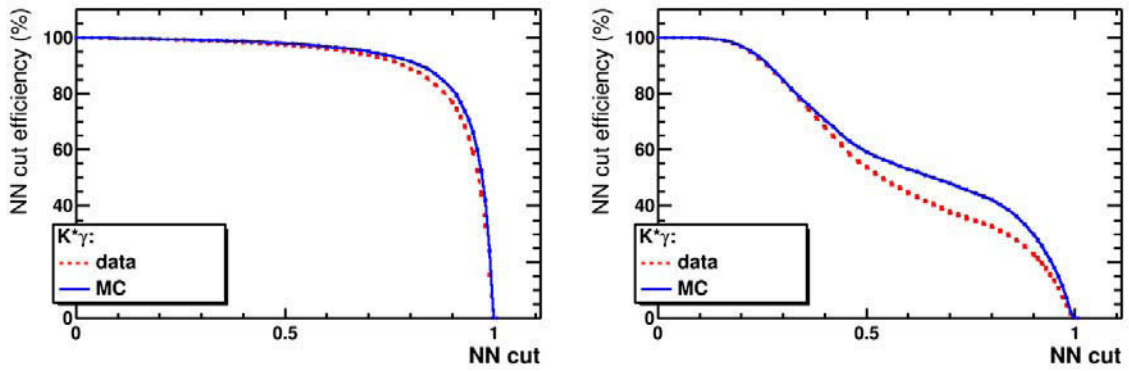

Figure 3.14: The MC (solid blue line) / data (dashed red line) efficiencies for both electron- (right) and non electromagnetic- (left).

3.5 γ/π^0 separation

A good γ/π^0 separation is an important pre-requisite for the study of radiative decays [46] so as to reduce the amount of background with merged π^0 misidentified as photons in the final state. Actually, the merged π^0 background amounts up to 50-60% of the background that lie below the signal invariant mass peak, named peaking background [94]. Besides,

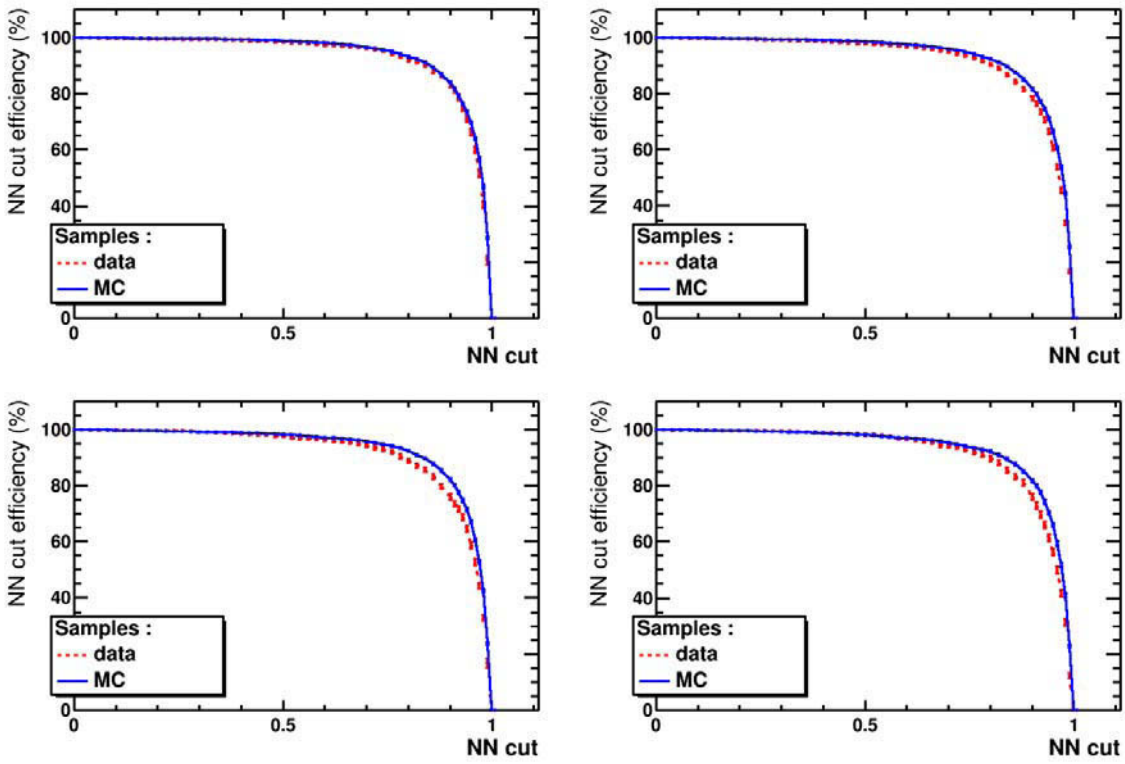

Figure 3.15: The MC (solid blue line) / data (dashed red line) efficiencies for non electromagnetic deposits in bin of the photon transverse momentum. Top left: $P_T \in [2500, 3500]$ MeV/c, top right: $P_T \in [3500, 4500]$ MeV/c, bottom left: $P_T \in [4500, 5500]$ MeV/c and bottom right: $P_T \in [5500, 6500]$ MeV/c.

this can be useful in the opposite case, rejecting photons when studying B decay modes with a π^0 in the final state. In the γ/π^0separation tool, the relevant information from the calorimeters is combined in a multivariate analysis. The tool uses the shape of the electromagnetic shower in the ECAL and the PS, the energy deposited in the PS and the ECAL and the multiplicities of PS cluster cells above four different energy thresholds (0, 15, 30, and 45 MeV). The multivariate analysis has been implemented in TMVA [91] and uses a multi-layer perceptron (3.3). The neural network is trained using $B^0 \to K^*(892)^0\gamma$ for photons as signal and different decays with merged π^0 candidate reconstructed assuming a photon hypothesis in the final state, as $B^0 \to K^+\pi^-\pi^0$, for merged π^0 as background. The MLP has been trained separately for each calorimeter region.

Using the trained MLP on a different sample, the distribution of the output obtained is shown in figure 3.19 for both signal and background and the three calorimeter regions.

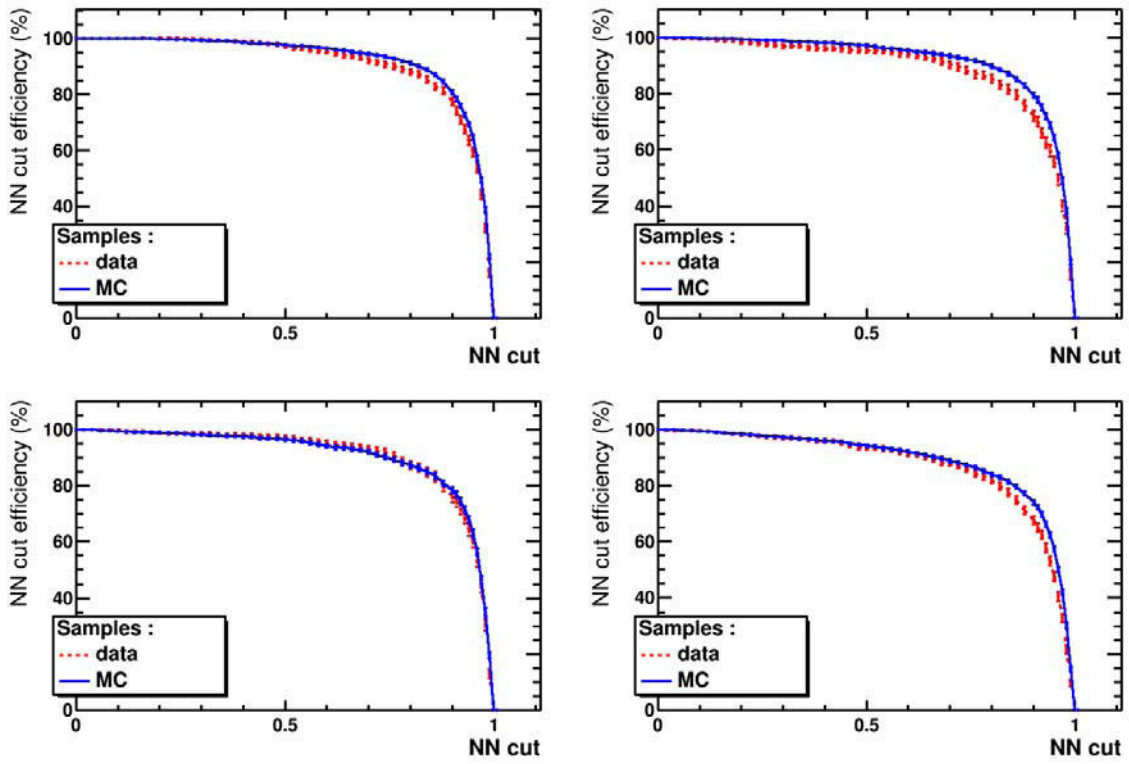

Figure 3.16: The MC (solid blue line) / data (dashed red line) discrepancies for non electromagnetic deposits in bin of the photon transverse momentum. Top left: $P_T \in [6500, 7500]$ MeV/c, top right: $P_T \in [7500, 8500]$ MeV/c, bottom left: $P_T \in [8500, 9500]$ MeV/c and bottom right: $P_T \in [9500, \text{saturation}]$ MeV/c.

Background rejection as function of the signal efficiency is shown in figure 3.20 for those simulated events.

Table 3.1 shows the signal and background efficiencies when cutting at 0.6 on the TMVA output. Note that the performance of the method is better for the inner region, and less efficient for the outer one since in the outer region, ECAL cell size is bigger and hence separating the two photons is harder given that the Moliere radius of the material in the ECAL is 3.5 cm. A high signal efficiency around 98% can be obtained with a rejection around 45% of the merged π^0 background.

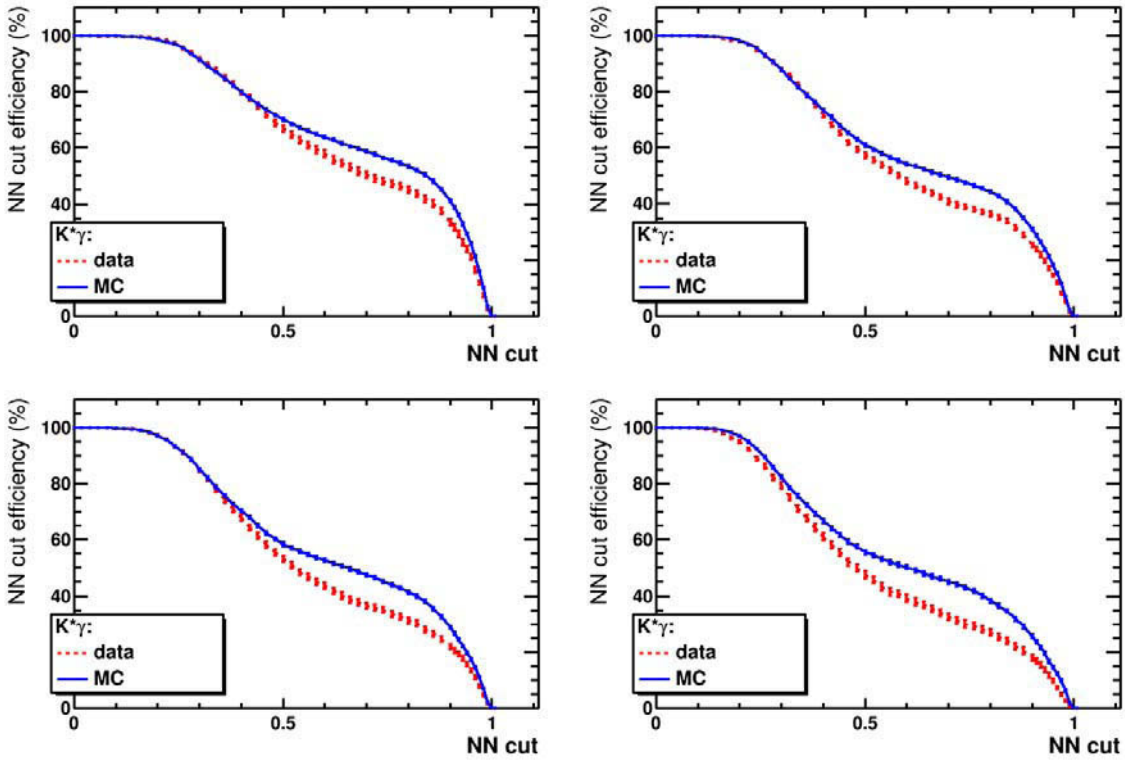

Figure 3.17: The MC (solid blue line) / data (dashed red line) discrepancies for electron in bin of the photon transverse momentum. Top left: $P_T \in [2500, 3500]$ MeV/c, top right: $P_T \in [3500, 4500]$ MeV/c, bottom left: $P_T \in [4500, 5500]$ MeV/c and bottom right: $P_T \in [5500, 6500]$ MeV/c.

region	ϵ_{sig}	ϵ_{bkg}
inner	97%	52%
middle	98%	55%
outer	98%	57%

Table 3.1: Efficiency for signal (photons) and background (π^0) requiring γ/π^0separation output variable to be >0.6.

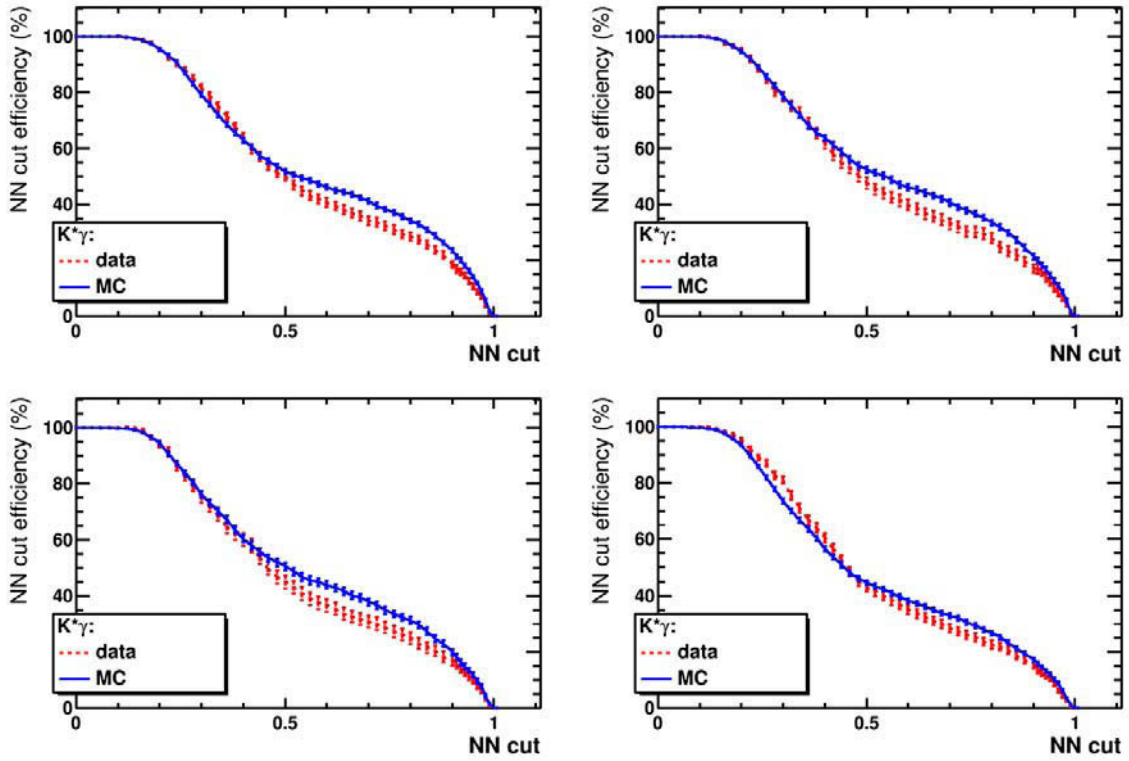

Figure 3.18: The MC (solid blue line) / data (dashed red line) discrepancies for electron in bin of the photon transverse momentum. Top left: $P_T \in [6500, 7500]$ MeV/c, top right: $P_T \in [7500, 8500]$ MeV/c, bottom left: $P_T \in [8500, 9500]$ MeV/c and bottom right: $P_T \in [9500, \text{saturation}]$ MeV/c.

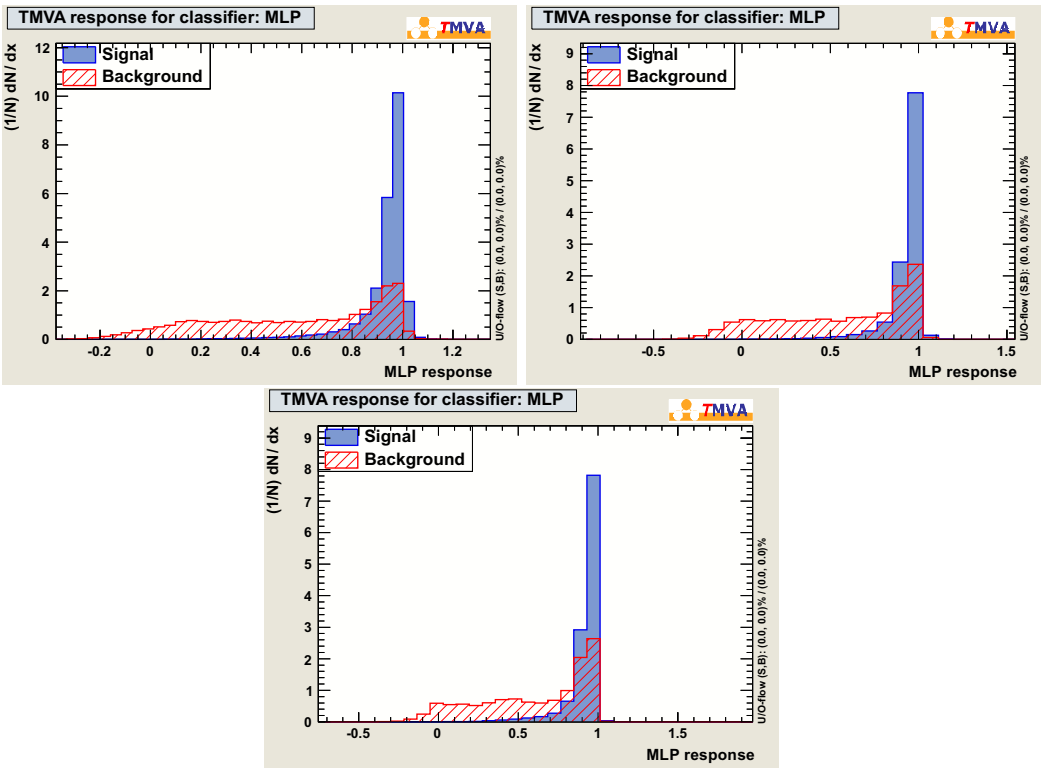

Figure 3.19: Output of the MLP for signal and background MC samples. For inner (top left), middle (top right) and outer (bottom) regions.

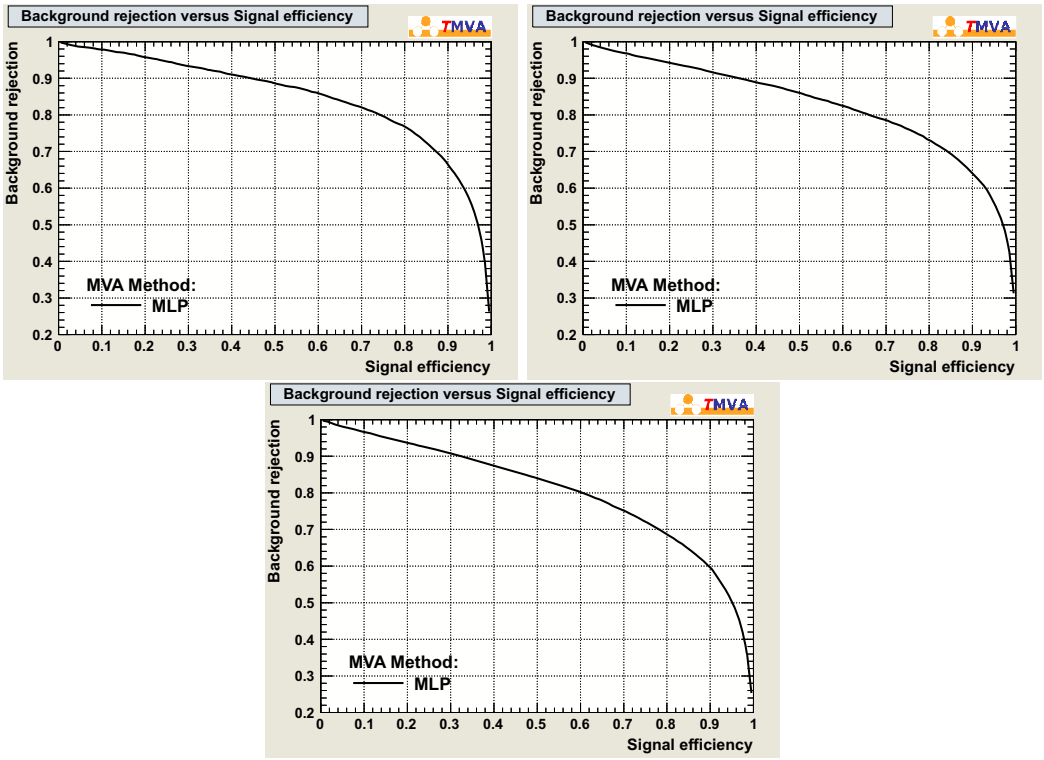

Figure 3.20: Performance of the MLP tool on the test sample, different than the training one. π^0 rejection vs photon efficiency for inner (top left), middle (top right) and outer (bottom) regions.

More details about the tool and its performance are discussed elsewhere [87, 90].

3.5.1 Calibration with real data

Due to MC/data discrepancies in the input variables used to build the γ/π^0separation tool, MC/data discrepancies are also expected in the output of the method. The MC/data discrepancy can be seen on figure 3.21 where the photon efficiency versus π^0 rejection for both data and MC is shown. The samples and how they are selected are explained in section 3.5.1.1.

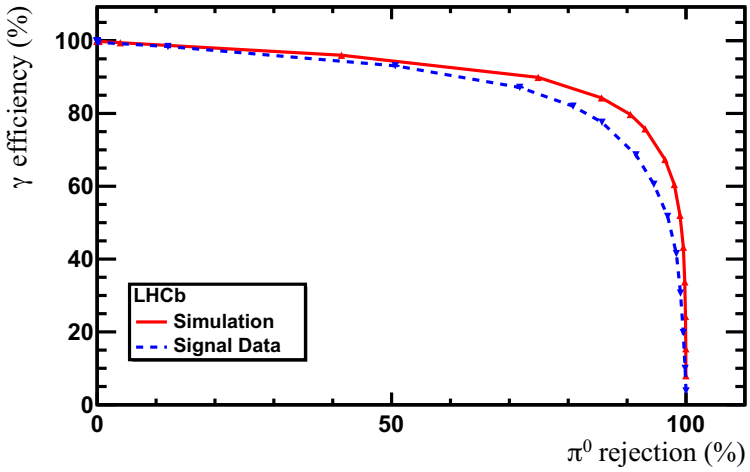

Figure 3.21: Photon identification efficiency as a function of π^0 rejection efficiency for the γ/π^0separation tool for simulation, the red solid line, and data, the blue dashed line.

For that, a data driven calibration tool has been developed. In order to calibrate the performance of the γ/π^0 tool, $B^0 \to K^*\gamma$ reconstructed events are used as a calibration sample for photons and $D^0 \to K\pi\pi^0$ events selected from $D^{*+} \to D^0\pi^+$ are used as a calibration sample for merged π^0. To justify the use of $D^0 \to K\pi\pi^0$ as a calibration sample, it is important to check that a π^0 reconstructed assuming a photon hypothesis (e.g. $K^*\pi^0$ background in $B^0 \to K^*\gamma$ analysis) have the same distribution of the γ/π^0separation variable as a π^0 reconstructed assuming a π^0 hypothesis (as in $D^0 \to K\pi\pi^0$calibration sample). Figure 3.22 shows the distribution of the γ/π^0 separation variable efficiency as a function of the cut value for a sample of merged π^0 reconstructed assuming a photon hypothesis compared to the same distribution for merged π^0 reconstructed assuming a merged π^0 hypothesis. The efficiency is calculated as the

ratio of the number of events after the cut to that before the cut. Regardless of the low statistics of $B \to K\pi\pi^0$ reconstructed as $B \to K\pi\gamma$, almost 80 events, it can be seen that the distribution of $B \to K\pi\pi^0$ and $B \to K\pi\pi^0$ reconstructed as $B \to K\pi\gamma$ follow roughly the same pattern.

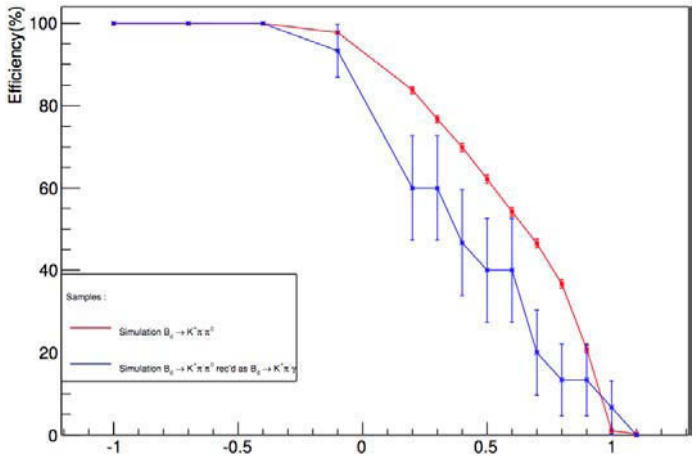

Figure 3.22: distribution of the γ/π^0 separation variable efficiency as a function of the cut value for $B^0 \to K^*\gamma$. Merged π^0 in red and reconstructed photon candidate matching a MC merged π^0 in blue.

3.5.1.1 Calibration samples selection

The $B^0 \to K^*\gamma$ sample takes into account the whole $B^0 \to K^*\gamma$ data collected by the LHCb detector over the 2011-2012 run period accounting for $3fb^{-1}$ of integrated luminosity. The offline selection applied to select signal events is summarized in [45]. In order to extract a pure $B^0 \to K^*\gamma$ sample to use for the calibration, the invariant mass distribution is modeled and the sPlot technique [95] is then used to extract weights for the signal component so as to have a background subtracted $B^0 \to K^*\gamma$ sample; with this selection 23×10^3 signal events are selected. The MC simulated sample provides 45×10^3 events.

The $D^0 \to K\pi\pi^0$ sample used takes into account only 2011 data. It has been selected from $D^{*+} \to D^0\pi^+$ with a very tight mass cut $|D^{*+}_M - D^0_M - 145.42| < 2$ MeV/c^2 hence resulting in a very clean $D^0 \to K\pi\pi^0$ sample. The offline selection applied and the invariant mass fit are explained in [87]. The sPlot technique is used to extract a

background subtracted $D^0 \to K\pi\pi^0$ sample; with this selection 123×10^3 signal events are selected. The MC sample provides 4×10^3 events.
The invariant mass distribution for $D^0 \to K\pi\pi^0$ and $B^0 \to K^*\gamma$ are shown on figure 3.23 [45, 87].

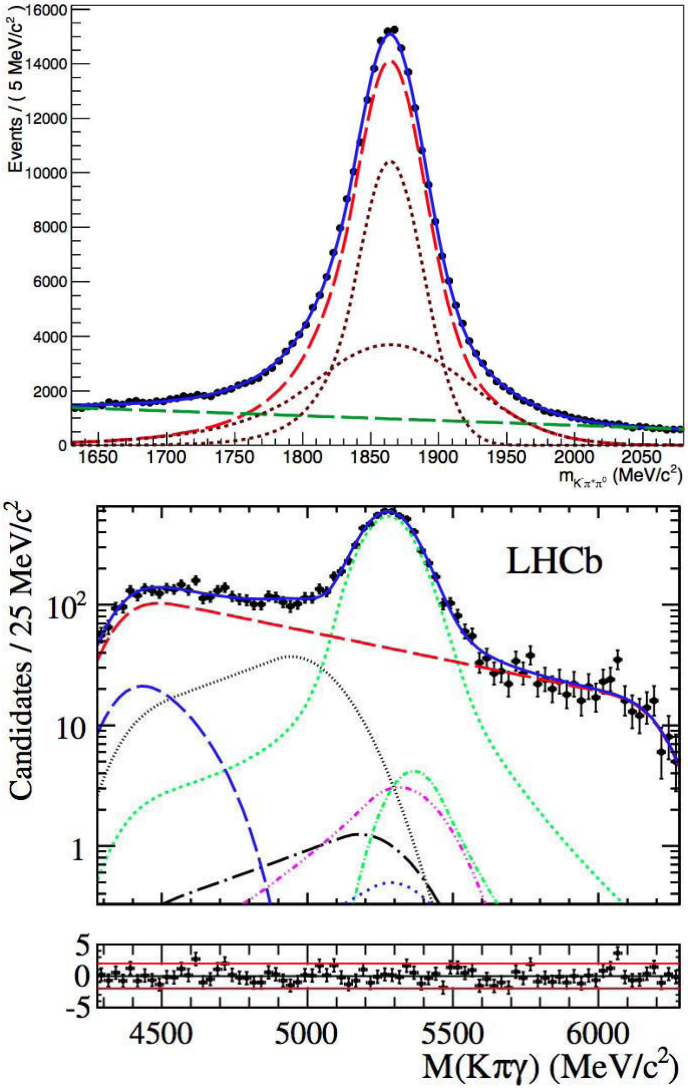

Figure 3.23: The invariant mass fit for $D^0 \to K\pi\pi^0$ [87] and $B^0 \to K^*\gamma$ [45]

3.5.1.2 Calibration tool

Since the performance of the γ/π^0 separation tool depends on the the photon/π^0 transverse momentum, the calibration is performed per bin of the transverse momentum. The inputs are the γ/π^0 cut value and the delta log-likelihood based photon ID cut value. The output is a table with the efficiencies and the errors on the efficiencies in bins of photon p_T. An example of the output table is shown in table 3.2. $B^0 \to K^*\gamma$ calibration sample is used to calibrate the performance of the γ/π^0separation tool when rejecting merged π^0 and $D^0 \to K\pi\pi^0$ calibration sample is used to calibrate the performance of the γ/π^0separation tool when rejecting photons.

The signal data efficiency found for the the set of cuts that we use, γ_{CL} >0.25 and γ/π^0 >0.6, are 95 % for $B^0 \to K^*\gamma$ and 50 % for $D^0 \to K\pi\pi^0$.

P_T range (MeV/c)	Efficiency on data (%)	Efficiency on simulation (%)
[2500,3000]	42.3 ± 0.5	50.0 ± 2.7
[3000,3500]	42.8 ± 0.4	51.5 ± 2.7
[3500,4000]	43.3 ± 0.4	47.5 ± 3.0
[4000,4500]	45.7 ± 0.4	53.4 ± 3.6
[4500,5000]	48.6 ± 0.4	53.2 ± 3.5
[5000,6000]	52.9 ± 0.4	54.5 ± 3.3
[6000,7000]	57.5 ± 0.5	62.5 ± 3.9
[7000,8000]	60.6 ± 0.6	80.7 ± 5.2
[8000,9000]	65.0 ± 0.7	75.0 ± 8.2
[9000,10000]	70.2 ± 0.9	82.4 ± 9.2
[10000→]	73.4 ± 1.2	75.0 ± 12.5

Table 3.2: An example table as given by the calibration method, the efficiencies and the errors on the efficiencies for MC simulation and data in bins of π^0 P_T from the $D^0 \to K\pi\pi^0$ calibration sample. The inputs are γ_{CL} >0.25 and γ/π^0 >0.8.

Chapter 4

The measurement of the photon polarization in $B_s^0 \to \phi\gamma$

Contents

The measurement of the photon polarization using $B_s^0 \to \phi\gamma$ is one of the seven LHCb key measurements described in [46]. It can be extracted from the analysis of the untagged time-dependent decay rate (see chapter 1). This analysis requires the precise knowledge of the experimental proper time acceptance. The strategy and the different steps of the analysis are detailed in chapter 4. Performance and preliminary results on 2011-2012 data are discussed in chapter 5

4.1 Introduction

The aim of this analysis is to extract the photon polarization through the measurement of the time-dependent decay rate in $B_s^0 \to \phi\gamma$ decays. The time-dependent decay rate is given by:

$$\begin{aligned}\Gamma_{B(\bar{B})^0_{(s)}\to\phi\gamma}(t) = |A|^2 e^{-\Gamma_{(s)}t}\big(&\cosh(\Delta\Gamma_{(s)}t/2) + \mathcal{A}_\Delta \sinh(\Delta\Gamma_{(s)}t/2) \\ &\pm\mathcal{C}_{\mathcal{CP}}\cos(\Delta m_{(s)}t) \mp \mathcal{S}_{\mathcal{CP}} sin(\Delta m_{(s)}t)\big)\end{aligned} \tag{4.1}$$

with [33]

$$\mathcal{A}_\Delta \;\sim\; sin2\Psi\cos\,\phi_s, \tag{4.2}$$

where Ψ is related to the fraction of wrongly-polarized photons as

$$\tan\Psi = \left|\frac{\mathcal{A}_R}{\mathcal{A}_L}\right| \tag{4.3}$$

It is worth to stress here that contributions from $\mathcal{S}_{\mathcal{CP}}$ and $\mathcal{C}_{\mathcal{CP}}$ vanish when considering the inclusive $\Gamma_{B_s} + \Gamma_{\bar{B}_s}$ assuming the $B_s/\bar{B}_s$ production asymmetry vanish. Therefore no flavor tagging is required for the extraction of A_Δ. The inclusive time-dependent decay rate is then given as

$$\Gamma_{B_s^0\to\phi\gamma}(t) = |A|^2 e^{-\Gamma_s t}\left(\cosh(\Delta\Gamma_s t/2) + \mathcal{A}_\Delta \sinh(\Delta\Gamma_s t/2)\right) \tag{4.4}$$

For the B_s system, in the SM, $\phi_s = -0.015 \pm 0.035$ [96] and hence one has for A_Δ

$$A_\Delta^{B_s^0} \sim \sin 2\Psi, \tag{4.5}$$

Therefore, the measurement of $\mathcal{A}_\Delta$ directly determines the fraction of wrongly-polarized photons [33].

The measurement of the photon polarisation is performed by adjusting the theoretical decay rate, equation 4.4, to the proper time distribution obtained from $B_s^0 \to \phi\gamma$ candidates selected during the 2011+2012 LHCb data taking period, taking into account the experimental resolution and acceptance.
The analysis consists in the following steps :

- $B_s \to (\phi \to K^+K^-)\gamma$ candidates reconstruction and selection: the experimental challenge of reconstructing $B_s^0 \to \phi\gamma$ is driven by the presence of the energetic photon in the final state. Calorimeter energy resolution limits the experimental resolution on the kinematical properties of the reconstructed Bs. In particular, the mass resolution of the reconstructed B is large, 90 MeV/c^2, compared to final state with charged tracks only which is of the order of 10-15 MeV/c^2. The misidentification or the partial reconstruction of other radiative decays ($B_d \to K\pi\gamma$, $\Lambda_b \to pK\gamma$, $B \to hh h\gamma$, ...) and the b-hadron decay with neutral pion in the final state ($B \to hh\pi^0$) forms a potentially large background contamination in the wide signal mass region. In addition, the important multiplicity of photon candidates reconstructed in LHCb events leads to a large contamination due to the accidental selection of (KK)+γ events (hereafter called combinatorial background) as the photon reconstruction brings no information about its origin vertex. The $B_s^0 \to \phi\gamma$ signal selection thus requires tight criteria to limit the contamination from the various source of backgrounds. In particular, criteria related to the separation of the $\phi \to KK$ decay vertex (SV) and the B origin vertex (PV) cannot be avoided. Such criteria strongly affect the distribution of proper time in the low values region where combinatorial background mostly contributes.

- Background subtraction: A background subtraction method is applied to reconstruct on a statistical basis the proper time distribution of the $B_s^0 \to \phi\gamma$ signal from the $KK\gamma$ selected sample. The method relies on the invariant mass distribution of the $KK\gamma$ reconstructed sample where the separate contributions from the $B_s^0 \to \phi\gamma$ signal and the various backgrounds are modeled and adjusted to the selected data. For that purpose the *sPlot* [95] technique is used.

- Signal proper time distribution: The adjustment of the time-dependent decay rate model to the background-subtracted $B_s^0 \to \phi\gamma$ proper time distribution requires a precise knowledge of the reconstructed proper time resolution and its experimental acceptance. The acceptance function can be controlled by the means of the study of other decays (control channels) with a topology similar to the $B_s^0 \to \phi\gamma$ signal and for which the time-dependent decay rate is well known. A natural choice for such a control channel is the radiative decay of the B^0 meson into $K^*\gamma$. Thanks to the negligible decay width difference for the B^0 meson, $\Delta\Gamma = -0.007 \pm 0.004$ [34], the expected time-dependent decay rate reduces to a single exponential. On the experimental side this channel benefits from a large statistics with respect to B_s signal and exhibits a similar final state. Important differences however occur in the decay vertex reconstruction that need to be accounted for, for example, the ϕ decaying at rest in contrary to the K^*. In addition such channel suffers as for the signal from a large background contamination.

  The channels $B^0 \to J/\psi X$ (where X stands to either K^* or ϕ) on the contrary can be reconstructed with a large efficiency and an almost negligible background contamination when considering the di-muon decay of the J/ψ meson. The obvious difference here comes from the final state dynamics where the heavy spin-1 J/ψ replaces the massless photon. A dedicated treatment is needed to account for the dynamical difference in order the di-muon channel reproduce the proper time acceptance of the radiative signal. This is the approach developed in this analysis where both $B^0 \to J/\psi K^*(892)^0$ and $B^0 \to K^*(892)^0\gamma$ channels can be simultaneously used to control the proper time acceptance of the $B_s^0 \to \phi\gamma$ signal. For what concerns $B^0 \to J/\psi\,\phi$, the expected time-dependent decay rate is more complicated and would require a dedicated angular analysis for a negligible gain in statistics - so it is not used as a proper control channel for the proper time analysis but serves to validate the dedicated treatment to align di-muon and radiative acceptance (see 4.4.2).

This chapter is organized as follows. The reconstruction and selection of the $B_s^0 \to \phi\gamma$ signal and of the different control channels is discussed in section 4.2. The mass model for radiative decays and statistical background subtraction is detailed in section 4.2.3. The study of the proper time reconstruction and acceptance on simulated data are discussed in section 4.3 and 4.4, respectively.

4.2 Signal and control channels selection

4.2.1 Trigger

Radiative channels

The radiative decays are reconstructed in a sample passing the following trigger criteria. At L0, this is achieved by the use of the L0 calorimeter, with E_T thresholds of 2.5 GeV in 2011, 2.72 GeV in the beginning of 2012 and 2.96 GeV after mid-2012. L0Photon or L0Electron are required to be triggered in order to account for both converted and unconverted photons.

The criteria of the used HLT1 line called "Hlt1TrackAllL0", listed in table 4.1, impose track requirements. For radiative decays, the efficiency can be improved by an additional 20% by using the Hlt1TrackPhoton line. Hlt1TrackPhoton requires L0PhotonHi and L0ElectronHi which are similar to L0Photon and L0Electron but with a higher threshold of $E_T > 4.2\,\text{GeV}$. The Hlt1TrackPhoton line uses looser track requirements after the higher E_T threshold in the L0 trigger. Since HLT1TrackPhoton can not be applied on the $B^0 \to J/\psi X$ samples, this line is not used in the radiative selection.

Finally, the exclusive HLT2 line selection is listed in table 4.2. It is applied for each decay: Hlt2Bs2PhiGamma for $B_s^0 \to \phi\gamma$ and Hlt2Bd2KstGamma for $B^0 \to K^*(892)^0\gamma$. The full trigger sequence is schematized in Fig. 4.1, where all the previously mentioned lines are triggered on signal (TOS). An event is classified as TOS if the trigger objects that are associated with the signal candidate are sufficient to trigger the event.

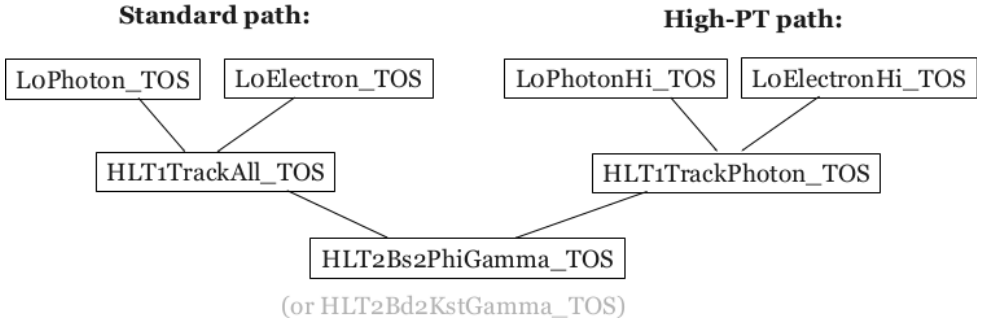

Figure 4.1: Schematic representation of the trigger path used to select $B^0 \to K^*(892)^0\gamma$ and $B_s^0 \to \phi\gamma$ at trigger level. In the approach followed in the analysis, only the left branch is used.

		Hlt1TrackAllL0	Hlt1TrackPhoton
L0 channel		L0 physics	L0PhotonHi or L0ElectronHi
Implicit L0 photon E_{T} in 2011(2012)	GeV	$> 2.5\,(2.72 - 2.96)$	> 4.2
VELO track hits		> 9	> 9
VELO missed hits		< 3	< 4
VELO track IP in 2011(2012)	μm	$-\,(> 100)$	> 100
Track p in 2011(2012)	GeV/c	$> 10\,(3)$	$> 6\,(3)$
Track P_T in 2011(2012)	GeV/c	$> 1.7\,(1.6)$	> 1.2
Track χ^2		< 2	< 2
Track χ^2_{IP}		> 16	> 16

Table 4.1: Selection requirements applied in 2011 (2012) on the HLT1 lines relevant to radiative decays. The implicit L0 photon E_{T} takes into account the L0 requirement of each line. The definition of some variables is given in appendix C.

		Hlt2Bs2PhiGamma	Hlt2Bd2KstGamma
L0 lines		L0Photon or L0Electron	
HLT1		HLT1 Physics	
Track p	MeV/c	> 3000	
Track p_{T}	MeV/c	> 300	
Track χ^2		< 5	
Track χ^2_{IP}		> 20	
V ΔM_{PDG}	MeV/c^2	< 20	< 100
V χ^2_{vtx}		< 25	< 16
Photon E_{T}	MeV	> 2600	
B p_{T}	MeV/c	> 3000	
B χ^2_{IP}		< 12	
B θ_{DIRA}	mrad	< 63	< 45
B ΔM_{PDG}	MeV/c^2	< 1000	

Table 4.2: Selection of the HLT2 exclusive lines for $B_s^0 \to \phi\gamma$ and $B^0 \to K^*(892)^0\gamma$. The definition of some variables is given in appendix C. V stands for vector.

Dimuon channels

The trigger path chosen for the $B^0 \to J/\psi X$ candidates is based on the muon trigger. This trigger path is proper time unbiased since it contains no explicit cuts on variables that induce a proper time acceptance. Nevertheless, residual bias in the proper time is observed and discussed in details in section 4.4.3. The trigger path is

- The L0 trigger used is L0Muon or L0DiMuon.
- In HLT1, the Hlt1DiMuonHighMass line is used, with a further TOS requirement on HLT1TrackAllL0 to align the selection to the radiative one. As will be shown in Section 4.4.3, only the HLT1 has an impact on the acceptance at high proper time relatively to the offline selection.
- In HLT2, the Hlt2DiMuonJPsiHighPT line is used.

4.2.2 Signal reconstruction and selection

At LHCb, the excellent vertex resolution of the VELO and the large boost of the B hadrons produced at the LHC makes possible to distinguish the primary vertex (PV), where the b-hadron is produced, from the secondary vertex (SV) where its decay takes place. Moreover, the high mass of the B mesons drives the kinematics of the decay and hence, most of the mass of the B is transformed in kinetic energy of the decay products which tend to scatter with large angles with respect to the direction of flight of the B. As a result, the B decay products have high transverse momenta.

For radiative decays as $B_s \to (\phi \to K^+K^-)\gamma$ and $B^0 \to (K^*(892)^0 \to K^+\pi^-)\gamma$, the final state consists of two tracks and a photon. To reconstruct such decays one looks for two tracks that form a well separated SV. The B candidate is associated with a PV on a geometrical basis requiring the angle between the reconstructed B momentum and the line connecting the PV and the SV to be small. Require that the particles associated to the selected tracks are of opposite charges and of high transverse momentum. Finally, the energy of the photon is reconstructed relying on the calorimeter. The invariant mass of the three body final state, i.e. the two hadrons and the photon, is required to be in the $\pm 1\text{GeV/c}^2$ range around the nominal B mass value.
For the selection of $B^0 \to (J/\psi \to \mu^+\mu^-)(K^*(892)^0 \to K^+\pi^-)$ and $B_s \to (J/\psi \to \mu^+\mu^-)(\phi \to K^+K^-)$ decays, similar criteria is applied. Performing tracks selection, SV

reconstruction, associating the reconstructed B hadron to the PV and applying PID and P_T cuts to select the desired particles.

The di-muon channels $B^0 \to J/\psi K^*(892)^0$ and $B_s^0 \to J/\psi\,\phi$ are used as control samples for the proper time acceptance. For this to be possible, and since the di-muon and radiative channels have the same hadronic part, the J/ψ in the di-muon channels should mimic the behavior of the photon in radiative decays. This is achieved by excluding the di-muon system from the B decay vertex reconstruction by increasing the covariance matrix element associated to the di-muon tracks to a very high value at which they no longer participate in the vertex computation of the B.

The main selection criteria are

- The two tracks are required to be of good quality. It can be tested looking at the χ^2/ndof of the track fit.
- The two tracks do not come from a PV, meaning that the impact parameter (IP) - being the shortest distance from the track to the PV - of their trajectories with respect to any PV has to be large.
- The two tracks form a secondary vertex. The χ^2 of the vertex fit is required to be small.
- The B meson comes from a PV. Its reconstructed IP is required to be small with respect to this point.
- The direction of flight of the B from the primary to the secondary vertices should match the direction of the momentum of the B, obtained as the vector sum of the momentum of the final particles. The matching is measured by the angle between the direction of flight of the B and the direction of the momentum of the B, θ_{DIRA}. θ_{DIRA} is required to be small.
- The transverse momentum (P_T) of the decay daughters is high.
- The invariant mass of the reconstructed decay final state is required to be in the $\pm 1\mathrm{GeV/c^2}$ range around the B mass.

The offline selection cuts applied are listed in table 4.3. As the HLT2 trigger lines contain a cut on the online θ_{DIRA} angle ($\theta_{\mathrm{DIRA}} < 0.063$ for $B_s^0 \to \phi\gamma$ and $\theta_{\mathrm{DIRA}} < 0.045$ for $B^0 \to K^*(892)^0\gamma$). Having these θ_{DIRA} angle cuts applied in the trigger was the main

reason that drove the application of an offline $\theta_{\rm DIRA}$ angle cut. As the online evaluation of $\theta_{\rm DIRA}$ is not exactly the same as it's offline determination due to different tracking resolution and different photon reconstruction, the $\theta_{\rm DIRA}$ is selected with a cut value that is slightly harder than the online cut to avoid edge resolution effect. The kinematical differences between $B^0 \to J/\psi X$ and radiative channels induce different $\theta_{\rm DIRA}$ and track-IP distributions. To obtain the same proper time acceptance when cutting on those variables a weighing and scaling procedure is applied as explained in section 4.4.1.

The fiducial cuts on tracks pseudo-rapidity (η), the z coordinate of the B vertex ($Z_{\rm PV}$) and the IP χ^2 with respect to the next best PV (IP$\chi^2_{\rm next}$) are implemented following what have been done in the $B \to J/\psi X$ lifetime measurements [97, 98]. The reconstruction efficiency depends on the location and phase space of the particle especially at the edges of the detector where a homogeneous reconstruction efficiency can not be guaranteed. Hence, these regions are cut away by imposing tracks to be within $2< \eta <4.5$ and PV z position to be $\pm$100 mm around zero. The cut on the $\chi^2_{\rm IP}$ of the B candidate with respect to the next best PV is introduced in order to reduce the component originating from wrongly associated PV. The B candidate is imposed to be consistent with only one PV requiring IP$\chi^2_{\rm next} > 50$.

4.2.3 Mass models and background subtraction

A detailed study is performed in [45] to understand the shape and the level of contribution of each background source in the radiative channels. For this purpose the simulated samples of each background source are reconstructed assuming the $K^*(892)^0\ \gamma$ ($\phi\gamma$) hypothesis and the resulting invariant B mass shape is studied. The level of contamination expected from these sources is computed as a fraction of the signal yield, denoted by C in the following

$$C_{H_b\to X} = \frac{N^{sel}(H_b \to X)}{N^{sel}(\text{SIGNAL})} = \frac{\epsilon_{MC}(H_b \to X)}{\epsilon_{MC}(\text{SIGNAL})} \times \frac{f_{H_b}}{f_{\rm SIGNAL}} \times \frac{BR(H_b \to X)}{BR(\text{SIGNAL})} \qquad (4.6)$$

Only background contributions with a contamination level above 0.1 % are included in the mass fits.

	$K^\star\gamma$ ‖ $\phi\gamma$	$J/\psi K^\star$ ‖ $J/\psi\phi$
K^+ Track IP χ^2	>55,	>47.80 ‖ >38.73 scaled
π/K Track IP χ^2	>55,	>52.38 ‖ >38.73 scaled
max[$P_{\mathrm{T,tracks}}$] (MeV/c)	>1200	>1200
min[$P_{\mathrm{T,tracks}}$] (MeV/c)	>500	>500
Track χ^2	<3	<3
Ghost probability	<0.3	<0.3
Track η	(2,4.5)	(2,4.5)
K probNNk	>0.2	>0.2
π probNNπ	>0.1	>0.1
π probNNk	<0.25	<0.25
γ P_T (MeV/c)	>3000	—
γ CL	>0.25	—
γ/π^0 separation	>0.6	—
$J/\psi P_T$ (MeV/c)	—	>3000
μ P_T (MeV/c)	—	>650
μ P (MeV/c)	—	>10000
μ $PID\mu$	—	>0
μ Track χ^2	—	<5
$\lvert J/\psi$ Vertex $\chi^2\rvert$	—	<20
$\lvert J/\psi \Delta M_{\mathrm{PDG}}\rvert$ (MeV/c^2)	—	<80
μ isMuon	—	=1
$K^*(892)^0/\phi$ ΔM_{PDG} (MeV/c^2)	<100(15)	<100(15)
$K^*(892)^0/\phi$ vertex χ^2	<9	<9
$\lvert\cos(\Theta_H)\rvert$	<0.8	<0.8
B P_T (MeV/c)	>3000	>3000
θ_{DIRA} (rad)	<0.04‖0.06	<0.023 ‖ <0.033 scaled
B IP χ^2	<9	<9
B vertex χ^2	<9	<9
Z_{PV} (cm)	<10	<10
nPVs=1‖B min(IP χ^2_{next})	>50	>50

Table 4.3: Selection cuts applied for the radiative and $B^0 \to J/\psi K^*(892)^0$ samples. "scaled" tags the cuts that have been scaled on the $B^0 \to J/\psi X$ sample following the procedure explained in section 4.4.1. The definition of the variables used in the selection is given in appendix C.

The background sources for radiative decays are separated into four categories

- Partially reconstructed background: these events have the same final state as signal taking into account that one or more particles from its actual final state are missing. For example, $B \to K\pi\pi\gamma$ with a pion missing in the final state or

$B \to K\pi\pi\pi^0$ with a pion missing in the final state and the π^0 is misidentified as a photon as background for $B^0 \to K^*(892)^0\gamma$.

- Decays with π^0 in the final state as $B^0 \to K\pi\pi^0$ background in $B^0 \to K^*(892)^0\gamma$ where the π^0 can be misidentified as a photon. Such decays constitute almost 50% of the peaking backgrounds and are reduced by the γ/π^0separation cut and the helicity angle cut.

- The baryonic radiative decay, $\Lambda_b \to \Lambda^*\gamma$, is one of the peaking backgrounds under the signal distribution.

- Background of the type $B \to X\gamma$ in the $B^0 \to K^*(892)^0\gamma$ where X can be a ϕ, ρ or w (mis-ID reflections). This background is present when a misidentification in one of the final state particles occurs. For example $B_s^0 \to \phi\gamma$ can contribute when one of the kaons from the ϕ decays is misidentified as a pion. $B^0 \to \rho^0\gamma$ contributes when one of the pions from the ρ^0 decays is misidentified as a kaon.

It is important to mention that in the case of $B_s^0 \to \phi\gamma$, the background is much reduced thanks to the narrow ϕ resonance.

The background subtraction method used in this analysis is the *sPlot* technique [95]. The *sPlot* technique is a statistical tool that unfolds the contributions of the different sources to the distribution of a data sample in a given variable "v". It can, on a statistical basis, subtract the background contributions from the data sample by assigning weights accordingly to the different contributions modeled in the sample. The validity of this technique is based on two main criteria. The first one is that the variable "v" has a good discriminating power between the different contributions to the distribution. The second criterium is that this variable "v" must be uncorrelated with other variables especially the ones that is used for the analysis, in this case the proper time. The best choice of such a variable is the invariant mass.
In the invariant mass distribution, the different contributions of signal and background are modeled to a very good approximation. Moreover, the proper time evaluated with a B mass constraint, as explained in section 4.3.2.1, is uncorrelated with the invariant mass.
Therefore, to subtract the background, the invariant mass distribution is fitted taking into account the different background contributions and then the *sPlot* technique is applied. The use of *sPlot* guaranties, to a very good extent, that the signal events are

separated from the background one on a statistical basis.

As for the di-muon channels, the background sources are mainly:

- Combinatorial background.
- Partially reconstructed backgrounds as $B^0 \to J/\psi K^*(892)^0$ + pion background for $B^0 \to J/\psi K^*(892)^0$ signal.
- The mis-ID reflection in $B^0 \to J/\psi K^*(892)^0$ ($B_s^0 \to J/\psi\,\phi$) from $B_s^0 \to J/\psi\,\phi$ ($B^0 \to J/\psi K^*(892)^0$).
- Background from $\Lambda_b \to (pK)J/\psi$ assuming a proton misidentification.

The mass models for radiative and di-muon decays are explained in the following. The mass fits are performed as extended unbinned likelihood fits using RooFit [99].
A 0.5 % bias in the reconstructed B mass of radiative decays has been observed. The origin of this bias is due to a photon energy bias of the order of 1 % at high energy. This bias is due to the calorimeter calibration at low energies using π^0 [54]. In radiative analysis [100], an ad-hoc calibration has been applied to the photon energy, the mass is henceforth calibrated. Photon calibration is explained in appendix B.

4.2.3.1 Mass model for radiative channels

Once the expected background contaminations are determined, the mass fit is built. In the final mass fit to the $B^0 \to K^*(892)^0\gamma$ ($B_s^0 \to \phi\gamma$) signal, the normalization of all the background components is left free with the exception of $\Lambda_b \to \Lambda(pK)\gamma$, $B^0 \to K^*(892)^0\pi^0$ ($B_s^0 \to \phi\pi^0$) and $B_s^0 \to \phi\gamma$ for $B^0 \to K^*(892)^0\gamma$ signal. The fit function to the invariant mass of B^0 (B_s^0) is built as an extended PDF

$$\mathrm{P}(m) = N_S \cdot S(m) + \sum_i N_i \cdot B_i(m) \tag{4.7}$$

where $S(m)$ is the signal PDF and $B_i(m)$ is the background PDF where the index i refers to the different contributions of the background. The invariant mass fit model is defined as

- Combinatorial background is modeled with an exponential function.

$$\text{Comb}(m;\tau) = \exp(m/\tau) \tag{4.8}$$

- Partially reconstructed background

  - Partially reconstructed background with a pion/kaon missing ($B^+ \to K^+\pi^-\pi^+\gamma$ or $B \to \phi K^+\gamma$) is modeled with an Argus PDF [101] convoluted with a Gaussian resolution with the parameters fixed from simulation

$$\text{Partial}(m;c,p,\mu,\sigma\,) = \text{Argus}(m;c,\mu-\mu_0,p) \otimes \text{Gauss}(0,\sigma) \tag{4.9}$$

    where $\mu_0 = m_\pi$ for $B^0 \to K^*(892)^0\gamma$ and $\mu_0 = m_K$ for $B_s^0 \to \phi\gamma$.

  - Partially reconstructed background of $B^0 \to K^+\pi^-\pi^0 X$ for $B^0 \to K^*(892)^0\gamma$ channel is modeled with an exponentially modified Gaussian (EMG) function, with parameters fixed from simulation except for the yields.

$$\text{EMG}(m;\mu,\sigma,\lambda\,) = \frac{\lambda}{2} e^{\frac{\lambda}{2}(2x+\lambda\sigma^2-2\mu)} \cdot \text{erfc}(\frac{x+\lambda\sigma^2-\mu}{\sqrt{2}\sigma}) \tag{4.10}$$

- Background from Λ_b^0 is modeled with a Crystal-Ball function [102], with parameters fixed from simulation

- Background from $B^0 \to K\pi\pi^0$ is modeled with a Crystal-Ball function, with parameters fixed from simulation. Since there is no simulated sample for $B_s^0 \to \phi\pi^0$, the parameters are assumed to be the same as $B^0 \to K\pi\pi^0$ reconstructed as $B^0 \to K^*(892)^0\gamma$, with mean value shifted due to higher B_s^0 mass.

- Background from $B \to V\gamma$, with V being either ρ, ϕ or ω, is modeled with a PDF consisting of two gaussian components.

4.2.3.2 Mass model for di-muon channels

The fit model for $B^0 \to J/\psi K^*(892)^0$ mass spectrum has the following components

- Combinatorial background modeled by an exponential function:

$$\text{Comb}(m;\tau) = \exp\,(m/\tau)$$

- Partially reconstructed $B^0 \to J/\psi K^*(892)^0$ + pion modeled by an Argus [101] convoluted with a Gaussian resolution:

$$\text{Partial}(m; c, p, \mu, \sigma) = \text{Argus}(m; c, \mu - \mu_0, p) * \text{Gauss}(0, \sigma)$$

- The mis-ID reflection from $B^0 \to J/\psi\,\phi$, i.e. reconstructing $B^0 \to J/\psi\,\phi$ as being $B^0 \to J/\psi K^*(892)^0$ by misidentifying one of the kaons to be a pion, modeled by a double tail Crystal-Ball function [102] with parameters fixed from MC simulation:

$$\text{CB}(m; \mu, \sigma, \alpha, n) = \begin{cases} A_L(B_L - \dfrac{m-\mu}{\sigma})^{-n_L}, & \text{for } \dfrac{m-\mu}{\sigma} \leq -\alpha_L \\ \exp(-\dfrac{(m-\mu)^2}{2\sigma^2}), & \text{for } -\alpha_L < \dfrac{m-\mu}{\sigma} < \alpha_R \\ A_R(B_R + \dfrac{m-\mu}{\sigma})^{-n_R}, & \text{for } \dfrac{m-\mu}{\sigma} \geq \alpha_R \end{cases}$$

where $\alpha_{L(R)} > 0$ and

$$A_i = (\frac{n_i}{|\alpha_i|})^{n_i} \exp(-\frac{|\alpha_i|^2}{2})$$
$$B_i = \frac{n_i}{|\alpha_i|} - |\alpha_i|$$

- The background from $\Lambda_b \to (pK)J/\psi$ modeled by an Argus convoluted with a Gaussian resolution:

$$\text{Partial}(m; c, p, \mu, \sigma) = \text{Argus}(m; c, \mu - \mu_0, p) * \text{Gauss}(0, \sigma)$$

- The signal $B^0 \to J/\psi K^*(892)^0$ is modeled by a CB function with an Apollonios core [103] and tail parameters fixed from MC simulation:

$$A(m; \mu, b, \delta, a, n) \propto \begin{cases} e^{-b\sqrt{1+\frac{t^2}{b}}} & \text{, if } t \geq -a \\ e^{-b.A} \times (1 - \frac{a}{nA}.(a+t))^{-n} & \text{, otherwise} \end{cases}$$

where t is the reduced mass $t = \frac{(m-\mu)}{\delta}$ and $A = \sqrt{1 + \frac{a^2}{b}}$.

A similar model is used for the $B_s^0 \to J/\psi\,\phi$ mass fit.

The yields for the mis-ID reflections are constrained to the signal yield using gaussian constraints calculated from the ratios of branching fractions and of selection efficiencies,

the PID cut efficiencies being corrected thanks to PID calibration package [104]. The other yields are free in the fit.

With the selection applied, the $B^0 \to J/\psi K^*(892)^0$ signal yield is 30×10^3 events and the $B_s^0 \to J/\psi\,\phi$ signal yield is 4×10^3 events on the $3fb^{-1}$ collected in 2011 and 2012. This can be compared to 24×10^3 events obtained in $B^0 \to K^*(892)^0\gamma$ and 3.5×10^3 events obtained for $B_s^0 \to \phi\gamma$ respectively. The invariant mass fits on data is shown on figure 4.2. It is clear that the selection applied on $B^0 \to J/\psi X$ channels is so tight that the sample is almost background free in the signal region.

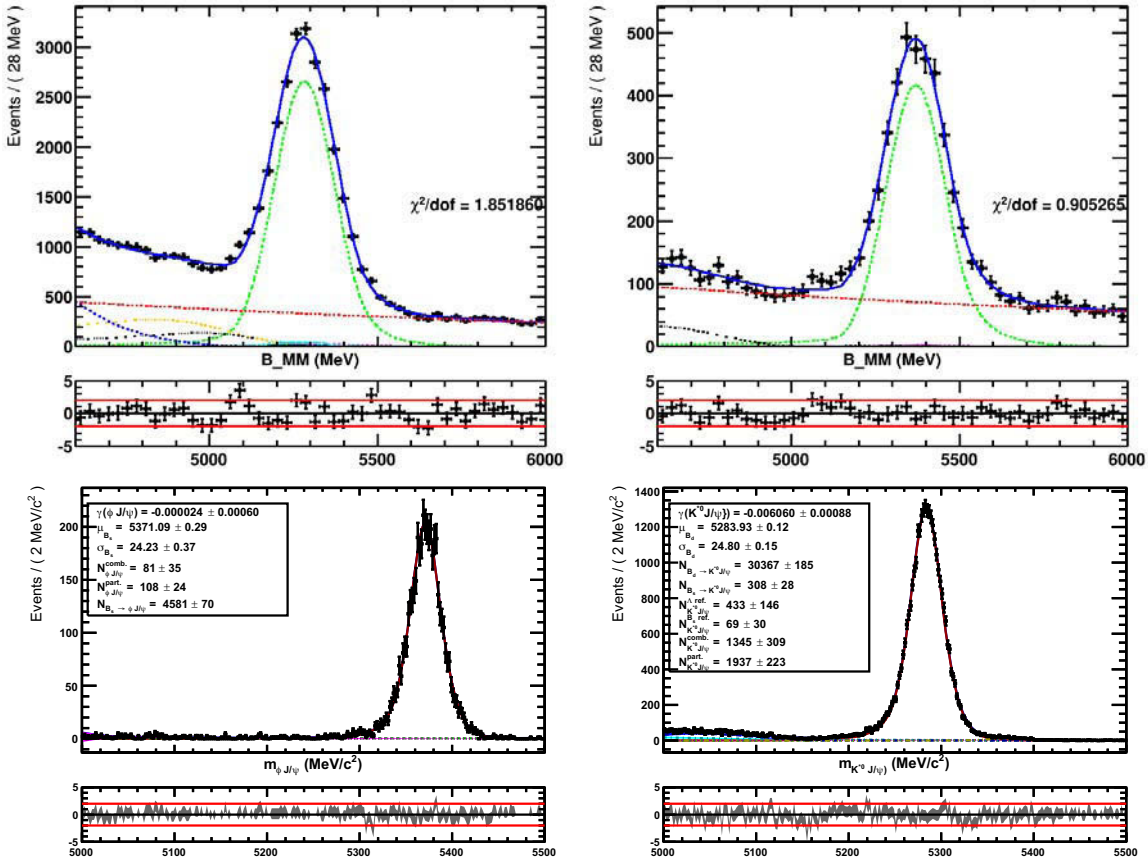

Figure 4.2: The invariant mass of $B^0 \to K^*(892)^0\gamma$ (top left), $B_s^0 \to \phi\gamma$ (top right), $B_s^0 \to J/\psi\,\phi$ (bottom left) and $B^0 \to J/\psi K^*(892)^0$ (bottom right).

Background subtraction In the following, data events will be taken in the reconstructed B mass range from 5240 to 5320 MeV/c^2 for $B^0 \to J/\psi K^*(892)^0$ and in the

range 5326 and 5406 for $B_s^0 \to J/\psi\,\phi$. As shown in figure 4.2, backgrounds are negligible in this region and hence, no dedicated background subtraction is needed.

As for the radiative channels, the *sPlot* technique [95] is used. Peaking backgrounds are taken as part of the signal distribution when performing the *sPlot* since for this type of background, the yields are fixed.

An alternative background subtraction method is also used by our collaborators. This method consists in evaluating the proper time distribution of the different backgrounds from simulation and subtract it from the proper time distribution in data using the yields obtained for each type of background from the mass fit. For the combinatorial background, the proper time distribution in the sidebands of the mass distribution of the data is subtracted from the whole proper time distribution. This background subtraction method is indifferent to the correlations between the mass and proper time in contrary to the *sPlot* technique.

4.3 The proper time

4.3.1 The proper time reconstruction

The proper time is reconstructed as

$$ct = \frac{L}{\beta\gamma} = \frac{M}{P} \times L \tag{4.11}$$

where L is the measured flight distance between the PV and the SV, M and P are the measured mass and momentum of the B meson. The proper time results from an adjustment with a B mass constraint applied. The choice of the B mass constrained proper time improves the proper time resolution. Moreover, this proper time has, by definition, uncorrelated errors with the reconstructed B mass. This is essential for the use of the *sPlot* technique [95] since this technique requires that the variable used to unfold the different contributions in the data sample should be uncorrelated with the other variables that are used to perform the analysis.

The photon energy bias (appendix B) affects the proper time. This effect has been studied and corrected for, the procedure is explained in section 4.3.2.3.

4.3.2 Proper time distribution model for signal

The probability density function used to fit the proper time is defined as

$$\begin{aligned} PDF &= [\text{Decay rate} \times \text{Acceptance}] * \text{Resolution} \\ \text{where decay rate} &= \begin{cases} e^{-t/\tau_{B^0}} \quad \text{for } \mathrm{B^0} \to \mathrm{K^*(892)^0}\gamma \text{ and } \mathrm{B^0} \to \mathrm{J/\psi\, K^*(892)^0} \\ e^{-t/\tau_{B^0_s}} \times (\cosh(\Delta\Gamma_s t/2) - A_\Delta \times \sinh(\Delta\Gamma_s t/2) \quad \text{for } \mathrm{B^0_s} \to \phi\gamma, \end{cases} \\ \text{acceptance} &= \frac{(a[t-t_0])^n}{1+(a[t-t_0])^n} \times e^{-\delta\Gamma t} \\ \text{and resolution} &= e^{-b\sqrt{1+\frac{(t-\mu)^2}{\sigma^2}}}. \end{aligned} \tag{4.12}$$

The time-dependent decay rate is introduced in 4.1. It can be seen that for the B system, the decay rate reduces down to a single exponential when neglecting $\Delta\Gamma$. Whereas for the B^0_s system the decay rate maintains the form with the hyperbolic sine and cosine.

The proper time resolution model is discussed in section 4.3.2.1. In the same section, proper time bias and its correction are discussed. The proper time acceptance and its parameterization are discussed in section 4.3.2.4.

An unbinned maximum likelihood fit is applied to the proper time distribution of the selected events using the Likelihood defined in 4.12 to extract A_Δ.

4.3.2.1 Proper time resolution

The proper time resolution obtained for the radiative decays is of the order of 40-50 fs. This resolution is evaluated using simulation. The effect of non perfect knowledge of the proper time resolution on the measurement of A_Δ has been studied in [105] and has been found to be negligible. Nevertheless, understanding and modeling the proper time resolution is an important issue.

4.3.2.2 Parametrization of the proper time resolution

The proper time resolution is studied using simulation. The quantity $\Delta t = t_{rec} - t_{true}$ for $K^*\gamma$, where t_{rec} is the reconstructed proper time obtained from 4.11 and t_{true} is the simulated proper time of the event is modeled by an Apollonios function defined as

$$\mathcal{A}(t) = e^{-b\sqrt{1+\frac{(t-\mu)^2}{\sigma^2}}}. \tag{4.13}$$

where μ is the mean of the distribution and b and σ parametrize, jointly, its resolution. The selection used to perform this study is summarized in table 4.3. Figure 4.3 shows on simulation the distribution of $\Delta t = t_{rec} - t_{true}$ for $K^*\gamma$.

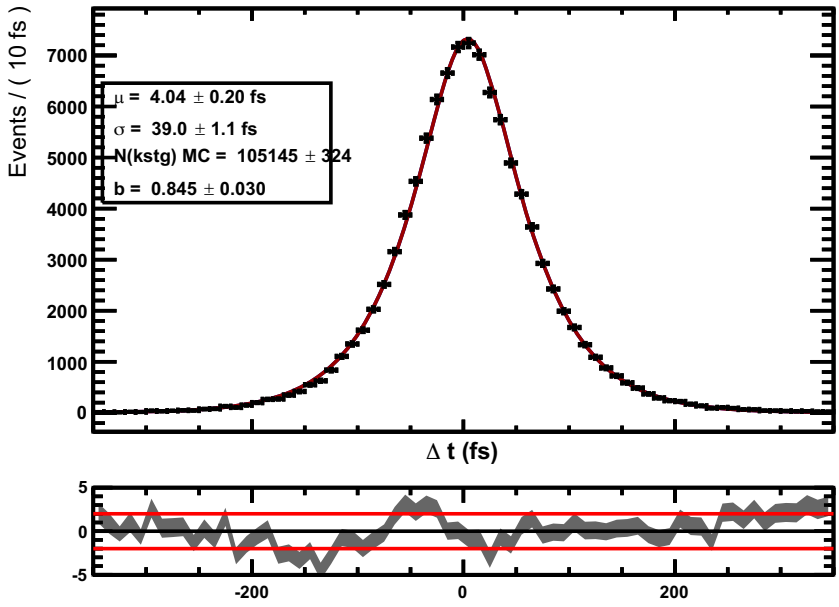

Figure 4.3: The distribution of Δt on $B^0 \to K^*\gamma$ MC simulation fitted with an Apollonios function. The proper time bias, μ, is of the order of 5 fs.

Figure 4.6 shows the evolution of the proper time resolution σ as a function of the reconstructed proper time. The evolution of σ is modeled with

$$\sigma(t) = \sigma_0 \times \frac{t^n}{1+\alpha t^n} \tag{4.14}$$

Due to selection acceptance effects, the proper time resolution is different at low and high proper time with a smaller resolution for low proper time and larger for high

proper time. This is shown in figures 4.4 and 4.5 for $B^0 \to K^*(892)^0\gamma$ events where the Δt distribution is fitted in different bins of the proper time with an Apollonios function fixing the parameter b to the fit value over the whole proper time range so as to evolution of σ. The resolution increases starting from 26 fs for a proper time in [0,0.5] ps range and going up to 59 fs for a proper time in [6.5,10] ps range.

Resolution parameters	$K^*\gamma$	$J/\psi K^*$	$\phi\gamma$	$J/\psi\phi$
μ fs	4.04 ± 0.20	1.61 ± 0.34	4.38 ± 0.29	2.62 ± 0.17
b	1.11 ± 0.06	0.87 ± 0.06	1.11 ± 0.06	0.89 ± 0.03
σ_0 fs	110.4 ± 10.0	143.7 ± 12.1	115.3 ± 9.9	174.1 ± 8.2
α	1.78 ± 0.24	2.51 ± 0.32	1.73 ± 0.22	2.90 ± 0.17
n	0.62 ± 0.06	0.84 ± 0.08	0.65 ± 0.05	0.82 ± 0.03

Table 4.4: Resolution parameters of the radiative and di-muon channels obtained from MC.

In the proper time fits, the proper time resolution parameter of equation (4.13) is parametrized according to this. Table 4.4 summarizes the resolution parameters obtained from MC for the radiative and di-muon channels.

4.3.2.3 Proper time bias study

The procedure to correct the photon energy-induced bias in the proper time is discussed in this section.

To investigate the bias properly, the distribution of $\Delta t = t_{rec} - t_{true}$ for $K^*\gamma$ is plotted for each photon type (converted or unconverted) and for each region of the calorimeter (inner, middle or outer). The distribution is fitted with an Apollonios function. Figures 4.7 show the fits to $B_s^0 \to \phi\gamma$ MC events of unconverted photon type (as per example, same conclusion is obtained for converted photons). Table 4.5 summarizes the results of the fits for the different categories of the fits (converted or unconverted: inner, middle and outer calorimeter regions).

It can be easily seen, looking at the means of the Apollonios function reported in table 4.5, that the distribution Δt is biased: ∼6 fs, ∼15 fs and ∼30 fs for the outer, middle and inner regions of the calorimeter respectively.

Calibrating the momentum of the B by calibrating the photon momentum (appendix B), reduced the proper time bias to a residual bias of about 5 fs constant over the different calorimeter regions and the different photon types. The calibration is performed

Δt (fs)	Inner	Middle	Outer
Converted	36.2±1.4	10.4±1.5	-5.8±1.6
Unconverted	36.8±1.0	16.2±1.1	6.7±1.2

Table 4.5: The mean of the distribution of Δt for the different photon types and in the different regions of the calorimeter extracted from a fit using the Apollonius function. The values reported are before calibration.

by refitting the proper time using the corrected momentum of the B meson. Table 4.6 shows the results of fits to the distribution of Δt, this time with the reconstructed proper time calibrated with the correct momentum. The corresponding plots for unconverted photons are shown in figure 4.8.

Δt (fs)	Inner	Middle	Outer
Converted	3.7±0.5	5.3±0.6	7.9±0.7
Unconverted	1.3±0.5	4.2±0.5	8.6±0.5

Table 4.6: The mean of the distribution of Δt for the different photon types and in the different regions of the calorimeter extracted from a fit using the Apollonius function. The values reported are after calibration.

The residual bias of ∼5 fs might not be related to the photon, its origin is under investigation and its effect on the measurement of the photon polarization will be taken as a systematic in the analysis.

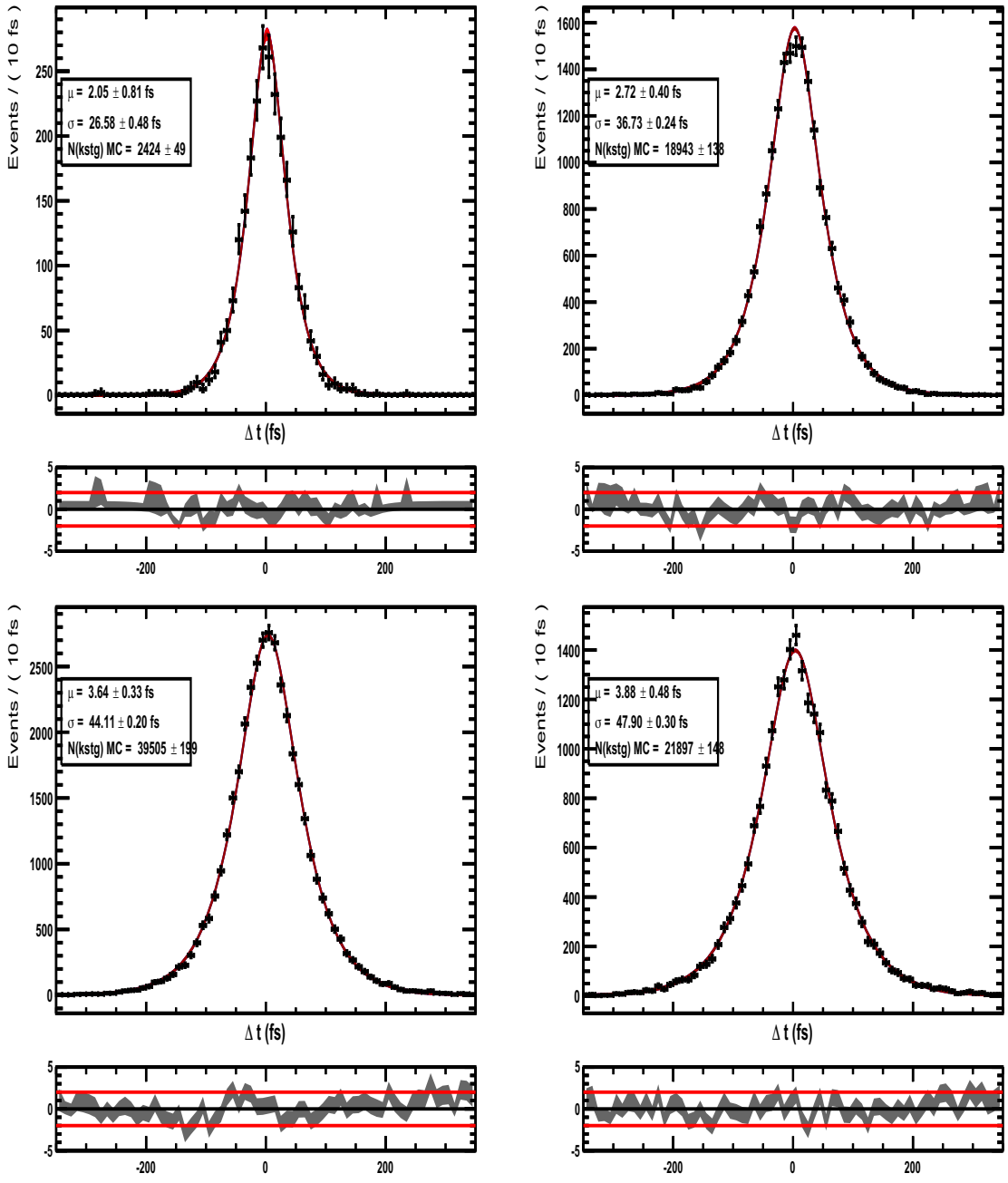

Figure 4.4: The distribution of Δt for $B^0 \to K^*\gamma$ simulated events in bins of the reconstructed proper time fitted with Apollonios function. Top left: [0,0.5] ps. Top right: [0.5,1.0] ps. Bottom left: [1.0,2.0] ps. Bottom right: [2.0,3.0] ps.

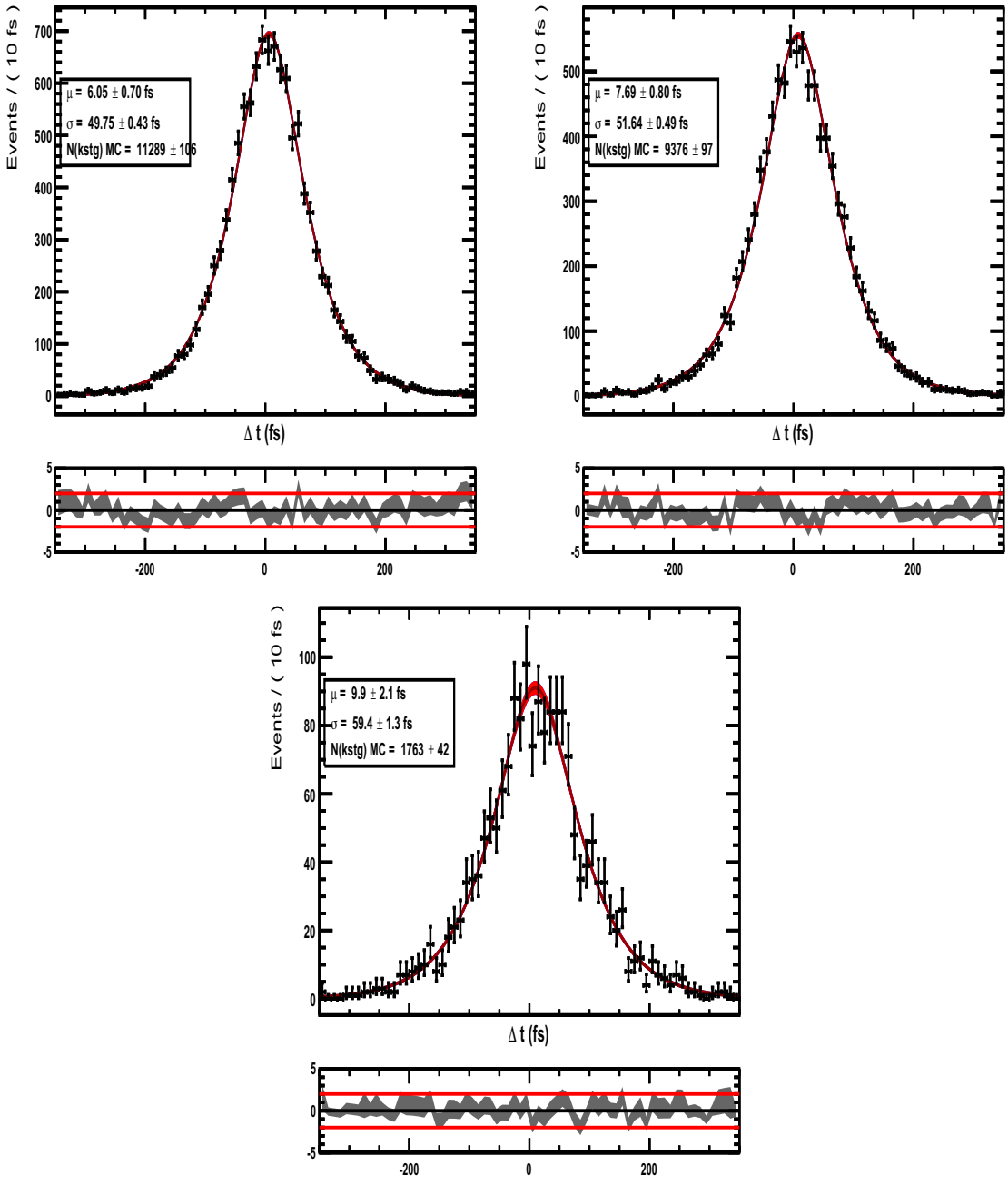

Figure 4.5: The distribution of Δt for $B^0 \to K^*\gamma$ simulated events in bins of the reconstructed proper time fitted with Apollonios function. Top left: [3.0,4.0] ps. Top right: [4.0,6.5] ps. Bottom: [6.5,10.0] ps.

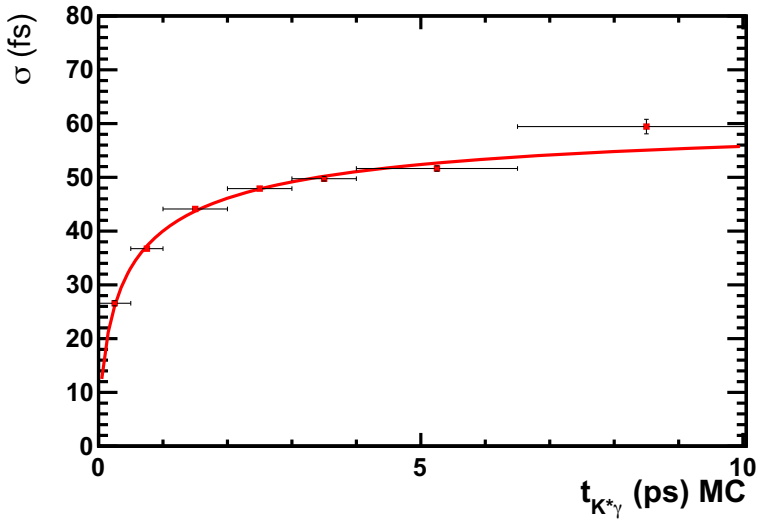

Figure 4.6: The proper time resolution σ as a function of the reconstructed proper time. The proper time evolution is fitted with equation 4.14.

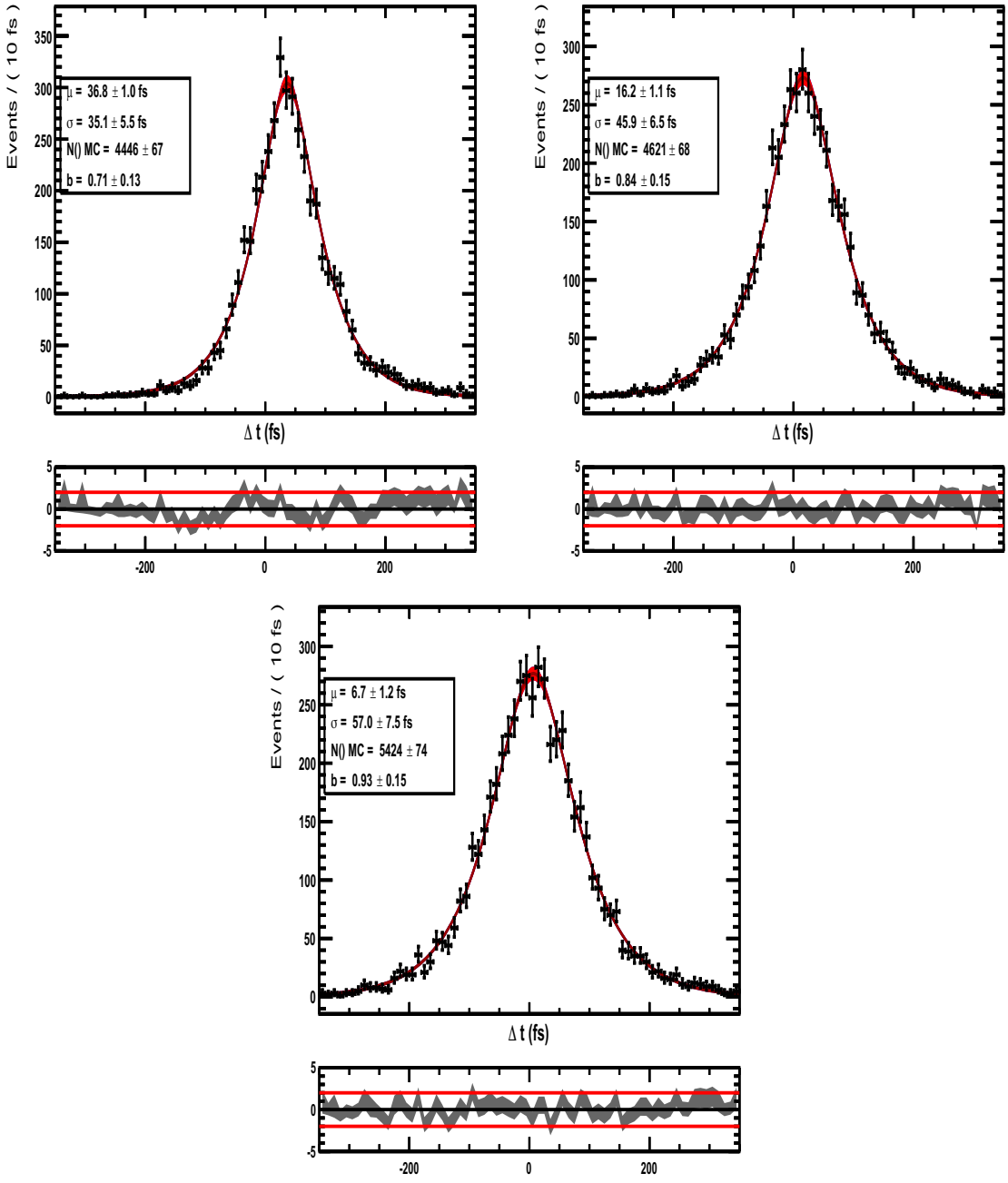

Figure 4.7: The distribution of Δt for $B_s^0 \to \phi\gamma$ simulated events in the inner (top left) middle (top right) and outer (bottom) regions of the calorimeter. The plots are for unconverted photons.

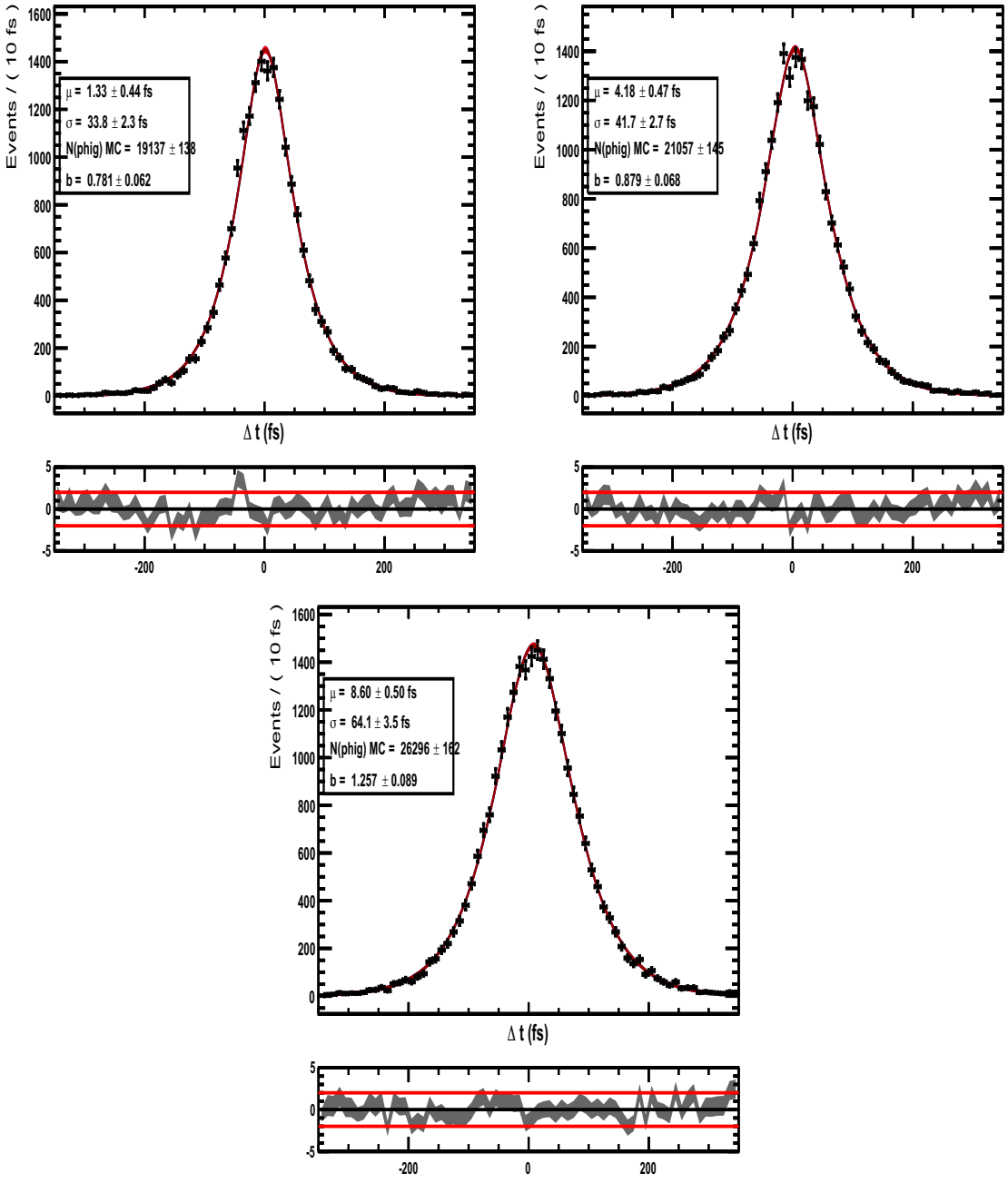

Figure 4.8: The distribution of Δt after correction for $B_s^0 \to \phi\gamma$ simulated events in the inner (top left) middle (top right) and outer (bottom) regions of the calorimeter. The plots are for unconverted photons.

4.3.2.4 Proper time acceptance parameterization

The proper time acceptance is defined as the efficiency to reconstruct and select the events as a function of the proper time (see Figure 4.9). The precise knowledge of the proper time acceptance is critical for the A_Δ measurement.

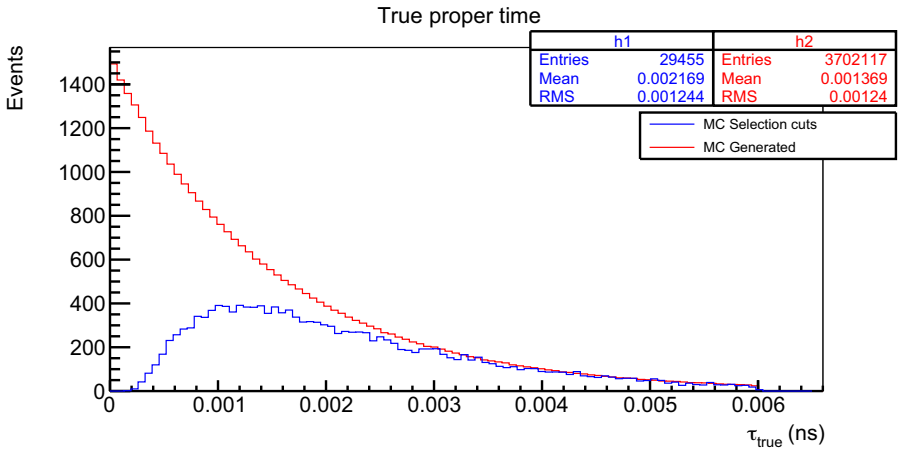

Figure 4.9: Monte Carlo generated proper time (in red) compared to the proper-time distribution after the trigger and stripping selection (in blue), for the $B_s \to \phi\gamma$ decay. The acceptance is defined as the ratio between the two.

The parametrization of the proper time acceptance is expressed as

$$\mathcal{A}(t) = \mathcal{A}(t)_{low} \times \mathcal{A}(t)_{high}, \tag{4.15}$$

$$\text{with } \mathcal{A}(t)_{low} = \frac{(a[t-t_0])^n}{1+(a[t-t_0])^n}, \tag{4.16}$$

$$\text{and } \mathcal{A}(t)_{high} = e^{-\delta\Gamma t}, \tag{4.17}$$

where low and high stand for acceptance at low (typically $< 2\,ps$) and high proper time respectively. The parameter $\delta\Gamma$ parametrizes the acceptance at high proper time while a, n and t_0 parameterize the acceptance at low proper time.

4.4 Proper time acceptance study on MC

In this section, a study based on simulation of the proper time is addressed. Both the acceptance at high and low proper time are detailed. The weighing and cut scaling procedure that is used to match the di-muon channels to the corresponding radiative ones is explained.

4.4.1 Acceptance at low proper time, $B^0 \to J/\psi X$ weighing and cut scaling procedure.

The difference in the decay kinematic between $B^0 \to J/\psi X$ and radiative channels is a consequence of the large mass difference between the photon and the J/ψ and the helicity difference between a vector-vector decay, $B^0 \to J/\psi X$, and a vector-photon decay, $B^0 \to X\gamma$. Table 4.7 lists the kinematical properties of the $K^*(\phi)$ in the $B^0(B_s)$ rest frame for $B^0 \to K^*(892)^0\gamma$ and $B^0 \to J/\psi K^*(892)^0$ ($B_s^0 \to \phi\gamma$ and $B_s^0 \to J/\psi\,\phi$). The acceptance at low proper time is mainly driven by two selection variables related to vertex displacement: the IP χ^2 of the tracks and the θ_{DIRA} angle. Figures 4.10 and 4.11 show that the distributions of those variables are different between $B^0 \to K^*(892)^0\gamma$ and $B^0 \to J/\psi K^*(892)^0$, same conclusion applies for $B_s^0 \to \phi\gamma$ and $B_s^0 \to J/\psi\,\phi$. Without a proper treatment, the acceptance at low proper times for $B^0 \to J/\psi X$ events would then not match the one of radiative events.

	$p^\star$ (MeV/c)	$E^\star$ (MeV/c^2)	$\beta^\star$	$\gamma^\star$
$B_s^0 \to \phi\gamma$	2583	2777	0.93	2.72
$J/\psi\phi$	1583	1883	0.84	1.85
Ratio	$\rho_p = 1.63$	$\rho_E = 1.47$	$\rho_\beta = 1.11$	
$B^0 \to K^*(892)^0\gamma$	2564	2714	0.944	3.04
$B^0 \to J/\psi K^*(892)^0$	1577	1808	0.872	2.02
Ratio	$\rho_p = 1.63$	$\rho_E = 1.50$	$\rho_\beta = 1.08$	

Table 4.7: Kinematical properties and their ratios of the K^*/ϕ in the B^0/B_s rest frame for $B^0 \to K^*\gamma / B_s^0 \to \phi\gamma$ and $B^0 \to J/\psi K^*(892)^0 / B_s^0 \to J/\psi\,\phi$ decays.

The weighing and cut scaling procedure is detailed in appendix A, a short summary is presented here. To match the acceptances of $B^0 \to J/\psi X$ and of radiative channels, the kinematical configurations of $B^0 \to J/\psi X$ should be matched to that of $B^0 \to X\gamma$. Let θ be the angle between the B momentum and the X vector momentum, and p_V be the

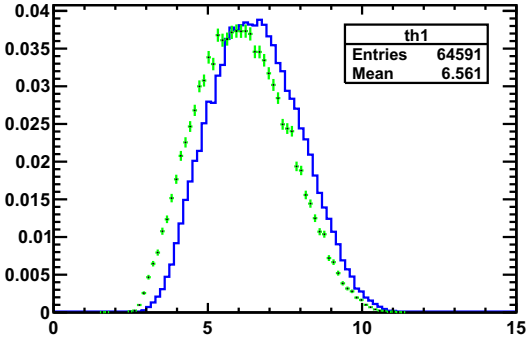

Figure 4.10: Minimum track IP χ^2 distributions for $B^0 \to K^\star\gamma$ (histogram) and $B^0 \to J/\psi K^*(892)^0$ (dots).

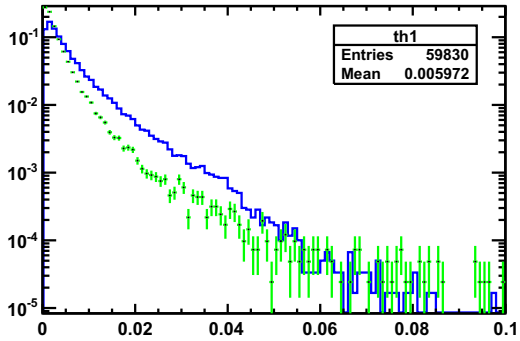

Figure 4.11: $\theta_{\rm DIRA}$ angle distribution for $B^0 \to K^\star\gamma$ (histogram) and $B^0 \to J/\psi K^*(892)^0$ (dots).

momentum of the vector X in the lab frame for $B^0 \to J/\psi X$ decay. Let the superscript "$\star$" denote the same quantities in the rest frame of the B meson. Let the superscript "$\prime$" denote those quantities for $B^0 \to X\gamma$ (see figure 4.12). It can be shown from relativistic calculations (see appendix A for details) that, for a given B decay time t, and in the limit of large B^0 boost ($\beta\gamma_B >> 1$) and small angles in the lab frame ($cos\theta \sim 1$), each kinematical configuration for $B^0 \to J/\psi X$, identified by $(p^\star, cos\,\theta^\star, \beta\gamma_B)$, can be related with one $B^0 \to X\gamma$ kinematical configuration, identified by $(p^{\star\prime}, cos\,\theta^{\star\prime}, \beta\gamma_B')$, while preserving the invariance of the kinematical product :

$$p_V \times cos(\theta^*) = p_V' \times cos(\theta^{\star\prime}). \tag{4.18}$$

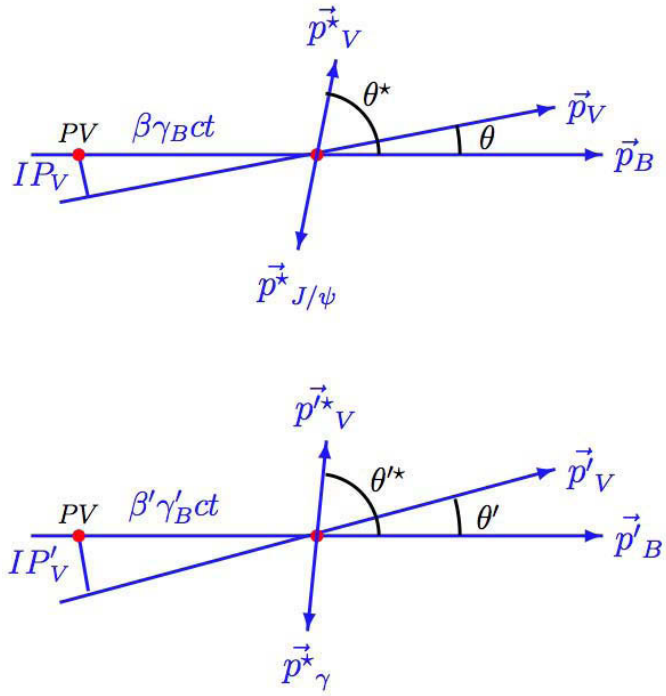

Figure 4.12: Sketches of the decay geometry for $B \to J/\psi X$ (top) and $B \to \gamma X$ (bottom).

Between the matched configurations of $B^0 \to J/\psi X$ and $B^0 \to X\gamma$, the ratio of several kinematical quantities are constant to a very good approximation :

$$\begin{aligned} \frac{p'_V}{p_V} &= \frac{\cos(\theta^*)}{\cos(\theta^{\star\prime})} = \rho_{\beta^*} \\ \frac{\gamma_B}{\gamma'_B} &\sim \frac{\rho_{E^**}}{\rho_{\beta^*}} \end{aligned}$$

where $\rho_{\beta^\star} = \frac{\beta_V^{\star\prime}}{\beta_V^\star}$ and $\rho_{E^\star} = \frac{E_V^{\star\prime}}{E_V^\star}$ are constant ratios derived from table 4.7. Useful relations on the geometrical quantities relying on the decay vertex displacement can be derived from the above kinematical matching. For instance it can be shown that the impact parameters of the vector meson and the direction angle variable, $\theta_{\rm DIRA}$, also exhibit an approximate constant ratio between the matched configurations. Because of the different helicity structure between $B^0 \to J/\psi X$ and $B^0 \to X\gamma$ decays, the impact parameters of the charged kaons and/or pion from the X vector decay are affecting differently the acceptance in the two decays. The helicity angle is then to be taken into account in the procedure of alignement of the proper time acceptance. Based on the above matching relation between $B^0 \to J/\psi X$ and $B^0 \to X\gamma$ decays, the following three-step procedure

is applied to align the acceptance at low proper time between the two different decays :

- The $B^0 \to J/\psi X$ candidates are reconstructed in such a way that the $J/\psi \to \mu^+\mu^-$ decay is not used in the decay vertex determination. This is achieved by applying an arbitrarily large factor to the relevant elements of the covariance matrix of the reconstructed muon tracks. The proper time acceptance is then generated only by the selection cuts applied on the vector meson and its decay products, as it is for the corresponding radiative decay.

- An event-by-event reweighing is applied on the $B^0 \to J/\psi X$ sample to statistically reproduce the $B^0 \to X\gamma$ distribution in the two-dimensional plane ($p.\cos(\theta^*)$,θ_H), where θ_H is the helicity angle of the X vector decay. The reweighing in the first direction ($p.\cos(\theta^*)$) aims at aligning the kinematics according to the matching relation discussed above while the helicity reweighing accounts for the different helicity-structure of the X vector decay.

- After the reweighing, the two different decays are assumed to exhibit almost-constant ratios for the vertex-related variables that induce the low proper time acceptance. A scaling factor is extracted for the relevant variables and the corresponding selection cuts are scaled accordingly.

Figure 4.13 shows the distribution of helicity angle and $p_V \times cos(\theta^\star)$ for the $B^0 \to K^*(892)^0\gamma$ and $B^0 \to J/\psi K^*(892)^0$ modes and the two-dimensional histograms ratio. Figure 4.14 shows the same distributions for $B_s^0 \to \phi\gamma$ and $J/\psi\phi$. The weights are extracted from the two-dimensional ratio after applying the full selection, then are cross-checked with weights extracted after applying the selection except for the cuts on the variables that drive the acceptance at low proper time, the $\theta_{\rm DIRA}$ angle and the tracks IP χ^2. The weights were found to be consistent.

The distribution of the $\theta_{\rm DIRA}$ angle is also different between the di-muon and the radiative channels. This difference comes mainly from the fact that the resolution on the B momentum direction is smaller in the di-muon than in the radiative channels since the radiative channel resolution is dominated by the presence of the photon. Applying same $\theta_{\rm DIRA}$ cuts would then produce different acceptances[1].

The procedures to align the acceptances induced by cuts on χ^2(IP) and the $\theta_{\rm DIRA}$ are identical. After performing the two dimensional reweighing, the cut on the variable

[1]Removing the $\theta_{\rm DIRA}$ cuts from the offline selection is not possible because online $\theta_{\rm DIRA}$ cuts is already applied in the exclusive HLT2 trigger.

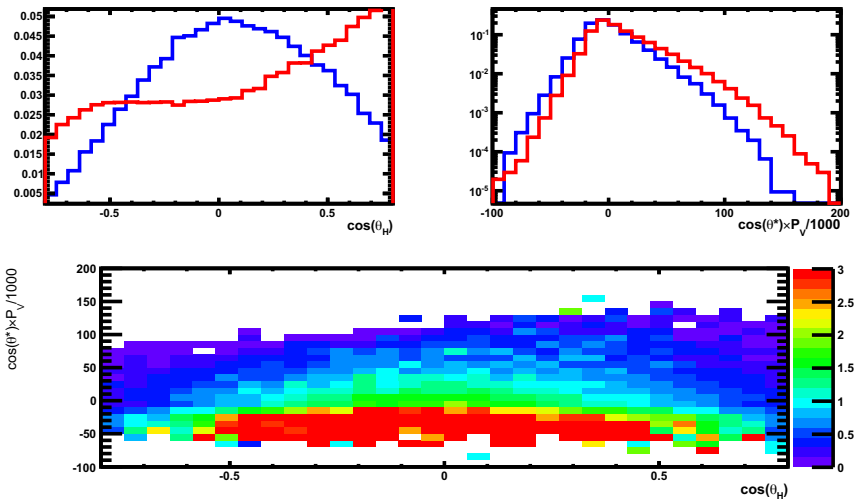

Figure 4.13: Top : the distributions of the helicity angle (left) and $p_v \times \cos(\theta^\star)$ (right) for $B^0 \to K^*(892)^0\gamma$ (blue) and $B^0 \to J/\psi K^*(892)^0$ (red). The distributions of the helicity angle are asymmetric due to the asymmetric decay of the K^*. Bottom: the two dimensional histogram of weights.

($\mathcal{V} = \theta_{\rm DIRA}$, $\chi^2(\rm IP_{K^+})$ or $\chi^2(\rm IP_{\pi^-})$ is rescaled by a given factor. The scaling factor is obtained plotting the distributions of the natural logarithm of the variable for $B^0 \to X\gamma$ and $B^0 \to J/\psi X$ MC events and computing the difference between the peak positions of the two distributions: $\ln(\mathcal{V}_{X\gamma}) - \ln(\mathcal{V}_{J/\psi X})$.

Figures 4.15, 4.17 and 4.19 show the distributions of the variables, where the full selection is applied except for the variable $\mathcal{V}$ in question, for $B^0 \to X\gamma$, $B^0 \to J/\psi X$, $B^0 \to J/\psi X$ after weighing and $B^0 \to J/\psi X$ after weighing and scaling. After weighing and scaling, each distribution for $B^0 \to J/\psi X$ is consistent with the corresponding one of $B^0 \to X\gamma$.

The scaling factors obtained from MC are reported in table 4.8. Figures 4.16 and 4.18 show that also in data the $\theta_{\rm DIRA}$, $\rm IP\chi^2_{K^+}$ and $\rm IP\chi^2_{\pi^-}$ distributions after weighing and scaling are in good agreement between $B^0 \to K^*(892)^0\gamma$ and $B^0 \to J/\psi K^*(892)^0$. Same conclusion applies to $B^0_s \to \phi\gamma$ and $B^0_s \to J/\psi\,\phi$.

4.4.2 Proper time in simulated data

Here and in the forthcoming sections, all fits are unbinned maximum likelihood fits performed with Roofit [71, 99]. After having fixed the selection and the reweighing of

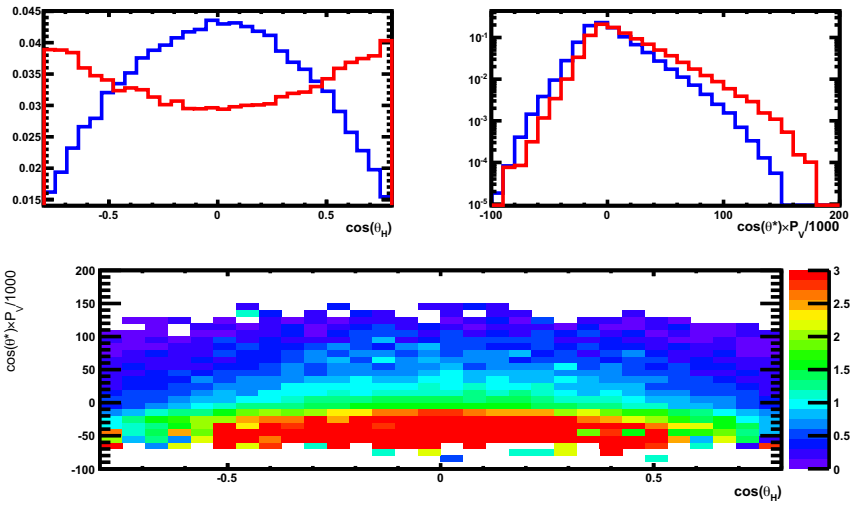

Figure 4.14: Top : the distributions of the helicity angle (left) and $p_v \times cos(\theta^\star)$ (right) for $B_s^0 \to \phi\gamma$ (blue) and $B_s^0 \to J/\psi\,\phi$ (red). The distributions are symmetric due to the symmetric decay of the ϕ. Bottom: the two dimensional histogram of weights.

	Scaling factor $B^0 \to J/\psi K^*(892)^0$	Scaling factor $B_s^0 \to J/\psi\,\phi$
$\theta_{\rm DIRA}$	1.78 ± 0.01	1.79 ± 0.01
$IP\chi^2_{K^+}$	1.15 ± 0.02	1.41 ± 0.02
$IP\chi^2_{\pi^-/K^-}$	1.05 ± 0.01	1.41 ± 0.02

Table 4.8: Values of the scaling factors obtained for $\theta_{\rm DIRA}$, $IP\chi^2_{K^+}$ and $IP\chi^2_{\pi^-/K^-}$.

the $B^0 \to J/\psi X$ control channel to reproduce the acceptance at low proper time of radiative channels, fits of the full proper time distributions have been performed on simulation. The samples used are MC2012 for the radiative channels and MC2011 + MC2012 for $B^0 \to J/\psi X$. In fits of simulated data, physical parameters ($\Delta\Gamma$, Γ and the lifetimeτ) are fixed to their generated value in the samples, the actual values are reported in table 4.9.

Table 4.10 reports the acceptance parameters extracted from independent proper time fits of each channel (see figures 4.20, 4.21 and 4.22). All proper time acceptance parameters are consistent between $B_s^0 \to \phi\gamma$ and $B^0 \to K^*(892)^0\gamma$. After weighing and cut scaling, the parameters of the acceptance at low proper time (a, n and t_0) for $B^0 \to J/\psi X$ are very close to the ones of the radiative channels. The parameter of the acceptance at high proper time ($\delta\Gamma$) is essentially not affected by the weighing procedure. The parameter of the acceptance at high proper time ($\delta\Gamma$) is smaller for $B^0 \to J/\psi X$ compared

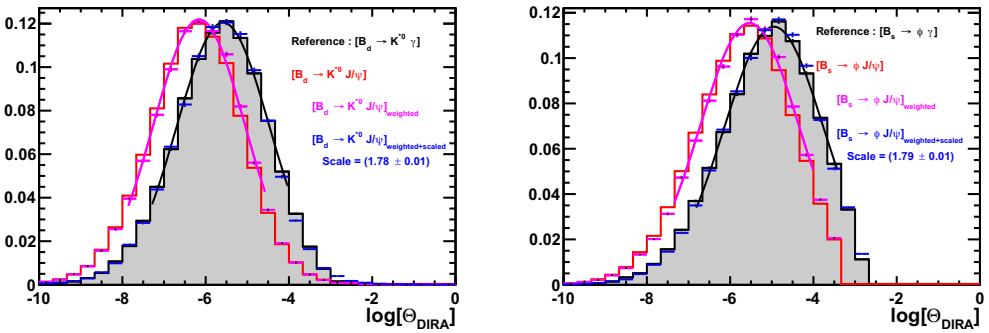

Figure 4.15: Scaling the θ_{DIRA} angle distribution. Color code: $B^0 \to K^*(892)^0\gamma$ (left) $B_s^0 \to \phi\gamma$ (right) (black histogram), $B^0 \to J/\psi K^*(892)^0$ (left) $B_s^0 \to J/\psi\,\phi$ (right) (red histogram), $B^0 \to J/\psi K^*(892)^0$ (left) $B_s^0 \to J/\psi\,\phi$ (right) after weighing (purple points) and $B^0 \to J/\psi K^*(892)^0$ (left) $B_s^0 \to J/\psi\,\phi$ (right) after weighing and scaling (blue points).

to that of the radiative channels. As discussed in 4.4.3, the trigger accounts for almost 15 ns^{-1} in $\delta\Gamma$. For the radiative channels the offline selection introduces a significant acceptance effect at high proper time.

It is important to point out that the use of $B_s^0 \to J/\psi\,\phi$ as a control sample requires a special treatment. In order to know the fractions of the amplitudes of the light and heavy eigenstates that fall in the acceptance, a dedicated angular analysis is needed. The study has been performed on MC assuming that the time-dependent decay rate is a single exponential. An accurate treatment would require an angular analysis that is not well motivated because of the limited $B_s^0 \to J/\psi\,\phi$ statistics. So only $B^0 \to K^*(892)^0\gamma$ and/or $B^0 \to J/\psi K^*(892)^0$ are used as control samples. Nevertheless, $B_s^0 \to J/\psi\,\phi$ is present at each step of the proper time study since it served as a validation of the weighing and cut scaling procedure.

	Simulation
τ_{B^0} ps	1.519
$\tau_{B_s^0}$ ps	1.510
Γ_s ns^{-1}	662
$\Delta\Gamma_s$ ns^{-1}	92
A_Δ	0

Table 4.9: The values of the physical parameters generated in the simulation.

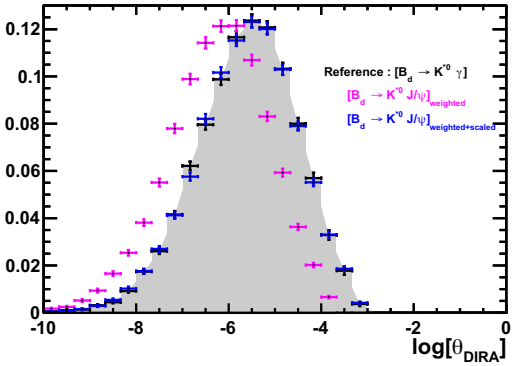

Figure 4.16: $\theta_{\rm DIRA}$ angle distributions in data. Color code: $B^0 \to K^*(892)^0\gamma$ (black histogram), $B^0 \to J/\psi K^*(892)^0$ (red histogram), $B^0 \to J/\psi K^*(892)^0$ after weighing (purple points) and $B^0 \to J/\psi K^*(892)^0$ after weighing and scaling (blue points).

Acceptance	$B_s^0 \to \phi\gamma B$	$^0 \to K^*(892)^0\gamma$	$B^0 \to J/\psi K^*(892)^0$	$B^0 \to J/\psi K^*(892)^0$ no weights
$\delta\Gamma$ ns^{-1}	44.4 ± 3.5	45.1 ± 3.5	17.0 ± 3.3	23.3 ± 3.9
a ps^{-1}	1.956 ± 0.030	1.925 ± 0.030	1.838 ± 0.026	1.453 ± 0.023
n	2.093 ± 0.071	2.087 ± 0.065	2.330 ± 0.059	2.096 ± 0.060
t_0 ps^{-1}	0.201 ± 0.007	0.203 ± 0.007	0.191 ± 0.005	0.224 ± 0.007

Table 4.10: Proper time acceptance parameters fitted independently on $B_s^0 \to \phi\gamma$, $B^0 \to K^*(892)^0\gamma$ and $B^0 \to J/\psi K^*(892)^0$ with and without the two dimensional weights.

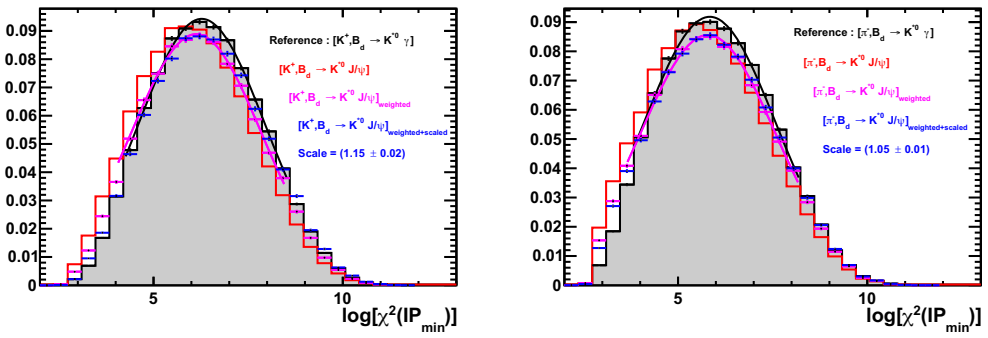

Figure 4.17: Scaling the K^+ (left) and π^- (right) IP χ^2 distributions. Color code: $B^0 \to K^*(892)^0\gamma$ (black histogram), $B^0 \to J/\psi K^*(892)^0$ (red histogram), $B^0 \to J/\psi K^*(892)^0$ after weighing (purple points) and $B^0 \to J/\psi K^*(892)^0$ after weighing and scaling (blue points).

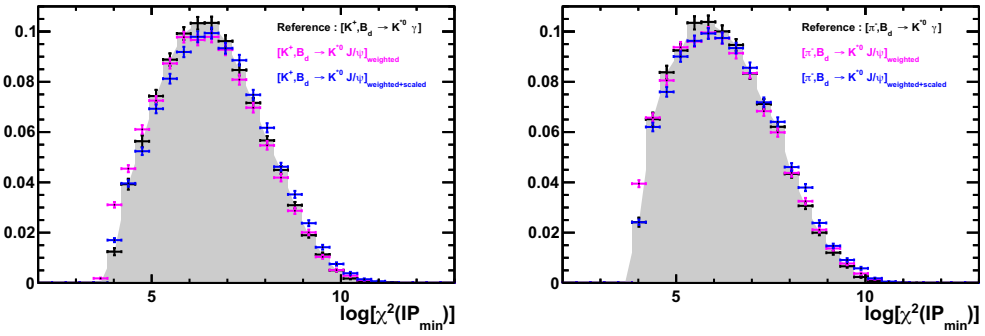

Figure 4.18: K^+ (left) and π^- (right) IP χ^2 distribution in data. Color code: $B^0 \to K^*(892)^0\gamma$ (black histogram), $B^0 \to J/\psi K^*(892)^0$ (red histogram), $B^0 \to J/\psi K^*(892)^0$ after weighing (purple points) and $B^0 \to J/\psi K^*(892)^0$ after weighing and scaling (blue points).

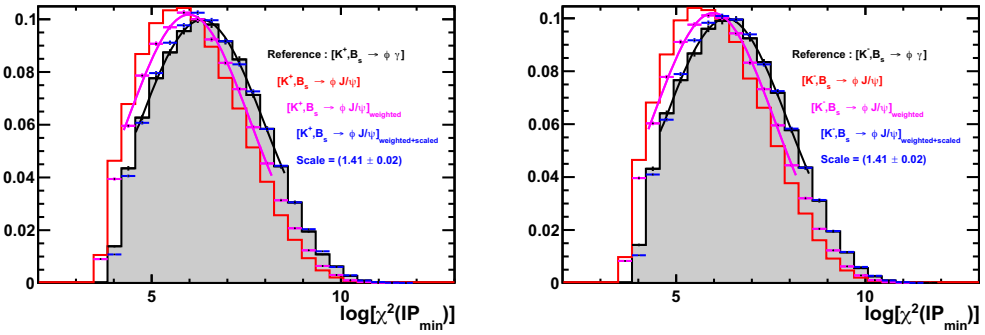

Figure 4.19: Scaling the K^+ (left) and K^- (right) IP χ^2 distributions. Color code:$B_s^0 \to \phi\gamma$ (black histogram), $B_s^0 \to J/\psi\,\phi$ (red histogram), $B_s^0 \to J/\psi\,\phi$ after weighing (purple points) and $B_s^0 \to J/\psi\,\phi$ after weighing and scaling (blue points).

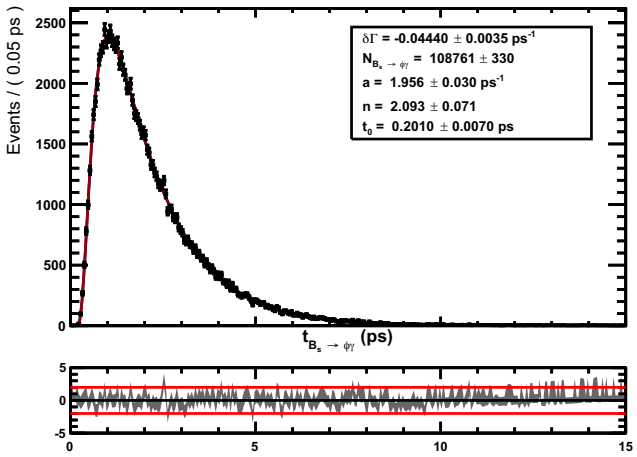

Figure 4.20: Fit of the MC proper time distribution for $B_s^0 \to \phi\gamma$.

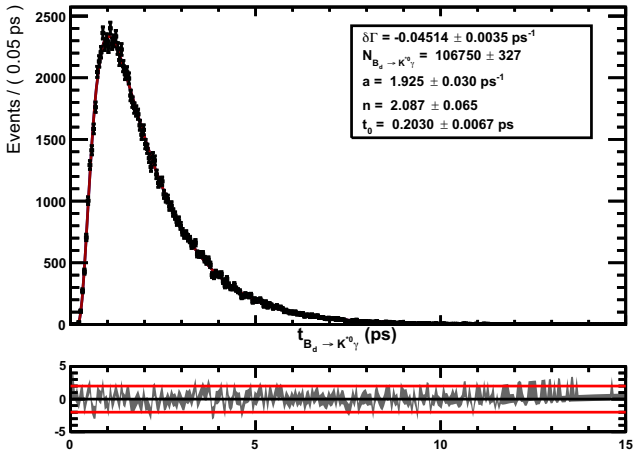

Figure 4.21: Fit of the MC proper time distribution for $B^0 \to K^*(892)^0\gamma$.

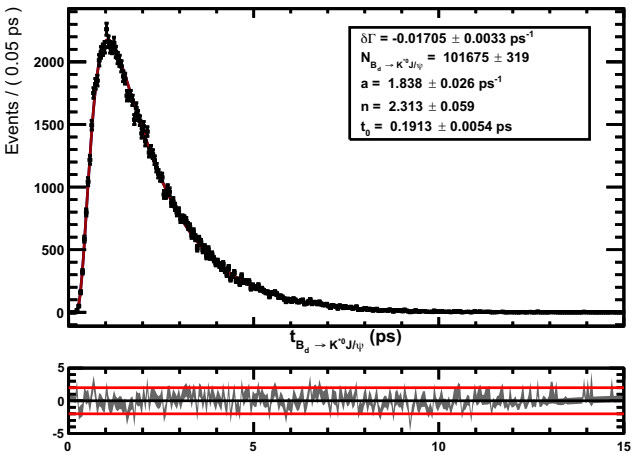

Figure 4.22: Fit of the MC proper time distribution for $B^0 \to J/\psi K^*(892)^0$.

4.4.3 Acceptance at high proper time introduced by the trigger

The global $\delta\Gamma$ obtained fitting the proper time distributions on MC is ~ 30 ns^{-1} for the $B^0 \to J/\psi X$ sample and ~ 40 ns^{-1} for the radiative samples (see section 4.4.2). This section addresses a study of the proper time acceptance introduced at high proper time (> 2 ps) by the trigger. The main sources of inefficiency at high decay times comes from VELO geometrical acceptance and the reconstruction of tracks.

4.4.3.1 MC study

Using $B_s^0 \to \phi\gamma$, $B^0 \to K^*(892)^0\gamma$, $B^0 \to J/\psi K^*(892)^0$ or $B_s^0 \to J/\psi\,\phi$ MC samples, the ratio of the proper time distribution with one specific trigger line applied plus the offline selection over the proper time distribution with only the offline selection applied is done. For each step of the trigger path this ratio is fitted starting from 2 ps with an exponential of the form $e^{-\delta\Gamma_{\text{triggerX}}.t}$ where the term $\delta\Gamma_{\text{triggerX}} = \delta\Gamma_{(\text{trigger X+offline selection})} - \delta\Gamma_{(\text{offline selection})}$ parametrizes the relative proper time acceptance at high proper time induced by this specific trigger line.
Figure 4.23 shows the ratio of the proper time distributions obtained from $B_s^0 \to \phi\gamma$ MC events. Table 4.11 reports the values of the $\delta\Gamma_{\text{triggerX}}$ fitted on $B_s^0 \to \phi\gamma$, $B^0 \to K^*(892)^0\gamma$, $B^0 \to J/\psi K^*(892)^0$ and $B_s^0 \to J/\psi\,\phi$ MC for different trigger criteria. As expected, the L0 tripper does not introduce any high proper time acceptance. The HLT2 contains cuts that affect the acceptance at high proper time but the HLT2 event reconstruction is relatively close to the offline one and those cuts are already present in the offline selection. Hence, the relative effect of the HLT2 with respect to the offline selection is very modest. On the other hand, because the HLT1 tracking is different from the offline one, the HLT1 introduces a significant inefficiency at high proper time even relatively to the offline selection. The overall $\delta\Gamma_{\text{HLT1}}$ introduced by the HLT1, or $\delta\Gamma_{\text{trigger}}$ introduced by the whole trigger given that HLT1 fully dominates here, is similar for the three samples, and is of the order of 20 ns^{-1} for $B_s^0 \to \phi\gamma$ and 10 ns^{-1} for $B^0 \to K^*(892)^0\gamma$ and the di-muon channels.

It has been shown in an other analysis [106] that about half of the acceptance slope introduced by the HLT1 TOS trigger requirement is related to a drop of the VELO reconstruction efficiency for tracks that are significantly displaced with respect to the beam axis. This inefficiency has been exhaustively studied for the $B(\Lambda_b) \to J/\psi X$ lifetime measurements [106]. The VELO reconstruction is done by the FastVelo algo-

rithm [107] with different online and offline versions. A detailed description can be found in [108]. The track finding procedure assumes that tracks originate approximately from the beam line. The VELO track reconstruction efficiency depends also on the event track multiplicity and p_T of the track. The effect is even worse in the case of the ϕ meson reconstruction because of the small opening angle between its decay products. Moreover, the Hlt1TrackAllL0 lines used in this analysis have additional requirements in the minimum number of VELO hits and T hits of the reconstructed tracks that are not applied for instance in the Hlt1DiMuon lines. These additional requirements, together with the p_T requirement on the track, modify further the acceptance.

4.4.3.2 Crosscheck on data

Since the HLT1TrackAllL0 TOS (applied only on the $K^*(\phi)$ decay products for $B^0 \to K^*(892)^0\gamma$ ($B_s^0 \to \phi\gamma$)) is not required in the di-muon trigger and stripping, its effect can be checked on data. Figure 4.24 show the ratio of the proper time distribution for this trigger requirement with respect to the offline selection as obtained for the $B^0 \to J/\psi K^*(892)^0$ data events. The fitted $\delta\Gamma_{\mathrm{HLT1TrackAllL0-TOS}}$ is 13.3 ± 4.4 ns^{-1} which is compatible with 5.0 ± 2.4 ns^{-1} obtained from the simulation. The same check is performed on $B_s^0 \to J/\psi\,\phi$, the obtained value for $\delta\Gamma_{\mathrm{HLT1TrackAllL0-TOS}}$ is -9.2 ± 12.4 ns^{-1} which is compatible with 7.7 ± 2.1 ns^{-1} obtained from simulation. Those results are reported in Table 4.12.

To conclude on this, it has been shown that, relative to the offline selection, only the HLT1 has a significant effect on the high proper time acceptance and it has been checked that for $B^0 \to J/\psi X$ the simulation reproduces in the limit of statistical uncertainty the effect of the HLT1TrackAllL0-TOS.

4.4.4 Proper time distribution of control samples in data

Independent fit to the proper time distributions of $B^0 \to K^*(892)^0\gamma$ and $B^0 \to J/\psi K^*(892)^0$ are performed on data. The physical lifetimes of the B^0 meson are fixed to the latest world average $\tau_{B^0} = 1.520 \pm 0.004$ ps [96]. The result are shown in table 4.13. The acceptance at low proper time for $B^0 \to K^*(892)^0\gamma$ and $B^0 \to J/\psi K^*(892)^0$ are consistent within errors thanks to the dedicated weighing and cut scaling procedure. From this it can be deduced that $B^0 \to J/\psi K^*(892)^0$ can be used in the data fit so as to constraint the acceptance at low proper time of the radiative channels.

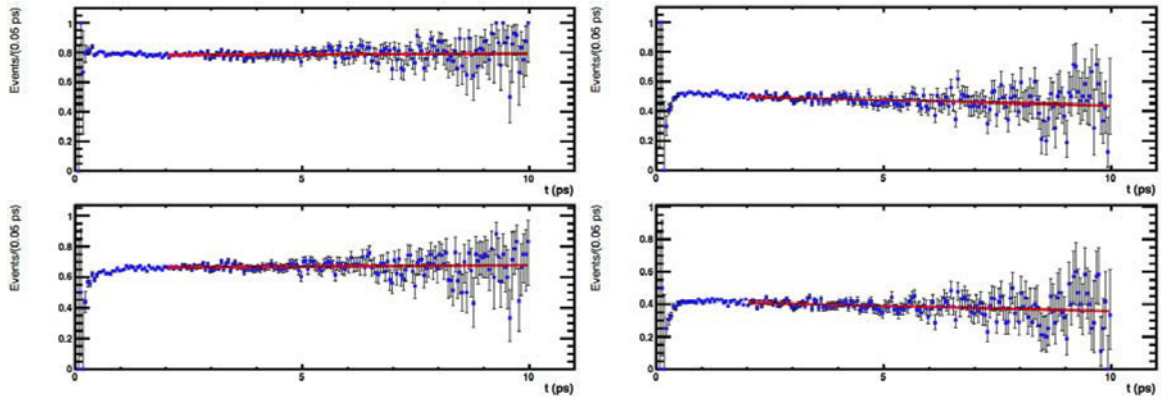

Figure 4.23: The ratio of the proper time distributions for $B_s^0 \to \phi\gamma$ simulated events with offline selection + L0 (top left), HLT1 (top right), HLT2 (bottom left) and all trigger applied (bottom right) over the proper time distribution with only the offline selection, fitted with $e^{-\delta\Gamma_{\mathrm{triggerX}} \cdot t}$.

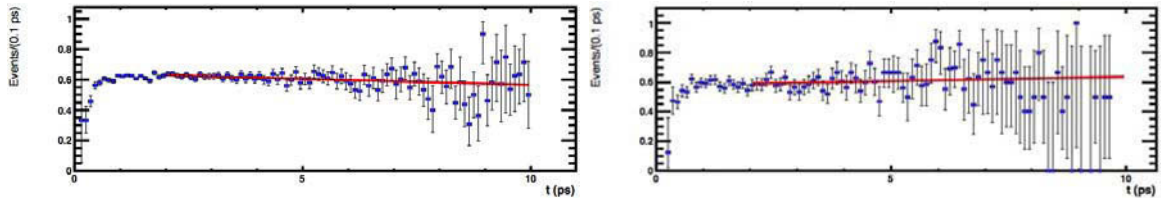

Figure 4.24: The ratio of the proper time distribution for $B^0 \to J/\psi K^*(892)^0$ (left) and $B_s^0 \to J/\psi\,\phi$ (right) data events with offline selection +HLT1TrackAllL0-TOS over the proper time distribution with only the offline selection, fitted with $e^{-\delta\Gamma_{\mathrm{HLT1TrackAllL0-TOS}} \cdot t}$.

The acceptance at high proper time is different between $B^0 \to K^*(892)^0\gamma$ and $B^0 \to J/\psi K^*(892)^0$. The amount of difference measured on data

$$\delta\Gamma_{B^0 \to K^*(892)^0\gamma\mathrm{data}} - \delta\Gamma_{B^0 \to J/\psi K^*(892)^0\mathrm{data}} = 37.9 \pm 12.6\ \mathrm{ns}^{-1},$$

is consistent within errors with what have been observed on simulation

$$\delta\Gamma_{B^0 \to K^*(892)^0\gamma\mathrm{MC}} - \delta\Gamma_{B^0 \to J/\psi K^*(892)^0\mathrm{MC}} = 28.1 \pm 4.8\ \mathrm{ns}^{-1}.$$

The simulation/data discrepancy in the acceptance at high proper time for the radiative channel is measured to be

$$\delta\Gamma_{B^0 \to K^*(892)^0\gamma\mathrm{data}} - \delta\Gamma_{B^0 \to K^*(892)^0\gamma\mathrm{MC}} = 52.5 \pm 10.4\ \mathrm{ns}^{-1},$$

trigger	$B_s^0 \to \phi\gamma B$	$^0 \to K^*(892)^0\gamma$	$B^0 \to J/\psi K^*(892)^0$	$B_s^0 \to J/\psi\,\phi$
L0	1.2 ± 1.3	-0.5 ± 1.3	0.0 ± 0.5	1.3 ± 0.8
HLT2 exclusive	1.8 ± 1.6	1.1 ± 1.7	0.3 ± 0.7	3.3 ± 1.0
HLT1TrackAllL0	19.1 ± 2.3	15.5 ± 2.3	5.0 ± 2.4	7.7 ± 2.1
HLT1DiMuon	—	—	7.0 ± 1.5	8.2 ± 0.9
All HLT1	—	—	10.8 ± 3.0	18.0 ± 2.5
All trigger	21.9 ± 2.9	16.0 ± 2.8	11.2 ± 3.1	18.1 ± 2.0

Table 4.11: The relative acceptance at high proper time induced by different trigger requirements on $B_s^0 \to \phi\gamma$, $B^0 \to K^*(892)^0\gamma$, $B^0 \to J/\psi K^*(892)^0$ and $B_s^0 \to J/\psi\,\phi$ simulated events. The numbers are the fitted values for $\delta\Gamma_{\text{triggerX}}$ in ns^{-1}.

HLT1TrackAllL0	$B^0 \to J/\psi K^*(892)^0$	$B_s^0 \to J/\psi\,\phi$
MC	5.0 ± 2.4	7.7 ± 2.1
Data	13.3 ± 4.4	−9.2 ± 12.4

Table 4.12: The relative acceptance at high proper time induced by HLT1TrackAllL0-TOS trigger requirement on $B^0 \to J/\psi K^*(892)^0$ and $B_s^0 \to J/\psi\,\phi$ simulated and data events. The numbers are the fitted values for $\delta\Gamma_{\text{HLT1TrackAllL0-TOS}}$ in ns^{-1}.

and for the di-muon channel, the difference is

$$\delta\Gamma_{B^0 \to J/\psi K^*(892)^0 \text{data}} - \delta\Gamma_{B^0 \to J/\psi K^*(892)^0 \text{MC}} = 42.7 \pm 8.6\ \text{ns}^{-1}.$$

The simulation/data discrepancy is consistent between the radiative and di-muon channels within 0.7 σ. Moreover, the difference between the radiative and dimuon channels in simulated samples is consistent with the difference measured on data within 0.7 σ. The simulation/data discrepancy in the high proper time acceptance is nevertheless to be understood and is under study.

The different strategies envisaged to measure A_Δ are presented in the next section.

4.4.5 Measurement strategies

A_Δ will be extracted from a simultaneous fit of the $B_s^0 \to \phi\gamma$ signal sample and of the control sample(s). Given that two control channels can be used, 3 simultaneous fits are

Acceptance	$B^0 \to K^*(892)^0\gamma$	$B^0 \to J/\psi K^*(892)^0$
$\delta\Gamma$ ns^{-1}	97.6 ± 9.8	59.7 ± 7.9
a ps^{-1}	1.941 ± 0.087	2.02 ± 0.10
n	1.66 ± 0.16	1.47 ± 0.088
t_0 ps^{-1}	0.264 ± 0.019	0.289 ± 0.009

Table 4.13: Proper time acceptance parameters fitted independently on $B^0 \to K^*(892)^0\gamma$ and $B^0 \to J/\psi K^*(892)^0$ data samples. The physical lifetimes of the B^0 meson are fixed to the latest world averages [96].

possible:

- **Strategy A**: $B_s^0 \to \phi\gamma$ + $B^0 \to K^*(892)^0\gamma$. This strategy is based on the fact that the selection has been specially designed so that the proper time acceptance for both $B_s^0 \to \phi\gamma$ and $B^0 \to K^*(892)^0\gamma$ are consistent. $B^0 \to K^*(892)^0\gamma$ is used in the simultaneous fit to constraint the proper time acceptance. The parameters of the simultaneous fit will be: a, n and t_0 which are common to both signal and control channels, $\delta\Gamma_{B^0 \to K^*(892)^0\gamma}$, $\Delta\delta\Gamma = \delta\Gamma_{B_s^0 \to \phi\gamma} - \delta\Gamma_{B^0 \to K^*(892)^0\gamma}$ and A_Δ. An external constraint on the value of $\Delta\delta\Gamma$ is extracted from simulation and injected in the fit to data. The lifetime of the B^0 and B_s^0 mesons and $\Delta\Gamma_s$ are constrained to the latest world averages [96].

  It is important to mention that another approach to measure A_Δ from $B_s^0 \to \phi\gamma$ data events using $B^0 \to K^*(892)^0\gamma$ to control the acceptance is under study by our collaborators in Valencia. This approach consists of fitting the ratio of the proper time distributions of $B_s^0 \to \phi\gamma$ and $B^0 \to K^*(892)^0\gamma$ assuming that both decays exhibit the same proper time acceptance. This alternative approach benefits from the cancellation at first order of several systematic effects in particular the uncertainties induced by the final state reconstruction and selection. Having both approaches based on different techniques, and thus exhibiting different sensitivities to systematics uncertainties, provides a worthwhile validation for the measurement robustness.

- **Strategy B**: $B_s^0 \to \phi\gamma$ + $B^0 \to J/\psi K^*(892)^0$. This strategy uses $B^0 \to J/\psi K^*(892)^0$ as a control sample. Performing the kinematical matching of $B^0 \to J/\psi K^*(892)^0$ to $B^0 \to K^*(892)^0\gamma$ the acceptance at low proper time of both channels becomes consistent. Given that the whole acceptance of $B^0 \to K^*(892)^0\gamma$ and $B_s^0 \to \phi\gamma$ are

consistent, the acceptance at low proper time of $B_s^0 \to \phi\gamma$ and $B^0 \to J/\psi K^*(892)^0$ are also consistent. The difference between the acceptance at high proper time, $\Delta\delta\Gamma = \delta\Gamma_{B_s^0\to\phi\gamma} - \delta\Gamma_{B^0\to J/\psi K^*(892)^0}$, is obtained from the study on simulated events. If the differences in the proper time acceptance between the simulation and data are well understood, the difference $\Delta\delta\Gamma$ from simulation is applied in the data fit as an external constraint in the simultaneous fit. The parameters of the simultaneous fit will be: a, n and t_0 which are common to both channels, $\delta\Gamma_{B^0\to J/\psi K^*(892)^0}$, $\Delta\delta\Gamma = \delta\Gamma_{B_s^0\to\phi\gamma} - \delta\Gamma_{B^0\to J/\psi K^*(892)^0}$ and A_Δ. An external constraint on the value of $\Delta\delta\Gamma$ is extracted from simulation and injected in the fit to data. The lifetime of the B^0 and B_s^0 mesons and $\Delta\Gamma_s$ are constrained to the latest world averages [96].

- **Strategy C**: $B_s^0 \to \phi\gamma$ + $B^0 \to K^*(892)^0\gamma$ + $B^0 \to J/\psi K^*(892)^0$. This strategy uses both $B^0 \to K^*(892)^0\gamma$ and $B^0 \to J/\psi K^*(892)^0$ as control samples. It takes into account the fact that the radiative decays have consistent acceptances both at low and high proper times. The acceptance at low proper time is consistent for the three channels. For strategy C, two options are possible.

  - $B^0 \to J/\psi K^*(892)^0$ is used only to constraint the acceptance at low proper time and $B^0 \to K^*(892)^0\gamma$ is used to constrain the acceptance of $B_s^0 \to \phi\gamma$. The parameters of the simultaneous fit will be: a, n, t_0 which are common to the three channels, $\delta\Gamma_{B^0\to K^*(892)^0\gamma}$, $\delta\Gamma_{B^0\to J/\psi K^*(892)^0}$, $\Delta\delta\Gamma = \delta\Gamma_{B_s^0\to\phi\gamma} - \delta\Gamma_{B^0\to K^*(892)^0\gamma}$ and A_Δ. An external constraint on the value of $\Delta\delta\Gamma$ is extracted from simulation and injected in the fit to data. The lifetime of the B^0 and B_s^0 mesons and $\Delta\Gamma_s$ are constrained to the latest world averages [96].
  - Both $B^0 \to K^*(892)^0\gamma$ and $B^0 \to J/\psi K^*(892)^0$ can be used to constrain the acceptance at low proper time and the acceptance at high proper time with a constraint on the difference $\Delta\delta\Gamma = \delta\Gamma_{B_s^0\to\phi\gamma} - \delta\Gamma_{B^0\to K^*(892)^0\gamma}$ and $\Delta\delta\Gamma = \delta\Gamma_{B^0\to K^*(892)^0\gamma} - \delta\Gamma_{B^0\to J/\psi K^*(892)^0}$ that are extracted from simulation. The parameters of the simultaneous fit will be: a, n, t_0 which are common to the three channels, $\delta\Gamma_{B^0\to J/\psi K^*(892)^0}$, $\Delta\delta\Gamma = \delta\Gamma_{B_s^0\to\phi\gamma} - \delta\Gamma_{B^0\to K^*(892)^0\gamma}$, $\Delta\delta\Gamma = \delta\Gamma_{B^0\to K^*(892)^0\gamma} - \delta\Gamma_{B^0\to J/\psi K^*(892)^0}$ and A_Δ. An external constraint on the values of both $\Delta\delta\Gamma$ is extracted from simulation and injected in the fit to data. The lifetime of the B^0 and B_s^0 mesons and $\Delta\Gamma_s$ are constrained to the latest world averages [96].

The choice between the strategies to measure A_Δ will be decided after all the systematics are evaluated. If one control sample happens to have much smaller systematic uncertainties than the other it will in fact be better to only use this control sample. The strategies are discussed in details in chapter 5.

Chapter 5

Preliminary results

Contents

The control of the proper time acceptance is the major difficulty in the precise determination of the photon polarization. It has been intensively discussed in chapter 4. The events selection has been specially designed to keep consistent the proper time acceptance between $B^0 \to K^*(892)^0\gamma$ and $B_s^0 \to \phi\gamma$. To control the $B^0 \to K^*(892)^0\gamma$ acceptance with the $B^0 \to J/\psi K^*(892)^0$ mode, a dedicated weighing and scaling procedure has been setup and is discussed in 4.4.1. $B^0 \to K^*(892)^0\gamma$ and $B^0 \to J/\psi K^*(892)^0$ are henceforth two possible control samples for the proper time acceptance in $B_s^0 \to \phi\gamma$. This chapter introduces the preliminary results for the extraction of A_Δ. First, the fit strategies with the different control samples are discussed in section 5.1. A validation of the fitting procedure is done by measuring the B^0 lifetime from $B^0 \to K^*(892)^0\gamma$ signal events using $B^0 \to J/\psi K^*(892)^0$ as a control sample, this is reported in section 5.2. Section 5.3 shows the preliminary fits for the different strategies presented along with the preliminary results obtained for A_Δ. The central value of A_Δ is not shown waiting for the analysis to be finalized and only the measured statistical uncertainty is discussed. Section 5.4 addresses the systematic uncertainties and section 5.5 gives the concluding remarks.

5.1 Fit strategies

As discussed in 4.4.5, three strategies can be set up to extract A_Δ:

- Strategy A: $B^0 \to K^*(892)^0\gamma$ is used as a control sample.
- Strategy B: $B^0 \to J/\psi K^*(892)^0$ is used as a control sample.
- Strategy C: $B^0 \to K^*(892)^0\gamma$ and $B^0 \to J/\psi K^*(892)^0$ are both used as control samples.
  - C1: $B^0 \to J/\psi K^*(892)^0$ is used to constrain the acceptance at low proper time.
  - C2: $B^0 \to J/\psi K^*(892)^0$ is used to constrain both the acceptance at low and high proper time. For the difference in the acceptance at high proper time, external constraints extracted from simulation are used in the data fits. This approach requires that possible differences in the acceptance between simulation and data are understood and well under control.

For $B_s^0 \to \phi\gamma$ and $B^0 \to K^*(892)^0\gamma$, the background contamination is statistically subtracted using the reconstructed $B_{(s)}$ mass as a separation variable, as presented in chapter 4.2.3. The background-subtracted distribution are used as input of the proper time fit. Figure 5.1 displays a zoom on the low proper time region of the background-subtracted distribution of the proper time for $B^0 \to K^*(892)^0\gamma$. Below $t < 0.3$ ps, the background-subtracted yield is consistent with zero, with a slightly negative weighing. This low proper time region, weakly populated and mostly dominated by backgrounds, is excluded from the proper time fit for all the considered channels.

For $B^0 \to J/\psi K^*(892)^0$, only events in the reconstructed B^0 mass range between 5240 and 5320 MeV/c^2 are considered. As shown in figure 4.2, this region is background free to a very good approximation.

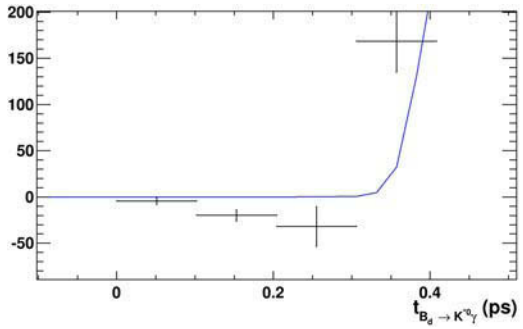

Figure 5.1: A zoom at low proper time of the proper time distribution of $B^0 \to K^*(892)^0\gamma$.

The background-subtracted signal yields are reported in table 5.1. The sensitivity to A_Δ scales as the ratio $R = N_S/N_C$ between the signal yield (N_S) and the yields of the control sample(s) (N_C): $\Delta R/R = \sqrt{1/N_S + 1/N_C}$. The relative sensitivities for the three possible strategies, with respect to what a control sample with infinite statistics would give, are reported in table 5.2. They are relatively close given that each of the two control samples have a much larger statistics than the signal sample.

In the baseline fit method used, the low proper time parameters (a, n and t_0) are common for all the channels in the simultaneous fits. On the other hand, each channel has its own high proper time acceptance parameter. The parametrization used for strategies A, B and C are reported in table 5.3. For the parametrization of acceptance at high proper time, the parameter $\delta\Gamma$ of one control sample is taken as reference and

$B_s^0 \to \phi\gamma B$	$^0 \to K^*(892)^0\gamma$	$B^0 \to J/\psi K^*(892)^0$
$3.5\ 10^3$	$24\ 10^3$	$30\ 10^3$

Table 5.1: Selected signal yields for t>0.3 ps. Background subtraction is applied for the radiative modes.

$N_C \to \infty$	A	B	C
1	1.071	1.058	1.032

Table 5.2: Relative sensitivities on A_Δ from the different strategies for the control sample(s).

the difference, $\Delta\delta\Gamma = \delta\Gamma_{\rm x} - \delta\Gamma_{\rm Ref}$, is (are) used for the other sample(s). For each strategy, the simultaneous fit is first performed on simulated events to extract the $\Delta\delta\Gamma$ parameter(s). The $\Delta\delta\Gamma$ obtained from the simulation is (are) then used as an external gaussian constraint(s) of the simultaneous fit on data. The constraint

$$\Delta\delta\Gamma_2 = \delta\Gamma_{B_s^0\to\phi\gamma} - \delta\Gamma_{B^0\to K^*(892)^0\gamma} = 3.0 \pm 2.9 \text{ ns}^{-1}$$

is used in strategies A, C1 and C2, the constraint

$$\Delta\delta\Gamma_3 = \delta\Gamma_{B_s^0\to\phi\gamma} - \delta\Gamma_{B^0\to J/\psi K^*(892)^0} = 36.0 \pm 2.9 \text{ ns}^{-1}$$

is used in strategy B and the constraint

$$\Delta\delta\Gamma_1 = \Delta\delta\Gamma_3 - \Delta\delta\Gamma_2 = \delta\Gamma_{B^0\to K^*(892)^0\gamma} - \delta\Gamma_{B^0\to J/\psi K^*(892)^0} = 32.8 \pm 3.0 \text{ ns}^{-1}$$

is used, along with $\Delta\delta\Gamma_2$ in strategy C2. In strategy C2, the correlation between $\Delta\delta\Gamma_1$ and $\Delta\delta\Gamma_2$ values is taken into account using the covariance matrix from the fit on the simulated samples.

The above parametrization of the simultaneous fit considers the parameters a, n and t_0, that models the acceptance at low proper time, as being common to both the $B_s^0 \to \phi\gamma$ signal and the control(s) channel(s). This is supported by the analysis of simulated data presented in 4.4.2. In order to evaluate the impact of this strong constraint on the measurement, an alternative parametrization of the simultaneous fits has been defined. As in the baseline approach, the a and n parameters of the acceptance at low proper time are common for all the samples considered in the simultaneous fit, while the t_0 parameter

is allowed to be different for each channel. The parametrization used in this case for strategies A, B and C are reported in table 5.4. As for the $\delta\Gamma$ parameters, one control sample is taken as reference for t_0 and the difference in t_0, $\Delta t_0 = t_{0\mathrm{X}} - t_{0\mathrm{Ref}}$, is (are) used for the other sample(s). For each strategy, the simultaneous fit is first performed on the simulation to extract the $\Delta\delta\Gamma$ and Δt_0 parameters. The $\Delta\delta\Gamma$ and Δt_0 obtained from the simulation are then used as external gaussian constraints of the simultaneous fit on data. The correlation between the constraints are taken into account using the covariance matrix from the simulation fits.

The values of the external physical parameters, τ_{B^0}, $\tau_{B^0_s}$ and $\Delta\Gamma_s$, used in the data fits are reported in table 5.5. The central value is fixed in the data fit and the associated systematic with this assumption is discussed in 5.4.

A	B	C1	C2
A_Δ	A_Δ	A_Δ	A_Δ
a	a	a	a
n	n	n	n
t_0	t_0	t_0	t_0
$\delta\Gamma_{K^*\gamma}$	$\delta\Gamma_{J/\psi K^*}$	$\delta\Gamma_{J/\psi K^*}$	$\delta\Gamma_{J/\psi K^*}$
$\Delta\delta\Gamma_2$	$\Delta\delta\Gamma_3$	$\delta\Gamma_{K^*\gamma}$ $\Delta\delta\Gamma_2$	$\Delta\delta\Gamma_1$ $\Delta\delta\Gamma_2$

Table 5.3: Fit parameters for the strategies A, B, C1 and C2 using the baseline fit option. The external gaussian constraint taken from the simulation are defined as: $\Delta\delta\Gamma_1 = \delta\Gamma_{K^*\gamma} - \delta\Gamma_{J/\psi K^*}$, $\Delta\delta\Gamma_2 = \delta\Gamma_{\phi\gamma} - \delta\Gamma_{K^*\gamma}$ and $\Delta\delta\Gamma_3 = \delta\Gamma_{\phi\gamma} - \delta\Gamma_{J/\psi K^*}$.

5.2 Extracting τ_{B^0} with $B^0 \to K^*(892)^0\gamma$ events

To validate the simultaneous fit procedure to control the acceptance, the B^0 lifetime is fitted using $B^0 \to K^*(892)^0\gamma$ as signal sample and $B^0 \to J/\psi K^*(892)^0$ as control sample constraining $\tau_{B^0}(B^0 \to J/\psi K^*(892)^0)$ to the world average value.
A simultaneous fit of $B^0 \to K^*(892)^0\gamma$ and $B^0 \to J/\psi K^*(892)^0$ is first performed on simulated events fixing the B^0 lifetime for both channels to the value used in the event simulation. From the fit on simulated samples, the difference, $\Delta\delta\Gamma_1$, in the acceptance at high proper time between $B^0 \to K^*(892)^0\gamma$ and $B^0 \to J/\psi K^*(892)^0$ is extracted. This difference is then injected as an external gaussian constraint in the simultaneous fit to

A	B	C1	C2
A_Δ	A_Δ	A_Δ	A_Δ
a	a	a	a
n	n	n	n
$t_{0K^*\gamma}$	$t_{0J/\psi K^*}$	$t_{0J/\psi K^*}$	$t_{0J/\psi K^*}$
$\delta\Gamma_{K^*\gamma}$	$\delta\Gamma_{J/\psi K^*}$	$\delta\Gamma_{J/\psi K^*}$	$\delta\Gamma_{J/\psi K^*}$
$\Delta\delta\Gamma_2$	$\Delta\delta\Gamma_3$	$\delta\Gamma_{K^*\gamma}$ $\Delta\delta\Gamma_2$	$\Delta\delta\Gamma_1$ $\Delta\delta\Gamma_2$
Δt_{02}	Δt_{03}	Δt_{01} Δt_{02}	Δt_{01} Δt_{02}

Table 5.4: Fit parameters for the strategies A , B, C1 and C2 using the Alternative fit parametrization. The external gaussian constraint taken from the simulation are defined as: $\Delta\delta\Gamma_1 = \delta\Gamma_{K^*\gamma} - \delta\Gamma_{J/\psi K^*}$, $\Delta\delta\Gamma_2 = \delta\Gamma_{\phi\gamma} - \delta\Gamma_{K^*\gamma}$ and $\Delta\delta\Gamma_3 = \delta\Gamma_{\phi\gamma} - \delta\Gamma_{J/\psi K^*}$. $\Delta t_{02} = t_{0K^*\gamma} - t_{0J/\psi K^*}$, $\Delta t_{02} = t_{0\phi\gamma}$ - $t_{0K^*\gamma}$ and $\Delta t_{02} = t_{0\phi\gamma} - t_{0J/\psi K^*}$.

	Data
τ_{B^0} ps	1.520 ± 0.004
$\tau_{B_s^0}$ ps	1.509 ± 0.004
$\Delta\Gamma_s$ ns^{-1}	81 ± 6
$\rho(\tau_{B_s^0}, \Delta\Gamma_s)$	0.271

Table 5.5: The values of the external physical parameters from the latest HFAG compilation [96]. The correlation between $\tau_{B_s^0}$ and $\Delta\Gamma_s$, $\rho(\tau_{B_s^0}, \Delta\Gamma_s)$, is also reported.

data where the B_0 lifetime parameter $\tau_{B^0}(B^0 \to K^*(892)^0\gamma)$ for the $B^0 \to K^*(892)^0\gamma$ channel is no longer constrained
The fits using the baseline option and the alternative option are presented in figures 5.2 and 5.3 respectively. The corresponding fitted parameters are reported in table 5.6 for the baseline fit option and in table 5.7 for the alternative fit parametrization.

The parameter $\tau_{B^0}(B^0 \to K^*(892)^0\gamma)$ extracted in the two fit models, 1.510 ± 0.015 ps and 1.511 ± 0.014 ps, are very close to each other and compatible with the world average value [96].

This result validates the assumption on the common acceptance at low proper time assumed in the baseline fitting option. As already discussed in 4.4.4, the acceptance at high proper time modeled with the parameter $\delta\Gamma_{J/\psi K^*}$ is significantly different between data and simulation. However, the simulation/data difference for $B^0 \to J/\psi K^*(892)^0$ is con-

sistent with the one for the radiative channels so that the $\Delta\delta\Gamma_1$ extracted from simulation well reproduce the data behavior and does not bias the measured $\tau_{B^0}(B^0 \to K^*(892)^0\gamma)$ lifetime on $B^0 \to K^*(892)^0\gamma$ signal data events. The origin of the simulation/data difference is however to be understood to asses the solidity of the procedure.

Acceptance	simulation	data
$\delta\Gamma_{J/\psi K^*}$ ns^{-1}	19.4 ± 3.8	59.9 ± 6.9
$\Delta\delta\Gamma_1$ ns^{-1}	33.1 ± 2.9	33.1 ± 2.9
τ_{B^0} ps	fixed to the value used in event simulation	1.510± 0.015
a ps^{-1}	1.940 ± 0.034	1.990 ± 0.071
n	1.98 ± 0.11	1.542 ± 0.087
t_0 ps	0.227 ± 0.014	0.279 ± 0.009

Table 5.6: Parameters obtained from a simultaneous fit of $B^0 \to K^*(892)^0\gamma$ and $B^0 \to J/\psi K^*(892)^0$. The first column reports the result of the simultaneous fit performed on simulation where the physical parameter, τ_{B^0}, is fixed to the value used in the event simulation for both $B^0 \to K^*(892)^0\gamma$ and $B^0 \to J/\psi K^*(892)^0$ channels. The second column reports the result of the simultaneous fit on the data where $\Delta\delta\Gamma_1$ from simulation is propagated as a gaussian constraint to the fit and τ_{B^0} is allowed to vary for the $B^0 \to K^*(892)^0\gamma$ channel. Baseline fit option is used.

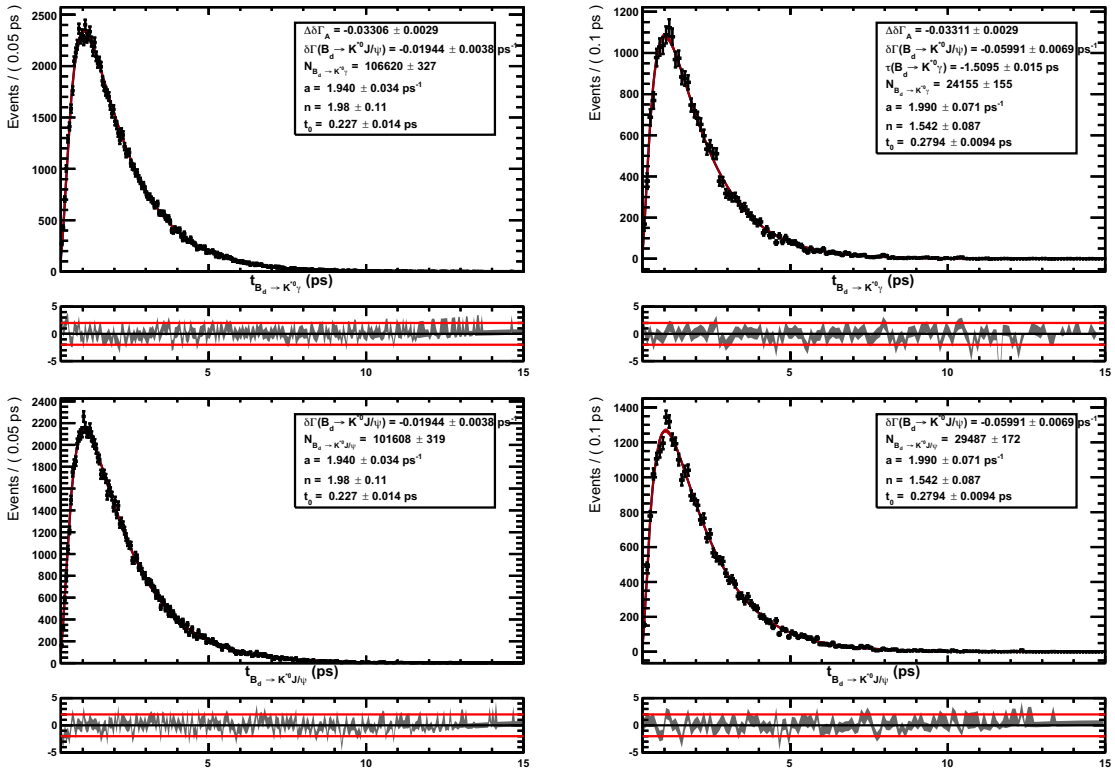

Figure 5.2: Results of the simultaneous fit of $B^0 \to K^*(892)^0\gamma$ (top) and $B^0 \to J/\psi K^*(892)^0$ (bottom) proper time, for both simulation (left) and data (right). Baseline fit option is used.

Acceptance		simulation	data
$\delta\Gamma_{J/\psi K^*}$ ns^{-1}		23.5 ± 2.0	62.8 ± 6.8
$\Delta\delta\Gamma_1$ ns^{-1}		24.8 ± 2.3	25.9 ± 2.3
τ_{B^0} ps	fixed to the value used in event simulation		1.511± 0.014
a ps^{-1}		1.941 ± 0.063	1.988 ± 0.070
n		1.977 ± 0.063	1.561 ± 0.088
$t_{0J/\psi K^*}$ ps		0.237 ± 0.007	0.284 ± 0.009
Δt_{01} ps		-0.0195 ± 0.0019	-0.0170 ± 0.0018

Table 5.7: Parameters obtained from a simultaneous fit of $B^0 \to K^*(892)^0\gamma$ and $B^0 \to J/\psi K^*(892)^0$. The first column reports the result of the simultaneous fit performed on simulation where the physical parameter, τ_{B^0}, is fixed to the value used in the event simulation for both $B^0 \to K^*(892)^0\gamma$ and $B^0 \to J/\psi K^*(892)^0$ channels. The second column reports the result of the simultaneous fit on the data where $\Delta\delta\Gamma_1$ and Δt_{01} from simulation are propagated as gaussian constraints to the fit taking into account the full covariance matrix from the simulation fit and τ_{B^0} is allowed to vary for the $B^0 \to K^*(892)^0\gamma$ channel. Alternative fit parametrization is used.

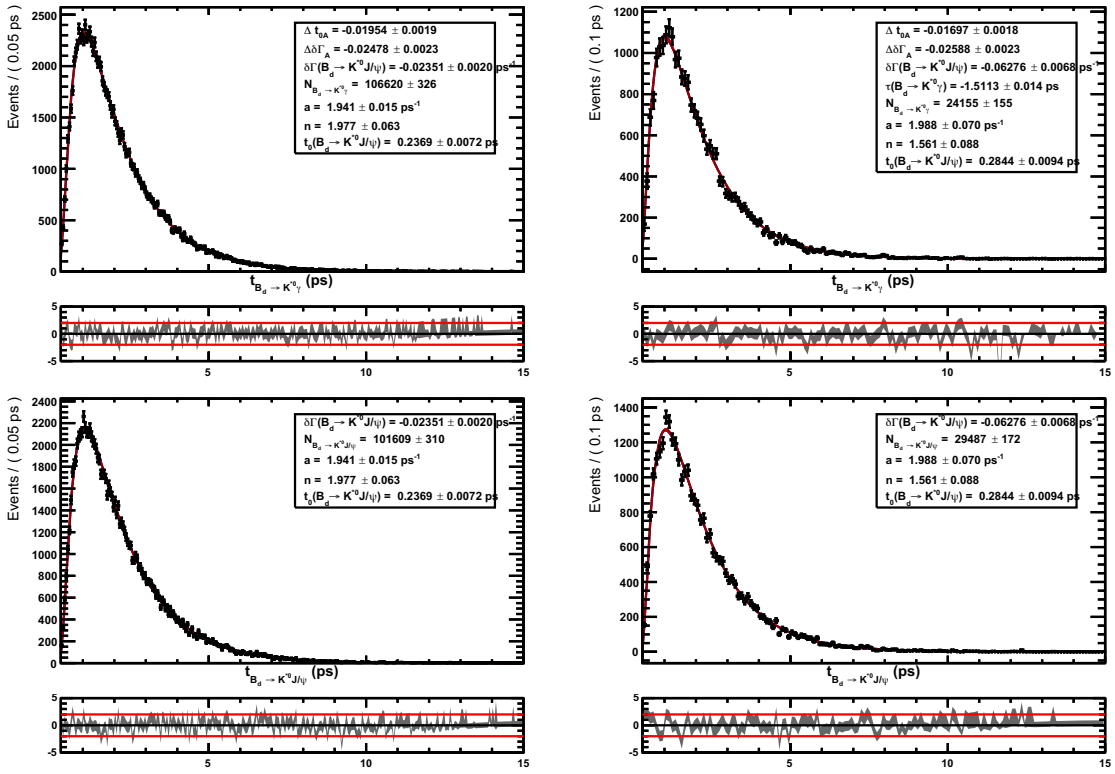

Figure 5.3: Results of the simultaneous fit of $B^0 \to K^*(892)^0\gamma$ (top) and $B^0 \to J/\psi K^*(892)^0$ (bottom) proper time, for both simulation (left) and data (right). Alternative fit parametrization is used.

5.3 Sensitivity on A_Δ

Waiting for the finalization of the analysis strategy and systematic uncertainty study, the extraction of the A_Δ parameter from the fit on $B_s^0 \to \phi\gamma$ data is performed in a "blind" way in order not to introduce any "experimentalist-induced" bias in the analysis. This is achieved by adding a random offset, defined from a uniform distribution between -2 and 2, to the A_Δ central value returned by the fit minimization. The fitted quantity is denoted as A_Δ^{blind}. The statistical resolution on A_Δ^{blind}, which is not affected by the blinding procedure, is discussed in this section.

5.3.1 Strategy A

This strategy is based on $B^0 \to K^*(892)^0\gamma$ as a control sample. A simultaneous fit of $B_s^0 \to \phi\gamma$ and $B^0 \to K^*(892)^0\gamma$ is first performed on simulation, where A_Δ is fixed to zero, to extract the difference, $\Delta\delta\Gamma_2$, between the two channels. This difference is injected in the data fit as an external gaussian constraint. This difference is compatible with zero for the radiative decays, $\Delta\delta\Gamma_2 = 3.0 \pm 2.9$ ns^{-1}.
Figure 5.4 displays the fit results for the baseline fitting option for both simulation and data. The fit parameters, for both simulation and data, are reported in table 5.8. Table 5.9 reports the results of the simultaneous fits on simulation and data considering the alternative fitting option.

The statistical resolution on the measured A_Δ is 0.38. The measured resolution on data is consistent with the statistical resolution expected from a toy procedure approach as discussed in section 5.4.
The baseline fit and the alternative fit give compatible results for the measured A_Δ. Moreover, there is a general data/simulation agreement for all the parameters except for the acceptance at high proper time, $\delta\Gamma_{K^*\gamma}$ as already mentioned.

Acceptance	simulation	data
$\delta\Gamma_{K^*\gamma}$ ns^{-1}	43.5 ± 8.4	98.1 ± 9.4
$\Delta\delta\Gamma_2$ ns^{-1}	3.0 ± 2.9	3.2 ± 2.9
a ps^{-1}	1.94 ± 0.12	1.93 ± 0.08
n	2.09 ± 0.38	1.72 ± 0.17
t_0 ps	0.203 ± 0.050	0.259 ± 0.020
A_Δ^{blind}	fixed to 0	0.57 ± 0.38

Table 5.8: Parameters obtained from a simultaneous fit of $B^0 \to K^*(892)^0\gamma$ and $B_s^0 \to \phi\gamma$ (strategy A). The first column reports the result of the simultaneous fit performed on simulation where the physical parameters, τ_{B^0}, τ_{B_s} and $\Delta\Gamma_s$, are fixed to the value used in the event simulation. The second column reports the result of the simultaneous fit on the data where the physical parameters are fixed to the latest world averages. $\Delta\delta\Gamma_2$ obtained from the fit to simulated data is propagated as a gaussian constraint to the data fit. Baseline fit option is used.

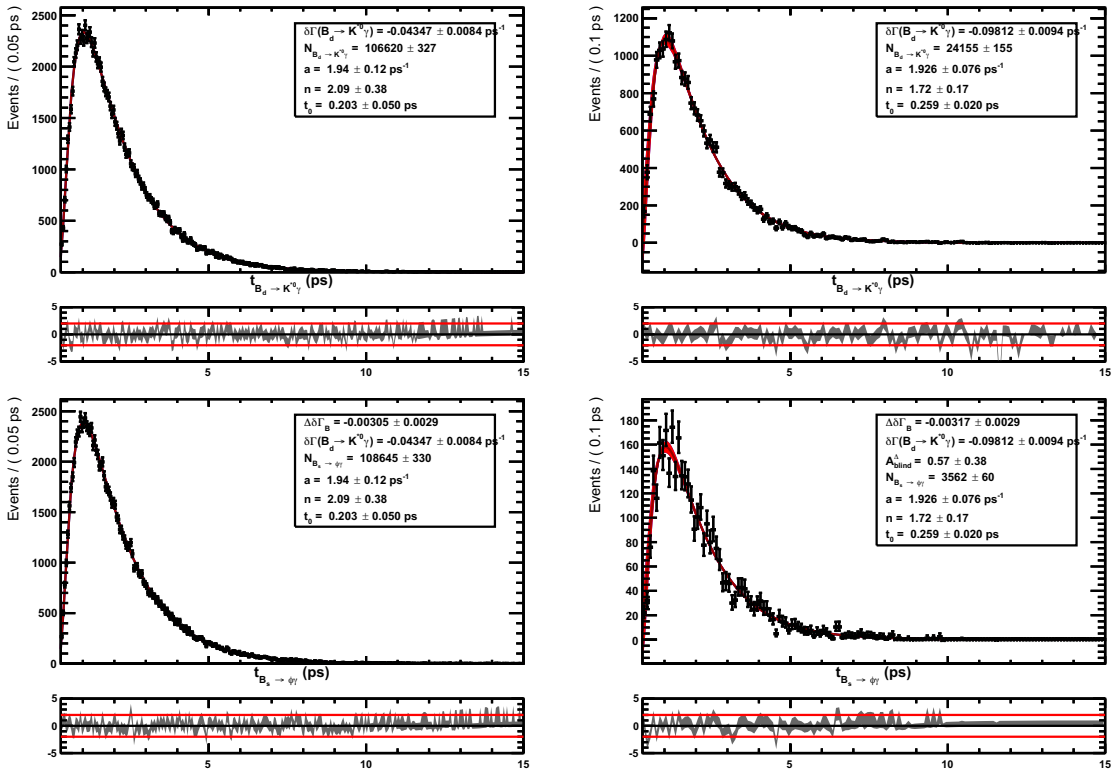

Figure 5.4: Results of the simultaneous fit of $B^0 \to K^*(892)^0\gamma$ (top) and $B_s^0 \to \phi\gamma$ (bottom) proper time (strategy A), for both simulation (left) and data (right). Baseline fit option is used.

Acceptance	simulation	data
$\delta\Gamma_{K^*\gamma}$ ns^{-1}	44.5 ± 9.9	98.3 ± 9.4
$\Delta\delta\Gamma_2$ ns^{-1}	0.9 ± 3.4	0.6 ± 3.4
a ps^{-1}	1.94 ± 0.14	1.93 ± 0.08
n	2.09 ± 0.43	1.72 ± 0.17
$t_{0K^*\gamma}$ ps	0.206 ± 0.012	0.259 ± 0.020
Δt_{02} ps	-0.0051 ± 0.0037	-0.0020 ± 0.0036
A_Δ^{blind}	0 in simulation	0.61 ± 0.37

Table 5.9: Parameters obtained from a simultaneous fit of $B^0 \to K^*(892)^0\gamma$ and $B_s^0 \to \phi\gamma$ (strategy A). The first column reports the result of the simultaneous fit performed on simulation where the physical parameters, τ_{B^0}, τ_{B_s} and $\Delta\Gamma_s$, are fixed to the value used in the event simulation. The second column reports the result of the simultaneous fit on the data where the physical parameters are fixed to the latest world averages. $\Delta\delta\Gamma_2$ and Δt_{02} obtained from the fit to simulated data are propagated as gaussian constraints to the data fit taking into account the full covariance matrix from the simulation fit. Alternative fit parametrization is used.

5.3.2 Strategy B

This strategy uses $B^0 \to J/\psi K^*(892)^0$ as a control sample. A simultaneous fit of $B_s^0 \to \phi\gamma$ and $B^0 \to J/\psi K^*(892)^0$ is first performed on simulation, where A_Δ is fixed to zero, to extract the difference, $\Delta\delta\Gamma_3$, between the two channels. This difference is injected in the data fit as an external constraint. From 5.2, it has been concluded that the difference in the acceptance at high proper time between the radiative channels and $B^0 \to J/\psi K^*(892)^0$ is compatible between data and simulation.
Figure 5.5 displays the fit results for the baseline fitting option for both simulation and data. The fit parameters, for both simulation and data, are reported in table 5.10. Table 5.11 reports the results of the simultaneous fits on simulation and data considering the alternative fitting option.

The statistical resolution on the measured A_Δ is compatible with what is expected from studies on toy data sets (see section 5.4). Moreover, it is also consistent with the statistical resolution obtained from strategy A with a slight improvement. This slight improvement is due to the fact that $B^0 \to J/\psi K^*(892)^0$ sample has almost 1.5 statistics on data than $B^0 \to K^*(892)^0\gamma$ sample. Same conclusion as for strategy A can be drawn concerning the data/simulation agreement for a, n and t_0 parameters. This implies that the acceptance at low proper time of $B_s^0 \to \phi\gamma$ is well reproduced by both control channels, $B^0 \to K^*(892)^0\gamma$ and $B^0 \to J/\psi K^*(892)^0$ data.

Acceptance	simulation	data
$\delta\Gamma_{J/\psi K^*}$ ns^{-1}	17.8 ± 3.8	60.2 ± 8.0
$\Delta\delta\Gamma_3$ ns^{-1}	36.0 ± 2.9	36.1 ± 2.9
a ps^{-1}	1.950 ± 0.035	2.011 ± 0.094
n	1.97 ± 0.11	1.53 ± 0.10
t_0 ps	0.225 ± 0.014	0.284 ± 0.011
A_Δ^{blind}	fixed to 0	0.71 ± 0.36

Table 5.10: Parameters obtained from a simultaneous fit of $B^0 \to J/\psi K^*(892)^0$ and $B_s^0 \to \phi\gamma$ (strategy B). The first column reports the result of the simultaneous fit performed on simulation where the physical parameters, τ_{B^0}, τ_{B_s} and $\Delta\Gamma_s$, are fixed to the value used in the event simulation. The second column reports the result of the simultaneous fit on the data where the physical parameters are fixed to the latest world averages. $\Delta\delta\Gamma_3$ obtained from the fit to simulated data is propagated as a gaussian constraint to the data fit. Baseline fit option is used.

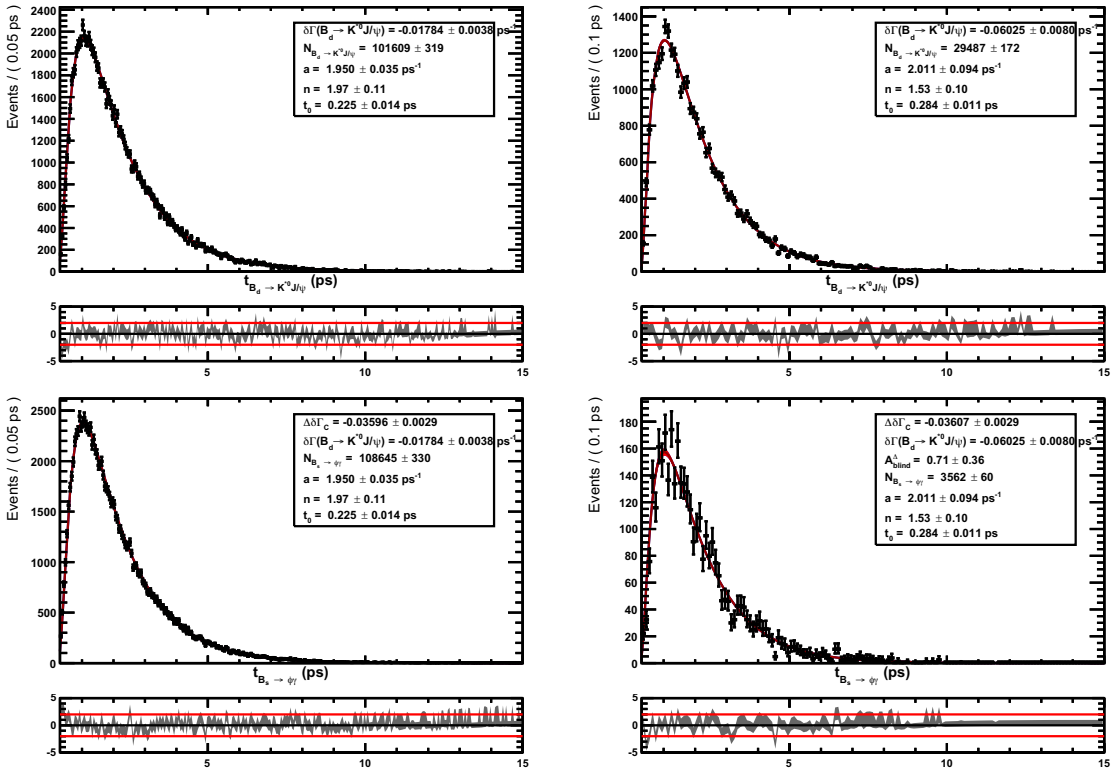

Figure 5.5: Results of the simultaneous fit of $B^0 \to J/\psi K^*(892)^0$ (top) and $B_s^0 \to \phi\gamma$ (bottom) proper time (strategy B), for both simulation (left) and data (right). Baseline fit option is used.

Acceptance	simulation	data
$\delta\Gamma_{J/\psi K^*}$ ns^{-1}	22.9 ± 3.7	61.3 ± 8.0
$\Delta\delta\Gamma_3$ ns^{-1}	25.7 ± 3.2	27.3 ± 3.2
a ps^{-1}	1.954 ± 0.033	2.00 ± 0.09
n	1.98 ± 0.10	1.53 ± 0.10
$t_{0J/\psi K^*}$ ps	0.238 ± 0.013	0.285 ± 0.010
Δt_{02} ps	-0.0244 ± 0.0031	-0.0273 ± 0.0032
A_Δ^{blind}	fixed to 0	0.67 ± 0.36

Table 5.11: Parameters obtained from a simultaneous fit of $B^0 \to J/\psi K^*(892)^0$ and $B_s^0 \to \phi\gamma$ (strategy B). The first column reports the result of the simultaneous fit performed on simulation where the physical parameters, τ_{B^0}, τ_{B_s} and $\Delta\Gamma_s$, are fixed to the value used in the event simulation. The second column reports the result of the simultaneous fit on the data where the physical parameters are fixed to the latest world averages. $\Delta\delta\Gamma_3$ and Δt_{02} obtained from the fit to simulated data are propagated as gaussian constraints to the data fit taking into account the full covariance matrix from the simulation fit. Alternative fit parametrization is used.

5.3.3 Strategy C1

This strategy uses both $B^0 \to K^*(892)^0\gamma$ and $B^0 \to J/\psi K^*(892)^0$ as a control samples. The sample $B^0 \to J/\psi K^*(892)^0$ is used to constraint the acceptance at low proper time. A simultaneous fit of $B_s^0 \to \phi\gamma$, $B^0 \to K^*(892)^0\gamma$ and $B^0 \to J/\psi K^*(892)^0$ is first performed on simulation, where A_Δ is fixed to zero, to extract the difference, $\Delta\delta\Gamma_2$, between the radiative channels. This difference is injected in the data fit as an external constraint.
Figure 5.6 displays the fit results for the baseline fitting option for both simulation and data. The fit parameters, for both simulation and data, are reported in table 5.12. Table 5.13 reports the results of the simultaneous fits on simulation and data considering the alternative fitting option.

The statistical resolution on the measured A_Δ is compatible with what is obtained from strategies A and B. As concluded separately from strategies A and B, the acceptance at low proper time, a, n and t_0, are consistent between the 3 channels. This is also validated with both the baseline and the Alternative fit parametrization.

As indicated, with this strategy, both the control samples $B^0 \to K^*(892)^0\gamma$ and $B^0 \to J/\psi K^*(892)^0$ are simultaneously used to constrain the acceptance at low proper time of $B_s^0 \to \phi\gamma$. This improves the statistical resolution of the parameters a, n and t_0 and has an indirect effect on the acceptance at high proper time via correlations between the acceptance parameters. This effect is marginal in the fit and adds no sizable statistical resolution improvement on the measured A_Δ. The only constraint that is applied on the acceptance at high proper time comes from $B^0 \to K^*(892)^0\gamma$ and hence the result obtained for A_Δ is similar to what is obtained from strategy A where $B^0 \to K^*(892)^0\gamma$ is used as a control sample.
However, $B^0 \to J/\psi K^*(892)^0$ can also add an extra constraint on the acceptance at high proper time similarly to what is done in strategy B. This strategy is discussed in the next section.

Acceptance	simulation	data
$\delta\Gamma_{J/\psi K^*}$ ns^{-1}	16.0 ± 3.5	60.1 ± 6.7
$\delta\Gamma_{K^*\gamma}$ ns^{-1}	48.9 ± 3.6	98.1 ± 7.2
$\Delta\delta\Gamma_2$ ns^{-1}	3.0 ± 2.9	3.1 ± 2.9
a ps^{-1}	1.943 ± 0.034	1.983 ± 0.065
n	2.01 ± 0.11	1.575 ± 0.087
t_0 ps	0.219 ± 0.014	0.277 ± 0.010
A_Δ^{blind}	fixed to 0	0.57 ± 0.36

Table 5.12: Parameters obtained from a simultaneous fit of $B^0 \to K^*(892)^0\gamma$, $B^0 \to J/\psi K^*(892)^0$ and $B_s^0 \to \phi\gamma$ (strategy C1). The first column reports the result of the simultaneous fit performed on simulation where the physical parameters, τ_{B^0}, τ_{B_s} and $\Delta\Gamma_s$, are fixed to the value used in the event simulation. The second column reports the result of the simultaneous fit on the data where the physical parameters are fixed to the latest world averages. $\Delta\delta\Gamma_2$ obtained from the fit to simulated data is propagated as gaussian constraints to the data fit taking into account the full covariance matrix from the simulation fit. Baseline fit option is used.

Acceptance	simulation	data
$\delta\Gamma_{J/\psi K^*}$ ns^{-1}	22.1 ± 3.5	63.0 ± 6.7
$\delta\Gamma_{K^*\gamma}$ ns^{-1}	46.8 ± 3.5	94.5 ± 7.2
$\Delta\delta\Gamma_2$ ns^{-1}	0.9 ± 3.2	0.6 ± 3.2
a ps^{-1}	1.946 ± 0.031	1.978 ± 0.064
n	2.009 ± 0.096	1.588 ± 0.083
$t_{0J/\psi K^*}$ ps	0.234 ± 0.012	0.282 ± 0.009
Δt_{01} ps	-0.0196 ± 0.0032	-0.0137 ± 0.0027
Δt_{02} ps	-0.0050 ± 0.0031	-0.0057 ± 0.0030
A_Δ^{blind}	fixed to 0	0.56 ± 0.37

Table 5.13: Parameters obtained from a simultaneous fit of $B^0 \to K^*(892)^0\gamma$, $B^0 \to J/\psi K^*(892)^0$ and $B_s^0 \to \phi\gamma$ (strategy C1). The first column reports the result of the simultaneous fit performed on simulation where the physical parameters, τ_{B^0}, τ_{B_s} and $\Delta\Gamma_s$, are fixed to the value used in the event simulation. The second column reports the result of the simultaneous fit on the data where the physical parameters are fixed to the latest world averages. $\Delta\delta\Gamma_2$, Δt_{01} and Δt_{02} obtained from the fit to simulated data are propagated as gaussian constraints to the data fit taking into account the full covariance matrix from the simulation fit. Alternative fit parametrization is used.

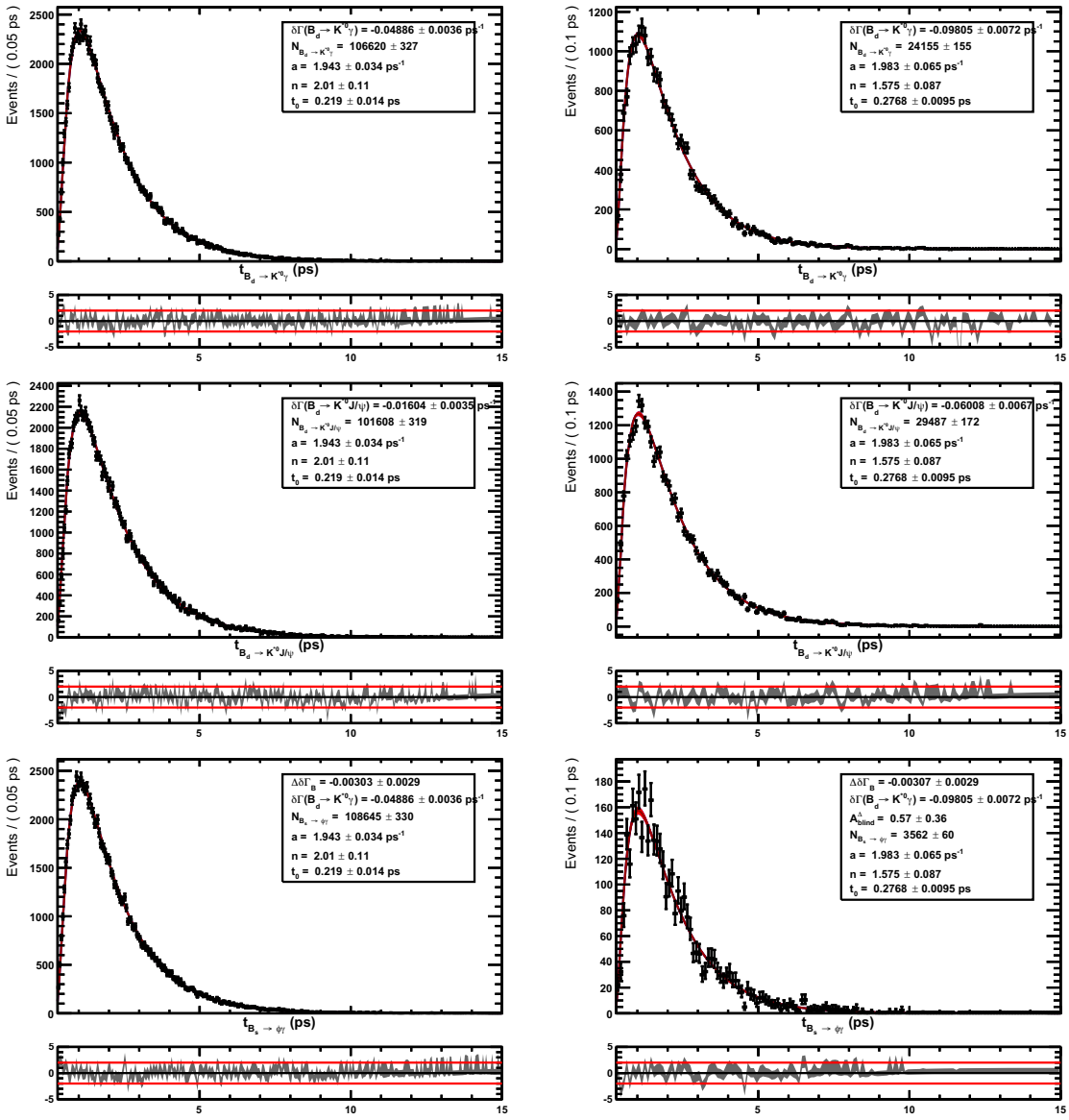

Figure 5.6: Results of the simultaneous fit of $B^0 \to K^*(892)^0\gamma$ (top), $B^0 \to J/\psi K^*(892)^0$ (middle) and $B_s^0 \to \phi\gamma$ (bottom) proper time (strategy C1), for both simulation (left) and data (right). Baseline fit option is used.

5.3.4 Strategy C2

This strategy uses both $B^0 \to K^*(892)^0\gamma$ and $B^0 \to J/\psi K^*(892)^0$ as a control samples. The sample $B^0 \to J/\psi K^*(892)^0$ is used to constraint both the acceptance at low and high proper time. A simultaneous fit of $B_s^0 \to \phi\gamma$, $B^0 \to K^*(892)^0\gamma$ and $B^0 \to J/\psi K^*(892)^0$ is first performed on simulation, where A_Δ is fixed to zero, to extract the difference, $\Delta\delta\Gamma_1$, between $B^0 \to K^*(892)^0\gamma$ and $B^0 \to J/\psi K^*(892)^0$ and the difference, $\Delta\delta\Gamma_2$, between the radiative channels. This difference is injected in the data fit as an external constraint taking into account the correlation between the two constraints.
Figure 5.7 displays the fit results for the baseline fitting option for both simulation and data. The fit parameters, for both simulation and data, are reported in table 5.14. Table 5.15 reports the results of the simultaneous fits on simulation and data considering the alternative fitting option.

This strategy takes into account the maximum number of constraints that can be added from both $B^0 \to K^*(892)^0\gamma$ and $B^0 \to J/\psi K^*(892)^0$ on the acceptance at high proper time of $B_s^0 \to \phi\gamma$. The statistical resolution on the measured A_Δ is slightly improved compared to strategies A, B and C1.

Acceptance	simulation	data
$\delta\Gamma_{J/\psi K^*}$ ns^{-1}	16.0 ± 3.5	61.8 ± 6.3
$\Delta\delta\Gamma_1$ ns^{-1}	32.8 ± 3.0	33.8 ± 2.7
$\Delta\delta\Gamma_2$ ns^{-1}	3.0 ± 2.9	2.6 ± 2.9
a ps^{-1}	1.943 ± 0.034	1.984 ± 0.065
n	2.01 ± 0.11	1.58 ± 0.08
t_0 ps	0.219 ± 0.014	0.277 ± 0.009
A_Δ^{blind}	fixed to 0	0.66 ± 0.35

Table 5.14: Parameters obtained from a simultaneous fit of $B^0 \to K^*(892)^0\gamma$, $B^0 \to J/\psi K^*(892)^0$ and $B_s^0 \to \phi\gamma$ (strategy C2). The first column reports the result of the simultaneous fit performed on simulation where the physical parameters, τ_{B^0}, τ_{B_s} and $\Delta\Gamma_s$, are fixed to the value used in the event simulation. The second column reports the result of the simultaneous fit on the data where the physical parameters are fixed to the latest world averages. $\Delta\delta\Gamma_1$ and $\Delta\delta\Gamma_2$ obtained from the fit to simulated data are propagated as gaussian constraints to the data fit taking into account the full covariance matrix from the simulation fit. Baseline fit option is used.

Acceptance	simulation	data
$\delta\Gamma_{J/\psi K^*}$ ns^{-1}	22.1 ± 3.5	64.4 ± 6.3
$\Delta\delta\Gamma_1$ ns^{-1}	24.7 ± 3.3	28.1 ± 2.9
$\Delta\delta\Gamma_2$ ns^{-1}	0.9 ± 3.2	1.6 ± 3.1
a ps^{-1}	1.946 ± 0.031	1.979 ± 0.064
n	2.009 ± 0.096	1.588 ± 0.089
$t_{0J/\psi K^*}$ ps	0.234 ± 0.012	0.282 ± 0.010
Δt_{01} ps	-0.0196 ± 0.0032	-0.0137 ± 0.0027
Δt_{02} ps	-0.0050 ± 0.0031	-0.0058 ± 0.0030
A_Δ^{blind}	fixed to 0	0.68 ± 0.33

Table 5.15: Parameters obtained from a simultaneous fit of $B^0 \to K^*(892)^0\gamma$, $B^0 \to J/\psi K^*(892)^0$ and $B_s^0 \to \phi\gamma$ (strategy C2). The first column reports the result of the simultaneous fit performed on simulation where the physical parameters, τ_{B^0}, τ_{B_s} and $\Delta\Gamma_s$, are fixed to the value used in the event simulation. The second column reports the result of the simultaneous fit on the data where the physical parameters are fixed to the latest world averages. $\Delta\delta\Gamma_1$, $\Delta\delta\Gamma_2$, Δt_{01} and Δt_{02} obtained from the fit to simulated data are propagated as gaussian constraints to the data fit taking into account the full covariance matrix from the simulation fit. Alternative fit parametrization is used.

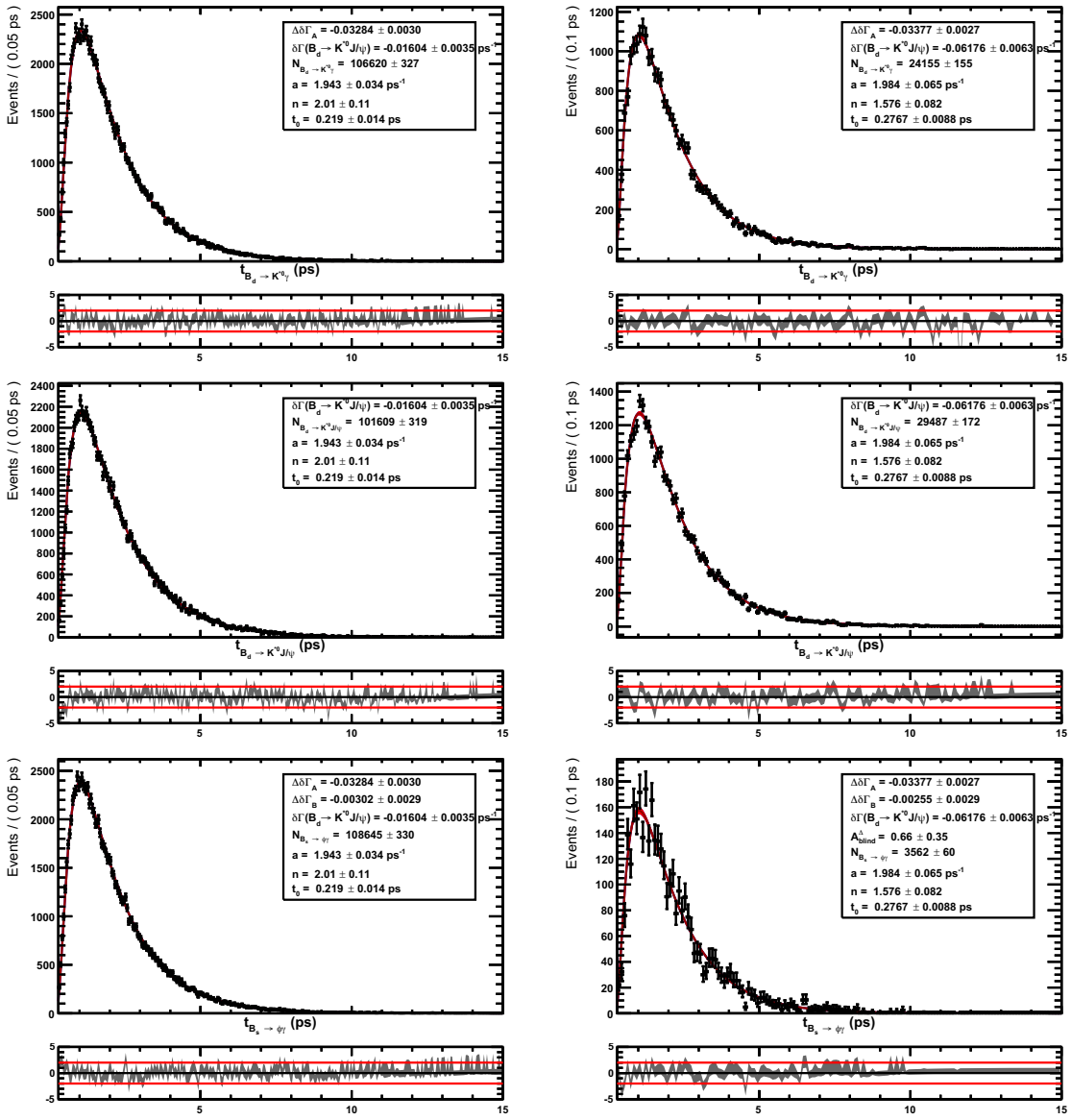

Figure 5.7: Results of the simultaneous fit of $B^0 \to K^*(892)^0\gamma$ (top), $B^0 \to J/\psi K^*(892)^0$ (middle) and $B_s^0 \to \phi\gamma$ (bottom) proper time (strategy C2), for both simulation (left) and data (right). Baseline fit parametrization is used.

5.3.5 Summary

The extracted values of A_{Δ}^{blind} for the different strategies are summarized in table 5.16. For the different strategies, the baseline and alternative fitting options give very close results.
Using the fact that the statistical error on A_{Δ} is driven by the signal yield N_S and the yield in the control sample N_C as $\sqrt{1/N_S + 1/N_C}$, the part of the statistical error associated to the control sample is estimated to be 0.12 for strategy A and 0.11 for strategy B. Strategies A and B then give statistically compatible results, at the level of 0.9σ.

Strategy	A	B	C1	C2
Baseline	0.57 ± 0.38	0.71 ± 0.36	0.57 ± 0.36	0.66 ± 0.35
Alternative	0.61 ± 0.37	0.67 ± 0.36	0.56 ± 0.37	0.68 ± 0.33

Table 5.16: A summary of the results on A_{Δ}^{blind}.

Using strategy C2, the statistical improvement is limited. This strategy may anyhow allow to have lower systematic uncertainties given that the systematic uncertainties from the two control samples are completely different. The choice of the control sample(s) that will be used will be decided after all the systematics are evaluated. If one control sample happen to have much smaller systematic uncertainties than the other it will in fact be better to only use this control sample. It is important to point out that in the sake of using the di-muon channel, the HLT1TrackPhoton trigger line has been removed from the selection at a cost of 20% of the statistics in the radiative channels. If the chosen control sample is $B^0 \to K^*(892)^0\gamma$, i.e. strategy A, this trigger line could be reintroduced in the allowed trigger paths and the analysis would benefit from a small extra statistical gain.

5.4 Systematic uncertainties study

The main sources of systematic uncertainty in the A_{Δ} determination are induced by the reconstruction and selection of the signal decay, the signal and background mass modeling and background subtraction procedure and the proper time fit strategy. The study of the various systematic effects is not yet completed. Preliminary results concerning some of the main sources of systematics are discussed here. The systematic uncertainties driven by the knowledge of the background contamination in the signal and control

samples and its subtraction procedure is discussed in 5.4.1 where a brief summary of the work performed by our collaborators in the EPFL Lausanne group is presented. The uncertainty due to the limited knowledge of the external physical parameters is addressed in 5.4.2. The impact of the scaling and weighing procedures is discussed in 5.4.3. Other systematics that are still under study are discussed in section 5.4.4.

5.4.1 Background contamination and modeling

The A_Δ extraction relies on the good control of the background subtraction procedure. For instance imperfections in the modeling of the reconstructed mass shape would alter the background-subtracted proper time distribution and thus affect the A_Δ determination. Moreover, the expected small contamination of the backgrounds peaking in the signal mass region is not subtracted in the procedure as explained in section 4.2.3.
Some of the systematic uncertainties due to the reliability of the background subtraction can be investigated by a toys procedure approach. This procedure consists in generating a large amount of simulated data sets using a defined fit model with varying the input parameters in the range of their error. These data sets are fitted with the same model letting free the parameters so as to test the bias that the used model introduce on the measured parameters. Moreover, simulated data sets can be generated assuming a given hypotheses for a model, and then fitted assuming a different hypotheses so as to study the effect of this given hypotheses on the measured value of the model's parameters.
Several systematic effects related to the level of background contamination have been studied this way and are discussed in the following. The impact on the measurement induced by an imperfect mass modeling is not fully addressed by those tests. Additional systematic uncertainties can be estimated by repeating the full analysis varying the mass shape description for the various contributions to the selected sample.

The validity of the fit model has been studied using the toy procedure. The study consists in generating the mass distribution with all the physical backgrounds, taking into account the number of events extracted from the fit to data. This mass distribution is then background subtracted and fitted following the procedure describe in 4.2.3. For radiative decays, background is subtracted using the *sPlot* technique where the background contamination peaking in the signal region are considered as part of signal. For $B^0 \to J/\psi K^*(892)^0$, signal data is selected by cutting around the mass peak. The simultaneous fits from strategies A, B and C2 are then performed on the signal proper time

	$\mu(A_{\Delta\text{FIT}} - A_{\Delta\text{INPUT}})$	$\sigma(A_{\Delta\text{FIT}})$
Strategy A	0.022±0.007	0.338±0.005
Strategy B	0.063±0.005	0.308±0.003
Strategy C2	0.022±0.007	0.307±0.006

Table 5.17: Average central value and resolution for A_Δ obtained from 1000 toys considering the mass and proper time fitting models.

distribution using the procedure described in 5.3 The average central value and resolution for the A_Δ parameters obtained from a large set of toys are reported in table 5.17. The average statistical resolution on A_Δ, of the order of 0.34 for strategy A and 0.31 for strategy B and C2, is compatible with what is measured on data. It can be noticed that the average expected resolution is slightly improved with strategy C2 compared to strategy A.
A bias on the central value of the order of 0.02 for strategy A and C2 and of the order of 0.06 for strategy B is observed. This bias is induced by the treatment of the background peaking in the signal mass region as explained in the following.
Figure 5.8 displays the pull distribution of the toy sample for the parameter A_Δ, defined as :

$$\frac{A_{\Delta\text{FIT}} - A_{\Delta\text{INPUT}}}{\sigma(A_{\Delta\text{FIT}})},$$

for strategies A, B and C2. The small bias on the A_Δ determination is quantified by the parameters of the gaussian fit of the pull distribution which are expected to be (μ, σ)=(0, 1) for an unbiased distribution in the limit of an infinite size sample.

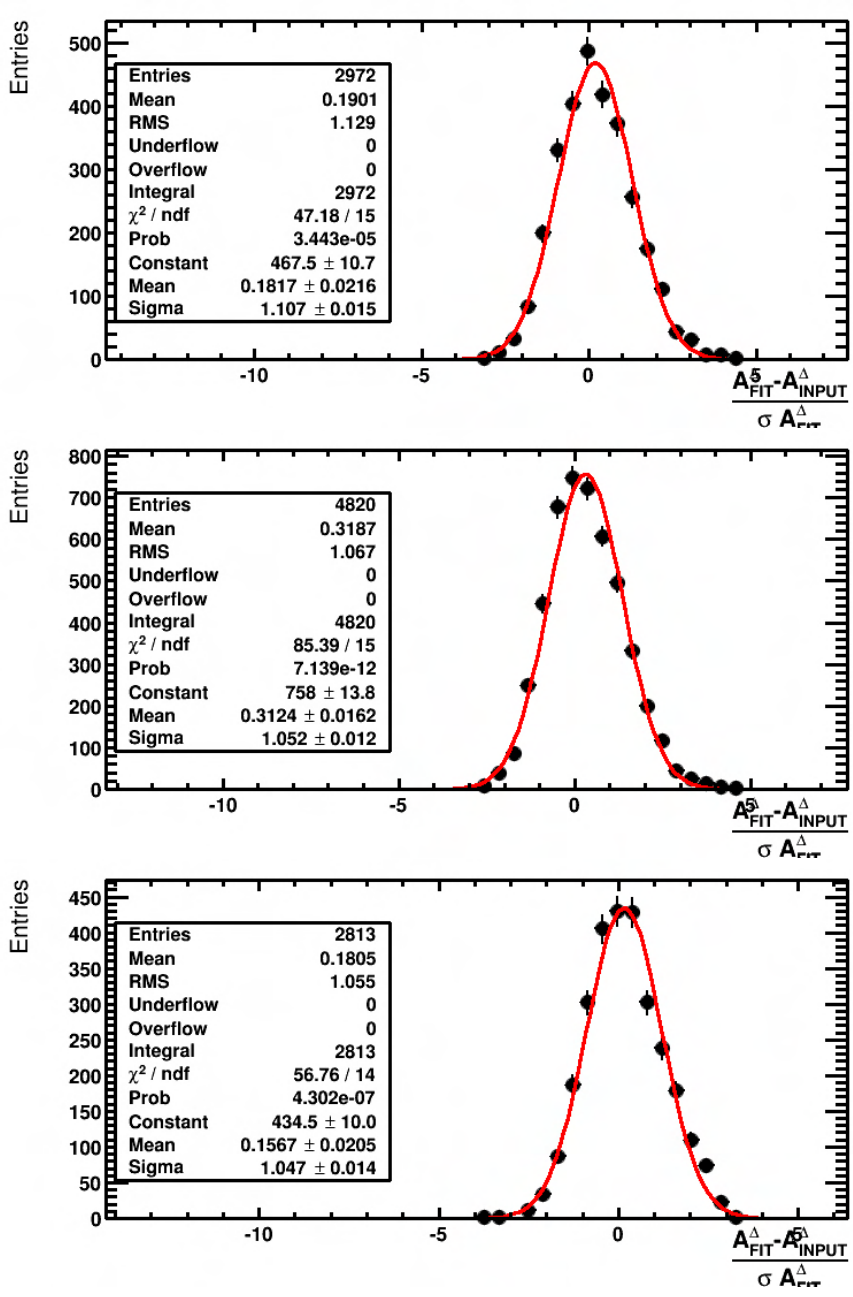

Figure 5.8: The distribution of the pull of A_Δ, $\frac{A_{\Delta\mathrm{FIT}} - A_{\Delta\mathrm{INPUT}}}{\sigma(A_{\Delta\mathrm{FIT}})}$, for strategy A (top), B (middle) and C2 (bottom).

	$\mu(A_{\Delta\text{FIT}} - A_{\Delta\text{INPUT}})$	$\sigma(A_{\Delta\text{FIT}})$
Strategy A	0.001±0.008	0.3529±0.0056
Strategy B	0.011±0.005	0.3174±0.0033
Strategy C2	0.010±0.007	0.3208±0.0061

Table 5.18: Average central value and resolution for A_Δ obtained from 1000 toys in the case of no peaking background in the signal mass region.

Strategy A	$\mu(A_{\Delta\text{FIT}} - A_{\Delta\text{INPUT}})$	$\sigma(A_{\Delta\text{FIT}})$
Generate only signal	0.00075±0.00388	0.2562±0.0027
Generate signal + 1% combinatorial bkg	0.0095±0.0037	0.2499±0.0025
Generate signal + 2% combinatorial bkg	0.0349±0.0037	0.2505±0.0024
Generate signal + 3% combinatorial bkg	0.0370±0.0038	0.2439±0.0023

Table 5.19: Average central value and resolution for A_Δ obtained from 1000 toys in the case where 1 %, 2 % or 3 % of combinatorial background is generated in the mass distribution of $B^0 \to K^*(892)^0\gamma$.

The small bias in the A_Δ determination highlighted by the toy study is due to the fact that small contamination from peaking backgrounds is neglected in the background subtraction procedure. This can be shown by repeating the toys study and removing all the peaking background contribution in the generated model. In that configuration no bias is observed as shown in table 5.18. The bias obtained by the toys study, reported in table 5.17, will be assigned as the systematics induced by the peaking background treatment to the A_Δ measurement.

In a similar way, the effect of a wrong subtraction of the combinatorial background is studied with toys. This is done by generating the proper time distribution for signal events and 1%, 2% or 3% of the number of generated signal events as combinatorial background in the $B^0 \to K^*(892)^0\gamma$ mass distribution and then fit the corresponding proper time distribution assuming that there is only signal.
The average central value and resolution for the A_Δ parameters are reported in table 5.19; the statistical resolution on A_Δ is around 0.25 since there is no background subtraction taking place. For 1 % of combinatorial background a bias of almost 0.01 is expected on A_Δ.

5.4.2 External physical inputs

In order to study the A_Δ sensitivity due to the external physical parameters, τ_{B^0}, $\tau_{B_s^0}$ and $\Delta\Gamma_s$ which are fixed to the world average central value in the fits presented above,

the proper time fit to the data events is repeated varying each external parameter by $\pm 2\sigma$. The variation of σ_{A_Δ} as a function of the external parameters value is shown on figure 5.9 and the values are reported in table 5.21.

The precise knowledge of τ_{B^0} and $\tau_{B_s^0}$ has not a significant effect on the statistical resolution of A_Δ whereas the variation of $\Delta\Gamma_s$ affects the resolution of A_Δ. This is due to the fact that the sensitivity on the A_Δ parameter vanishes in case of vanishing $\Delta\Gamma_s$ as discussed in 1.2.2. Hence, a precise knowledge of the external inputs, and especially $\Delta\Gamma_s$, is important for a precise determination of A_Δ.

The current knowledge of those external parameters can be injected in the simultaneous fits as a 3 dimension correlated gaussian constraint. The latest world averages of τ_{B^0}, $\tau_{B_s^0}$ and $\Delta\Gamma_s$ are reported in table 5.5. The simultaneous fit from strategy A is repeated adding the 3 dimensional constraint on the external parameters. The result of this fit, reported in table 5.20, are consistent with the previous results reported in table 5.8. The statistical resolution on the measured A_Δ slightly increases from 0.38 to 0.39.

Fit parameters	
$\delta\Gamma_{K^*\gamma}$ ns^{-1}	98.1 ± 9.5
$\Delta\delta\Gamma_2$ ns^{-1}	3.2 ± 2.9
a ps^{-1}	1.926 ± 0.076
n	1.72 ± 0.17
t_0 ps	0.259 ± 0.020
A_Δ^{blind}	0.57 ± 0.39
τ_{B^0} ps	1.520 ± 0.004
$\tau_{B_s^0}$ ps	1.509 ± 0.004
$\Delta\Gamma_s$ ns^{-1}	0.081±0.006

Table 5.20: Parameters obtained from a simultaneous fit of $B^0 \to K^*(892)^0\gamma$ and $B_s^0 \to \phi\gamma$ (strategy A) on data. $\Delta\delta\Gamma_2$ extracted from a simultaneous fit on simulation is propagated as a gaussian constraint to the data fit. The external parameters τ_{B^0}, $\tau_{B_s^0}$ and $\Delta\Gamma_s$ are injected in the data fit as external constraints. Baseline fit option is used.

5.4.3 Scaling and weighing procedure

The effect of the weighing and cut scaling procedure, discussed in 4.4.1, on the measured A_Δ is studied by repeating the fit from strategy C2 changing the number of bins used

Standard deviation (σ)	-2	-1	0	1	2
σ_{A_Δ} ($\tau_{B_s^0}$)	0.33	0.33	0.35	0.34	0.35
σ_{A_Δ} (τ_{B^0})	0.34	0.35	0.35	0.35	0.35
σ_{A_Δ} ($\Delta\Gamma_s$)	0.38	0.36	0.35	0.32	0.30

Table 5.21: The statistical resolution on the measured A_Δ^{blind} obtained changing the value of the physical parameters $\tau_{B_s^0}$, τ_{B^0} and $\Delta\Gamma_s$ within $\pm 2\sigma$ from the central value.

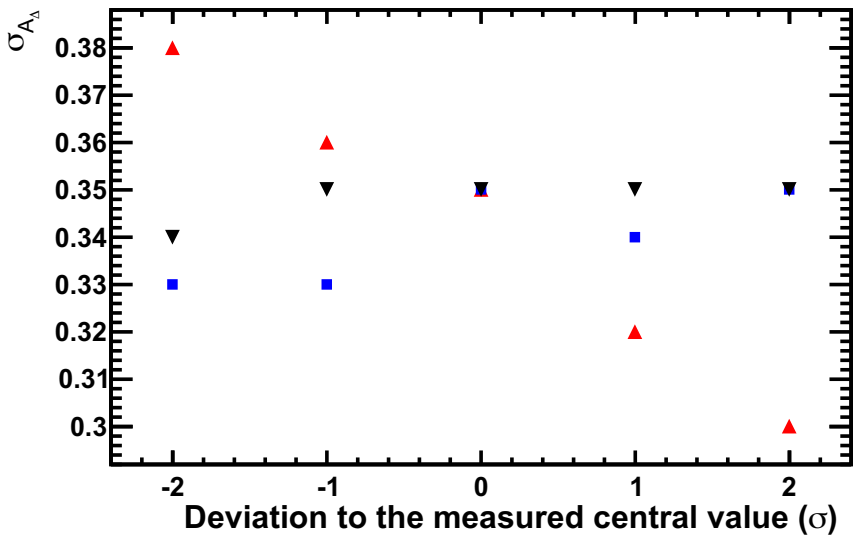

Figure 5.9: The variation of the statistical resolution on the measured A_Δ as a function of the change in the standard deviations (σ) in the external physical parameters. $\Delta\Gamma_s$: up triangles, τ_{B^0}: down triangles and $\tau_{B_s^0}$: squares.

to extract the two dimensional weights and changing the scaling factors used.

The weights are extracted assuming three different binning schemes dividing the the range of the used variables in the weighing on 30, 60 and 90 bins. The effect of varying the number of bins on the measured statistical error of A_Δ is negligible as reported in table 5.22.

The scaling factors values are changed by $\pm 10\%$ to study the effect of scaling the $B^0 \to J/\psi K^*(892)^0$ selection cuts on A_Δ. The effect is found to be negligible and the results of the study are reported in table 5.23.

Number of bins	30	60	90
σ_{A_Δ}	0.35	0.34	0.35

Table 5.22: The statistical resolution on the measured A_Δ^{blind} extracted changing the number of bins used to obtain two dimensional weights of $B^0 \to J/\psi K^*(892)^0$. The eventual change in the central value is to be taken as a systematic. Strategy C1 is used.

Scaling factor deviation	-10%	0%	+10%
σ_{A_Δ} (changing θ_{DIRA})	0.35	0.35	0.34
σ_{A_Δ} (changing $\chi^2(IP_{K^+})$)	0.34	0.35	0.35
σ_{A_Δ} (changing $\chi^2(IP_{\pi^-})$)	0.33	0.35	0.34

Table 5.23: The statistical resolution on the measured A_Δ^{blind} extracted changing the scaling factors by $\pm 10\%$. The eventual change in the central value is to be taken as a systematic. Strategy C1 is used.

5.4.4 Other systematics

Many other possible systematics effects are being investigated:

- The effect on A_Δ due to fixing the shapes of the different contributions to the mass model for $B^0 \to K^*(892)^0\gamma$ and $B_s^0 \to \phi\gamma$ from simulation.

- The effect on A_Δ due to the photon calibration, discussed in appendix B, can be studied by varying the photon energy in $B^0 \to K^*(892)^0\gamma$ and $B_s^0 \to \phi\gamma$.

- The effect of assuming the parameters of the acceptance at low proper time to be common for the signal and control sample(s), mainly parameters a and n, can be studied by performing a fit where a and n are assumed to not be common for the channels, as done for t_0 in the alternative fit, and add a constraint, extracted from the fit to simulated events, on the difference Δa and Δn in the data fit.

- The effect of changing the analytical parametrization of the proper time acceptance on the measured A_Δ can be studied by choosing a different acceptance function and redoing the proper time fits.

- The effect of the possible correlations between mass and proper time can be studied by toys similar to the full toy study except that simulation events are used for the signal and for the control samples.

- The time-dependent decay rate for the untagged $B_s^0 \to \phi\gamma$ decay given in equation 4.4 and used in the proper time fit model relies on the cancellation of the flavor dependent oscillation terms. Due to a possible small flavor asymmetry in B_s production at LHC, measured to be $A_P(B_s) = (1.09 \pm 2.61 \pm 0.66)\%$ [109], the cancellation might not realize perfectly and the systematic effect has to be propagated on the A_Δ determination. The related uncertainty is however expected to be negligible thanks to the small measured B_s production asymmetry and the expected small $\mathcal{C}_{CP}$ and $\mathcal{S}_{CP}$ terms.

5.5 Conclusions

In this work, four different strategies to measure A_Δ have been studied. The different strategies give statistically compatible results for A_Δ. The expected statistical uncertainty on the measured A_Δ is of about 0.35. This is compatible with the expected resolution obtained from the study based on a large toys sample. Strategy C2, where both $B^0 \to K^*(892)^0\gamma$ and $B^0 \to J/\psi K^*(892)^0$ are used as control samples, has a slightly better statistical resolution on A_Δ.

The baseline fit option has shown that there is a good control of the acceptance at low proper time. This is validated by an alternative fit parametrization where one of the parameters modeling the acceptance at low proper time is considered to not be the same for the different channels in the simultaneous fit. Both the baseline fit and the alternative fit give compatible results.

The analysis is in the finalization phase with the following steps to be completed before performing a final unblinded measurement:

- Some of the systematic uncertainties are studied, mainly the systematic due to the mis-knowledge of the level of contamination of the different backgrounds, the effect due to the external physical parameters and the effect of the weighing and cut scaling procedure performed to align the acceptance of $B^0 \to J/\psi K^*(892)^0$ with $B^0 \to K^*(892)^0\gamma$. Other systematic effects are under study.

- The difference in the acceptance at high proper time between data and simulation remains to be understood.

- The performance of the A_Δ extraction is to be compared with the proper time ratio fit approach developed by our collaborators from Valencia. Preliminary comparison shows a similar statistical sensitivity for both extraction methods. The compared sensitivity to systematical effects is under investigation.

Conclusion

B physics is an important field of research providing a concret testing ground of the Standard Model (SM) on the experimental and the theoretical sides. In this context, studying the radiative decays of the B meson stands as a probe of New Physics (NP) phenomena. The measurement of the photon polarization in $b \to s\gamma$ radiative penguin transition can put some constraints on NP scenarios.

With the data collected during its first phase of operation, LHCb has already demonstrated its capability to reconstruct radiative decays, many of which have already been analyzed and studied. The first measurement of the photon polarization is addressed in several analysis at LHCb. An angular analysis of $B \to K^* e^+ e^-$ is performed to measure the polarization of low virtual photons. The photon polarization can also be measured from an angular analysis of $B \to K^+\pi^-\pi^+\gamma$. In this case, the extraction of the photon polarization would then require a complete amplitude analysis to separate the different $K\pi\pi$ resonance states. Finally, the time-dependent analysis of $B_s^0 \to \phi\gamma$ gives a direct access to the polarization for real photon.

In this thesis, two main points have been carried out. The first point was the improvement of the photon identification procedure at LHCb which is essential for radiative decay reconstruction and selection. The second one is the measurement of the photon polarization in $b \to s\gamma$ penguin transition using $B_s^0 \to \phi\gamma$ events collected by LHCb during the run I period.
The main results of this work are summarized in the following.

Photon identification

An improved photon identification procedure has been introduced. This tool is based on the neural net method and has shown a significant improvement compared to the initial identification procedure implemented at LHCb for the analysis of the first data. This improved tool is essential for future radiative analysis and is therefore incorporated as the standard identification procedure for the final analysis of the run I data and to be applied to the data that will be collected in the coming period.
A calibration of the γ/π^0separation performance is developed in this context. This calibration tool is of general interest to evaluate systematics for several analysis involving high energy π^0 or photons.

Photon polarization

The analysis of $B_s^0 \to \phi\gamma$ events to measure the photon polarization is detailed. The selection criteria used to select signal events is discussed along with the mass fit and background subtraction method used. A delicate treatment has been done to understand the proper time distribution and the selection acceptance affecting it. Data driven control methods are presented and the different strategies to measure the photon polarization are introduced.

As the analysis is still ongoing, the results obtained are still blinded and only the measured statistical resolution on A_Δ is discussed. The expected statistical uncertainty on the measurement of A_Δ is around 0.35. The systematics uncertainties affecting the measurement are under investigation. Preliminary estimation concerning some of them have been presented.

The expected sensitivity on the measured A_Δ is quite limited with the data collected during run I. During the run II phase, the LHC will be running at a center of mass energy of $\sqrt{s} = 13$ TeV in 2015 and is expected to increase to $\sqrt{s} = 14$ TeV in 2016 and 2017. An additional integrated luminosity of 5-6 fb^{-1} is to be added to the 3 fb^{-1} already collected in run I. The cross-sections for $b\bar{b}$-production should be around 500 μb at $\sqrt{s} = 14$ TeV, i.e. 1.8 times that of run I. At high energy, the occupancy of the calorimeter is expected to increase, the reconstruction and selection of photons will have to be adapted to the new running conditions and the photon identification tools,

presented in this thesis, are to be readjusted. Assuming similar performance as in the selection of run I data, the LHCb is expected to increase by a factor of five the $B_s^0 \to \phi\gamma$ sample collected so far. With this amount of statistics, the statistical resolution on the measured A_Δ will go down to 0.15.
The LHCb detector upgrade is scheduled for 2018 and consists of a complete redesign of the readout system and the trigger in order to read out the full detector at the bunch crossing rate and perform the triggering in only software to allow selecting efficiently the interesting flavor decay chain. With the upgrade, a significant increase of statistics is expected. The experiment should operate at an instantaneous luminosity of up to $2 \times 10^{33}\text{cm}^{-2}\text{s}^{-1}$. Almost 5 fb^{-1} of integrated luminosity is to be collected each year. Precise measurements in beauty and charm sector with experimental precision of the order of the theoretical uncertainties will be carried out.
For what concerns the analysis presented here, this increase in statistics will not only reduce the statistical resolution on the measured A_Δ to the few percent, but it will also make the analysis sensitive to the flavor-dependent terms in the time-dependent decay rate, $\mathcal{S}_{CP}$ and $\mathcal{C}_{CP}$, which provides information on the photon polarization, and hence, a full flavor-tagged analysis can be envisaged.

The measurement of the photon polarization will be one of the important measurements addressed by several analysis at LHCb in the coming years. The analysis presented in this thesis demonstrates, along with other analysis, the capability of LHCb to perform precision measurements with radiative decays. The work done stands as a corner stone on which future analysis that aim to measure the photon polarization will be built. This measurement will be one of the unique key measurements in the LHCb physics program.

Appendices

Appendix A

$B \to V\gamma$ and $B \to VJ/\psi$ time acceptance alignment

Based on kinematical considerations a procedure is proposed to align the selection acceptance at low proper time of two different decays of the B meson to (quasi) two-body final states with a common resonance. The kinematical basis of the procedure is addressed in section A.1. The derived procedure for the time alignment and its validation is discussed in section A.2.

A.1 Kinematical basis of the procedure

A.1.1 Definitions

Let's consider two different decays, denoted $(\mathcal{A})$ and $(\mathcal{B})$, of a particle X to (quasi) two-body final states with a common component Y :

$$\begin{aligned} (\mathcal{A}) : X &\to Y + Z_{\mathcal{A}} \\ (\mathcal{B}) : X &\to Y + Z_{\mathcal{B}} \end{aligned}$$

In the decay rest frame, the momentum of the Y component, denoted $p^*_{\mathcal{A}}$ and $p^*_{\mathcal{B}}$ for the decays $(\mathcal{A})$ and $(\mathcal{B})$ respectively, is determined by the mass relation :

$$p^*_{\mathcal{A}(\mathcal{B})} = \frac{\sqrt{(m_X^2 - m_Y^2 - m^2_{Z_{\mathcal{A}(\mathcal{B})}})^2 - 4.m_Y^2.m^2_{Z_{\mathcal{A}(\mathcal{B})}}}}{2.m_X}$$

As an illustration, the table A.1 compares the kinematics of the K^{*0} and the ϕ resonances in the $B_{(s)}$ decay frame for the radiative and $c\bar{c}$ modes ($B^0 \to K^{*0}\gamma$, $B^0 \to K^{*0}J/\psi$) and ($B_s \to \phi\gamma$, $B_s \to \phi_s J/\psi$), respectively.

	$p^\star$ (Mev/c)	$E^\star$ (MeV)	$\beta^\star = \frac{p^* c}{E^*}$
$B^0 \to K^{*0}\gamma$	2564	2714	0.944
$B^0 \to K^{*0}J/\psi$	1577	1808	0.872
ratio	$\rho_{p^*} = 1.63$	ρ_{E^*} =1.50	ρ_{β^*} =1.08
$B_s \to \phi\gamma$	2583	2777	0.93
$B_s \to \phi J/\psi$	1583	1883	0.84
ratio	$\rho_{p^*} = 1.63$	ρ_{E^*} =1.47	ρ_{β^*} =1.11

Table A.1: *Kinematics of the K^{*0} meson in the rest-frame of the $B^0 \to K^*\gamma$ and $B^0 \to K^{*0}J/\psi$ decays (top) and the ϕ meson in the $B_s \to \phi\gamma$ and $B_s \to \phi J/\psi$ decays (bottom).*

In the limit of large boost of the mother particle ($\beta = \frac{p_X}{E_X} \sim 1$), the projections with respect to the boost-axis of the Y momentum in the lab-frame, $\vec{p}$, is given by the approximate Lorentz transformation :

$$p_\parallel = p.cos(\theta) = \gamma.[E^* + \beta.p^*.cos(\theta^*)] \sim \gamma.[E^* + p^*.cos(\theta^*)] \quad (A.1)$$

$$p_\perp = p.sin(\theta) = p^*.sin(\theta^*) \quad (A.2)$$

where $\gamma = (1-\beta^2)^{-\frac{1}{2}}$ is the Lorentz factor and θ and θ^* are the angle of the Y momentum with the boost-axis in the lab-frame and in the decay rest-frame respectively. A given kinematical configuration in the lab frame is completely defined by the set $(p*, \theta^*, \gamma)$ (the direction of the boost, independent of the decay type, is omitted as irrelevant for the discussion addressed here)

A.1.2 Kinematical matching

Let's connect the kinematical configuration $(p^*_{\mathcal{B}}, \theta^*_{\mathcal{B}}, \gamma_{\mathcal{B}})$ of the decay $\mathcal{B}$ to a configuration $(p^*_{\mathcal{A}}, \theta^*_{\mathcal{A}}, \gamma_{\mathcal{A}})$ of the decay $\mathcal{A}$, via a matching relation denoted $\mathcal{M}_0^{\mathcal{B}\to\mathcal{A}}$:

$$\mathcal{M}_0^{\mathcal{B}\to\mathcal{A}} = \begin{cases} p^*_{\mathcal{B}}.\cos(\theta^*_{\mathcal{B}}) \times \rho_{E^*} = & p^*_{\mathcal{A}}.cos(\theta^*_{\mathcal{A}}) \\ \gamma_{\mathcal{B}}/cos(\theta_{\mathcal{B}}) \times \dfrac{\rho_{p^*}}{\rho^2_{E^*}} = & \gamma_{\mathcal{A}}/cos(\theta_{\mathcal{A}}), \end{cases} \quad (A.3)$$

where $\rho_{E^*} = \frac{E^*_{\mathcal{A}}}{E^*_{\mathcal{B}}}$ and $\rho_{p^*} = \frac{p^*_{\mathcal{A}}}{p^*_{\mathcal{B}}}$ are constant ratios (see table A.1 for specific values).

It is worth noticing that in case of an acceptance limited to the very forward region ($cos(\theta_{\mathcal{A}}) \sim cos(\theta_{\mathcal{B}}) \sim 1$), the ratio of the Lorentz factors is essentially independent of the angular kinematics : $\gamma_{\mathcal{A}}/\gamma_{\mathcal{B}} \sim \rho_{p^*}/\rho^2_{E^*} = \rho_{\beta^*}/\rho_{E^*}$.
The Y momenta in the lab-frame for the decays ($\mathcal{A}$) and ($\mathcal{B}$) are related as :

$$\begin{aligned} p_{\mathcal{A}}.cos(\theta_{\mathcal{A}}) &= \gamma_{\mathcal{A}}[E^*_{\mathcal{A}} + p^*_{\mathcal{A}}.cos(\theta^*_{\mathcal{A}})] \\ &= \gamma_{\mathcal{B}}[E^*_{\mathcal{B}} + p^*_{\mathcal{B}}.cos(\theta^*_{\mathcal{B}})] \times [\frac{cos(\theta_{\mathcal{A}})}{cos(\theta_{\mathcal{B}})}.\frac{\rho_{p^*}}{\rho_{E^*}}] = p_{\mathcal{B}}.cos(\theta_{\mathcal{A}}) \times \frac{\rho_{p^*}}{\rho_{E^*}}. \end{aligned} \quad (A.4)$$

Combining relations A.3 and A.4 we obtain :

$$\frac{p_{\mathcal{A}}}{p_{\mathcal{B}}} = \frac{\rho_{p^*}}{\rho_{E^*}} = \rho_{\beta^*} = \frac{cos(\theta^*_{\mathcal{B}})}{cos(\theta^*_{\mathcal{A}})}. \quad (A.5)$$

In other words, the kinematical quantity $p.cos(\theta^*)$ is conserved between decays ($\mathcal{A}$) and ($\mathcal{B}$) under the matching relation $\mathcal{M}_0^{\mathcal{B}\to\mathcal{A}}$ in the limit of large boost :

$$\boxed{p_{\mathcal{A}}.cos(\theta^*_{\mathcal{B}}) = p_{\mathcal{B}}.cos(\theta^*_{\mathcal{A}})}$$

The invariance of the transverse momentum with respect to the boost direction (A.2) provides the relation :

$$\frac{sin(\theta_{\mathcal{A}})}{sin(\theta_{\mathcal{B}})} = \frac{\rho_{p^*}}{\rho_{\beta^*}}.\frac{sin(\theta^*_{\mathcal{A}})}{sin(\theta^*_{\mathcal{B}})} = \rho_{E^*}.\frac{sin(\theta^*_{\mathcal{A}})}{sin(\theta^*_{\mathcal{B}})} = \frac{\rho_{E^*}}{\rho_{\beta^*}}.\frac{\sqrt{\rho^2_{\beta^*} - cos^2(\theta^*_{\mathcal{B}})}}{\sqrt{1 - cos^2(\theta^*_{\mathcal{B}})}}. \quad (A.6)$$

The domain of validity of the matching relation and other possible matching choices are discussed in section A.1.4.

A.1.3 Geometrical matching

In the case of a long-lived particle X, useful relations on the geometrical quantities relying on the decay vertex displacement can be derived from the above kinematical matching $\mathcal{M}_0^{\mathcal{B}\to\mathcal{A}}$. The relevant kinematical and geometrical quantities are reported on the decay sketch on figure A.1

- **Flight distance and related quantities**
  The decay time of the mother particle X being independent of the decay final

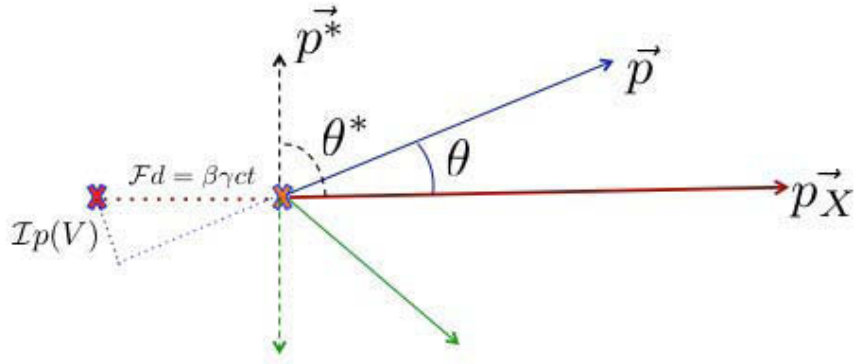

Figure A.1: *Sketch of the decay in the rest-frame (dashed) and in the lab-frame (solid). The relevant kinematical and geometrical quantities are indicated.*

state, the flight distances $\mathcal{F}d = \beta\gamma ct$ for the configurations of $(\mathcal{A})$ are related to the one of $(\mathcal{B})$ in the same ratio as the Lorentz factors under $\mathcal{M}_0^{\mathcal{B}\to\mathcal{A}}$. The latter ratio is constant in a very good approximation for boosted decays in the forward region covered by the LHCb acceptance.

$$\frac{\mathcal{F}d_{\mathcal{A}}}{\mathcal{F}d_{\mathcal{B}}} = \frac{\gamma_{\mathcal{A}}}{\gamma_{\mathcal{B}}} = \frac{\rho_{\beta^*}}{\rho_{E^*}} \cdot \frac{cos(\theta_A)}{cos(\theta_B)} \sim \frac{\rho_{\beta^*}}{\rho_{E^*}}$$

Other geometrical quantities depending on the relative position of the decay vertex with respect to the origin vertex also exhibits a scale relation under $\mathcal{M}_0^{\mathcal{B}\to\mathcal{A}}$.

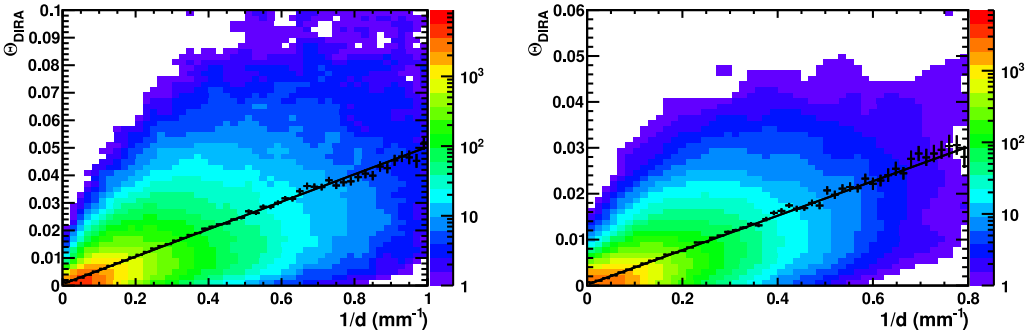

Figure A.2: *Distribution of simulated $B^0 \to K^{*0}\gamma$ (left) and $B^0 \to K^{*0}J/\psi$ (right) events in the 2-dimensional plane (Θ_{DIRA},$\mathcal{F}d^{-1}$). Linear fit of the profile histograms is superimposed.*

This is the case for the direction angle, $cos(\Theta_{DIRA}) = \vec{u}_d . \vec{u}_X$ where $\vec{u}_d$ and $\vec{u}_X$ are the unit vectors associated to the measured flight distance and X momentum, respectively. As shown on figure A.2, this quantity is strongly anti-correlated to

the flight distance. The average Θ_{DIRA} varies almost linearly with the inverse of $\mathcal{F}d$. From a linear fit, $< \Theta_{DIRA} >= \alpha/\mathcal{F}d$, of the profile histograms displayed on the figure A.2, the ratio of slopes α is found to be :

$$\frac{\alpha_{\mathcal{A}}}{\alpha_{\mathcal{B}}} = (1.32 \pm 0.01)$$

for the decay pair $(\mathcal{A}, \mathcal{B})$=$(B^0 \to K^{*0}\gamma, B^0 \to K^{*0}J/\psi)$. As a consequence, Θ_{DIRA} scaling under $\mathcal{M}_0^{\mathcal{B}\to\mathcal{A}}$ is roughly expected to be :

$$\frac{< \Theta_{\mathcal{A}} >}{< \Theta_{\mathcal{B}} >} = \frac{\alpha_{\mathcal{A}}}{\alpha_{\mathcal{B}}}.\frac{\mathcal{F}d_{\mathcal{B}}}{\mathcal{F}d_{\mathcal{A}}} \sim 1.32 \times \frac{\rho_{E^*}}{\rho_{\beta^*}} \sim 1.84 \tag{A.7}$$

for that decay pair. Similar behavior is obtained for $(\mathcal{A}, \mathcal{B})$=$(B_s \to \phi\gamma, B_s \to \phi J/\psi)$

Another related quantity, is the isolation vertex variable, $\Delta\chi^2_{min}$, which quantifies the compatibility of the decay vertex with any other track coming from the origin vertex. This variable propagates the same information as the distance of closest approach of the track with the decay vertex which increases proportionally to the flight distance.

- **Impact parameters**
  The impact parameter of the Y resonance is defined as $\mathcal{I}p(Y) = \mathcal{F}d.sin(\theta)$, leading to the relation under $\mathcal{M}_0^{\mathcal{B}\to\mathcal{A}}$:

$$\frac{\mathcal{I}p(Y)_{\mathcal{A}}}{\mathcal{I}p(Y)_{\mathcal{B}}} = \frac{\gamma_{\mathcal{A}}.sin(\theta_{\mathcal{A}})}{\gamma_{\mathcal{B}}.sin(\theta_{\mathcal{B}})} = \frac{\rho_{\beta^*}}{\rho_{E^*}}.\frac{sin(2\theta_{\mathcal{A}})}{sin(2\theta_{\mathcal{B}})}$$

  In the limit of small angles in the lab frame and using (A.6) we obtain :

$$\frac{\mathcal{I}p(Y)_{\mathcal{A}}}{\mathcal{I}p(Y)_{\mathcal{B}}} = \rho_{\beta^*}.\frac{sin(\theta^*_{\mathcal{A}})}{sin(\theta^*_{\mathcal{B}})} = \rho_{\beta^*}.\frac{\sqrt{1 - cos^2(\theta^*_{\mathcal{B}})/\rho^2_{\beta^*}}}{\sqrt{1 - cos^2(\theta^*_{\mathcal{B}})}}. \tag{A.8}$$

  In the case of a large boost in a limited forward acceptance and with $\rho^2_{\beta^*} \sim 1$, the $\mathcal{I}p(Y)$ ratio turns to be approximatively constant :

$$\frac{\mathcal{I}p(Y)_{\mathcal{A}}}{\mathcal{I}p(Y)_{\mathcal{B}}} \sim \rho_{\beta^*}.$$

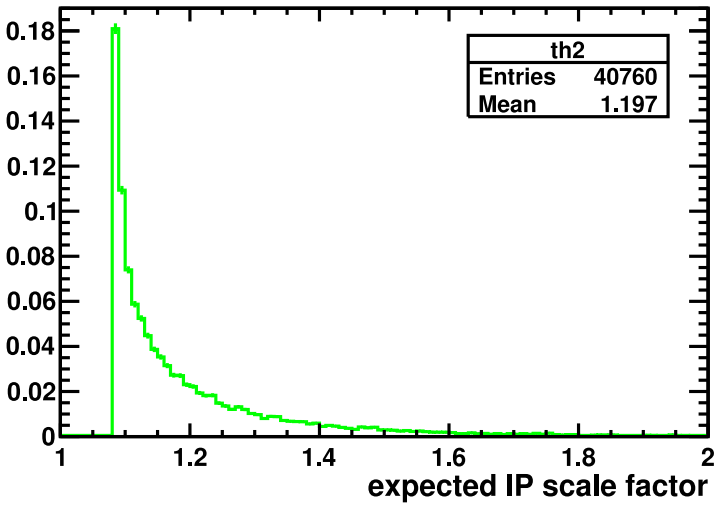

Figure A.3: *Distribution of* $\mathcal{I}p(K^{*0})_{\mathcal{A}}/\mathcal{I}p(K^{*0})_{\mathcal{B}}$ *from eq.(A.8). The rest-frame angle* $\theta^*_{\mathcal{B}}$ *is obtained from* $(\mathcal{B})$*=*$B^0 \to K^{*0}J/\psi$ *simulated events and* ρ_{β^*}*=1.08 corresponds to* $(\mathcal{A})$*=*$B^0 \to K^{*0}\gamma$ *decay.*

This is the case in a reasonable approximation for the $(B \to V\gamma, B \to VJ/\psi)$ decays in the LHCb acceptance. Figure A.3 display the distribution of

$$\mathcal{I}p(K^{*0})_{\mathcal{A}}/\mathcal{I}p(K^{*0})_{\mathcal{B}} = \rho_{\beta^*}.\frac{\sqrt{1-\cos^2(\theta^*_{\mathcal{B}})/\rho^2_{\beta^*}}}{\sqrt{1-\cos^2(\theta^*_{\mathcal{B}})}}$$

where $\theta^*_{\mathcal{B}}$ is obtained from $(\mathcal{B})$=$B^0 \to K^{*0}J/\psi$ simulated events and ρ_{β^*}=1.08 corresponds to $(\mathcal{A})$=$B^0 \to K^{*0}\gamma$ decay.
As expected the distribution exhibits a large accumulation of events around the ρ_{β^*} value with a right tail shifting the average ratio to $< \mathcal{I}p(K^{*0})_{\mathcal{A}}/\mathcal{I}p(K^{*0})_{\mathcal{B}} >$=1.20. Similar behavior and average value ($< \mathcal{I}p(\phi)_{\mathcal{A}}/\mathcal{I}p(\phi)_{\mathcal{B}} >$=1.22) is obtained when applying the matching relation to the decay pair $(\mathcal{A},\mathcal{B})$=$(B_s \to \phi\gamma, B_s \to \phi J/\psi)$.

The above relation directly propagates to the $\chi^2_{\mathcal{I}p}(Y)$ variable defined as $\chi^2_{\mathcal{I}p}(Y) = \mathcal{I}p^2(Y)/\sigma^2_{\mathcal{I}p(Y)}$. Assuming a smooth variation of the $\mathcal{I}p(Y)$ resolution, $\sigma_{\mathcal{I}p(Y)}$, the expected scaling factor for that quantity is :

$$\frac{\chi^2_{\mathcal{I}p}(Y)_{\mathcal{A}}}{\chi^2_{\mathcal{I}p}(Y)_{\mathcal{B}}} = \left[\frac{\mathcal{I}p(Y)_{\mathcal{A}}}{\mathcal{I}p(Y)_{\mathcal{B}}}\right]^2.$$

In case the particle Y is a short-living resonance, the X selection usually relies on the impact parameter of the charged products of the Y decay. Let's assume the two-body decay $Y \to h^+h^-$. The impact parameters of h^+ and h^- are correlated to the Y impact parameter convoluted with the angular decay distribution in the Y rest-frame. In case the Y resonance has a different helicity structure between decay $(\mathcal{A})$ and $(\mathcal{B})$ the almost-constant scaling feature of the $\mathcal{I}p(Y)$ variable does not propagate to the impact parameter of the decay products, $\mathcal{I}p(h^{\pm})$ state. This is the case for the decay pair $(B \to V\gamma, B \to VJ/\psi)$, where V is the vector meson K^{*0} or ϕ. The radiative decay $V\gamma$ of the pseudo-scalar B only allows for transversal helicities of the vector meson V while the VJ/ψ mode receives a longitudinal contribution. In that case the helicity distribution of the V decay must be taken into account in the alignment procedure as described in section A.2. It is worth noticing, however, that in the specific case $V = \phi \to K^+K^-$, the impact parameters of the two charged kaons produced almost at rest in the ϕ rest-frame are mostly insensitive to the helicity structure of the decay and then satisfy $\mathcal{I}p(\phi) \sim \mathcal{I}p(K^{\pm})$.

A.1.4 Comments of the matching procedure

- *Validity of the method*
  It is clear from the trigonometric relation (A.5) and (A.6) that the matching condition $\mathcal{M}_0^{\mathcal{B}\to\mathcal{A}}$ is only valid on a truncated space of the kinematical configurations for the decays $\mathcal{A}$ or $\mathcal{B}$. For instance, there is no physical configuration of the decay $(\mathcal{B})$ that can be matched to a configuration of $(\mathcal{A})$ with $\rho_{\beta^*}.cos(\theta^*_{\mathcal{A}}) = cos(\theta^*_{\mathcal{B}}) > 1$, i.e. the configuration space of $(\mathcal{A})$ covered by the matching condition $\mathcal{M}_0^{\mathcal{B}\to\mathcal{A}}$ is possibly truncated when $\rho_{\beta^*} > 1$. Oppositely, it might exist configurations of $(\mathcal{B})$ that are unmatched to any configuration of $(\mathcal{A})$ when $\rho_{\beta^*} < 1$. The validity domain of the matching is thus limited to the angular configurations $|cos(\theta^*_{\mathcal{A}})| < 1/\rho_{\beta^*}$ and $|cos(\theta^*_{\mathcal{B}}) < \rho_{\beta^*}|$. These validity conditions are both verified for the considered decay pairs $(\mathcal{A}) : B \to V\gamma$ and $(\mathcal{B}) : B \to VJ/\psi$ reconstructed in the forward LHCb acceptance. For both $V = K^{*0}$ and $V = \phi$, the ratio ρ_{β^*} exceeds the unity by 10% only and the $|cos(\theta^*_{\mathcal{A}})|$ accepted range is limited to $\sim [-0.8, +0.8]$ as shown on the figure A.4.

- *Validity of the approximations*
  High boosts ($\beta \sim 1$) and low angles ($\cos(\theta) \sim 1$) have been assumed to establish

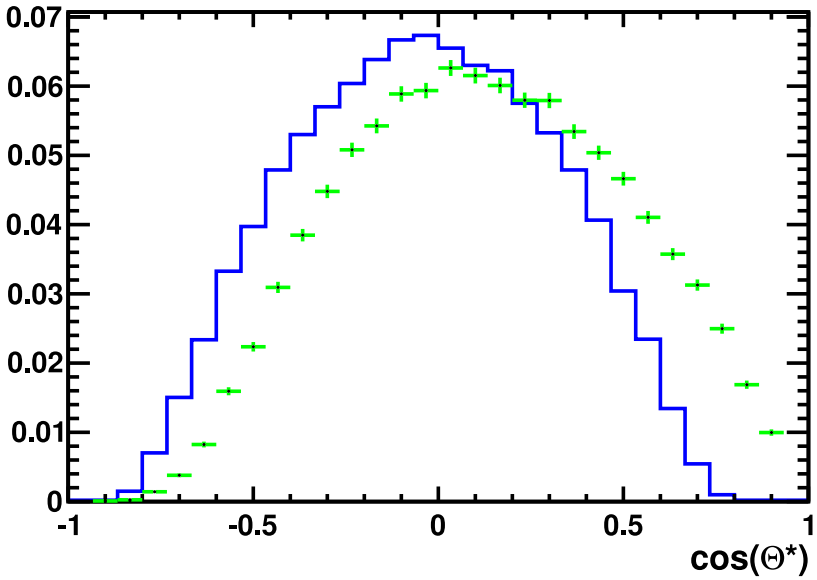

Figure A.4: *Distribution of* $cos(\theta^*)$ *for the selected sample of simulated* $B^0 \to K^{*0}\gamma$ *events (solid histogram) and* $B^0 \to K^{*0}J/\psi$ *events (points).*

the above scale relations between properties of the decay ($\mathcal{A}$) and the decay ($\mathcal{B}$). These approximations are valid at the level of few per mille for the considered decays in LHCb. The average velocity and angular aperture for the $B \to V\gamma$ ($B \to VJ/\psi$) selected events are $< \beta >$=0.998 (0.999) and $< cos(\theta) >$=0.998 (0.999), respectively.

- *Other matching relations*
  The choice of the matching relation $\mathcal{M}_0^{\mathcal{B}\to\mathcal{A}}$ is not unique. Another relevant choice is :

$$\mathcal{M}_1^{\mathcal{B}\to\mathcal{A}} = \begin{cases} sin(\theta_{\mathcal{B}}) \times \rho_{E^*} = & sin(\theta_{\mathcal{A}}) \\ cos(\theta^*_{\mathcal{B}})/\rho_{\beta^*} = & cos(\theta^*_{\mathcal{A}}) \end{cases} \tag{A.9}$$

  With that choice the kinematical quantity $p.cotan(\theta^*)$ is conserved between decays ($\mathcal{A}$) and ($\mathcal{B}$) in the limit of large boost :

$$p_{\mathcal{A}}.cotan(\theta^*_{\mathcal{B}}) = p_{\mathcal{B}}.cotan(\theta^*_{\mathcal{A}})$$

  This matching choice however provides exactly the same relation between impact parameters as the default choice $\mathcal{M}_0^{\mathcal{B}\to\mathcal{A}}$ (see eq. A.8). It can be shown the cancelation of the angular dependency in the $\mathcal{I}p$ ratio can only be achieved with a matching condition $\mathcal{M}_{\mathcal{I}P}^{\mathcal{B}\to\mathcal{A}}$ that preserves the quantity $p.sin(\theta).cos(\theta^*)$. However,

the distributions of this kinematical quantity for the $B \to V\gamma$ and $B \to VJ/\psi$ decays in the LHCb acceptance have a very short overlap and this matching can't be used for our time alignement purpose.

A.2 Alignment of the proper time acceptance

The acceptance at low proper time is induced by the selection cuts relying on the B decay vertex displacement (impact parameters, direction angle, ...). In the case of a radiative $B \to V\gamma$ decay, the vertex decay information is only provided by the charged tracks coming from the decay of the vector meson V. Due to the different decay kinematics and helicity structure between $B \to V\gamma$ and $B \to VJ/\psi$, the same selection induces different acceptance. Based on the above discussion on the kinematical matching (A.1) the following three-step procedure is proposed to align the acceptance at low proper time between the two different decays :

- The $B \to VJ/\psi$ candidates are reconstructed in such a way the $J/\psi \to \mu^+\mu^-$ decays is not used in the decay vertex determination. This is achieved by applying an arbitrarily large factor to the relevant elements of the covariance matrix of the reconstructed muon tracks. The proper time acceptance is then generated only by the selection cuts applied on the vector meson and its decay products, as it is for the corresponding radiative decay.

- An event-by-event reweighing is applied on the $B \to VJ/\psi$ sample to statistically reproduce the $B \to V\gamma$ distribution in the two-dimensional plane ($p.cos(\theta^*)$,θ_H), where θ_H is the helicity angle of the V decay. The reweighing in the first direction ($p.cos(\theta^*)$) aims at aligning the kinematics according to the matching relation $\mathcal{M}_0^{\mathcal{B}\to\mathcal{A}}$ discussed above while the helicity reweighing accounts for the different helicity-structure of the V decay.

- After the reweighing, the two different decays are assumed to exhibits almost-constant ratios for the vertex-related variables that induces the low proper time acceptance. A scaling factor is extracted for the relevant variables and the corresponding selection cuts are scaled accordingly.

Appendix B

Photon calibration

In radiative B meson decays analysis [45], a bias in the reconstructed invariant mass of the B meson has been observed both on data and simulation. This bias is estimated to be around 0.5 % and it is due to a bias in the photon energy estimated to be of the order of few percents, depending on the ECAL region and the photon category (unconverted photon or lately converted photon identified with a SPD hit in front of the ECAL cluster). This bias in the energy of the photon is induced by the calibration procedure performed with the low energy photons coming from the π^0 decays. A set of ad-hoc calibration coefficients are applied to the photon energy on both data and simulation to correct for this systematical bias. These coefficients are listed in tables B.1 and B.2 for the sim06 and sim08 simulation versions respectively and in table B.3 for 2011 and 2012 data. This a-posteriori correction coefficients are only applied at the analysis level, and thus, were neither included in the stripping nor the HLT processing.

Calorimeter area	Inner	Middle	Outer
Converted Photons	1.037	1.003	0.982
Unconverted photons	1.034	1.010	1.001

Table B.1: Calibration coefficients applied to the photon energy on events simulated with sim06 simulation version.

Calorimeter area	Inner	Middle	Outer
Converted Photons	1.044	1.010	0.989
Unconverted photons	1.041	1.017	1.008

Table B.2: Calibration coefficients applied to the photon energy on events simulated with sim08 simulation version.

Calorimeter area	Inner	Middle	Outer
Converted Photons	1.019	0.999	0.959
Unconverted photons	1.001	0.994	0.976

Table B.3: Calibration coefficients applied to the photon energy on 2011 and 2012 data samples.

Appendix C

Definition of the different variables used for selections

The definitions of the different variables used for the selection are introduced here

- The flight distance ($\mathcal{F}d$) is the distance covered by the reconstructed B meson from its creation at the interaction point, named primary vertex (PV), to the point where it decays, named secondary vertex (SV). The flight distance is related to the proper time of the B meson through $Fd = \beta\gamma ct$ where β and γ are the Lorentz factors, c is the speed of light and t is the proper time of the B meson.

- The DIRection Angle, θ_{DIRA}, is the angle between the line connecting the PV and the SV and the direction of the momentum of the B meson. It is given as $cos(\Theta_{\mathrm{DIRA}}) = \vec{u}.\vec{v}$ where $\vec{u}$ and $\vec{v}$ are the unit vectors associated to the measured flight distance direction and B momentum, respectively.

- The Impact Parameter (IP) of a given track x relative to a PV is the distance of closest approach between the extrapolated track and the PV. It is defined as $IP = \mathcal{F}d.sin(\theta_x)$ where θ_x is the angle defined by the track x and the flight distance direction.

- η is the pseudo rapidity defined as $\eta = -ln(tan(\theta/2))$ with θ being the angle between the momentum of the particle and the beam axis.

- P is the momentum of a given particle.

- E_T is the transverse energy with respect to the beam line: $E_T = E\sin\theta$.

- P_T is the transverse momentum of a given particle with respect to the beam line: $P_T = P \sin\theta$
- γ/π^0 separation is the output variable from the classifier trained to separate photons from merged π^0 discussed in 3.5.
- γ_{CL} is the photon confidence level. This variable is a transformation in the [0,1] range of the likelihood estimator discussed in 3.4.1 .
- In the selection cuts, M refers to the mass and ΔM refers to a mass range.
- The vertex χ^2 of a reconstructed resonance quantifies the compatibility of the tracks to decay from vertex.
- The vertex isolation cut of the B, $\Delta\chi^2$, quantifies the compatibility of the decay vertex with any other track not associated with the decay's tracks.
- Z_{PV} is the z coordinate of the B reconstructed vertex.
- nPV is the number of reconstructed primary vertices in the event.
- IPχ^2_{next} quantifies the compatibility of a given b hadron with the second most probable PV that it can be associated with.
- The helicity angle for $B \to (V \to h^+h^-)\gamma$ decay, θ_H is the angle between the momentum of the B and the momentum of h^+ in h^+ rest frame.
- The Particle IDentification (PID) variables for charged particles exist in two version:
  - Variables named ProbNN rely on the Neural Net (NN) procedure implemented at LHCb in 2012 (explained briefly in chapter 2.3.7) and are used as: xProbNNx(y) is the hypothesis of identifying (misidentifying) x as being x (y).
  - Variables named PID rely on the ΔLL procedure implemented since the start of LHCb (explained briefly in chapter 2.3.7) and are used as: xPIDx(y) is the hypothesis of identifying (misidentifying) x as being x (y).
- The ghost probability of a track is the probability for this track to be reconstructed from hits in the tracking system that belong to two separate tracks.

- isMuon is a veto applied to select true muons. The veto is defined by the number of hits in the muon stations.

Bibliography

[1] S.L. Glashow. Partial Symmetries of Weak Interactions. *Nucl.Phys.*, 22:579–588, 1961.

[2] Steven Weinberg. *The Quantum Theory of fields*, volume I: Foundations. Cambridge University Press., May 2005.

[3] F. Englert and R. Brout. Broken Symmetry and the Mass of Gauge Vector Mesons. *Phys. Rev. Lett.*, 13:321–323, Aug 1964.

[4] G. S. Guralnik, C. R. Hagen, and T. W. B. Kibble. Global conservation laws and massless particles. *Phys. Rev. Lett.*, 13:585–587, Nov 1964.

[5] Peter W. Higgs. Broken symmetries and the masses of gauge bosons. *Phys. Rev. Lett.*, 13:508–509, Oct 1964.

[6] Peter W. Higgs. Spontaneous symmetry breakdown without massless bosons. *Phys. Rev.*, 145:1156–1163, May 1966.

[7] Georges Aad et al. Observation of a new particle in the search for the Standard Model Higgs boson with the ATLAS detector at the LHC. *Phys.Lett.*, B716:1–29, 2012.

[8] Serguei Chatrchyan et al. Observation of a new boson at a mass of 125 GeV with the CMS experiment at the LHC. *Phys.Lett.*, B716:30–61, 2012.

[9] Nicola Cabibbo. Unitary Symmetry and Leptonic Decays. *Phys.Rev.Lett.*, 10:531–533, 1963.

[10] Makoto Kobayashi and Toshihide Maskawa. CP Violation in the Renormalizable Theory of Weak Interaction. *Prog.Theor.Phys.*, 49:652–657, 1973.

[11] Patricia Ball, Gareth W. Jones, and Roman Zwicky. $b \to v\gamma$ beyond qcd factorization. *Phys. Rev. D*, 75:054004, Mar 2007.

[12] Benjamin Grinstein, Yuval Grossman, Zoltan Ligeti, and Dan Pirjol. Photon polarization in $b \to x\gamma$ in the standard model. *Phys. Rev. D*, 71:011504, Jan 2005.

[13] Matthias Neubert. Radiative b decays: Standard candles of flavor physics. pages 252–264, 2002.

[14] Tobias Hurth. Present status of inclusive rare b decays. *Rev. Mod. Phys.*, 75:1159–1199, Oct 2003.

[15] A. Ali, B.D. Pecjak, and C. Greub. Towards $b \to v\gamma$ decays at nnlo in scet. *The European Physical Journal C*, 55(4):577–595, 2008.

[16] Mikocaj Misiak and Matthias Steinhauser. Three-loop matching of the dipole operators. *Nuclear Physics B*, 683(1,Äì2):277 – 305, 2004.

[17] Martin Gorbahn and Ulrich Haisch. Effective hamiltonian for non-leptonic decays at {NNLO} in {QCD}. *Nuclear Physics B*, 713(1,Äì3):291 – 332, 2005.

[18] Michal Czakon, Ulrich Haisch, and Mikolaj Misiak. Four-Loop Anomalous Dimensions for Radiative Flavour-Changing Decays. *JHEP*, 0703:008, 2007.

[19] Benjamin Grinstein and Dan Pirjol. *cp* asymmetry in $b^0(t) \to k_S\pi^0\gamma$ in the standard model. *Phys. Rev. D*, 73:014013, Jan 2006.

[20] Lisa L. Everett, Gordon L. Kane, S. Rigolin, Lian-Tao Wang, and Ting T. Wang. Alternative approach to $b \to s\gamma$ in the uMSSM. *JHEP*, 0201:022, 2002.

[21] Michael Gronau, Yuval Grossman, Dan Pirjol, and Anders Ryd. Measuring the photon polarization in $B \to K\pi\pi\gamma$. *Phys.Rev.Lett.*, 88:051802, 2002.

[22] Michael Gronau and Dan Pirjol. Photon polarization in radiative B decays. *Phys.Rev.*, D66:054008, 2002.

[23] Aaij et al. Observation of photon polarization in the $b \to s\gamma$ transition. *Phys. Rev. Lett.*, 112(arXiv:1402.6852. CERN-PH-EP-2014-026. LHCB-PAPER-2014-001):161801. 17 p, Feb 2014.

[24] V. Orlovsky and V. Shevchenko. Photon polarization in radiative $b \to \phi k\gamma$ decay. *Phys. Rev. D*, 77:093003, May 2008.

[25] D. Melikhov, N. Nikitin, and S. Simula. Probing right-handed currents in $B \to K^* l^+ l^-$ transitions. *Phys.Lett.*, B442:381–389, 1998.

[26] C. Kim, Yeong Kim, Cai-Dian Lü, and Takuya Morozumi. Azimuthal angle distribution in $b \to k^*(\to k\pi) l^+ l^-$ in the low invariant $m_{l^+l^-}$ region. *Phys. Rev. D*, 62:034013, Jul 2000.

[27] Yuval Grossman and Dan Pirjol. Extracting and using photon polarization information in radiative b decays. *Journal of High Energy Physics*, 2000(06):029, 2000.

[28] Frank Krüger, Lalit Sehgal, Nita Sinha, and Rahul Sinha. Angular distribution and *CP* asymmetries in the decays $\overline{B} \to K^- \pi^+ e^- e^+$ and $\overline{B} \to \pi^- \pi^+ e^- e^+$. *Phys. Rev. D*, 61:114028, May 2000.

[29] J Lefrançois and M H Schune. Measuring the photon polarization in $b \to s\gamma$ using the $B \to K^* e^+ e^-$ decay channel. Technical Report LHCb-PUB-2009-008. CERN-LHCb-PUB-2009-008. LHCb-INT-2009-007, CERN, Geneva, Jun 2009.

[30] Aaij et al. Measurement of the $b \to k^*(892)^0 e^+ e^-$ branching fraction at low dilepton mass. *Journal of High Energy Physics*, 2013(5), 2013.

[31] Aaij et al. Angular analysis of the decay $b \to k^*(892)^0 e^+ e^-$ in the low-q^2 region. 2015.

[32] Damir Becirevic and Elia Schneider. On transverse asymmetries in $b \to k^* l^+ l^-$. *Nuclear Physics B*, 854(2):321 – 339, 2012.

[33] David Atwood, Tim Gershon, Masashi Hazumi, and Amarjit Soni. Mixing-induced *cp* violation in $b \to P_1 P_2 \gamma$ in search of clean new physics signals. *Phys. Rev. D*, 71:076003, Apr 2005.

[34] J. Beringer et al. Review of particle physics. *Phys. Rev. D*, 86:010001, Jul 2012.

[35] Bernard Aubert et al. Measurement of Time-Dependent CP Asymmetry in $B^0 \to K^0_S \pi^0 \gamma$ Decays. *Phys.Rev.*, D78:071102, 2008.

[36] Y. Ushiroda et al. Time-Dependent CP Asymmetries in $B^0 \to K^0_S \pi^0 \gamma$ transitions. *Phys.Rev.*, D74:111104, 2006.

[37] Franz Muheim, Yuehong Xie, and Roman Zwicky. Exploiting the width difference in $b_s \to \phi\gamma$. *Physics Letters B*, 664(3):174–179, 2008.

[38] Thomas Mannel and Stefan Recksiegel. Flavour-changing neutral current decays of heavy baryons. *Journal of Physics G: Nuclear and Particle Physics*, 24(5):979, 1998.

[39] Gudrun Hiller and Alex Kagan. Probing for new physics in polarized Lambda(b) decays at the Z. *Phys.Rev.*, D65:074038, 2002.

[40] Federica Legger and Thomas Schietinger. Photon helicity in $\Lambda_b \to pK\gamma$ decays. *Phys.Lett.*, B645:204–212, 2007.

[41] G. Hiller T. Blake, T. Gershon. Rare b hadron decays at the lhc. 2015.

[42] R Aaij et al. Measurements of the $\Lambda_b^0 \to J/\psi\Lambda$ decay amplitudes and the Λ_b^0 polarisation in pp collisions at $\sqrt{s} = 7$ TeV. *Phys.Lett.*, B724:27–35, 2013.

[43] D. Be*f*çirevi*f*á, E. Kou, A. Le Yaouanc, and A. Tayduganov. Future prospects for the determination of the wilson coefficient $c'_{7\gamma}$. *Journal of High Energy Physics*, 2012(8), 2012.

[44] Bharucha et al. Implications of lhcb measurements and future prospects. *The European Physical Journal C*, 73(4), 2013.

[45] R Aaij et al. Measurement of the ratio of branching fractions BR(B0 -> K*0 gamma)/BR(Bs0 -> phi gamma) and the direct CP asymmetry in B0 -> K*0 gamma. *Nucl.Phys.*, B867:1–18, 2013.

[46] B. Adeva et al. Roadmap for selected key measurements of LHCb. 2009.

[47] Lyndon Evans and Philip Bryant. Lhc machine. *Journal of Instrumentation*, 3(08):S08001, 2008.

[48] The LHCb Collaboration. Absolute luminosity measurements with the lhcb detector at the lhc. *Journal of Instrumentation*, 7(01):P01010, 2012.

[49] R Aaij et al. Measurement of B meson production cross-sections in proton-proton collisions at $\sqrt{s} = 7$ TeV. *J. High Energy Phys.*, 08(arXiv:1306.3663. CERN-PH-EP-2013-095. LHCB-PAPER-2013-004):117. 13 p, Jul 2013. Comments: 13 pages, 12 figures, 1 table, submitted to JHEP.

[50] A. Augusto Alves et al. The LHCb Detector at the LHC. *JINST*, 3:S08005, 2008.

[51] M. Adinolfi et al. Performance of the lhcb rich detector at the lhc. *The European Physical Journal C*, 73(5), 2013.

[52] C Abellan Beteta et al. Time alignment of the front end electronics of the lhcb calorimeters. *Journal of Instrumentation*, 7(08):P08020, 2012.

[53] Irina Machikhiliyan and the LHCb calorimeter group. Current status and performance of the lhcb electromagnetic and hadron calorimeters. *Journal of Physics: Conference Series*, 293(1):012052, 2011.

[54] J Lefrançois, F Machefert, and A Martens. Calibration of the LHCb calorimeters with energy flow. Technical Report LHCb-INT-2010-021. CERN-LHCb-INT-2010-021, CERN, Geneva, Apr 2010.

[55] Ivan Belyaev, Victor Egorychev, and Daria Savrina. ECAL calibration within Kali framework: A Mass distribution fit, A method calibration with the real data. Technical Report LHCb-INT-2011-049. CERN-LHCb-INT-2011-049, CERN, Geneva, Oct 2011.

[56] A Arefev, S Barsuk, I Belyaev, B Bobchencko, L Camilleri, V Egorychev, Yu Gilitsky, A Golutvin, O Gouchtchine, I Korolko, T Kvaratskheliia, I Machikhilian, M Martemyanov, E Melnikov, A Morozov, M Prokudin, D Roussinov, V Rusinov, A Schopper, S Schuvalov, A Soldatov, E Tarkovski, and K Voronchev. Beam Test Results of the LHCb Electromagnetic Calorimeter. Technical Report LHCb-2007-149. CERN-LHCb-2007-149, CERN, Geneva, May 2008. revised version submitted on 2008-05-15 09:09:53.

[57] Andrew Powell. Reconstruction and PID performance of the LHCb RICH detectors. *Nucl.Instrum.Meth.*, A639:260–263, 2011.

[58] Antunes-Nobrega et al. *LHCb trigger system: Technical Design Report*. Technical Design Report LHCb. CERN, Geneva, 2003. revised version number 1 submitted on 2003-09-24 12:12:22.

[59] Vladimir V Gligorov. A single track HLT1 trigger. Technical Report LHCb-PUB-2011-003. CERN-LHCb-PUB-2011-003. LHCb-INT-2010-053, CERN, Geneva, Jan 2011.

[60] Roel Aaij and Johannes Albrecht. Muon triggers in the High Level Trigger of LHCb. Technical Report LHCb-PUB-2011-017. CERN-LHCb-PUB-2011-017, CERN, Geneva, Sep 2011.

[61] M Williams, Vladimir V Gligorov, C Thomas, H Dijkstra, J Nardulli, and P Spradlin. The HLT2 Topological Lines. Technical Report LHCb-PUB-2011-002. CERN-LHCb-PUB-2011-002, CERN, Geneva, Jan 2011.

[62] Byron P. Roe, Hai-Jun Yang, Ji Zhu, Yong Liu, Ion Stancu, et al. Boosted decision trees, an alternative to artificial neural networks. *Nucl.Instrum.Meth.*, A543:577–584, 2005.

[63] S Tolk, J Albrecht, F Dettori, and A Pellegrino. Data driven trigger efficiency determination at LHCb. Technical Report LHCb-PUB-2014-039. CERN-LHCb-PUB-2014-039, CERN, Geneva, May 2014.

[64] Albert Puig Navarro and Ricardo Graciani Diaz. *First measurements of radiative B decays in LHCb*. PhD thesis, Barcelona U., 2012. Presented 09 Mar 2012.

[65] Aaij et al. Absolute luminosity measurements with the LHCb detector at the LHC. *J. Instrum.*, 7(arXiv:1110.2866. LHCB-PAPER-2011-015. CERN-PH-EP-2011-157):P01010. 47 p, Oct 2011.

[66] Roel Aaij et al. Precision luminosity measurements at LHCb. *JINST*, 9:12005, 2014.

[67] P Mato. GAUDI-Architecture design document. Technical Report LHCb-98-064, CERN, Geneva, Nov 1998.

[68] G. Barrand, I. Belyaev, P. Binko, M. Cattaneo, R. Chytracek, et al. GAUDI - A software architecture and framework for building HEP data processing applications. *Comput.Phys.Commun.*, 140:45–55, 2001.

[69] Antunes-Nobrega et al. *LHCb computing: Technical Design Report*. Technical Design Report LHCb. CERN, Geneva, 2005. Submitted on 11 May 2005.

[70] R. Brun and F. Rademakers. ROOT: An object oriented data analysis framework. *Nucl.Instrum.Meth.*, A389:81–86, 1997.

[71] The root project. `http://root.cern.ch/`.

[72] I. Belyaev, P. Charpentier, S. Easo, P. Mato, J. Palacios, et al. Simulation application for the LHCb experiment. *eConf*, C0303241:TUMT003, 2003.

[73] I Belyaev, T Brambach, N H Brook, N Gauvin, G Corti, K Harrison, P F Harrison, J He, P H Hilten, C R Jones, M Lieng, G Manca, S Miglioranzi, P Robbe, V Vagnoni, M Whitehead, and J Wishahi. Handling of the generation of primary events in Gauss, the LHCb simulation framework. Nov 2010.

[74] Torbjorn Sjostrand, Stephen Mrenna, and Peter Z. Skands. PYTHIA 6.4 Physics and Manual. *JHEP*, 0605:026, 2006.

[75] D.J. Lange. The EvtGen particle decay simulation package. *Nucl.Instrum.Meth.*, A462:152–155, 2001.

[76] Elisabetta Barberio, Bob van Eijk, and Zbigniew Was. PHOTOS: A Universal Monte Carlo for QED radiative corrections in decays. *Comput.Phys.Commun.*, 66:115–128, 1991.

[77] S. Agostinelli et al. GEANT4: A Simulation toolkit. *Nucl.Instrum.Meth.*, A506:250–303, 2003.

[78] The LHCb collaboration. The boole project. `http://lhcb-release-area.web.cern.ch/LHCb-release-area/DOC/boole/`.

[79] The LHCb collaboration. The brunel project. `http://lhcb-release-area.web.cern.ch/LHCb-release-area/DOC/brunel/`.

[80] The LHCb collaboration. The moore project. `http://lhcb-release-area.web.cern.ch/LHCb-release-area/DOC/moore/`.

[81] The LHCb collaboration. The davinci project. `http://lhcb-release-area.web.cern.ch/LHCb-release-area/DOC/davinci/`.

[82] O Callot. Calorimeter data format and 2-D zero suppression scheme. Technical Report LHCb-99-037, CERN, Geneva, Oct 1999.

[83] V. Breton, N. Brun, and P. Perret. A clustering algorithm for the LHCb electromagnetic calorimeter using a cellular automaton. 2001.

[84] R. Hollebeek. Topics in calorimetry for high-energy physics. 1991.

[85] O. Deschamps, F.P. Machefert, M.H. Schune, G. Pakhlova, and I. Belyaev. Photon and neutral pion reconstruction. 2003.

[86] K.A. Olive et al. Review of Particle Physics. *Chin.Phys.*, C38:090001, 2014.

[87] Diego Alejandro Roa Romero and Pascal Perret. *Study of charmless $B^0_{d,s} \to h^+h'^-\pi^0$ decays in LHCb*. PhD thesis, Clermont-Ferrand U., May 2013. Presented 24 May 2013.

[88] OLIVIER DESCHAMPS. *Recherche du boson de higgs du modele standard minimal dans les etats finals hadroniques avec le detecteur aleph a lep 2*. PhD thesis, 1999. Thèse de doctorat dirigée par Gay, Pascal Physique Clermont Ferrand 2 1999.

[89] F P Machefert. Photon Identification. Technical Report LHCb-2004-032, CERN, Geneva, Apr 2004.

[90] Krzysztof Grzegorz Sobczak. *Study of charmless three-body decays of neutral B mesons with the LHCb spectrometer*. PhD thesis, 2011. 2011CLF22202.

[91] Andreas Hoecker, Peter Speckmayer, Joerg Stelzer, Jan Therhaag, Eckhard von Toerne, and Helge Voss. TMVA: Toolkit for Multivariate Data Analysis. *PoS*, ACAT:040, 2007.

[92] G. W. Corder and D. I. Foreman. *onparametric Statistics for Non-Statisticians: A Step-by-Step Approach*. John Wiley and Sons, Inc., 2009.

[93] Lior Rokach and Oded Z Maimon. *Data mining with decision trees: theory and applications*, volume 69. World Scientific Pub Co Inc, 2008.

[94] L Shchutska, A Golutvin, and I Belyaev. "Study of radiative penguin decays $B \to K^{*0}\gamma$ and $B_s \to \phi\gamma$ at LHCb". Technical Report LHCb-2007-030. CERN-LHCb-2007-030, CERN, Geneva, May 2007.

[95] Muriel Pivk and Francois R. Le Diberder. SPlot: A Statistical tool to unfold data distributions. *Nucl.Instrum.Meth.*, A555:356–369, 2005.

[96] Heavy Flavor Averaging Group. Averages of b-hadron, c-hadron, and τ-lepton properties as of summer 2014. 2014.

[97] b-hadron lifetime measurements with exclusive $b \to J/\psi X$ decays reconstructed in the 2010 data. Mar 2011. LHCb-ANA-2011-001.

[98] Roel Aaij et al. Measurement of the B_c^+ meson lifetime using $B_c^+ \to J/\psi\mu^+\nu_\mu X$ decays. *Eur.Phys.J.*, C74(5):2839, 2014.

[99] The roofit project. `https://root.cern.ch/drupal/content/roofit`.

[100] R. Aaij et al. Measurement of the ratio of branching fractions $\mathcal{B}(B^0 \to K^{*0}\gamma)/\mathcal{B}(B_s^0 \to \phi\gamma)$ and the direct CP asymmetry in $B^0 \to K^{*0}\gamma$. *Nucl. Phys.*, B867:1–18, 2013.

[101] Argus Collaboration. Search for hadronic $b \to u$ decays. *Physics Letters B*, 241:278–282, May 1990.

[102] M. Oreglia. A Study of the Reactions $\psi' \to \gamma\gamma\psi$. 1980.

[103] D. Martinez Santos and F. Dupertuis. Mass distributions marginalized over per-event errors. *Nuclear Instruments and Methods in Physics Research Section A: Accelerators, Spectrometers, Detectors and Associated Equipment*, 764(0):150 – 155, 2014.

[104] LHCb collaboration. A package for extracting pid performance from data and mc. `https://twiki.cern.ch/twiki/bin/view/LHCb/PIDCalibPackage`.

[105] Fatima Soomro. *Radiative decays of B mesons at LHCb.* PhD thesis.

[106] Roel Aaij et al. Measurements of the B^+, B^0, B_s^0 meson and Λ_b^0 baryon lifetimes. *JHEP*, 1404:114, 2014.

[107] O. Callot. FastVelo, a fast and efficient pattern recognition package for the Velo. September 2011.

[108] K. Wyllie, F. Alessio, R. Jacobsson, and N. Neufeld. Electronics Architecture of the LHCb Upgrade. 2011.

[109] Aaij et al. Measurement of the $\bar{B}^0 - B^0$ and $\bar{B}_s^0 - B_s^0$ production asymmetries in pp collisions at $\sqrt{s} = 7$ TeV. *Phys. Lett. B*, 739(arXiv:1408.0275. CERN-PH-EP-2014-181. LHCB-PAPER-2014-042):218. 24 p, Aug 2014. Comments: Updated to v2 after journal review.

Résumé

Cette thèse est dédiée à l'étude des désintégrations $B_s^0 \to \phi\gamma$ au LHCb afin de mesurer la polarisation du photon . Au niveau des quarks, ces désintégrations procèdent via une transition pingouin $b \to s\gamma$ et sont sensibles aux eventuelles contributions virtuelles de Nouvelle Physique. La mesure de la polarisation du photon permet de tester la structure $V - A$ du couplage du Modèle Standard dans les processus des diagrammes de boucles de pingouin. Cette mesure peut être réalisée en étudiant le taux de désintégration dépendant du temps des mésons B. Une analyse délicate a été faite pour comprendre la distribution du temps propre et l'acceptance de sélection qui affecte cette distribution. Afin de contrôler l'acceptance de temps propre, des méthodes basées sur les données ont été développées. Plusieurs stratégies utilisées dans la mesure de la polarisation des photons sont introduites et des résultats préliminaires sont présentés. De plus, une étude de certains effets systématiques est discutée. Dans le cadre de l'étude des désintégrations radiatives, une nouvelle procedure d'identification de photons a été développée et nous avons fourni un outil pour calibrer la performance de la variable de séparation photon/pion neutre sur la simulation. Ces outils sont d'intérêt général pour la collaboration LHCb et sont largement utilisés.

Abstract

This thesis is dedicated to the study of the photon polarization in $B_s^0 \to \phi\gamma$ decays at LHCb. At the quark level, such decays proceed via a $b \to s\gamma$ penguin transition and are sensitive to possible virtual contributions from New Physics. The measurement of the photon polarization stands also as a test of the $V - A$ structure of the Standard Model coupling in the processes mediated by loop penguin diagrams. The measurement of the photon polarization can be done through a study of the time-dependent decay rate of the B meson. A delicate treatment has been done to understand the proper time distribution and the selection acceptance affecting it. To control the proper time acceptance, data driven control methods have been developed. Several possible strategies to measure the photon polarization are introduced and preliminary blinded results are presented. A study of some of the systematic effects is discussed. In the context of studying radiative decays, the author has developed a new photon identification procedure and has provided a tool to calibrate the performance of the photon/neutral pion separation variable on simulation. Those tools are of general interest for the LHCb collaboration and are widely used.

Keywords: LHCb detector - Heavy Flavor Physics - Radiative Decays - Effective Field Theories - $B_s^0 \to \phi\gamma$ - Photon Polarization - Proper Time - Photon Identification - γ/π^0 separation.